PROJECT FIRE

FLOW FIELD PREDICTION AND ANALY

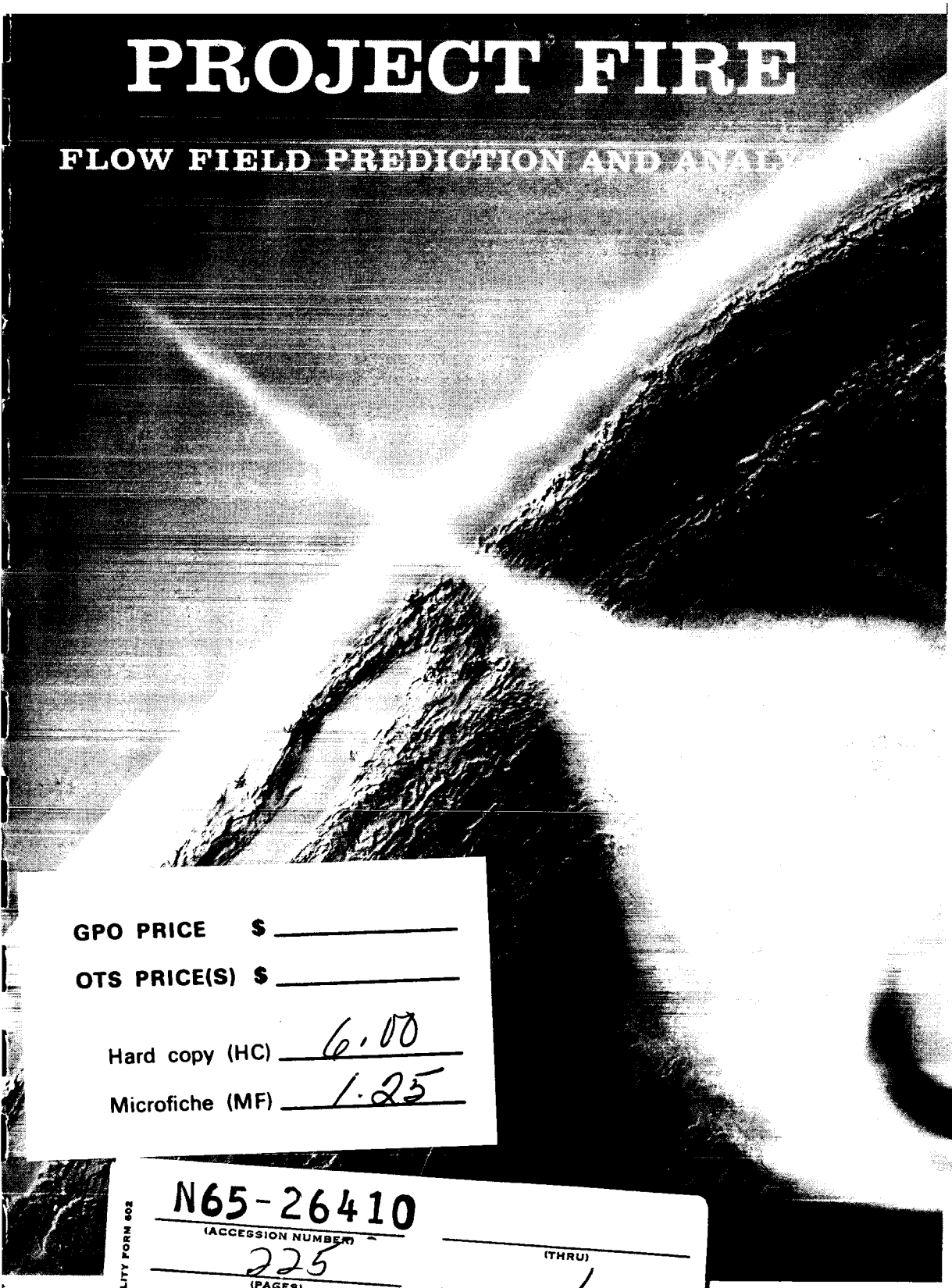

Lockheed MISSILES & SPACE COMPANY

A GROUP DIVISION OF LOCKHEED AIRCRAFT CORPORATION

SUNNYVALE, CALIFORNIA

TECHNICAL REPORT

PROJECT FIRE

FLOW FIELD PREDICTION AND ANALYSIS

FINAL REPORT

by

M. Vinokur

W. E. Nicolet

A. C. Buckingham

H. Hoshizaki

M-12-65-1 **MARCH 1965**

Work Carried Out Under Contract NASA 1-3417

Lockheed MISSILES & SPACE COMPANY

A GROUP DIVISION OF LOCKHEED AIRCRAFT CORPORATION

SUNNYVALE, CALIFORNIA

FOREWORD

The work described in this report was completed for the National Aeronautics and Space Administration , Flight Reentry Programs Office, Langley Research Center, Hampton, Virginia; under the terms and specifications of Contract NASA 1-3417.

The work was performed in Lockheed Missiles & Space Company's Aerospace Sciences Laboratory under R. E. Gaumer, Director.

Prepared by:

M. Vinokur, Member
Aerospace Sciences Laboratory

W. E. Nicolet, Member
Aerospace Sciences Laboratory

A. C. Buckingham, Member
Aerospace Sciences Laboratory

H. Hoshizaki, Senior Member
Aerospace Sciences Laboratory

Approved by:

R. Capiaux, Senior Member
Aerospace Sciences Laboratory

H. Hoshizaki, Senior Member
Aerospace Sciences Laboratory

ABSTRACT

This report presents the technical discussion of the methods used and the results of calculations on the details of the flow field, and convective and radiative heating predictions for the NASA "FIRE" Reentry Package at two trajectory points. The first point (Cases I and II) corresponds to a time 25 seconds after entry at 400, 000 ft altitude. The vehicle velocity 25 seconds after entry is 34, 582 ft/sec and the altitude is 171, 611 ft. Case I is based on axisymmetric flow conditions (zero angle-of-attack) while Case II is slightly asymmetric (5 degree angle-of-attack) with respect to incident stream. Case III corresponds to a time after entry of 15 seconds, with a vehicle velocity of 37, 439 ft/sec and altitude of 259, 113 ft. Case III is based on axisymmetric flow conditions. Actual vehicle geometry varies between the two trajectory points as a result of the planned detachment of the outer heat shield during the interval between the two flight trajectory points. The calculations reflect this change in geometry. Thermodynamic properties of the free stream are from the proposed atmospheric model, supplied in tabulated form by NASA (Proposed Revision of U. S. Standard Atmosphere, 0-700 km).

The calculations include determination of the complete inviscid flow fields, finite rate chemistry for the nonequilibrium flow, convective heating as well as both equilibrium and nonequilibrium radiative heating calculations. The effect of self-absorption on the equilibrium radiation is estimated by considering the spectral distribution of the emission coefficient. Results given include state of the shock-layer gas (to the region of separation streamline closure) magnitude and distributions of the components of the heat transfer (radiation and convection) over the entire vehicle surface for the axisymmetric equilibrium case, and in the angle-of-attack plane for the asymmetric case. The nonequilibrium analysis, Case III, results in similar heat-transfer distributions over the front face of the reentry package. In addition, the spectral intensity and distributions of the radiative heating at the stagnation point are supplied. Results of

the calculations appear in graphical form with some additional flow-field data supplied in tabulated form. Descriptions of analytical techniques used, with supporting data and reference to governing principles, as well as related investigations are given in the report.

Added discussion on the computer codes used in the calculations and supplemental topics appear in appendixes to the report.

ACKNOWLEDGMENTS

The authors would like to express their sincere appreciation for the work of their associates in the laboratory on various technical topics, written contributions, and final preparation of this report. Particular acknowledgment and thanks are extended to R. Capiaux for his Program Management, many overall suggestions, critiques, and aid in the calculations; O. R. Burggraf for his work on the base heating; G. Hohnstreiter for his work on the radiation heating; and the following laboratory members for their work in coding the equations for computer operation, modification of existing codes, preparation of input data and reduction of results; H. R. Kirch, E. M. Kimball, M. Washington, and R. D. Clark.

CONTENTS

ILLUSTRATIONS

TABLES

NOTATION

A	enthalpy constant defined by Eq. (2.5)
A	constant defined by Eq. (3.16)
A	Einstein transition probability
A_i	functions of η_o defined by Eq. (A.4)
A_2	designates a diatomic molecule in an unexcited state
A_2^*	designates a diatomic molecule in an excited state
A_{38i}	functions of η in Eq. (A.1)
a	speed of sound
$\bar{a}$	nondimensional speed of sound $\left(\bar{a} \equiv a/V_\infty\right)$
a_i	functions defined by Eq. (A.6)
B	shock wave bluntness parameter defined by Eq. (3.1)
B	constant defined by Eq. (3.16)
B	Einstein transition probability
B_ν	Planck function $\left(\text{watts cm}^{-2}\ \text{ster}^{-1}\ \text{ev}^{-1}\right)$
b_i	constants in Eq. (3.18)
b_i	functions defined by Eq. (A.7)
C	constant (p. 2-88)
C	constant defined by Eq. (3.16)
c	velocity of light
$\bar{c}_{p_i}$	nondimensional specific heat at constant pressure, i^{th} specie $\left(\bar{c}_{p_i} \equiv \frac{c_{p_i}}{\hat{R}}\right)$

D	constant defined by Eq. (3.16)
D_e	dissociation energy of a specified electronic level of a diatomic molecule
E	the emissivity of a plane slab, as defined by Eq. (3.75)
e	charge of an electron
e^-	designates a free electron
$\bar{e}_{D_i}, \bar{e}_{I_i}$	nondimensional dissociation, ionization energy, i^{th} specie $\left(\bar{e}_i \equiv \frac{e_i}{V_\infty^2}\right)$
F^{j-k}	fractional parentage coefficient
f_i	functions of η defined by Eq. (3.8)
f_i	functions of $\bar{R}$ defined by Eq. (3.18)
f_{LU}	electronic oscillator strength
G_{bf}^{j-k}	bound-free Gaunt factor (p. 3-31)
g	statistical weight
g_{ff}	free-free Gaunt factor
g_i	functions of η defined by Eq. (3.10)
h	specific enthalpy
h	altitude
h	Planck's constant
h_i	functions of η defined by Eq. (3.9)
$h\nu$	frequency in energy units (ev)
$\bar{h}(x)$	nondimensional local enthalpy (subsection 3.2) $\left(\bar{h}(x) \equiv \frac{h(x)}{V_\infty^2}\right)$
$I_{h\nu}$	spectral intensity $\left(\text{watts cm}^{-2}\ \text{ster}^{-1}\ \text{ev}^{-1}\right)$
I_{OT}	total intensity, as calculated by the thin gas assumption

I_{SA}	total intensity, as calculated by methods which include the effects of self-absorption
I_ν	spectral intensity $\left(\text{watts cm}^{-2}\ \text{ster}^{-1}\ \text{sec}\right)$
$\mathcal{J}_\nu$	nonequilibrium source function (p. 2-78)
j	integrated emission coefficient $\left(\text{watts cm}^{-3}\ \text{ster}^{-1}\right)$
$j_{h\nu}$	spectral emission coefficient $\left(\text{watts cm}^{-3}\ \text{ster}^{-1}\ \text{ev}^{-1}\right)$
j_ν	spectral emission coefficient $\left(\text{watts cm}^{-3}\ \text{ster}^{-1}\ \text{sec}\right)$
K	shock wave curvature
$\bar{K}$	nondimensional shock wave curvature $\left(\bar{K} \equiv R_B K\right)$
$K_{F_i}, K_{R_i}, K_{C_i}$	foward, reverse chemical reaction rate constants; equilibrium constant, i^{th} specie (subsection 3.2)
$K_2 K_4^\gamma$	function of M_∞ and γ defined by Eq. (A.2)
k	Boltzmann constant
k_f	forward rate coefficient for radiative reactions
k_r	reverse rate coefficient for radiative reactions
L_i/θ_i	component of species production i^{th} reaction (subsection 3.2)
M	Mach number
M	designates a noninteracting particle in a chemical reaction
M_e	equivalent Mach number defined by Eq. (3.13)
m_e	electron mass
$N_2^+\left(B^2\Sigma^+\right)$	standard spectroscopic notation for the $B^2\Sigma^+$ electronic level of the N_2^+ ion (see Ref. 52)
n_k^j	number of particles per cm^3 of the k^{th} specie in its j^{th} electronic level

n	principal quantum number
$\bar{n}_i(x)$	nondimensional molar fraction, i^{th} specie (subsection 3.2) $\left(\bar{n}_i(x) \equiv \frac{n_i(x)}{n_o}\right)$
n_o	inverse of the molecular weight of ambient air (subsection 3.2)
p	pressure
$\bar{p}$	nondimensional pressure $\left(p \equiv \frac{p}{\rho_\infty V_\infty^2}\right)$
p_o	standard atmospheric pressure
p_{ST}	stagnation point pressure
Q	partition function
q', q''	Franck-Condon factors
q_C, q_c	convective heat-transfer rate
q_R	radiative heat-transfer rate
q_T	total heat-transfer rate
R	spherical radial coordinate
R	nose radius (p. 2-88)
R	gas constant for undissociated air
$\hat{R}$	universal gas constant
$\bar{R}$	nondimensional radius $\left(\bar{R} \equiv R/R_B\right)$
Ry	Rydberg constant
$\mathcal{R}$	streamline radius of curvature
r	cylindrical coordinate normal to the shock axis of symmetry
$\tilde{r}$	cylindrical coordinate normal to the body axis of symmetry, Case II

$\bar{r}$	nondimensional cylindrical coordinate $\left(\bar{r} \equiv r/R_B\right)$
S	specific entropy
s	geometrical length of a ray (p. 2-75)
s	distance along streamline
T	temperature (° K, ° R)
T_e	a constant used in the determination of the energy levels of diatomic molecules
T_i	kinetic temperature (° K)
$\bar{T}(x)$	nondimensional local temperature (subsection 3.2) $\left(\bar{T}(x) = \dfrac{T(x) \cdot \hat{R} \cdot n_o}{V_\infty^2}\right)$
t	time
$\bar{u}$	velocity in the x direction, nondimensionalized by V_∞
$\vec{V}, V$	velocity vector, magnitude
V	volume
$\bar{V}$	nondimensional velocity $(\bar{V} \equiv V/V_\infty)$
V_θ, V_R	velocity components in θ, R direction
$\bar{v}$	velocity in the r direction, nondimensionalized by V_∞
w	weight factor (p. 3-42)
X_i	ionization energy of the i^{th} species
x	cartesian or cylindrical coordinate parallel to the shock axis of symmetry
x	intrinsic streamline distance, measured from the shock front origin (subsection 3.2)

$\tilde{x}$	cartesian or cylindrical coordinate parallel to the body axis of symmetry, Case II
y	cartesian coordinate normal to the shock axis of symmetry
$\tilde{y}$	cartesian coordinate normal to the body axis of symmetry, Case II
z	transformed x coordinate defined by Eq. (B.3)
$\bar{z}$	nondimensional cylindrical coordinate parellel to the axis of symmetry, Case III (p. 3-11)

Greek Notation

α	angle-of-attack of the body
α	angle between shock normal and free-stream direction
α	recombination coefficient
β	stagnation point velocity gradient
β	flow angle relative to free stream
β	angle between shock and body coordinates
Γ	radiation loss parameter
γ	isentropic index defined by Eq. (3.5)
γ'	equivalent perfect gas value of γ defined on p. 3-7
ΔI	integral defined on p. 3-42
δ	flow angle relative to free stream
δ	asymmetric flow parameter defined on p. 3-3
δ	length of ray
ϵ	angle-of-attack of the shock wave
η	orthoginal shock oriented coordinate defined in p. 3-1
η_o	value of η at which $f_0(\eta) = 0$
θ	spherical polar coordinate

θ	flow angle relative to free stream
θ	temperature of bound electronic states
θ	angle between radiation ray and stagnation streamline or body normal
λ	wavelength
λ_S	particle mean free path based on Sutherland law cross section (Appendix C)
$\lambda(i)$	i^{th} particle mean free path (Appendix C)
μ	reduced molecular mass
μ	coefficient of kinematic viscosity
μ_P	Planck mean absorption coefficient
μ'_ν	spectral absorption coefficient (corrected for induced emission)
ν	frequency (sec^{-1})
ξ	orthogonal shock oriented coordinate
ξ	binding energy of an electron
ρ	density
$\bar{\rho}$	nondimensional density $\left(\bar{\rho} \equiv \frac{\rho}{\rho_\infty}\right)$
σ	cross section
σ	Stefan-Boltzmann constant
τ_e	significant time (p. 3-37)
ϕ	shock angle relative to free stream
φ	azimuthal angular coordinate
ψ	stream function for Case III defined by Eq. (3.14)
$\psi_1 \psi_2$	stream function for Cases I and II defined in p. 3-2

$\bar{\psi}, \bar{\psi}_1, \bar{\psi}_2$	nondimensional stream function $\left(\bar{\psi} = \psi/\rho_\infty V_\infty , \bar{\psi}_1 = \psi_1/\rho_\infty V_\infty , \bar{\psi}_2 = \psi_2/\rho_\infty V_\infty\right)$
ω	solid angle
ω_e	a constant used in the determination of the energy levels of diatomic molecules
$\omega_e x_e$	a constant used in the determination of the energy levels of diatomic molecules
$\omega_e y_e$	a constant used in the determination of the energy levels of diatomic molecules

Superscripts

j	a property of an electronic state of an atomic species
j-k	a property of the transition from the j^{th} state to the k^{th} state
k	a property of an electronic state of an ionic species
k-j	a property of the transition from the k^{th} state to the j^{th} state
T	total
'	a property of a vibrational level in an upper electronic state
''	a property of a vibrational level in a lower electronic state
–	nondimensional variable
*	critical (sonic) conditions
~	coordinate referred to body axes (Case II)

Subscripts

a	atomic property
a^+	ionic property
B, b	conditions on the body
bf	bound-free transition

e, e^-	property of a free electron
f	forward
fb	free-bound transition
ff	free-free transition
$h\nu$	a spectral quantity
I	an induced quantity
L	a property of a lower electronic state
LU or L-U	a property of the transition between a lower and an upper electronic state
LV"	a property of a vibrational level of the lower electronic state
m	a molecular property
m	a measured quantity (p. 2-54)
o	standard atmospheric reference conditions
OT	a property calculated by using the thin gas approximation
r	reverse
S, s	conditions behind the shock wave
SA	a property calculated by methods which include the effects of self-absorption
U	a property of an upper electronic state
UV'	a property of a vibrational level of an upper electronic level
V'V" or V'-V"	a property of the transition between a vibrational level of an upper electronic state and a vibrational level of a lower electronic level
∞	free-stream conditions

Section 1
INTRODUCTION

Shock-layer flow fields enveloping blunt reentry configurations moving through the upper atmosphere at superorbital velocity are governed by a variety of complex, high-temperature physical-chemical processes. Even if one disregards the sometimes encountered near noncontinuum effects in rarefied gas flow (e.g., thickened bow shock front, partial to complete viscous domination of the shock layer, etc.) adequate theoretical description of the interrelated physical effects represents a formidable task. The "FIRE" flow fields described in this report develop from just such reentry flight conditions. Thus, analysis requires the use of theoretical procedures relating the disciplines of atomic physics, chemical kinetics, and fluid mechanics to describe the shock-layer flow environment and, ultimately, to predict the heating environment encountered by the reentry package.

Physically, the strong bow shock wave generated by the blunt configuration in hypersonic flow is the locus for initiating energetic excitation of the basic constituent species in the gas. The total kinetic energy available in the flow at the flight conditions investigated for the "FIRE" studies is of the order required to initiate significant dissociation and ionization as well as contributing to molecular vibration and rotation modes and to populate bound electronic states of the components. Hence, conditions are developed which govern, in a complicated way, the production of subspecies components, the variable state of the gas, and the transport of energy through convection and radiation processes within the shock layer. The consideration of coupled, finite-rate chemical processes has a strong effect not only on the distribution of species and the local state of the gas, but also on the source and intensity of the radiation transport processes (and the level of complexity associated with these calculations).

The primary inviscid flow-field calculations incorporate the effects of the change in the forebody shape (analytically simulating the detachment of the outer heat shield; an event which, in concept, occurs between the trajectory point corresponding to Cases I and II and the earlier point corresponding to Case III). The calculations include the effects of a small asymmetry in the basic flow (corresponding to an angle-of-attack of 5°) and extend downstream to approximately the region of separation streamline closure.

The calculations described in the text of the report can be categorized by the following general topics:

- Subsonic and supersonic inviscid shock-layer flow-field calculations for axisymmetric and slightly asymmetric flow over the extent of the reentry package and including the separated flow region behind the vehicle base;
- Nonequilibrium calculation of the coupled finite chemical rate processes resulting in distribution of species and gaseous states;
- Equilibrium and nonequilibrium radiation transport calculations resulting in the radiative heat-flux distribution around the body, based on the states of the gas and species concentrations;
- Boundary-layer convective-heating calculations based on the spatial distribution of gaseous states and species concentrations.

Details of various analysis, governing equations, and source of information are discussed in separate sections contained in the body of the report. Wherever possible or considered necessary, figures, sketches, and graphs have been included to help supplement the discussion in the text.

The present report presents useful information in keeping with the general purpose of the "FIRE" analysis. It includes the necessary quantitative prediction of flow-field data, gaseous states, equilibrium and nonequilibrium radiation and convective heating to the specified "FIRE" vehicle at selected trajectory points, as well as detailed description of the analytical techniques as a guideline for future studies and comparison with flight data.

Section 2
SUMMARY OF THEORETICAL METHODS AND DISCUSSION OF RESULTS

2.1 GENERAL

This section presents a summary of the theoretical methods which were used to predict the flow field and the associated aerodynamic heating for the Project FIRE reentry package. A discussion of the main results follows the discussion of the theoretical methods. Three specified conditions, referred to as Case I, Case II, and Case III, were considered. The reentry package shape and dimensions for Cases I and II are depicted in Fig. 1. The corresponding flight conditions represent the instant at which the first calorimeter had previously melted off and the adjacent layer of ablative material has just been ejected. The original reentry package shape, depicted in Fig. 2, was used for Case III, whose flight conditions are such that the radiation is primarily from a gas which is not in equilibrium. The free-stream conditions for the three cases are shown in Table 1.

Table 1
FREE-STREAM CONDITIONS

Quantity	Cases I and II	Case III
Altitude (ft)	171,611	259,113
(meters)	52,307.2	78,977.9
Velocity (ft/sec)	34,582	37,439
(m/sec)	10,541	11,411
Temperature (°K)	270.65	184.62
(°R)	487.17	332.32
Pressure (mb)	0.60068	0.012492
(lb/ft^2)	1.2546	0.026091
Density (g/m^3)	0.77316	0.023573
($slugs/ft^3$)	1.4995×10^{-6}	4.5718×10^{-8}
Mach Number	31.962	41.894

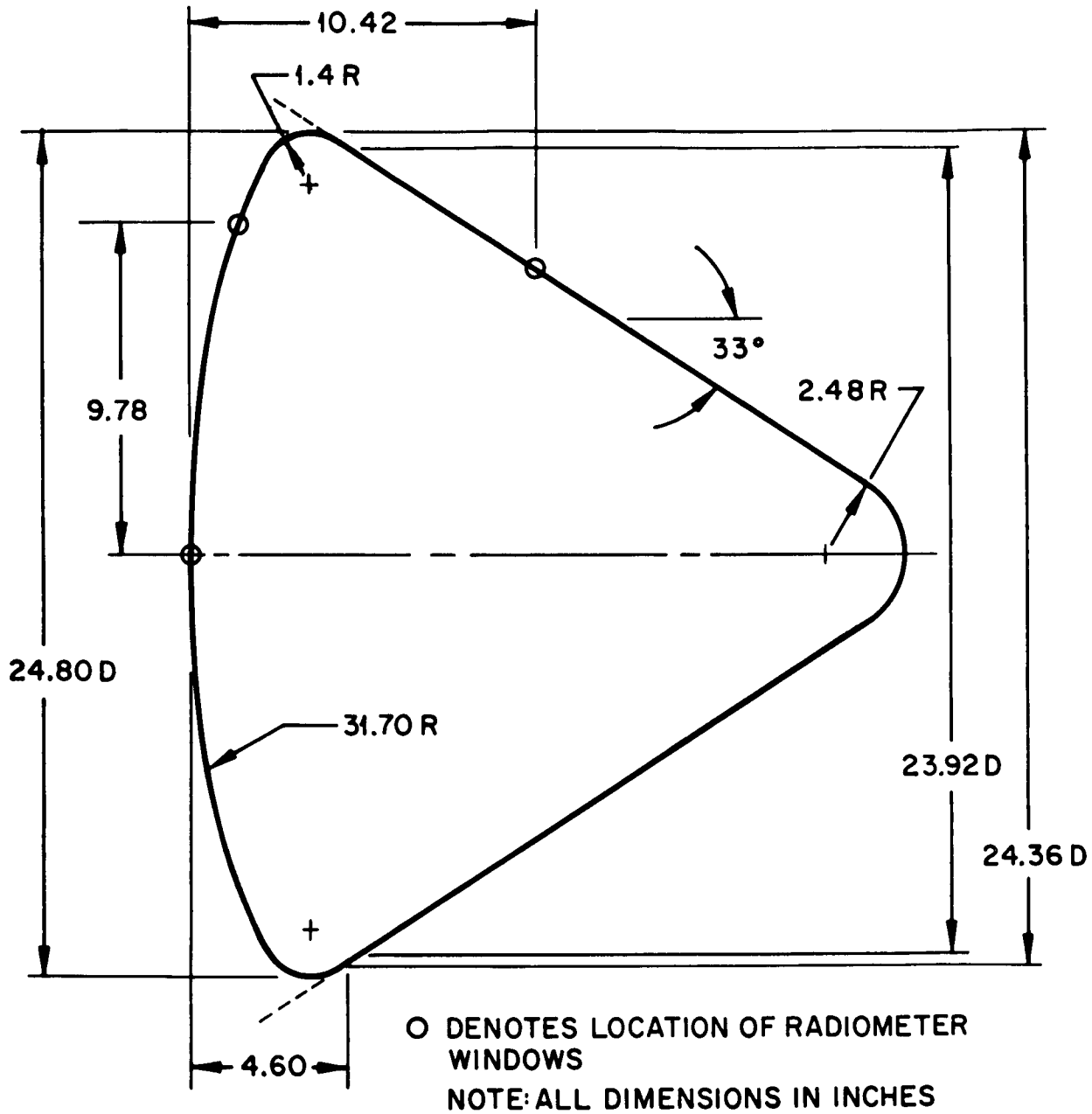

Fig. 1 Body Shape for Cases I and II

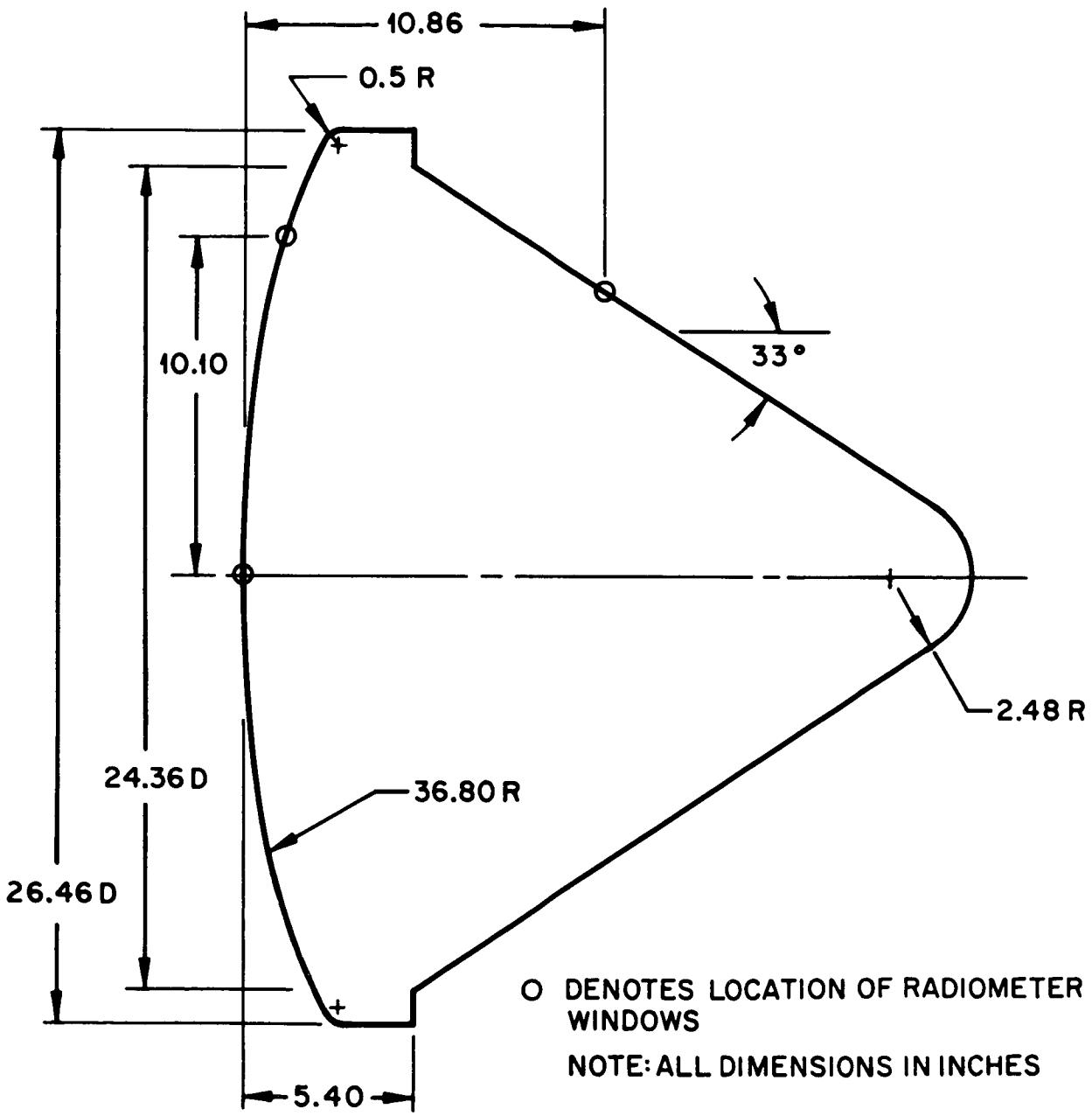

Fig. 2 Body Shape for Case III

The ambient conditions for the given altitudes were calculated from the "Proposed Revision of the U.S. Standard Atmosphere, 0−700 km," as found in Ref. 1. The angle-of-attack was specified as 0° for Cases I and II, and 5° for Case II. The purpose of the analyses was to predict the state of the gas throughout the flow field to enable prediction of both the radiative and convective heating rate distribution over the reentry package. For Case II the distribution was required only in the angle-of-attack plane, while for Case III it was required only over the heat-shield face (i.e., from the stagnation point to the backward facing step). In addition, the frequency distribution of the normal component of the specific intensity of radiation at the forward point on the body axis of symmetry was required. The various methods used to make these calculations are outlined briefly below. Fuller details on these methods will be found in Section 3.

2.2 FLOW-FIELD ANALYSIS

2.2.1 General Description

A schematic picture of the flow around the FIRE reentry package is shown in Fig. 3.

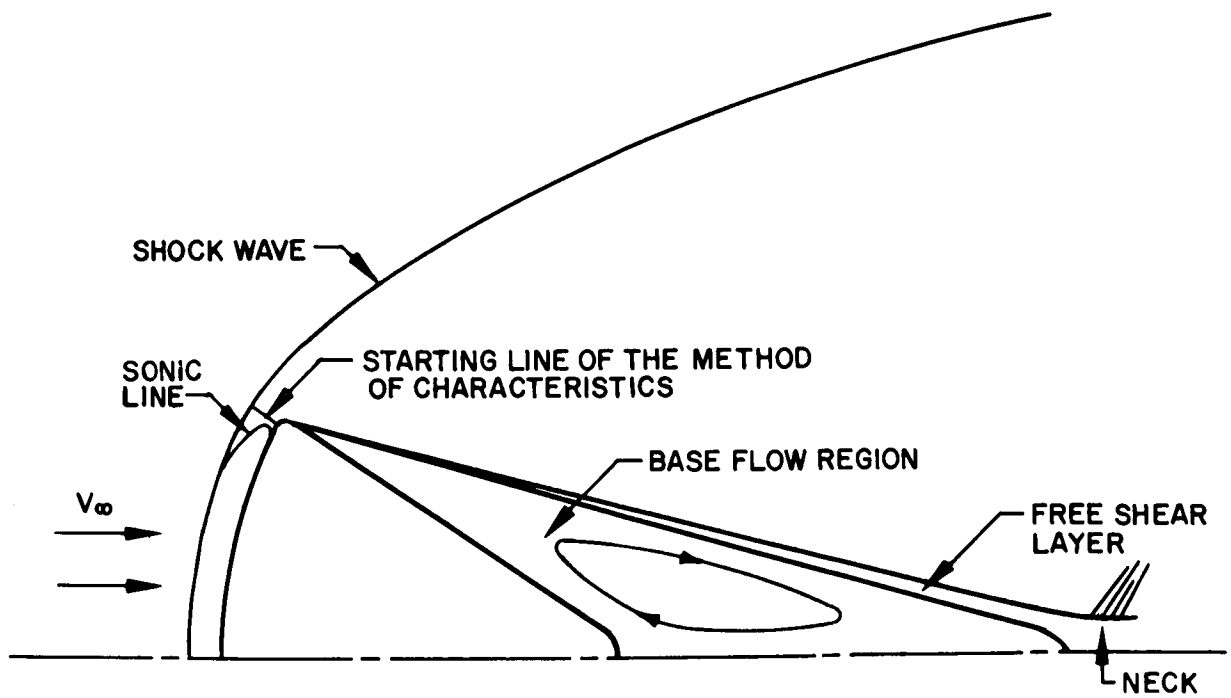

Fig. 3 Flow-Field Schematic Diagram

The flow field of interest lies between the body and the detached shock wave. The flow separates from the body before it reaches the back conical portion, the separating streamlines nearly coming together at a "neck" region downstream of the body. The region between the body and the separating streamlines is termed the base flow region. For Cases I and II, one can assume that the flow between the body and shock wave, and outside the base flow region, is steady and inviscid. The shock wave becomes a discontinuous surface, while viscous effects are confined to a thin boundary layer adjacent to the body and a thin free-shear layer along the separating streamline. The base flow region contains a low-velocity recirculating flow at a constant pressure, which is also the pressure throughout the entire free-shear layer. For Case III, the viscous region occupies a larger fraction of the shock layer. The shock wave, however, can still be considered to be a discontinuity.

In general, the inviscid flow can be out of equilibrium (due to chemical reactions at high temperatures) and nonadiabatic (due to radiation cooling). The approach used here was to calculate the flow assuming equilibrium, adiabatic conditions as a first approximation and then to correct the flow to account for nonequilibrium and nonadiabatic effects. Actually, it turned out that for all three cases the nonadiabatic correction was negligible, so that only the chemistry correction had to be carried out.

The equations governing the steady, inviscid, equilibrium, adiabatic flow of a gas are written as:

$$\nabla \cdot (\rho \vec{V}) = 0 \tag{2.1}$$

$$\rho \vec{V} \cdot \nabla \vec{V} + \nabla p = 0 \tag{2.2}$$

$$\vec{V} \cdot \nabla S = 0 \tag{2.3}$$

$$h + \frac{V^2}{2} = \text{const.} \tag{2.4}$$

where $\vec{V}$, ρ, p, S, and h are the velocity vector, density, pressure, specific entropy, and specific enthalpy, respectively. Equations (2.3) and (2.4) are two different forms of the energy equation, Eq. (2.4) representing the condition of adiabatic flow, while Eq. (2.3) contains the assumption of equilibrium flow. These equations must be supplemented by equations of state relating the various thermodynamic variables, and by appropriate boundary conditions. The latter are the Rankine-Hugoniot conditions across the shock wave, the condition of zero normal velocity at a solid surface, and the constant pressure condition on the separating streamline. The problem is made difficult by the fact that the location and shape of the shock wave and separating streamline, as well as the value of the base pressure, are all initially unknown.

Since the governing equations are elliptic in the subsonic region, and hyperbolic in the supersonic region, different methods have to be utilized in solving them. The next two subsections describe briefly the techniques utilized to obtain the solution in the subsonic (and slightly into the supersonic) region of the flow for the three separate cases. The final subsection analyzes the supersonic region of the flow, including the determination of the separating streamline.

2.2.2 Inverse Method for the Subsonic Flow Regions of Cases I and II

An inverse method was chosen to obtain the subsonic flow regions for Cases I and II. The method, in which the partial differential equations are numerically integrated from a prescribed shock wave until a body is reached, was first developed for symmetric flows by Van Dyke (Refs. 2 and 3). Swigart (at LMSC) modified the method to the solution of ordinary differential equations and extended it to asymmetric flows (Refs. 4 through 6).

At the present state of development of the method, the detached shock wave is assumed to be a surface of revolution which is generated by a conic section. An orthogonal coordinate system containing the shock wave as a coordinate surface is employed. A "locally" perfect gas law is assumed, namely,

$$h = \frac{\gamma}{\gamma-1}\frac{p}{\rho} + A \qquad (2.5)$$

where γ is the isentropic index, assumed constant, and A is an enthalpy constant. The unknowns are chosen to be the density ρ, and either a single stream function ψ_1 (for the axisymmetric case) or two stream functions ψ_1 and ψ_2 (for the angle-of-attack case). The method of solution essentially consists of separation of variables by expanding the unknowns and the boundary conditions in a MacLaurin series about the axis of symmetry. For $\epsilon \neq 0$, (where ϵ is the angle-of-attack of the shock wave), there is an additional expansion in ϵ. In this manner one obtains sets of ordinary differential equations in the coordinate perpendicular to the shock wave. These are integrated numerically by standard means from the shock wave until the resulting body is reached.

We turn our attention first to Case I. One difficulty encountered in attempting to duplicate the Case I shape is that the sonic region near the body turns out to be close to the limit of convergence of the expansion away from the axis, thus making the solution invalid there. A further difficulty is that the desired shape has a large discontinuity in curvature, while the method, by its nature, can only generate analytic body shapes.

To overcome these difficulties, it was decided to utilize the inverse solution where it was valid (i.e., outside the sonic region near the body) and to estimate the solution in the region of invalidity. This was done by extrapolating results of numerical solutions and experimental data for spheres, spherical segments, and rounded flat-face cylinders, found in Refs. 3, 7, 8, and 9, to the Case I body shape and flight conditions. This provided an estimate of the shock standoff distance (in terms of a body dimension). Since the sonic region is fairly well defined on the body, an overall continuity check from the assumed shock wave to the body in the sonic region (which is relatively insensitive to the detailed flow near the body) was used to further refine the guesses. The check was made on the starting line for the method of characteristics in order to provide consistent input data for the latter program. By repeated trials, the conic shock wave that gave the best overall approximation to the actual shock wave was obtained. Since the actual shock wave is not strictly a conic, local differences would

be expected. In order to insure proper conditions in the critical sonic region, a standoff distance on the axis slightly larger than the estimated one was produced. This was not considered serious, since the extrapolation producing the estimate involved a fair degree of uncertainty.

With the conic shock wave determined, the inverse solution was calculated. To patch the resulting solution with that in the sonic region near the body, use was made of the observation from the above references that for given hypersonic free-stream conditions, the location of a specified flow condition on the body in this region depends primarily on the local body slope, and is weakly dependent on the overall body shape. Since the sonic line from the body initially curves away from the axis (due to the small shoulder radius), the $M = 1.2$ point was estimated on the body. (This resulted in a minimum Mach number of 1.05 on the starting line for the method of characteristics.) The gradients of all flow quantities normal to the body at that point were then determined exactly from the flow equations, the known shock radius on the axis, and the shoulder radius. The solution along the body normal, chosen as the starting line, was then graphically extrapolated to merge with the machine solution of the inverse method.

This latter graphical extrapolation presented serious problems. Whereas, for generally spherical bodies, flow quantities along a body normal vary approximately linearly between the body and the shock, this is far from true for normals to a sudden shoulder with a small radius. In the case of the velocity, the distribution is not even monotonic, as shown by the initial gradient at the body. Thus, the extrapolation, from the known gradients at the body to a point where smooth merging with the solution emanating from the shock can be affected, is somewhat uncertain. It may be thought that the use of a local continuity (i.e., streamtube) check would be helpful. Unfortunately, most of the unknown part of the starting line has Mach numbers sufficiently close to $M = 1$, that the product ρV is very close to its sonic value (on each streamline). As a result, while the entropy distribution (which is monotonic) can be estimated fairly well, the velocity and flow angle distribution (which are both

nonmonotonic) can be determined only within broad limits. The starting line distribution (as shown in Table 5) for Case I thus represents considerable guesswork. The machine solution was found to be applicable for approximately half the distance from the shock to the body. Along the body, where the entropy is known from the normal shock solution, the pressure was determined by extrapolating backwards the distribution determined from the characteristics solution. This extrapolation was assumed valid up to the curvature discontinuity point, where a discontinuity in pressure gradient results. The pressure distribution on the body upstream, as determined from the machine solution, was then extrapolated forward to achieve the value at the curvature discontinuity point. As a result, the machine solution was found to apply for approximately two-thirds of the distance from the stagnation point to the curvature discontinuity point.

Concurrent with the above problem was the question of choosing the best value of γ and A in Eq. (2.5). Since the results of the subsonic program would be utilized partly to obtain starting-line data for the method of characteristics, and the critical portions of the starting line, where the Mach number is just slightly supersonic, is near the body, it was finally decided to choose γ and A so as to duplicate conditions at the body sonic point. The values were determined by trial and error from the charts of Ref. 10, which are based on the thermodynamic data of Ref. 11, the same data stored in the characteristics program. With the body entropy known, and an initial guess for the sonic enthalpy, the sonic pressure and density were determined from the charts. By a graphical differentation the corresponding value of γ [as defined by Eq. (3.5)] was determined. The speed of sound could then be calculated, and a new value for the enthalpy obtained from Eq. (2.4), with the velocity set equal to the speed of sound. After convergence was reached, the value of A was given by Eq. (2.5). The resultant values for Cases I and II were $\gamma = 1.192$, and $A/V_\infty^2 = 0.1188$. Actually, in obtaining solutions for Cases I and II, it was necessary to employ programs which had been coded only for a perfect gas law ($A = 0$). The problem was resolved by utilizing a fictitious equivalent γ and Mach number, as discussed in subsection 3.1.1. As a result, the thermodynamic state of the gas was

only approximately satisfied. Unfortunately, in obtaining the solution along the starting line for the characteristics program, it was important to match the real thermodynamic state as closely as possible, to prevent large oscillations in the initial solution. Using the arguments justifying the streamtube approximation (see subsection 2.3), it was decided that the pressure and flow geometry (i.e., streamline pattern) were the least sensitive and therefore chosen to be correct. The entropy could then be obtained by tracing the streamline to its origin at the shock wave, where the exact value of the entropy is known. The remaining variables were then determined from Ref. 10.

The results of the Case I solution were used to provide input data for the method of characteristics (subsection 2.2.4) and also the radiative heating program (subsection 3.3.8). Representative state variables are tabulated in Table 2. The distribution of quantities on the body surface served as input for the convective heating calculation (subsection 2.5.2). Typical of such quantities are the pressure and the velocity, which are plotted in Fig. 4. The Case I solution provided the results up to the curvature discontinuity point. The distribution of velocity starts out linearly with distance, but increases as the rounded shoulder is approached. Concurrently, the pressure is seen to decrease rapidly in this region.

Turning now to Case II (5° angle-of-attack), one encounters the same problems found in Case I. The question of what shock shape to assume was resolved by assuming that for the small angle-of-attack found here, and considering the body nose shape to be spherical, the closest axisymmetric shock shape to the actual shape was the same shape as in the zero angle-of-attack problem. (It is obvious that the actual shock shape is asymmetric, but the degree of asymmetry would be expected to be negligible for small angles-of-attack. This assumption is probably good in the stagnation region, but would become increasingly poor as one moved out from the axis. The assumption is forced on us by the limitations of the inverse method.)

Table 2

THERMODYNAMIC STATE DATA – CASE I

Cartesian* Coordinates		Static Pressure	Normalized Enthalpy**	Normalized Entropy
x (cm)	y (cm)	p/p_o (atm)	h/h_r	S/R
-4.454	0	0.786	1.924	60.78
-2.389	19.42	0.748	1.831	60.0
-1.095	24.27	0.720	1.736	59.39
0.673	29.12	0.674	1.635	58.29
-0.590	19.03	0.758	1.888	60.48
0.552	23.78	0.717	1.848	60.25
2.111	28.54	0.651	1.792	59.90
1.443	18.64	0.757	1.920	60.75
2.413	23.30	0.709	1.892	60.70
3.737	27.96	0.630	1.854	60.59
-3.962	9.708	0.778	1.904	60.62
-2.411	0	0.809	1.924	60.78
-1.978	9.514	0.798	1.920	60.70
0.2660	9.319	0.803	1.924	60.77
0	0	0.815	1.932	60.78
1.858	18.59	0.753	1.914	60.78
2.915	23.18	0.708	1.899	60.78
5.493	29.23	0.52	1.829	60.78
2.315	32.52	0.61	1.481	56.82
3.215	31.88	0.594	1.685	59.10
3.269	34.187	0.5915	1.435	56.33
4.428	31.029	0.554	1.780	60.18

*Origin is at the stagnation point, x-axis points downstream.
**$h_r = 3.125 \times 10^8$ ft^2/sec^2 = 12.476 Btu/lb.

Table 2 (cont.)

Cartesian* Coordinates		Static Pressure	Normalized Enthalpy**	Normalized Entropy
x (cm)	y (cm)	p/p_o (atm)	h/h_r	S/R
3.879	33.712	0.552	1.583	58.17
4.203	35.708	0.558	1.353	55.46
5.593	30.207	0.4303	1.778	60.69
4.979	35.439	0.452	1.493	57.56
5.809	37.906	0.483	1.173	53.32
5.901	29.99	0.368	1.754	60.78
5.494	35.61	0.408	1.514	58.01
6.890	39.18	0.444	1.080	52.16
7.333	39.668	0.429	1.046	51.73
6.682	30.79	0.211	1.643	60.78
7.882	34.32	0.216	1.581	60.06
7.112	31.07	0.152	1.582	60.78
7.918	32.52	0.152	1.563	60.57
7.648	31.30	0.100	1.510	60.78
8.172	40.55	0.404	0.986	50.96
11.733	43.83	0.327	0.805	48.55
21.03	50.68	0.225	0.564	45.12
27.906	54.79	0.186	0.472	43.73
38.347	60.25	0.148	0.381	42.25
55.626	67.98	0.110	0.288	40.53
84.724	78.94	0.0817	0.219	38.93
165.9[illegible]	104.04	0.0520	0.148	37.09
239.74	122.35	0.0345	0.106	35.89
16.384	37.94	0.0587	1.359	59.90
29.051	46.68	0.050	1.160	57.25
50.076	58.41	0.044	0.750	50.72
79.397	71.61	0.0426	0.417	44.56

*Origin is at the stagnation point, x-axis points downstream.
**$h_r = 3.125 \times 10^8$ ft^2/sec^2 = 12.476 Btu/lb.

Table 2 (cont.)

Cartesian* Coordinates		Static Pressure	Normalized Enthalpy**	Normalized Entropy
x (cm)	y (cm)	p/p_o (atm)	h/h_r	S/R
106.56	82.03	0.047	0.273	41.14
8.037	31.41	0.0716	1.455	60.78
218.24	0.574	0.0146	1.237	60.78
127.11	11.68	0.0146	1.237	60.78
220.25	38.55	0.010	1.063	58.60
86.35	16.98	0.0146	1.237	60.78
55.05	21.89	0.0146	1.237	60.78
144.50	42.106	0.010	1.038	58.17
214.52	59.809	0.00789	0.8071	54.43
29.09	26.749	0.0146	1.237	60.78
9.653	31.394	0.0146	1.237	60.78
22.41	32.678	0.0133	1.2115	60.55
39.70	35.192	0.0120	1.1791	60.20
61.42	38.974	0.0109	1.1308	59.58
115.48	49.860	0.00875	0.9506	56.86
186.41	64.790	0.00704	0.7218	53.00
251.34	78.203	0.00591	0.5556	49.98
50.425	62.671	0.0702	0.5019	45.57
29.852	53.007	0.0946	0.7546	49.63
8.098	34.835	0.2121	1.565	59.92
13.271	43.154	0.1965	1.126	54.25
8.050	39.729	0.354	1.195	54.19

*Origin is at the stagnation point, x-axis points downstream.
**$h_r = 3.125 \times 10^8$ ft^2/sec^2 = 12.476 Btu/lb.

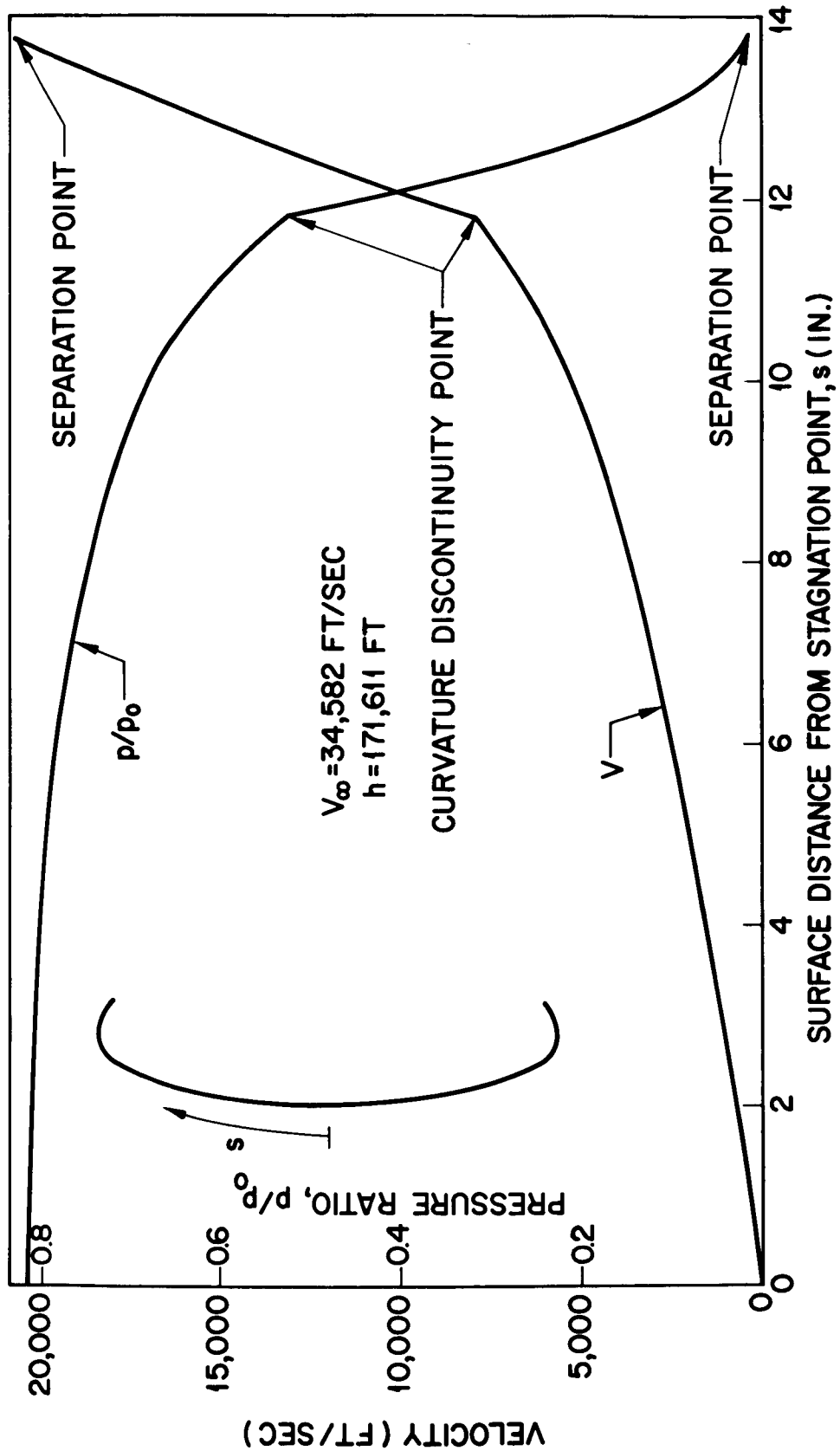

Fig. 4 Pressure and Velocity Distribution on Body for Case I

In reducing the data to obtain ψ_1 , it was discovered that, even near the shock wave, the solution broke down as one went far enough out to reach the starting-line region of the flow. Specifically, the terms of order ϵ were found to be almost of the same order as the zero-order terms, thus making the expansion to first order in ϵ only, worthless. This was not completely unexpected since the assumption of a symmetric shock wave of the same shape as the zero angle-of-attack shock wave was certainly poor, far from the axis. Furthermore, the angle-of-attack solution included only terms up to third order in the expansion in distance from the axis, while the axisymmetric solution had been carried out to fourth order. It was therefore necessary to modify the attempts to obtain complete details of the flow field for the angle-of-attack case.

Useful results could be obtained by utilizing the solution in the stagnation region. By considering the expression for the body shape and looking for its axis of symmetry, it was determined (see Appendix A. 2) that the angle-of-attack of the body α was equal to the angle-of-attack of the shock wave ϵ (to first order in ϵ) . This was not a surprising result, since, for the spherical nose at hypersonic speeds, one would expect the Newtonian theory to hold in the stagnation region, predicting that the shock would "wrap" itself around the body. Furthermore, the calculation of the pressure distribution on the body in the stagnation region confirmed that the stagnation point on the body had also shifted, approximately, 5 degrees. The remainder of the pressure distribution up to the curvature discontinuity point was determined in the following manner. On the leeward side, the pressure at the curvature discontinuity point was decreased by $\cos^2 (\theta_{cd} + 5)/\cos^2 \theta_{cd}$, where θ_{cd} is the body inclination (in degrees) at the curvature discontinuity point. This correction tacitly assumes that the pressure at the shoulder varies in a Newtonian fashion. It is not assumed that the pressure is given by the Newtonian approximation. The pressure distribution between the stagnation point and the shoulder was then obtained by fairing the zero angle-of-attack distribution to the corrected value at the curvature discontinuity point. A similar correction was made on the windward side. The expansion behind the shoulder was assumed to be identical to the $\epsilon = 0$ case. The flow was assumed to separate after it had gone through the same expansion (in terms of body angle) as

in the zero angle-of-attack case. This places the separation point about 0.1 in. from the zero angle-of-attack separation point. On the windward side, similar corrections were made to determine the pressure distribution up to the separation point. The resulting pressure distribution is shown in Fig. 5. The asymmetry of the distribution is evident, and makes itself felt in the resultant convective heating distribution. Representative state variables in the subsonic region of Case II are tabulated in Table 3. As discussed earlier, the values for the points furthest from the axis are quantitatively poor.

2.2.3 Analytic Solution for the Subsonic Flow Region of Case III

Since the Case III body has a much smaller corner radius than that for Case I (in fact, the front face is close to being a spherical segment), it is evident that the inverse method utilized for Case I would not be applicable here. It was, therefore, decided to modify an existing approximate analytic solution for spheres, developed at LMSC, by taking into account the presence of a sonic corner. The resulting solution would be expected to be valid everywhere except in the vicinity of the small rounded corner, where the solution could be estimated in a manner similar to that in Case I. The sphere solution is basically an outgrowth of the constant-density sphere solution of Lighthill (Ref. 12). It was first extended by M. Vinokur to arbitrary conic-section bodies of revolution (Refs. 13 and 14). Subsequently, the restriction of constant density was removed in order to obtain an approximate solution in the whole subsonic region. These results were first reported in Ref. 15. The complete details of the analysis, restricted to the case of a sphere, will appear in a forthcoming publication (Ref. 16). A condensed version may be found in subsection 3.1.2.

A spherical coordinate system (R, θ, φ) based on the given body, with the $\theta = 0$ axis pointing upstream, is employed. The flow geometry is shown in Fig. 6.

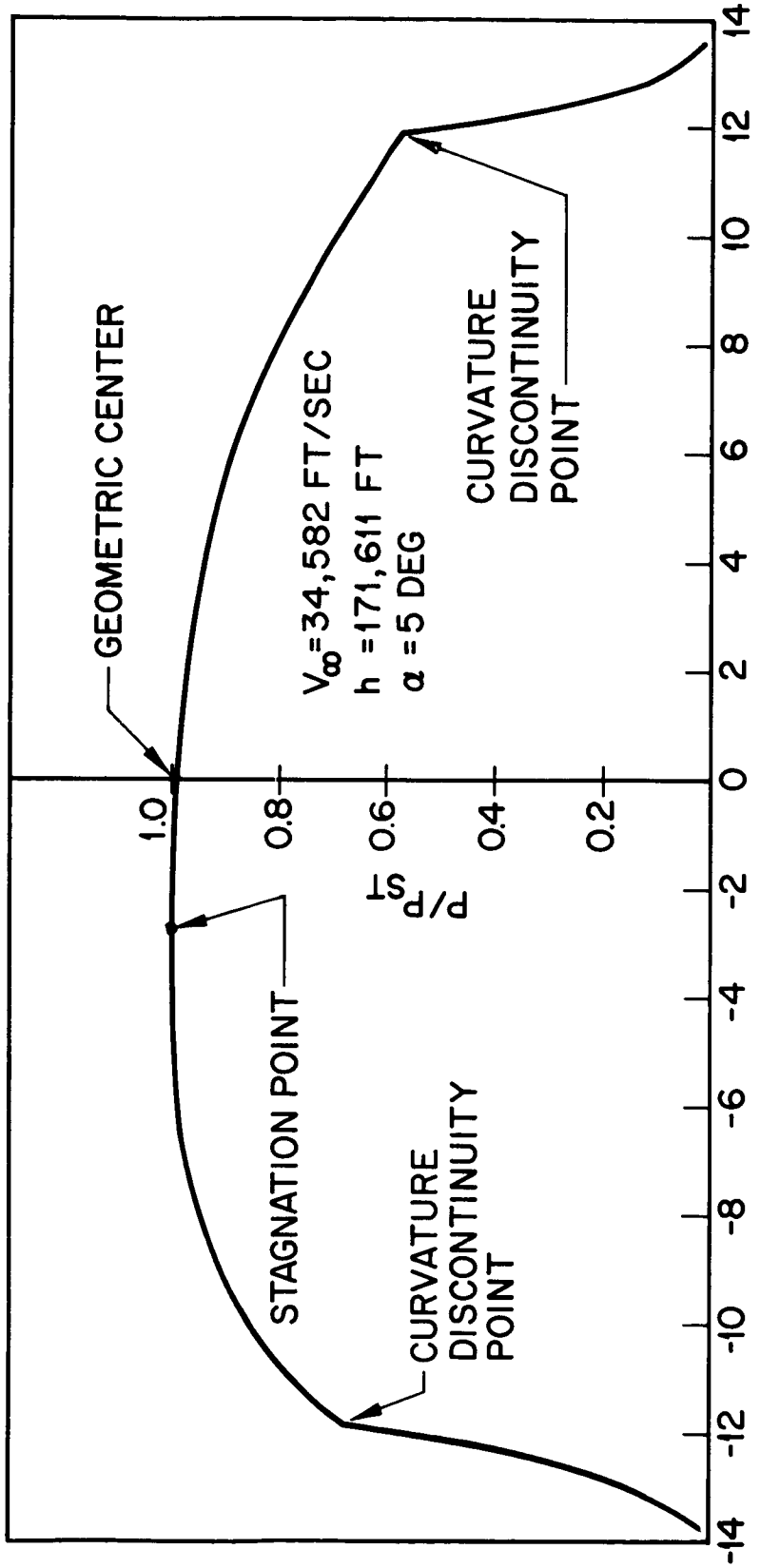

Fig. 5 Pressure Distribution for Case II

Table 3

THERMODYNAMIC STATE DATA – CASE II

Cartesian Coordinates*		Static Pressure	Normalized Entropy
$\tilde{x}$ (cm)	$\tilde{y}$ (cm)	p/p_o (atm)	S/R
-4.454	0	0.7904	60.78
-3.9616	+9.7078	0.7675	60.35
-3.9616	-9.7078	0.7904	60.78
-2.389	+19.415	0.7225	59.41
-2.389	-19.415	0.7805	60.59
-1.095	+24.269	0.6835	58.58
-1.095	-24.269	0.7600	60.17
0.6728	+29.123	0.622	57.11
0.6728	-29.123	0.7175	59.35
-2.411	0	0.8089	60.78
-1.977	+9.514	0.7792	60.58
-1.977	-9.514	0.8173	60.78
-0.590	+19.028	0.7170	60.20
-0.590	-19.028	0.7992	60.78
0.552	+23.784	0.6634	59.87
0.552	-23.784	0.7708	60.64
2.111	+28.541	0.5843	59.31
2.111	-28.541	0.7175	60.47
0	0	0.815	60.78
0.2660	+9.319	0.7803	60.78
0.2660	-9.319	0.815	60.78
1.858	+18.584	0.6923	60.78
1.858	-18.584	0.7998	60.78
2.915	+23.185	0.6034	60.78
2.915	-23.185	0.7746	60.78

*The $\tilde{y}$ coordinate is measured from the axis of symmetry of the body. The stagnation point of the flow occurs at $\tilde{y} < 0$. The origin is on the body.

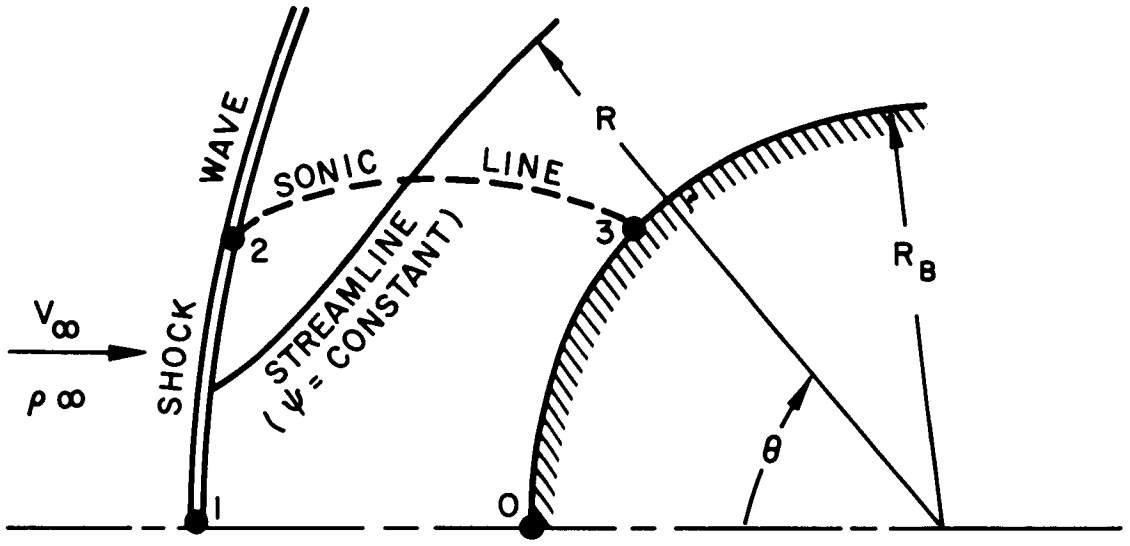

Fig. 6 Flow Geometry for Spheres

The basic equations can be combined to yield a single, nonlinear equation for the Stokes stream function ψ . The nonlinearities arise from variations in density and shock curvature. The present solution replaces the nonlinear terms by a linear function in R and cos θ , thus introducting four unknown constants to be determined later. A formal solution of the linear problem satisfying boundary conditions on the body, can now be obtained. The four unknown constants are evaluated in terms of six parameters which specify the flow geometry at the points labeled 1, 2, and 3 in Fig. 6. By applying boundary conditions at these three points, and with some algebraic reduction, one finally arrives at a set of six nonlinear algebraic equations for the six geometric parameters. These are solved on a computer using Newton's iteration of initial guesses. Convergence is good with any reasonable guess, except for low supersonic Mach numbers, or very strong shock waves, when the initial guesses are more critical. Knowledge of the stream function gives us the shock shape and, therefore, the entropy along each streamline. Using an appropriate equation of state, the complete flow field can then be obtained.

The above method had been programmed for a perfect gas. In order to apply it to Case III, one first had to determine the equivalent perfect gas conditions which would duplicate the body sonic-point conditions, as was done for Case II. The duplication was required for consistent input to the equilibrium characteristics program, realizing that the actual state would differ due to nonequilibrium effects. The resulting conditions were found to be $\gamma' = 1.1172$ and $M_e = 81.63$. The next task was to modify the solution for flow around a sphere by fixing the location of the body sonic point (i.e., fixing θ_3) and by dropping the corresponding sonic throat boundary condition. This reduced the problem to one of five equations in five unknowns. Due to the absence of the simple sonic throat conditions, this set was actually algebraically more complicated than the original six, and convergence was more difficult to obtain. The procedure employed was first to use the original program to obtain the sphere solution for the desired free-stream conditions. Then the sonic angle, θ_3, was successively decreased in small steps, using the new program, until the limit of convergence was reached. This gave a good enough representation of the flow away from the corner region, so that a "patching", similar to that of Case I, with a solution in the neighborhood of the actual corner radius was possible. This provided necessary starting-line data for the method of characteristics, as well as input data for the streamtube chemistry program. The pressure and velocity distribution, up to the beginning of the rounded shoulder for Case III, is shown in Fig. 7. The velocity distribution shown is actually the corrected distribution resulting from the application of the chemistry program of subsection 2.3. The rapid change in slope for both quantities near the shoulder is more pronounced than in Case I, due to the greater severity of the shoulder.

2.2.4 Method of Characteristics

The supersonic flow for Cases I and III was calculated by the standard method of characteristics. For Case III, as discussed in subsection 2.3, only the streamline geometry and pressure distribution were utilized, the remaining state variables being subsequently determined by the streamtube chemistry program. The method was programmed at LMSC (Ref. 17), following the procedure of Ref. 18. Details of

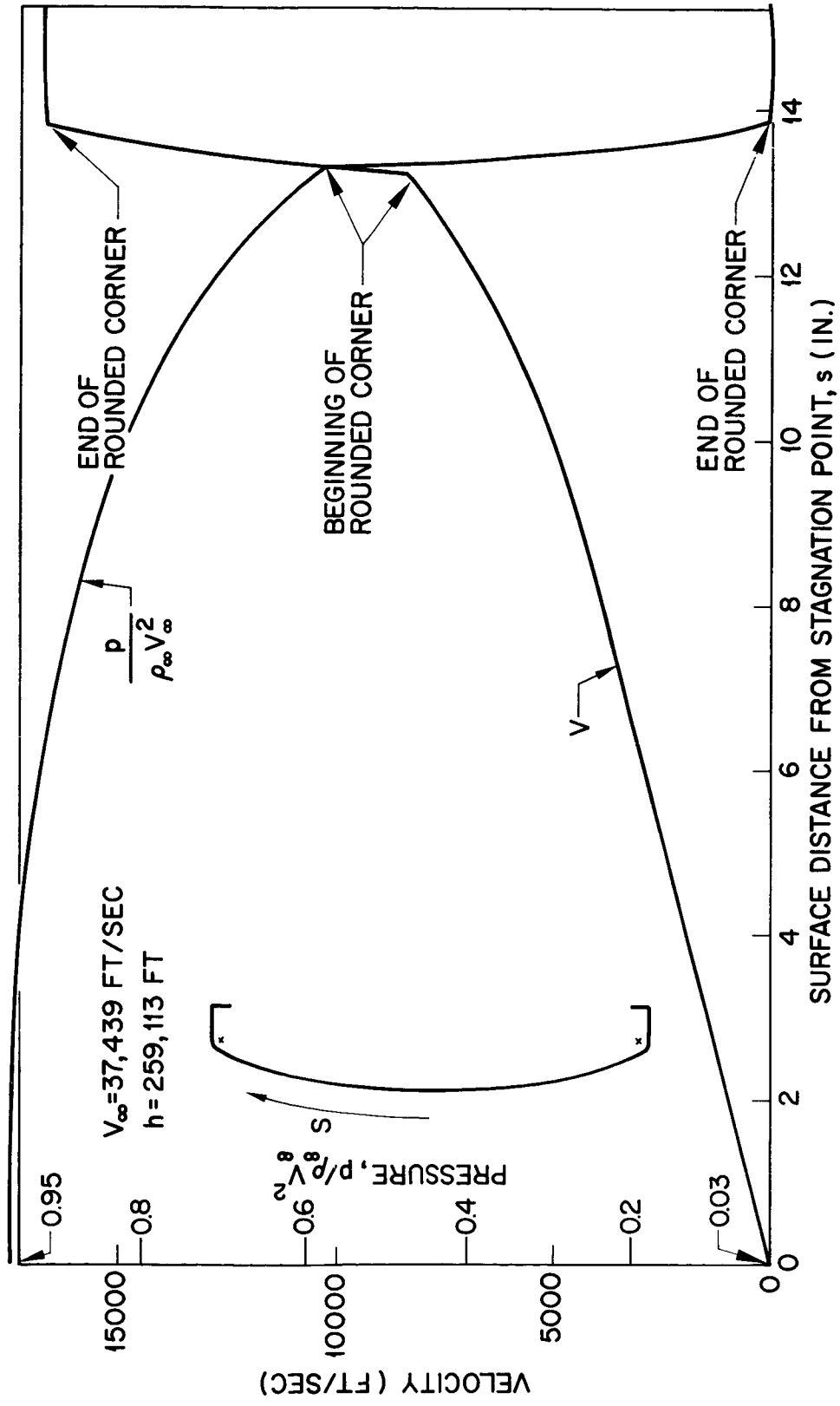

Fig. 7 Pressure and Velocity Distribution on Body for Case III

the method may be found in the above references. Polynomial curve fits for equilibrium air presented in Ref. 19 were extended to the higher enthalpy and entropy ranges required for Project FIRE, using the least-squares code of Ref. 20. This provided the coefficients for the expansions of log p/p_o , log ρ/ρ_o , and T as double polynomials in h/RT_o and S/R , where T is the temperature, R is the undissociated gas constant for air, and the subscript o refers to standard reference conditions. Separate curve fits were generated for different sections of the Mollier Diagram to insure accuracy within two percent. The data fitted were obtained from Ref. 11. The final coefficients were then stored in the characteristics program. The coefficients for the extended curve fits are tabulated in Table 4, using the nomenclature of Ref. 19.

The body of revolution can consist of several regions, each of which may be defined by an equation, or by a table. The basic unknowns which are used are V , S/R , and θ , where θ is the flow inclination. These quantities are specified at an arbitrary set of points on a noncharacteristic starting line extending from the shock wave to the body. The shock angle ϕ must also be specified. Starting-line data for Cases I and III, as determined from the subsonic solutions of subsections 2.2.2 and 2.2.3, are tabulated in Tables 5 and 6. For given free-stream conditions, the program automatically calculates the flow along left-running characteristics. (The original method of calculating along right-running characteristics was changed to facilitate the handling of backward conical positions, such as found on Project FIRE.) The program automatically generates the shock shape, calculates Prandtl-Meyer expansion fans at corners, and calculates a constant pressure streamline emanating from any prescribed point on the body (including the middle of a corner expansion region), if desired. The calculation of each new point in the flow requires an iteration process which is controlled by a specified convergence criterion on the velocity, and a specified bound on the number of iterations permitted. In order to prevent an excessively large characteristic mesh, and the resultant loss of accuracy, maximum step sizes are specified at the shock, at each body segment, and on the constant pressure streamline. The program automatically subdivides the mesh if the distance between successive points on the shock, body, or contact pressure streamline exceeds the allowable maximum.

Table 4

CURVE-FIT COEFFICIENTS FOR EQUILIBRIUM AIR*

		$\log_{10}\rho/\rho_o = f_1(x, y)$	$T = f_2(x, y)$	$\log_{10} p/p_o = f_3(x, y)$
$400 \leq h/RT_o < 600$	a	-0.25455851^{1}	0.75396962^{4}	-0.81496277
	b	-0.15132117^{1}	-0.10638086^{4}	-0.15619305^{1}
	c	0.33279940	0.10126655^{4}	0.40346465
	d	0.18695336^{-1}	0.25422191^{3}	0.24099334^{-1}
	e	0.40027560^{-1}	0.24464457^{2}	0.48209645^{-1}
	f	-0.30746464^{-1}	0.65746319^{2}	-0.32002148^{-1}
	g	-0.38911540^{-2}	-0.45889898^{2}	-0.42823758^{-2}
	h	-0.27183122^{-2}	0.16483811^{1}	-0.27612809^{-2}
	i	-0.66638900^{-2}	-0.11713630^{2}	-0.81647895^{-2}
	j	0.45745844^{-2}	-0.34289908^{2}	0.26123463^{-2}
$600 \leq h/RT_o \leq 825$	a	-0.14769915^{1}	0.11784659^{5}	0.48388687
	b	-0.13890489^{1}	-0.16583058^{4}	-0.14369193^{1}
	c	0.22255757	0.97822092^{3}	0.26737183
	d	0.22287781^{-1}	0.15359633^{3}	0.21800762^{-1}
	e	0.33281241^{-1}	-0.28164980^{3}	0.29530291^{-1}
	f	-0.11669045^{-1}	-0.23606187^{2}	-0.14206643^{-1}
	g	-0.14206614^{-2}	-0.17756879^{2}	-0.14851446^{-2}
	h	0.18415757^{-2}	0.33197547^{2}	0.20729524^{-2}
	i	-0.77477457^{-3}	0.21858158^{1}	-0.36742778^{-3}
	j	0.70358078^{-3}	0.34515422^{1}	0.10108147^{-2}

*General Equation:

$$f_n(x, y) = a + bx + cy + dx^2 + exy + fy^2 + gx^3 + hx^2y + ixy^2 + jy^3$$

Transformation Equations:

$x = 0.14285714\ S/R - 8.2857143 \qquad 400 \leq h/RT_o \leq 825$

$y = 0.02\ h/RT_o - 10.0 \qquad 400 \leq h/RT_o < 600$

$y = 0.017777778\ h/RT_o - 12.666667 \qquad 600 \leq h/RT_o \leq 825$

Table 5

STARTING LINE DATA – CASE I

Coordinates*		Magnitude of Velocity Vector V (ft/sec)	Angle of Velocity Vector** θ (rad)	Entropy S/R	Shock Angle* ϕ (rad)
x (cm)	y (cm)				
2.315	32.52	16,794	0.955	56.82	1.067
2.363	32.49	16,370	0.956	57.10	
2.438	32.43	15,840	0.958	57.42	
2.633	32.30	14,740	0.962	58.05	
2.875	32.13	13,640	0.965	58.58	
3.215	31.89	12,420	0.968	59.10	
3.749	31.51	10,920	0.971	59.67	
4.429	31.03	9,760	0.970	60.18	
5.011	30.62	9,400	0.967	60.48	
5.351	30.38	9,500	0.964	60.61	
5.593	30.21	9,820	0.961	60.69	
5.788	30.07	10,240	0.958	60.74	
5.901	29.99	10,558	0.956	60.78	

*Origin is at the stagnation point.
**Angles are measured from the (downstream pointing) x coordinate.

Table 6

STARTING LINE DATA – CASE III

Coordinates*		Magnitude of Velocity Vector V (ft/sec)	Angle of Velocity Vector** θ (rad)	Entropy S/R	Shock Angle* ϕ (rad)
x (cm)	y (cm)				
1.959	35.13	11,563	1.082	69.45	1.262
2.337	34.97	11,110	1.097	69.61	
2.687	34.84	10,800	1.106	69.78	
3.155	34.66	10,431	1.116	70.01	
3.622	34.48	10,086	1.122	70.22	
4.089	34.30	9,780	1.122	70.44	
4.557	34.10	9,578	1.107	70.66	
5.024	33.79	9,505	1.076	70.89	
5.492	33.47	9,656	1.03	71.09	
5.784	33.27	10,000	0.998	71.20	
5.936	33.16	10,435	0.978	71.26	
6.017	33.10	10,855	0.968	71.30	
6.085	33.06	11,407	0.9599	71.32	

*Origin is at the stagnation point.
**Angles are measured from the (downstream pointing) x coordinate.

To predict the separating streamline for Case I, the theory of Denison and Baum (Ref. 21), which extended Chapman's original work on the base flow region (Ref. 22) to include the presence of an initial boundary layer at the separation point, was used. Following Chapman, it was assumed that the recompression region where the recirculating flow turns back is small in extent. As a result, the total pressure on the dividing streamline is equal to the static pressure behind the recompression region. For isentropic recompression, and an adiabatic free shear layer with Prandtl number one, the latter assumption is equivalent to

$$M_2^2/M_1^2 = 1 - (u_D^*)^2 \tag{2.6}$$

where M_1 and M_2 are the inviscid Mach numbers before and after recompression, and u_D^* is defined in Ref. 21 as the ratio of the velocity along the dividing streamline to the inviscid velocity at the outer edge of the free-shear layer. u_D^* can be obtained from Fig. 5 of Ref. 21 as a function of s^*, which is a transformed distance along the dividing streamline measured from the separation point, and also defined in that figure.

A trial-and-error procedure was employed to calculate the correct separating streamline. For an assumed separation point on the body, a characteristics solution, including the separating constant-pressure streamline, was obtained. Due to the breakdown of the finite-difference equations in the vicinity of the axis, the calculated separating streamline curves sharply downward as it approaches the axis. The flow angle at the neck was therefore assumed to be the minimum angle achieved on the calculated streamline. Using this angle and the value of M_1 given by the characteristics solution, the value of M_2 corresponding to isentropic compression to the free-stream direction was obtained with the aid of the gas tables of Ref. 23. A numerical integration using the results of the characteristics solution also determined the transformed distance s^* corresponding to the neck location. The corresponding value of u_D^* from Fig. 5 was then compared to the value given by Eq. (2.6). The separation point was varied and the calculations repeated until the two values agreed.

The complete flow geometry for Case I is shown in Fig. 8. Representative state variables from the characteristics solution are tabulated in Table 2, and provided input data for the radiative heating program. The pressure and velocity distributions on the body up to the separation point are plotted in Fig. 4. The curves have been extrapolated backwards to the curvature discontinuity point, where they meet the solution derived from the subsonic program. The discontinuity in curvature results in discontinuities in the slopes of the pressure and velocity curves. It is seen that the slopes are much steeper over the rounded corner regions than they are just ahead of it. For Case II, an approximate pressure distribution was utilized in the supersonic region, as discussed in subsection 2.2.2, and shown in Fig. 5.

The complete flow geometry for Case III is shown in Fig. 9. Representative streamlines have been traced for use in the streamtube chemistry program (subsection 2.3). In the subsonic region these were obtained directly from the solution of subsection 2.2.3. In the supersonic region they were derived by interpolation from the characteristics solution. The pressure distribution as a function of arc length along each streamline was used as input for the chemistry program. The pressure and velocity distributions (the latter already corrected for the chemistry) on the body from the beginning of the rounded shoulder to the backward-facing step are shown in Fig. 7. The discontinuity in slope is much larger here than was true in Case I.

2.3 FLOW CHEMISTRY – PRODUCTION AND DISTRIBUTION OF SPECIES

The streamtube treatment is used in conjunction with a previously computed equilibrium flow field in predicting the nonequilibrium species distribution. The procedure followed treats the flow field, initially, as an inviscid, adiabatic, equilibrium region. The results of these calculations are next used to establish pressure distributions along an arbitrary number of streamlines traced throughout the equilibrium shock layer. The pressure distributions, in turn, govern the motion of the chemically reacting fluid element through a coupling of the one-dimensional (streamwise) momentum equation with an array of differential species production equations. Solution of this system of

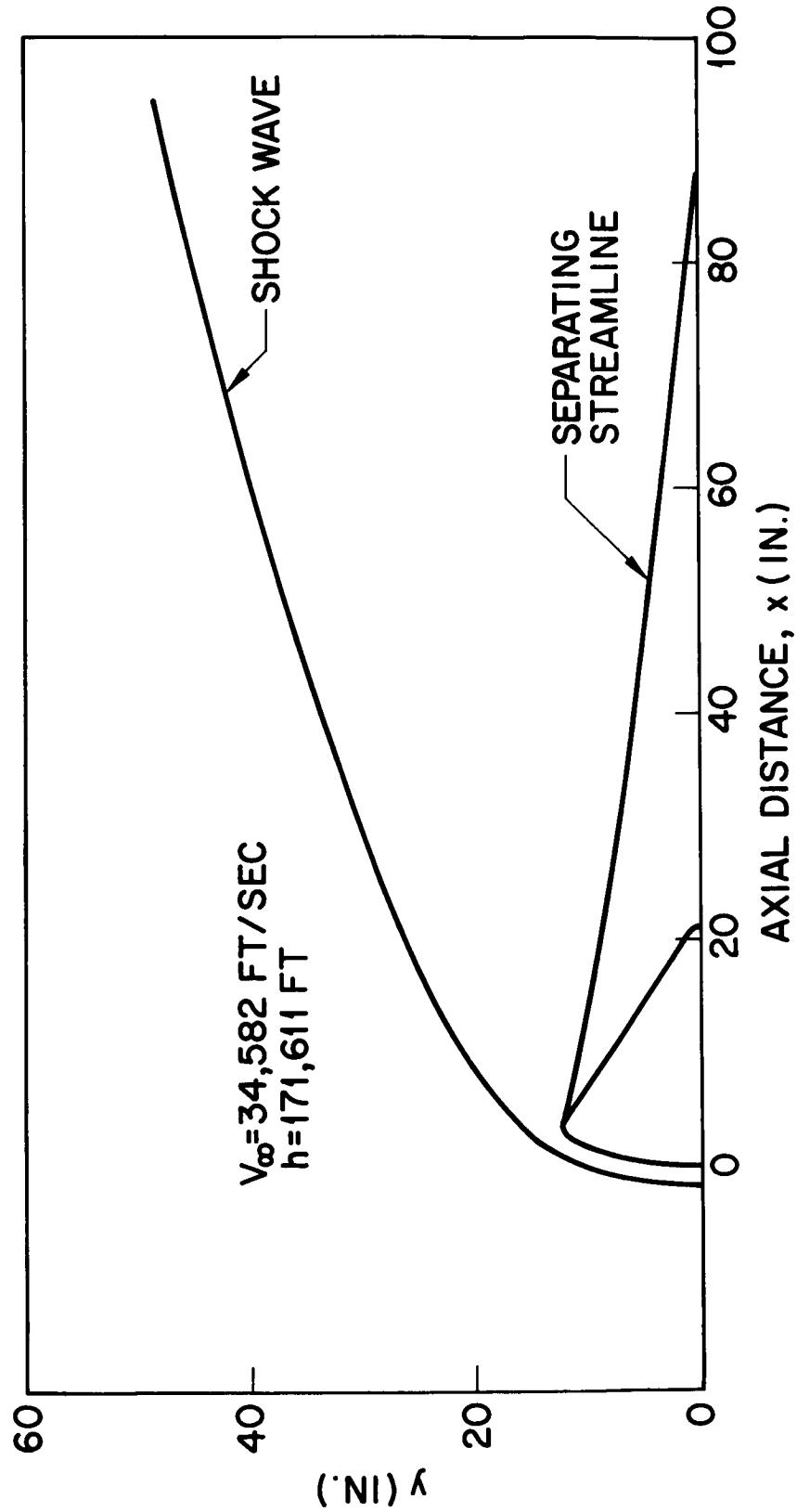

Fig. 8 Flow Geometry for Case I

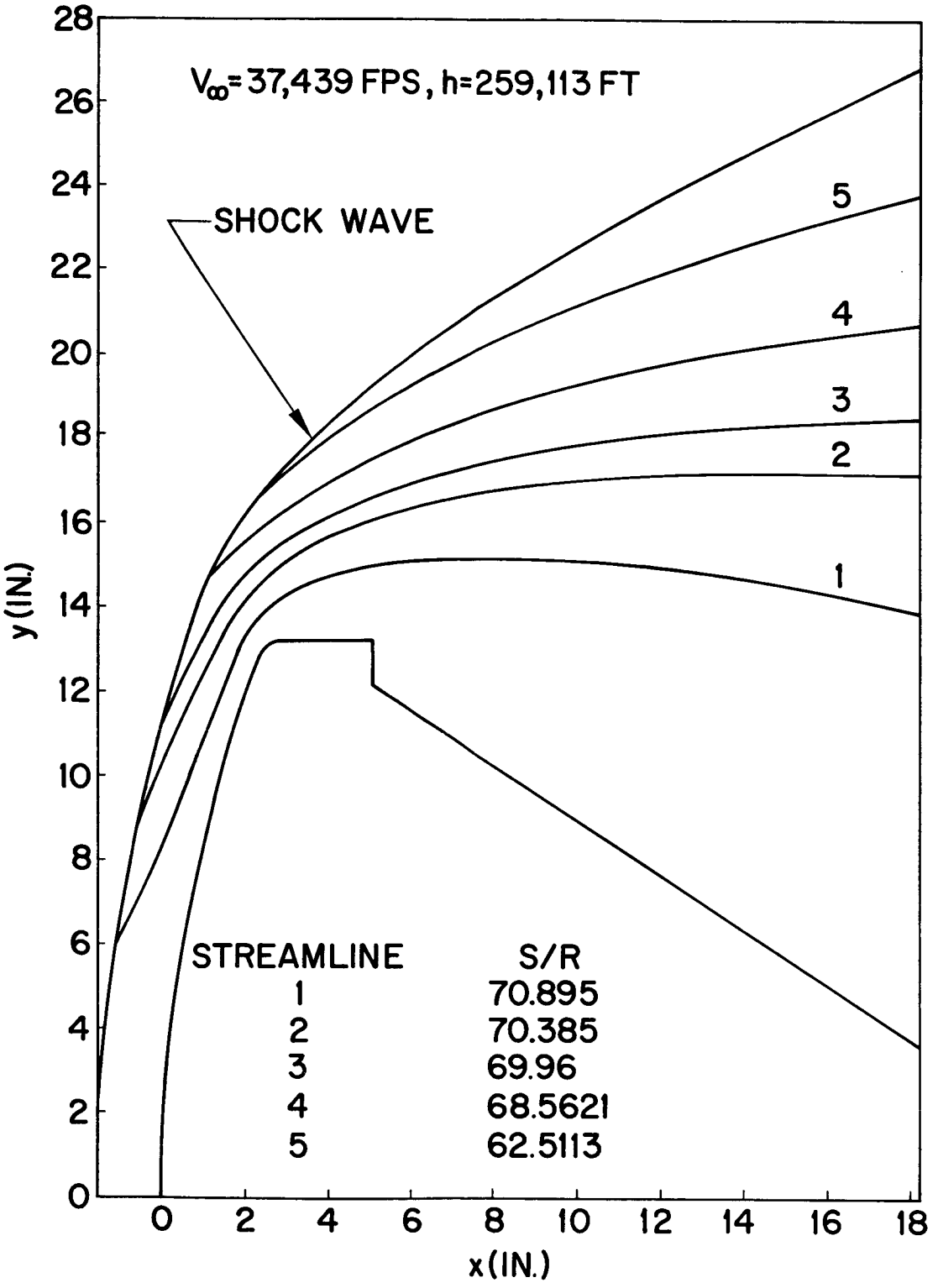

Fig. 9 Flow Geometry for Case III

equations is accomplished by numerical forward integration of the equation array from inside the bow shock surface continuing over the extent of the streamline traced. The explicit formulation, additional discussion of rate processes, and sources of pertinent physical constants appear in subsection 3.2 of this report.

A basic assumption in the streamtube rate chemistry calculations is that the governing equilibrium pressure distribution and streamline patterns are insensitive to subsequent chemical kinetic processes. The assumption is that, on the average, the macroscopic pressure (or its kinetic theory equivalent, the time rate of change of directed particle momenta in normal collisions within a moving fluid element) is relatively unaffected by the chemical processes. (Although, rather obviously, the inverse of this assumption is not valid; since altering the rate of change of particle collisions clearly affects to a significant degree the chemical kinetics.)

A physical argument for the foregoing assumption can be examined from a simple illustration. Consider a group of elementary diatomic molecules (no complex interactions or field effects) possessing a certain thermal motion or temperature (the frame of reference is moving with respect to the macroscopic or "streaming" velocity). A fraction of these molecules conceptually dissociate into their constituent atoms. In the energy bath associated with the particle ensemble, the atoms achieve increased thermal velocity consistent with their mass reduction from the molecular state in accordance with elementary kinetic theory. However, the apparent disparity caused by increase in thermal velocity and increased particle population through changes from the molecular state is, to a large extent, offset by the decrease of the dissociated particle mass on the statistical average over the collisional momenta. It follows that, at a fixed point in space and time, the momenta, averaged over a large number of collisions by atoms and more massive but slower residual molecules in accordance with the rate chemistry, change only slightly relative to the average momenta in directed collisions corresponding to equilibrium population composition. Hence, the thermal contributions to the macroscopic pressure change little from the equilibrium level predicted locally. The preceding illustration is only reasonable if instantaneous large magnitude changes to the local chemical compositions are not encountered. However, such changes in the inviscid flow model

resemble infinitely fast rate processes (equilibrium chemistry) or discontinuities (shock waves) which are treated separately in the initial equilibrium flow-field calculation. The additional, second-order effects of particle diffusion on the streamline traces are neglected in the treatment. These, of course, become important only in the viscous region of the flow near the body surface.

An additional assumption applied to the rate chemistry analysis has to do with the manner in which the chemical kinetic processes are uncoupled from the internal thermodynamic degrees of freedom available to the species.

The streamtube computer code used to determine finite-rate chemical kinetics in the flowing gas essentially uncouples the rate chemistry from all internal energy modes available to the gas particles. The significant assumption is that there exists immediate full excitation and equilibration of vibrational and rotational degrees of freedom with the translational mode. Conceptually, full excitation of rotational and vibrational levels is considered accomplished by fluid particles immediately after transition across the shock front. The shock front itself is considered to be the usual gas dynamic discontinuity.

A sound basis for the theoretical determination of the rate of excitation of the bound electronic levels is not currently available (see J. G. Hall, Ref. 24). However, because of the relatively small amount of the total energy absorbed in the electronic states, the rate chemistry can be (and was) effectively uncoupled from this mode of internal energy absorption. Estimates of the electronic excitation of the species and the electronic temperature are of importance, however, in the radiation calculations. The procedure for estimating the electronic temperature is discussed separately in the section on radiation calculations.

The streamtube approximation is not valid in the stagnation region, where the velocity decreases and ultimately vanishes. In order to calculate conditions along the axial streamline the following method was used. A streamtube integration was performed at

constant pressure (and therefore constant velocity). The distance is then exactly proportional to the time. Since the actual pressure distribution is nearly constant on the real axial streamline this solution gives a good approximation to the correct distribution as a function of time. In order to map this into the real physical distance along the axial streamline, use is made of the continuity and momentum equations in the shock layer (unchanged by the chemistry). This provides a relationship between density, distance, and time in the real situation. Using the density vs. time distribution from the constant-pressure streamtube solution, it is then possible to find the mapping between this time and the real physical distance. Details are to be found in Appendix B. The body surface streamline integration starts at a point 11 cm from the stagnation point, where conditions were identical to the equilibrium conditions behind the normal shock wave. These conditions were obtained from tabulated normal shock wave calculations (see Marrone, Ref. 25).

Some of the results of the rate-chemistry calculations have been arranged in graphs for ease in comparison and discussion. The results used in the establishment of species population and distribution for the radiation calculations included several additional streamline traces which are not shown. However, the two prepared figures illustrate, in general, the characteristics of the flow chemistry found for Case III. Detailed tabulations of these results for all streamlines traced appear in Table 7.

The axial streamline distributions of the molar fractions for the 10 subspecie components considered appear in Fig. 10. The molar fractions are given in terms of the fraction of the ith specie ratioed to the ambient value on a molar mass basis. This ratio is a convenient form for species calculations and may be converted to the usual concentration fraction by dividing the molar mass fraction or ordinate value at any point by Z, the molecular compressibility factor. The compressibility factor is easily determined at any point. It is the sum over all component molar fractions at the position of interest. The calculation starts immediately behind the shock front (the $x \rightarrow 0$ limit implied by the figure) and extends, as shown, over a streamline distance considered in the calculation. This intrinisic streamline distance is measured in cm.

Table 7

NONEQUILIBRIUM SPECIES DISTRIBUTIONS AND FLOW-FIELD DATA – CASE III
(Consisting of Tables 7.1 Through 7.7)

Table 7.1

TABULATED DATA – AXIAL STREAMLINE

Cartesian Coordinates		$\bar{V}$*	$\bar{p}$*	T (°K)	ρ (gm/cc)	$\bar{N}_{10}$ (e^-)	Mole Fractions*		$\bar{N}_3$ (NO)	$\bar{N}_4$ (O)	$\bar{N}_5$ (N)	$\bar{N}_6$ (NO^+)	$\bar{N}_7$ (N_2^+)	$\bar{N}_8$ (O^+)	$\bar{N}_9$ (N^+)
x (cm)	y (cm)						$\bar{N}_1$ (O_2)	$\bar{N}_2$ (N_2)							
-3.92087	0	1.2534^{-1}	8.7507^{-1}	4.9748^{+4}	1.8600^{-7}	0	2.10^{-1}	7.90^{-1}	0	0	0	0	0	0	0
-3.851	0	1.196^{-1}	8.806^{-1}	4.521^{+4}	1.741^{-7}	6.401^{-5}	8.744^{-2}	7.161^{-1}	1.124^{-2}	2.391^{-1}	1.425^{-1}	5.116^{-8}	1.103^{-8}	3.202^{-5}	3.193^{-5}
-3.796	0	1.157^{-1}	8.840^{-1}	4.115^{+4}	1.681^{-7}	2.763^{-4}	8.775^{-3}	6.252^{-1}	2.002^{-2}	3.916^{-1}	3.201^{-1}	7.491^{-7}	1.544^{-7}	1.479^{-4}	1.275^{-4}
-3.713	0	1.120^{-1}	8.871^{-1}	3.681^{+4}	1.689^{-7}	8.446^{-4}	9.528^{-4}	4.742^{-1}	2.153^{-2}	4.062^{-1}	6.210^{-1}	5.608^{-6}	1.753^{-6}	3.867^{-4}	4.505^{-4}
-3.568	0	1.064^{-1}	8.915^{-1}	3.117^{+4}	1.760^{-7}	2.201^{-3}	5.359^{-4}	2.631^{-1}	1.490^{-2}	4.102^{-1}	1.045	4.882^{-5}	2.318^{-5}	7.755^{-4}	1.354^{-3}
-3.416	0	9.771^{-2}	8.984^{-1}	2.777^{+4}	1.850^{-7}	3.743^{-3}	2.634^{-4}	1.335^{-1}	8.028^{-3}	4.140^{-1}	1.307	2.156^{-4}	1.206^{-4}	1.075^{-3}	2.332^{-3}
-2.898	0	7.204^{-2}	9.165^{-1}	2.426^{+4}	2.022^{-7}	1.001^{-2}	1.665^{-5}	1.090^{-2}	5.943^{-4}	4.169^{-1}	1.549	1.900^{-3}	1.271^{-3}	1.772^{-3}	5.067^{-3}
-2.431	0	5.170^{-2}	9.276^{-1}	2.357^{+4}	2.089^{-7}	1.769^{-2}	8.883^{-7}	6.346^{-4}	3.283^{-5}	4.155^{-1}	1.563	3.282^{-3}	2.717^{-3}	2.747^{-3}	8.940^{-3}
-1.936	0	3.334^{-2}	9.347^{-1}	2.300^{+4}	2.147^{-7}	2.835^{-2}	1.346^{-8}	9.443^{-6}	4.854^{-7}	4.136^{-1}	1.555	2.841^{-3}	3.422^{-3}	4.862^{-3}	1.722^{-2}
-1.433	0	1.846^{-2}	9.383^{-1}	2.197^{+4}	2.231^{-7}	4.843^{-2}	1.266^{-9}	6.062^{-8}	1.730^{-8}	4.097^{-1}	1.540	1.561^{-3}	2.263^{-3}	9.514^{-3}	3.510^{-2}
-9.329^{-1}	0	7.978^{-3}	9.397^{-1}	1.989^{+4}	2.412^{-7}	9.467^{-2}	2.006^{-9}	1.124^{-7}	3.215^{-8}	4.000^{-1}	1.505	7.097^{-4}	8.598^{-4}	1.982^{-2}	7.328^{-2}
-4.369^{-1}	0	1.834^{-3}	9.400^{-1}	1.657^{+4}	2.787^{-7}	1.766^{-1}	4.156^{-9}	5.311^{-7}	9.422^{-8}	3.813^{-1}	1.442	2.453^{-4}	2.286^{-4}	3.858^{-2}	1.376^{-1}

*Nondimensional quantities defined in the nomenclature.

Table 7.2

TABULATED DATA – BODY STREAMLINE

Cartesian Coordinates		$\bar{V}$*	$\bar{p}$*	T (°K)	ρ (gm/cc)	$\bar{N}_{10}$ (e^-)	Mole Fractions*		$\bar{N}_3$ (NO)	$\bar{N}_4$ (O)	$\bar{N}_5$ (N)	$\bar{N}_6$ (NO^+)	$\bar{N}_7$ (N_2^+)	$\bar{N}_8$ (O^+)	$\bar{N}_9$ (N^+)
x (cm)	y (cm)						$\bar{N}_1$ (O_2)	$\bar{N}_2$ (N_2)							
6.390^{-1}	1.098^{+1}	5.6328^{-2}	9.4410^{-1}	1.029^{+4}	4.17820^{-7}	3.486^{-1}	5.366^{-8}	7.503^{-5}	2.853^{-6}	3.655^{-1}	1.286	1.490^{-5}	5.980^{-6}	5.445^{-2}	2.941^{-1}
6.500^{-1}	1.101^{+1}	5.641^{-2}	9.440^{-1}	1.029^{+4}	4.178^{-7}	3.486^{-1}	5.366^{-8}	7.503^{-5}	2.853^{-6}	3.655^{-1}	1.286	1.490^{-5}	5.980^{-6}	5.445^{-2}	2.941^{-1}
6.750^{-1}	1.108^{+1}	5.684^{-2}	9.436^{-1}	1.029^{+4}	4.177^{-7}	3.486^{-1}	4.983^{-8}	7.500^{-5}	2.805^{-6}	3.655^{-1}	1.286	1.843^{-5}	5.460^{-6}	5.445^{-2}	2.941^{-1}
7.750^{-1}	1.190^{+1}	6.150^{-2}	9.387^{-1}	1.026^{+4}	4.164^{-7}	3.486^{-1}	4.721^{-8}	7.436^{-5}	2.666^{-6}	3.655^{-1}	1.286	1.818^{-5}	5.375^{-6}	5.445^{-2}	2.941^{-1}
1.050	1.386^{+1}	7.133^{-2}	9.272^{-1}	1.021^{+4}	4.133^{-7}	3.486^{-1}	4.648^{-8}	7.358^{-5}	2.628^{-6}	3.655^{-1}	1.286	1.777^{-5}	5.178^{-6}	5.445^{-2}	2.941^{-1}
1.350	1.582^{+1}	8.151^{-2}	9.137^{-1}	1.015^{+4}	4.097^{-7}	3.486^{-1}	4.599^{-8}	7.350^{-5}	2.610^{-6}	3.655^{-1}	1.286	1.729^{-5}	4.950^{-6}	5.445^{-2}	2.941^{-1}
2.350	2.088^{+1}	1.081^{-1}	8.705^{-1}	9.959^{+3}	3.979^{-7}	3.485^{-1}	4.508^{-8}	7.540^{-5}	2.602^{-6}	3.655^{-1}	1.286	1.579^{-5}	4.264^{-6}	5.444^{-2}	2.941^{-1}
3.507	2.568^{+1}	1.399^{-1}	8.054^{-1}	9.656^{+3}	3.798^{-7}	3.485^{-1}	4.375^{-8}	7.939^{-5}	2.600^{-6}	3.656^{-1}	1.286	1.360^{-5}	3.336^{-6}	5.443^{-2}	2.941^{-1}
4.425	2.875^{+1}	1.664^{-1}	7.417^{-1}	9.343^{+3}	3.614^{-7}	3.485^{-1}	4.198^{-8}	8.276^{-5}	2.568^{-6}	3.656^{-1}	1.286	1.156^{-5}	2.550^{-6}	5.443^{-2}	2.940^{-1}
4.750	2.978^{+1}	1.771^{-1}	7.138^{-1}	9.201^{+3}	3.532^{-7}	3.485^{-1}	4.106^{-8}	8.401^{-5}	2.545^{-6}	3.656^{-1}	1.286	1.070^{-5}	2.484^{-6}	5.442^{-2}	2.940^{-1}
5.075	3.070^{+1}	1.898^{-1}	6.797^{-1}	9.022^{+3}	3.430^{-7}	3.485^{-1}	3.982^{-8}	8.540^{-5}	2.509^{-6}	3.656^{-1}	1.286	9.674^{-6}	1.899^{-6}	5.442^{-2}	2.940^{-1}
5.400	3.155^{+1}	2.019^{-1}	6.457^{-1}	8.839^{+3}	3.326^{-7}	3.485^{-1}	3.852^{-8}	8.662^{-5}	2.468^{-6}	3.656^{-1}	1.286	8.693^{-6}	1.591^{-6}	5.442^{-2}	2.940^{-1}
5.750	3.239^{+1}	2.172^{-1}	6.014^{-1}	8.591^{+3}	3.187^{-7}	3.485^{-1}	3.677^{-8}	8.794^{-5}	2.409^{-6}	3.656^{-1}	1.286	7.471^{-6}	1.237^{-6}	5.442^{-2}	2.940^{-1}
6.250	3.320^{+1}	3.337^{-1}	2.551^{-1}	6.112^{+3}	1.900^{-7}	3.485^{-1}	3.021^{-8}	8.921^{-5}	2.251^{-6}	3.656^{-1}	1.286	9.744^{-7}	4.613^{-8}	5.442^{-2}	2.940^{-1}
6.820	3.360^{+1}	4.433^{-1}	3.267^{-2}	2.822^{+3}	5.270^{-8}	3.484^{-1}	2.559^{-8}	8.966^{-5}	2.112^{-6}	3.656^{-1}	1.286	3.175^{-10}	4.908^{-14}	5.442^{-2}	2.940^{-1}
8.255	3.360^{+1}	4.441^{-1}	3.186^{-2}	2.794^{+3}	5.191^{-8}	3.484^{-1}	2.462^{-8}	8.982^{-6}	2.055^{-6}	3.656^{-1}	1.286	2.924^{-10}	1.842^{-14}	5.442^{-2}	2.940^{-1}
9.200	3.360^{+1}	4.448^{-1}	3.126^{-2}	2.773^{+3}	5.132^{-8}	3.484^{-1}	2.375^{-8}	8.997^{-5}	2.001^{-6}	3.656^{-1}	1.286	2.629^{-10}	1.512^{-14}	5.442^{-2}	2.940^{-1}
1.010^{+1}	3.360^{+1}	4.443^{-1}	3.166^{-2}	2.787^{+3}	5.172^{-8}	3.484^{-1}	2.293^{-8}	9.012^{-5}	1.949^{-6}	3.656^{-1}	1.286	2.797^{-10}	1.664^{-14}	5.442^{-2}	2.940^{-1}
1.1096^{+1}	3.360^{+1}	4.424^{-1}	3.359^{-2}	2.854^{+3}	5.358^{-8}	3.484^{-1}	2.214^{-8}	9.028^{-5}	1.899^{-6}	3.656^{-1}	1.286	3.856^{-10}	2.960^{-14}	5.442^{-2}	2.940^{-1}
1.2910^{+1}	3.360^{+1}	4.352^{-1}	4.123^{-2}	3.099^{+3}	6.057^{-8}	3.484^{-1}	2.047^{-8}	9.059^{-5}	1.800^{-6}	3.656^{-1}	1.286	1.142^{-9}	2.142^{-13}	5.442^{-2}	2.940^{-1}

*Nondimensional quantities defined in the nomenclature.

Table 7.3

TABULATED DATA – STREAMLINE 1 (S/R = 70.895)

Cartesian Coordinates		$\bar{V}$*	$\bar{p}$*	T (°K)	ρ (gm/cc)	$\bar{N}_{10}$ (e^-)	Mole Fractions*		$\bar{N}_3$ (NO)	$\bar{N}_4$ (O)	$\bar{N}_5$ (N)	$\bar{N}_6$ (NO^+)	$\bar{N}_7$ (N_2^+)	$\bar{N}_8$ (O^+)	$\bar{N}_9$ (N^+)
x (cm)	y (cm)						$\bar{N}_1$ (O_2)	$\bar{N}_2$ (N_2)							
-2.810	1.495^{+1}	1.556^{-1}	9.235^{-1}	5.2505^{+4}	1.8806^{-7}	0	2.10^{-1}	7.90^{-1}	0	0	0	0	0	0	0
-2.766	1.498^{+1}	1.559^{-1}	9.232^{-1}	4.320^{+4}	1.809^{-7}	1.141^{-4}	4.676^{-2}	6.902^{-1}	1.490^{-2}	3.185^{-1}	1.927^{-1}	1.609^{-7}	3.086^{-8}	6.095^{-5}	5.293^{-5}
-2.718	1.499^{+1}	1.562^{-1}	9.228^{-1}	3.845^{+4}	1.775^{-7}	5.210^{-4}	1.955^{-3}	5.527^{-1}	2.181^{-2}	4.042^{-1}	4.641^{-1}	2.500^{-6}	6.222^{-7}	2.625^{-4}	2.553^{-4}
-2.650	1.520^{+1}	1.564^{-1}	9.225^{-1}	3.490^{+4}	1.794^{-7}	1.101^{-3}	8.173^{-4}	4.248^{-1}	2.055^{-2}	4.069^{-1}	7.202^{-1}	1.061^{-5}	3.683^{-6}	4.767^{-4}	6.102^{-4}
-2.600	1.530^{+1}	1.566^{-1}	9.223^{-1}	3.217^{+4}	1.828^{-7}	1.734^{-3}	6.399^{-4}	3.235^{-1}	1.736^{-2}	4.088^{-1}	9.238^{-1}	3.004^{-5}	1.274^{-5}	6.615^{-4}	1.030^{-3}
-2.550	1.550^{+1}	1.570^{-1}	9.218^{-1}	2.824^{+4}	1.911^{-7}	3.135^{-3}	3.479^{-4}	1.766^{-1}	1.036^{-2}	4.127^{-1}	1.220	1.507^{-4}	7.881^{-5}	9.670^{-4}	1.939^{-3}
-2.400	1.590^{+1}	1.574^{-1}	9.212^{-1}	2.496^{+4}	2.027^{-7}	5.794^{-3}	9.814^{-5}	5.814^{-2}	3.333^{-3}	4.163^{-1}	1.458	7.859^{-4}	4.682^{-4}	1.313^{-3}	3.227^{-3}
-2.200	1.635^{+1}	1.575^{-1}	9.211^{-1}	2.365^{+4}	2.093^{-7}	8.937^{-3}	2.676^{-5}	1.820^{-2}	9.742^{-4}	4.169^{-1}	1.536	1.841^{-3}	1.180^{-3}	1.589^{-3}	4.327^{-3}
-2.000	1.680^{+1}	1.572^{-1}	9.216^{-1}	2.309^{+4}	2.129^{-7}	1.221^{-2}	7.718^{-6}	5.667^{-3}	2.902^{-4}	4.164^{-1}	1.558	2.846^{-3}	1.980^{-3}	1.885^{-3}	5.497^{-3}
-1.600	1.775^{+1}	1.593^{-1}	9.186^{-1}	2.258^{+4}	2.160^{-7}	1.747^{-2}	8.869^{-7}	6.910^{-4}	3.419^{-5}	4.154^{-1}	1.563	3.751^{-3}	3.152^{-3}	2.533^{-3}	8.031^{-3}
-1.100	1.870^{+1}	1.627^{-1}	9.135^{-1}	2.227^{+4}	2.174^{-7}	2.151^{-2}	1.211^{-7}	9.642^{-5}	4.709^{-6}	4.148^{-1}	1.560	3.666^{-3}	3.728^{-3}	3.263^{-3}	1.085^{-2}
3.000^{-1}	2.005^{+1}	1.713^{-1}	9.001^{-1}	2.174^{+4}	2.186^{-7}	2.816^{-2}	4.490^{-9}	2.718^{-6}	1.449^{-7}	4.137^{-1}	1.554	2.852^{-3}	3.700^{-3}	4.817^{-3}	1.680^{-2}
1.300	2.425^{+1}	1.925^{-1}	8.644^{-1}	2.075^{+4}	2.186^{-7}	4.023^{-2}	1.620^{-9}	8.390^{-8}	2.425^{-8}	4.112^{-1}	1.546	1.868^{-3}	2.506^{-3}	7.814^{-3}	2.805^{-2}
3.000	2.885^{+1}	2.241^{-1}	8.040^{-1}	1.958^{+4}	2.141^{-7}	5.211^{-2}	1.978^{-9}	1.173^{-7}	3.256^{-8}	4.086^{-1}	1.538	1.340^{-3}	1.633^{-3}	1.067^{-2}	3.847^{-2}
4.200	3.260^{+1}	2.637^{-1}	7.186^{-1}	1.846^{+4}	2.023^{-7}	5.775^{-2}	2.297^{-9}	1.644^{-7}	4.159^{-8}	4.074^{-1}	1.534	1.105^{-3}	1.257^{-3}	1.204^{-2}	4.335^{-2}
5.300	3.435^{+1}	3.509^{-1}	5.101^{-1}	1.606^{+4}	1.651^{-7}	5.859^{-2}	2.693^{-9}	2.190^{-7}	5.466^{-8}	4.072^{-1}	1.533	8.898^{-4}	9.773^{-4}	1.234^{-2}	4.438^{-2}
6.000	3.510^{+1}	4.005^{-1}	3.892^{-1}	1.442^{+4}	1.402^{-7}	5.827^{-2}	2.969^{-9}	2.600^{-7}	6.602^{-8}	4.073^{-1}	1.534	7.055^{-4}	7.693^{-4}	1.236^{-2}	4.444^{-2}
6.750	3.570^{+1}	4.468^{-1}	2.819^{-1}	1.271^{+4}	1.153^{-7}	5.785^{-2}	3.261^{-9}	3.114^{-7}	8.057^{-8}	4.074^{-1}	1.534	4.986^{-4}	5.400^{-4}	1.236^{-2}	4.445^{-2}
8.750	3.675^{+1}	5.107^{-1}	1.524^{-1}	1.002^{+4}	7.901^{-8}	5.723^{-2}	3.652^{-9}	4.165^{-7}	1.103^{-7}	4.075^{-1}	1.535	2.027^{-4}	2.141^{-4}	1.236^{-2}	4.445^{-2}
1.315^{+1}	3.820^{+1}	5.672^{-1}	6.778^{-2}	7.346^{+3}	4.796^{-8}	5.689^{-2}	3.672^{-9}	5.732^{-7}	1.472^{-7}	4.076^{-1}	1.535	3.730^{-5}	3.018^{-5}	1.236^{-2}	4.445^{-2}

*Nondimensional quantities defined in the nomenclature.

Table 7.4

TABULATED DATA – STREAMLINE 2 (S/R = 70.385)

Cartesian Coordinates		$\bar{V}$*	$\bar{p}$*	T (°K)	ρ (gm/cc)	$\bar{N}_{10}$ (e^-)	Mole Fractions*		$\bar{N}_3$ (NO)	$\bar{N}_4$ (O)	$\bar{N}_5$ (N)	$\bar{N}_6$ (NO^+)	$\bar{N}_7$ (N_2^+)	$\bar{N}_8$ (O^+)	$\bar{N}_9$ (N^+)
x (cm)	y (cm)						$\bar{N}_1$ (O_2)	$\bar{N}_2$ (N_2)							
-1.310	2.298^{+1}	2.225^{-1}	8.751^{-1}	4.9757^{+4}	1.8804^{-7}	0	2.10^{-1}	7.90^{-1}	0	0	0	0	0	0	0
-1.123	2.342^{+1}	2.254^{-1}	8.701^{-1}	2.644^{+4}	1.903^{-7}	3.540^{-3}	2.830^{-4}	1.546^{-1}	8.865^{-3}	4.135^{-1}	1.264	2.757^{-4}	1.427^{-4}	1.024^{-3}	2.098^{-3}
-1.015	2.364^{+1}	2.261^{-1}	8.689^{-1}	2.407^{+4}	1.995^{-7}	5.626^{-3}	1.101^{-4}	6.953^{-2}	3.847^{-3}	4.160^{-1}	1.435	9.060^{-4}	5.153^{-4}	1.250^{-3}	2.955^{-3}
-9.050^{-1}	2.387^{+1}	2.263^{-1}	8.685^{-5}	2.295^{+4}	2.051^{-7}	7.774^{-3}	4.720^{-5}	3.348^{-2}	1.755^{-3}	4.166^{-1}	1.506	1.737^{-3}	1.045^{-3}	1.408^{-3}	3.584^{-3}
-8.860^{-1}	2.432^{+1}	2.277^{-1}	8.658^{-1}	2.199^{+4}	2.104^{-7}	1.175^{-2}	1.109^{-5}	8.919^{-3}	4.365^{-4}	4.163^{-1}	1.551	3.225^{-3}	2.163^{-3}	1.686^{-3}	4.676^{-3}
-4.620^{-1}	2.655^{+1}	2.314^{-1}	8.580^{-1}	2.154^{+4}	2.120^{-7}	1.489^{-2}	3.052^{-6}	2.592^{-3}	1.230^{-4}	4.158^{-1}	1.561	4.043^{-3}	3.084^{-3}	1.974^{-3}	5.786^{-3}
1.200	2.835^{+1}	2.385^{-1}	8.430^{-1}	2.109^{+4}	2.122^{-7}	1.883^{-2}	3.101^{-7}	2.746^{-4}	1.274^{-5}	4.152^{-1}	1.561	4.165^{-3}	4.054^{-3}	2.567^{-3}	8.039^{-3}
2.750	3.200^{+1}	2.641^{-1}	7.859^{-1}	2.024^{+4}	2.056^{-7}	2.300^{-2}	9.269^{-9}	7.294^{-6}	3.497^{-7}	4.146^{-1}	1.558	3.355^{-3}	4.109^{-3}	3.606^{-3}	1.193^{-2}
3.600	3.380^{+1}	2.857^{-1}	7.351^{-1}	1.963^{+4}	1.982^{-7}	2.429^{-2}	3.550^{-9}	1.800^{-6}	1.046^{-7}	4.144^{-1}	1.558	3.061^{-3}	3.826^{-3}	4.006^{-3}	1.340^{-2}
5.350	3.640^{+1}	3.920^{-1}	4.686^{-1}	1.639^{+4}	1.513^{-7}	2.410^{-2}	2.876^{-9}	7.285^{-7}	7.038^{-8}	4.144^{-1}	1.558	2.502^{-3}	3.115^{-3}	4.242^{-3}	1.424^{-2}
7.500	3.835^{+1}	4.708^{-1}	2.794^{-1}	1.340^{+4}	1.103^{-7}	2.253^{-2}	3.288^{-9}	7.232^{-7}	9.019^{-8}	4.148^{-1}	1.560	1.756^{-3}	2.226^{-3}	4.259^{-3}	1.429^{-2}
9.200	3.965^{+1}	5.128^{-1}	1.916^{-1}	1.159^{+4}	8.750^{-8}	2.139^{-2}	3.589^{-9}	7.955^{-7}	1.105^{-7}	4.151^{-1}	1.562	1.217^{-3}	1.616^{-3}	4.260^{-3}	1.430^{-2}
1.860^{+1}	4.250^{+1}	5.866^{-1}	7.192^{-2}	8.029^{+3}	4.744^{-8}	1.941^{-2}	3.730^{-9}	1.037^{-6}	1.594^{-7}	4.156^{-1}	1.564	3.108^{-4}	5.480^{-4}	4.260^{-3}	1.430^{-2}

*Nondimensional quantities defined in the nomenclature.

Table 7.5

TABULATED DATA – STREAMLINE 3 (S/R = 69.96)

Cartesian Coordinates		$\bar{V}$*	$\bar{p}$*	T (°K)	ρ (gm/cc)	$\bar{N}_{10}$ (e^-)	Mole Fractions*		$\bar{N}_3$ (NO)	$\bar{N}_4$ (O)	$\bar{N}_5$ (N)	$\bar{N}_6$ (NO^+)	$\bar{N}_7$ (N_2^+)	$\bar{N}_8$ (O^+)	$\bar{N}_9$ (N^+)
x (cm)	y (cm)						$\bar{N}_1$ (O_2)	$\bar{N}_2$ (N_2)							
4.900^{-2}	2.858^{+1}	2.654^{-1}	8.800^{-1}	5.0038^{+4}	1.8803^{-7}	0	2.10^{-1}	7.90^{-1}	0	0	0	0	0	0	0
4.961^{-2}	2.862^{+1}	2.654^{-1}	8.801^{-1}	4.563^{+4}	1.955^{-7}	8.560^{-6}	1.817^{-1}	7.636^{-1}	3.377^{-3}	5.481^{-2}	5.114^{-2}	2.059^{-9}	7.050^{-10}	3.429^{-6}	5.129^{-6}
7.276^{-2}	2.867^{+1}	2.654^{-1}	8.801^{-1}	4.364^{+4}	1.887^{-7}	3.861^{-5}	1.226^{-1}	7.346^{-1}	8.477^{-3}	1.703^{-1}	1.069^{-1}	2.905^{-8}	6.577^{-9}	1.907^{-5}	1.951^{-5}
1.111^{-1}	2.874^{+1}	2.653^{-1}	8.802^{-1}	4.034^{+4}	1.809^{-7}	1.489^{-4}	3.214^{-2}	6.782^{-1}	1.653^{-2}	3.468^{-1}	2.159^{-1}	3.621^{-7}	6.327^{-8}	8.357^{-5}	6.495^{-5}
1.562^{-1}	2.883^{+1}	2.653^{-1}	8.803^{-1}	3.787^{+4}	1.792^{-7}	3.497^{-4}	5.235^{-3}	6.082^{-1}	2.084^{-2}	3.982^{-1}	3.537^{-1}	1.730^{-6}	3.434^{-7}	1.909^{-4}	1.568^{-4}
2.033^{-1}	2.893^{+1}	2.652^{-1}	8.804^{-1}	3.564^{+4}	1.799^{-7}	6.388^{-4}	1.353^{-3}	5.308^{-1}	2.186^{-2}	4.053^{-1}	5.078^{-1}	5.251^{-6}	1.307^{-6}	3.201^{-4}	3.122^{-4}
2.945^{-1}	2.901^{+1}	2.652^{-1}	8.804^{-1}	3.189^{+4}	1.836^{-7}	1.340^{-3}	7.293^{-4}	3.932^{-1}	1.946^{-2}	4.076^{-1}	7.837^{-1}	2.468^{-5}	8.623^{-6}	5.629^{-4}	7.441^{-4}
4.789^{-1}	2.948^{+1}	2.653^{-1}	8.803^{-1}	2.706^{+4}	1.944^{-7}	2.886^{-3}	3.838^{-4}	2.092^{-1}	1.166^{-2}	4.120^{-1}	1.154	1.846^{-4}	8.712^{-5}	9.153^{-4}	1.698^{-3}
6.940^{-1}	2.990^{+1}	2.656^{-1}	8.795^{-1}	2.416^{+4}	2.049^{-7}	4.720^{-3}	1.681^{-4}	1.046^{-1}	5.766^{-3}	4.151^{-1}	1.364	6.898^{-4}	3.674^{-4}	1.144^{-3}	2.519^{-3}
9.343^{-1}	3.004^{+1}	2.662^{-1}	8.781^{-1}	2.273^{+4}	2.119^{-7}	6.634^{-3}	7.875^{-5}	5.574^{-2}	2.921^{-3}	4.162^{-1}	1.462	1.450^{-3}	8.209^{-4}	1.286^{-3}	3.078^{-3}
1.300	3.135^{+1}	2.680^{-1}	8.738^{-1}	2.148^{+4}	2.187^{-7}	1.007^{-2}	2.379^{-5}	1.959^{-2}	9.506^{-4}	4.164^{-1}	1.532	2.919^{-3}	1.814^{-3}	1.483^{-3}	3.857^{-3}
1.750	3.230^{+1}	2.724^{-1}	8.626^{-1}	2.085^{+4}	2.208^{-7}	1.306^{-2}	7.842^{-6}	6.996^{-3}	3.250^{-4}	4.160^{-1}	1.554	3.993^{-3}	2.783^{-3}	1.677^{-3}	4.607^{-3}
2.200	3.330^{+1}	2.804^{-1}	8.419^{-1}	2.042^{+4}	2.195^{-7}	1.500^{-2}	3.088^{-6}	2.879^{-3}	1.307^{-4}	4.157^{-1}	1.560	4.424^{-3}	3.454^{-3}	1.852^{-3}	5.269^{-3}
2.750	3.410^{+1}	2.941^{-1}	8.058^{-1}	1.996^{+4}	2.147^{-7}	1.614^{-2}	1.445^{-6}	1.397^{-3}	6.241^{-5}	4.156^{-1}	1.562	4.495^{-3}	3.854^{-3}	1.994^{-3}	5.800^{-3}
3.750	3.507^{+1}	3.342^{-1}	6.957^{-1}	1.874^{+4}	1.972^{-7}	1.711^{-2}	4.457^{-7}	4.687^{-4}	2.019^{-5}	4.155^{-1}	1.562	4.255^{-3}	4.158^{-3}	2.187^{-3}	6.507^{-3}
5.000	3.725^{+1}	3.947^{-1}	5.256^{-1}	1.677^{+4}	1.665^{-7}	1.682^{-2}	2.108^{-7}	2.491^{-4}	1.025^{-5}	4.157^{-1}	1.563	3.793^{-3}	3.972^{-3}	2.267^{-3}	6.792^{-3}
8.750	4.003^{+1}	5.032^{-1}	2.459^{-1}	1.252^{+4}	1.044^{-7}	1.430^{-2}	1.132^{-7}	1.747^{-4}	6.531^{-6}	4.164^{-1}	1.566	2.398^{-3}	2.752^{-3}	2.287^{-3}	6.861^{-3}
1.300^{+1}	4.240^{+1}	5.559^{-1}	1.388^{-1}	1.010^{+4}	7.308^{-8}	1.250^{-2}	8.569^{-8}	1.702^{-4}	5.786^{-6}	4.169^{-1}	1.568	1.467^{-3}	1.886^{-3}	2.288^{-3}	6.862^{-3}
2.530^{+1}	4.505^{+1}	6.188^{-1}	4.832^{-2}	6.902^{+3}	3.734^{-8}	1.034^{-2}	4.225^{-8}	1.712^{-4}	4.273^{-6}	4.175^{-1}	1.571	3.916^{-4}	7.937^{-4}	2.288^{-3}	6.862^{-3}
3.960^{+1}	4.645^{+1}	6.348^{-1}	2.577^{-2}	5.522^{+3}	2.484^{-8}	9.621^{-3}	2.305^{-8}	1.724^{-4}	3.233^{-6}	4.177^{-1}	1.572	1.034^{-4}	3.671^{-4}	2.288^{-3}	6.862^{-3}

*Nondimensional quantities defined in the nomenclature.

Table 7.6

TABULATED DATA – STREAMLINE 4 (S/R = 68.5621)

Cartesian Coordinates		$\bar{V}$*	$\bar{p}$*	T (°K)	ρ (gm/cc)	$\bar{N}_{10}$ (e^-)	Mole Fractions*		$\bar{N}_3$ (NO)	$\bar{N}_4$ (O)	$\bar{N}_5$ (N)	$\bar{N}_6$ (NO^+)	$\bar{N}_7$ (N_2^+)	$\bar{N}_8$ (O^+)	$\bar{N}_9$ (N^+)
x (cm)	y (cm)						$\bar{N}_1$ (O_2)	$\bar{N}_2$ (N_2)							
2.590	3.691^{+1}	3.723^{-1}	8.138^{-1}	4.6287^{+4}	1.8799^{-7}	0	2.10^{-1}	7.90^{-1}	0	0	0	0	0	0	0
2.626	3.695^{+1}	3.741^{-1}	8.081^{-1}	4.264^{+4}	1.959^{-7}	4.016^{-6}	1.932^{-1}	7.726^{-1}	2.238^{-3}	3.248^{-2}	3.366^{-2}	9.702^{-10}	3.308^{-10}	1.642^{-6}	2.372^{-6}
2.675	3.699^{+1}	3.759^{-1}	8.026^{-1}	4.137^{+4}	1.908^{-7}	1.837^{-5}	1.597^{-1}	7.535^{-1}	5.535^{-3}	9.769^{-2}	7.034^{-2}	1.261^{-8}	3.078^{-9}	8.839^{-6}	9.514^{-6}
2.700	3.700^{+1}	3.787^{-1}	7.943^{-1}	3.907^{+4}	1.829^{-7}	6.536^{-5}	8.942^{-2}	7.220^{-1}	1.129^{-2}	2.351^{-1}	1.306^{-1}	1.267^{-7}	2.176^{-8}	3.645^{-5}	2.876^{-5}
2.800	3.705^{+1}	3.816^{-1}	7.857^{-1}	3.700^{+4}	1.778^{-7}	1.463^{-4}	3.568^{-2}	6.867^{-1}	1.625^{-2}	3.399^{-1}	1.990^{-1}	5.935^{-7}	9.001^{-8}	8.575^{-5}	5.981^{-5}
2.900	3.715^{+1}	3.848^{-1}	7.766^{-1}	3.535^{+4}	1.751^{-7}	2.613^{-4}	1.181^{-2}	6.474^{-1}	1.951^{-2}	3.858^{-1}	2.760^{-1}	1.805^{-6}	2.852^{-7}	1.519^{-4}	1.073^{-4}
3.000	3.730^{+1}	3.918^{-1}	7.567^{-1}	3.254^{+4}	1.730^{-7}	5.855^{-4}	1.688^{-3}	5.617^{-1}	2.188^{-2}	4.046^{-1}	4.461^{-1}	8.571^{-6}	1.737^{-6}	3.097^{-4}	2.655^{-4}
3.200	3.765^{+1}	4.048^{-1}	7.188^{-1}	2.821^{+4}	1.723^{-7}	1.352^{-3}	7.116^{-4}	4.198^{-1}	1.981^{-2}	4.074^{-1}	7.305^{-1}	5.496^{-5}	1.615^{-5}	5.774^{-4}	7.034^{-4}
3.950	3.840^{+1}	4.335^{-1}	6.310^{-1}	2.223^{+4}	1.718^{-7}	3.202^{-3}	3.443^{-4}	2.358^{-1}	1.197^{-2}	4.118^{-1}	1.101	5.367^{-4}	2.128^{-4}	8.920^{-4}	1.561^{-3}
4.750	3.910^{+1}	4.555^{-1}	5.606^{-1}	1.959^{+4}	1.670^{-7}	4.629^{-3}	2.124^{-4}	1.717^{-1}	8.391^{-3}	4.135^{-1}	1.229	1.253^{-3}	5.265^{-4}	9.750^{-4}	1.875^{-3}
5.400	3.975^{+1}	4.772^{-1}	4.905^{-1}	1.770^{+4}	1.587^{-7}	5.891^{-3}	1.485^{-4}	1.379^{-1}	6.410^{-3}	4.142^{-1}	1.297	2.007^{-3}	8.598^{-4}	1.009^{-3}	2.016^{-3}
6.150	4.004^{+1}	4.942^{-1}	4.363^{-1}	1.648^{+4}	1.503^{-7}	6.681^{-3}	1.200^{-4}	1.220^{-1}	5.466^{-3}	4.145^{-1}	1.328	2.507^{-3}	1.084^{-3}	1.022^{-3}	2.069^{-3}
8.400	4.201^{+1}	5.376^{-1}	3.054^{-1}	1.386^{+4}	1.237^{-7}	7.675^{-3}	8.291^{-5}	1.017^{-1}	4.220^{-3}	4.149^{-1}	1.368	3.127^{-3}	1.399^{-3}	1.033^{-3}	2.117^{-3}
1.030^{+1}	4.320^{+1}	5.627^{-1}	2.373^{-1}	1.250^{+4}	1.063^{-7}	7.603^{-3}	7.120^{-5}	9.710^{-2}	3.867^{-3}	4.151^{-1}	1.378	3.039^{-3}	1.407^{-3}	1.034^{-3}	2.123^{-3}
1.500^{+1}	4.505^{+1}	6.040^{-1}	1.416^{-1}	1.030^{+4}	7.691^{-8}	6.795^{-3}	5.479^{-5}	9.439^{-2}	3.422^{-3}	4.157^{-1}	1.384	2.412^{-3}	1.225^{-3}	1.034^{-3}	2.124^{-3}
2.003^{+1}	4.760^{+1}	6.306^{-1}	9.289^{-2}	8.881^{+3}	5.853^{-8}	5.949^{-3}	4.200^{-5}	9.423^{-2}	3.041^{-3}	4.163^{-1}	1.385	1.778^{-3}	1.012^{-3}	1.034^{-3}	2.124^{-3}
3.880^{+1}	5.180^{+1}	6.738^{-1}	3.620^{-2}	6.457^{+3}	3.140^{-8}	4.510^{-3}	1.944^{-5}	9.501^{-2}	2.123^{-3}	4.174^{-1}	1.385	7.410^{-4}	6.108^{-4}	1.034^{-3}	2.124^{-3}

*Nondimensional quantities defined in the nomenclature.

Table 7.7

TABULATED DATA – STREAMLINE 5 (S/R = 62.5113)

Cartesian Coordinates		$\bar{V}$*	$\bar{p}$*	T (°K)	ρ (gm/cc)	$\bar{N}_{10}$ (e^-)	Mole Fractions*		$\bar{N}_3$ (NO)	$\bar{N}_4$ (O)	$\bar{N}_5$ (N)	$\bar{N}_6$ (NO^+)	$\bar{N}_7$ (N_2^+)	$\bar{N}_8$ (O^+)	$\bar{N}_9$ (N^+)
x (cm)	y (cm)						$\bar{N}_1$ (O_2)	$\bar{N}_2$ (N_2)							
5.650	4.195^{+1}	6.283^{-1}	5.7461^{-1}	3.2725^{+4}	1.8774^{-7}	0	2.10^{-1}	7.90^{-1}	0	0	0	0	0	0	0
5.721	4.205^{+1}	6.295^{-1}	5.682^{-1}	2.974^{+4}	1.968^{-7}	5.749^{-6}	1.871^{-1}	7.750^{-1}	3.555^{-3}	4.392^{-2}	2.827^{-2}	1.786^{-8}	2.559^{-9}	3.146^{-6}	2.582^{-6}
5.758	4.209^{+1}	6.302^{-1}	5.649^{-1}	2.915^{+4}	1.946^{-7}	1.421^{-5}	1.683^{-1}	7.670^{-1}	5.684^{-3}	8.041^{-2}	4.342^{-2}	7.967^{-8}	9.716^{-9}	8.190^{-6}	5.932^{-6}
5.798	4.213^{+1}	6.308^{-1}	5.616^{-1}	2.849^{+4}	1.922^{-7}	2.727^{-5}	1.451^{-1}	7.586^{-1}	7.947^{-3}	1.256^{-1}	5.902^{-2}	2.456^{-7}	2.588^{-8}	1.637^{-5}	1.063^{-5}
5.875	4.221^{+1}	6.321^{-1}	5.548^{-1}	2.708^{+4}	1.880^{-7}	6.786^{-5}	9.372^{-2}	7.413^{-1}	1.247^{-2}	2.259^{-1}	9.152^{-2}	1.317^{-6}	1.116^{-7}	4.261^{-5}	2.382^{-5}
6.952	4.229^{+1}	6.336^{-1}	5.476^{-1}	2.581^{+4}	1.851^{-7}	1.259^{-4}	5.123^{-2}	7.233^{-1}	1.641^{-2}	3.087^{-1}	1.258^{-1}	4.437^{-6}	3.392^{-7}	7.939^{-5}	4.175^{-5}
6.350	4.252^{+1}	6.375^{-1}	5.280^{-1}	2.359^{+4}	1.817^{-7}	3.285^{-4}	7.966^{-3}	6.757^{-1}	2.232^{-2}	3.920^{-1}	2.180^{-1}	2.970^{-5}	2.427^{-6}	1.886^{-4}	1.078^{-4}
7.100	4.345^{+1}	6.462^{-1}	4.855^{-1}	2.066^{+4}	1.782^{-7}	8.383^{-4}	9.097^{-4}	5.893^{-1}	2.471^{-2}	4.045^{-1}	3.895^{-1}	1.764^{-4}	2.048^{-5}	3.579^{-4}	2.835^{-4}
7.800	4.410^{+1}	6.535^{-1}	4.509^{-1}	1.884^{+4}	1.748^{-7}	1.260^{-3}	7.203^{-4}	5.367^{-1}	2.411^{-2}	4.051^{-1}	4.946^{-1}	3.770^{-4}	5.174^{-5}	4.300^{-4}	4.015^{-4}
8.600	4.470^{+1}	6.620^{-1}	4.091^{-1}	1.713^{+4}	1.692^{-7}	1.739^{-3}	6.437^{-4}	4.914^{-1}	2.293^{-2}	4.057^{-1}	5.855^{-1}	6.716^{-4}	1.022^{-4}	4.733^{-4}	4.924^{-4}
9.400	4.535^{+1}	6.691^{-1}	3.758^{-1}	1.602^{+4}	1.634^{-7}	2.084^{-3}	6.003^{-4}	4.659^{-1}	2.205^{-2}	4.061^{-1}	6.367^{-1}	9.146^{-4}	1.448^{-4}	4.905^{-4}	5.344^{-4}
1.175^{+1}	4.700^{+1}	6.884^{-1}	2.896^{-1}	1.376^{+4}	1.429^{-7}	2.778^{-3}	5.272^{-4}	4.267^{-1}	2.044^{-2}	4.068^{-1}	7.154^{-1}	1.453^{-3}	2.378^{-4}	5.073^{-4}	5.800^{-4}
1.350^{+1}	4.820^{+1}	7.022^{-1}	2.342^{-1}	1.250^{+4}	1.260^{-7}	3.061^{-3}	4.955^{-4}	4.133^{-1}	1.978^{-2}	4.071^{-1}	7.423^{-1}	1.686^{-3}	2.767^{-4}	5.102^{-4}	5.886^{-4}
1.810^{+1}	5.007^{+1}	7.206^{-1}	1.696^{-1}	1.099^{+4}	1.031^{-7}	3.216^{-3}	4.508^{-4}	4.022^{-1}	1.890^{-2}	4.075^{-1}	7.647^{-1}	1.811^{-3}	3.009^{-4}	5.116^{-4}	5.926^{-4}
2.240^{+1}	5.290^{+1}	7.360^{-1}	1.239^{-1}	9.863^{+3}	8.374^{-8}	3.119^{-3}	4.111^{-4}	3.987^{-1}	1.810^{-2}	4.081^{-1}	7.723^{-1}	1.721^{-3}	2.937^{-4}	5.118^{-4}	5.932^{-4}
3.175^{+1}	5.650^{+1}	7.547^{-1}	7.890^{-2}	8.555^{+3}	6.146^{-8}	2.794^{-3}	3.421^{-4}	3.979^{-1}	1.659^{-2}	4.091^{-1}	7.747^{-1}	1.427^{-3}	2.612^{-4}	5.119^{-4}	5.934^{-4}

*Nondimensional quantities defined in the nomenclature.

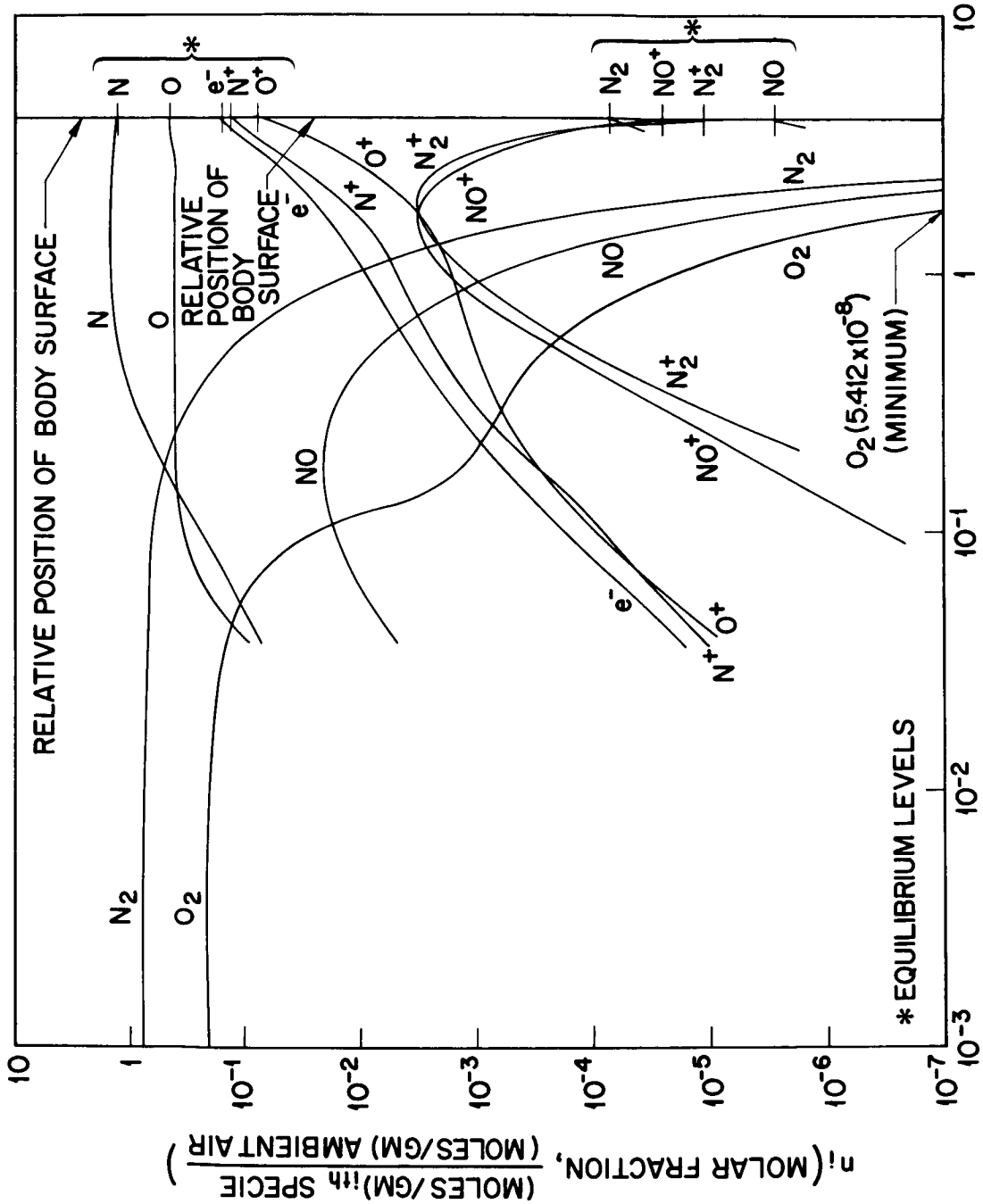

Fig. 10 Distribution of Nonequilibrium Species Components Along Axial Streamline for Case III

The chemical processes are seen to be initially dominated by molecular dissociation, which is almost completed prior to the onset of significant ionization. The dissociation of the ambient molecular components is virtually complete in a distance of the order of 1 cm. The dissociation rates are seen to cause a relatively steep slope in the initial decay of the ambient molecular species. This reflects the high probability or cross section for energetic exchange at the dissociation level consistent with the relatively high energy available in the flow.

The onset of ionization may be traced by the increase of the positive ionic components and corresponding buildup of free electrons. This growth is seen to be more gradual at first (indicating the initial, less efficient ionization probability corresponding to atomic collisions). Subsequently, the ion fraction profiles steepen rapidly in response to the appearance of the ions and free electrons with their associated increased efficiency as ion-production collision partners. These two well-defined phases in ionization simulate the ionization phenomena where the initial gas is cool and relatively unexcited (see Hall, Ref. 24 and Bortner, Ref. 26). The ionization processes appear to be still in progress, hence, somewhat out of chemical equilibrium at the "end" of the axial layer trace, 3.92 cm. At this limit the free-electron mole fraction has attained a level of about 0.152. This corresponds to a number density of about 1.35×10^{15} $(cc)^{-1}$ at the local gas density level.

Principal contributors to the free-electron population near the stagnation point limit are the single detachment of electrons from the atomic nitrogen and oxygen available. Contributions of the additional ion sources considered in the present system, nitric oxide and molecular nitrogen, are negligible near the limit of this trace, as expected. These two sources, which donate significant electron populations at lower gas temperatures (below the level associated with significant single atomic ionization), have probability peaks in the intermediate temperature range of 2000 to 4000°K. At higher temperatures the dissociation probability for these contributors dominates, hence they decay into their atomic components. The neglect of the possible contribution of the single ionization of molecular oxygen reflects the fact that its recombination cross

sections are of the same order as its electron detachment cross sections throughout the life of the molecule. This production "balance" is somewhat less in evidence for the molecular nitrogen single ionization reaction, included in the system.

Superimposed on the figure are the equilibrium levels of the species associated with the conditions existing behind the normal shock in equilibrium flow. Those values were obtained from the detailed Cornell tables for normal shock equilibrium (see Marrone, Ref. 25).

Figure 11 shows the species distributions computed along a somewhat cooler streamline trace (S/R = 70.895). This particular streamline is of interest in that its length and position help illustrate the apparent asymptotic "frozen" levels toward which the component species are driven. The considerable length over which the governing equations are applied, coupled to the flow velocity, results in most of the rate processes tending toward a quasi-constant, frozen level (although small changes persist, since the flow is still expanding to the limit of the streamline).

Similar to the axial trace, primary dissociation of the ambient molecular constituents is seen to be essentially complete prior to the onset of the ionization processes. The variation in the thermal energy content in comparison to the axial streamline may be deduced from the maximum level reached by the free electron molar fraction (roughly 6×10^{-2} as compared to the value of 1.52×10^{-1} observed on the previous figure). Again, the flow is hot enough so that the principal electron contributors are from atomic single ionization. The secondary ionization of nitric oxide and singly ionized molecular nitrogen peaks to a value of about 4×10^{-3} at around 4 cm from the shock origin. The maximum free electron concentration is reached well back in the flow (at about 18.4 cm). The maximum electron number density corresponding to the local gas density is about 2.44×10^{14} $(cc)^{-1}$ at this location. This is a decrease of almost an order of magnitude in comparison to the maximum values determined on the axial streamline. The point at which the streamline encounters the start of the corner expansion, hence the origin of the expansion zone, is identified on the graph.

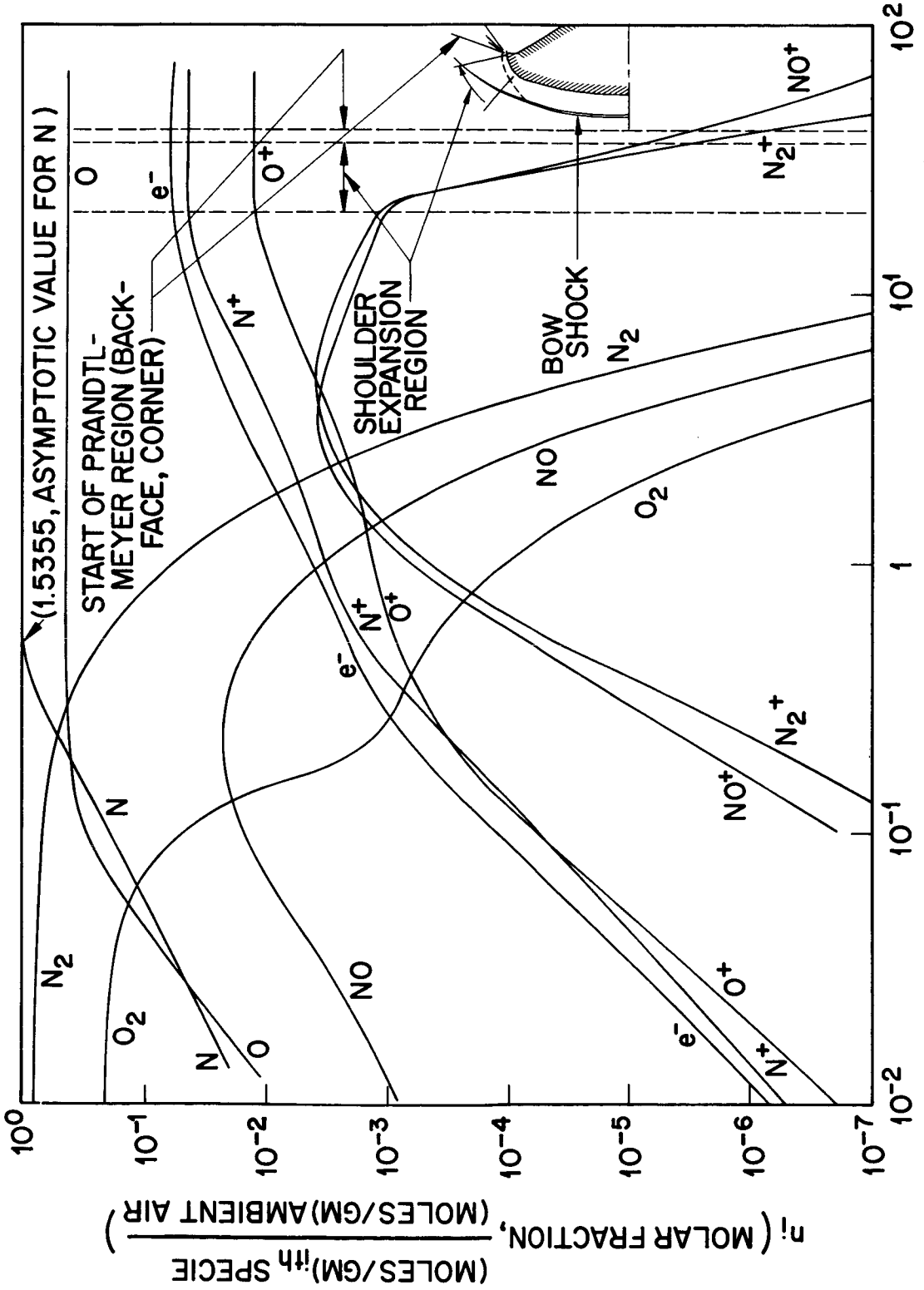

Fig. 11 Distribution of Nonequilibrium Species Components Along Shock-Layer Streamline (Entropy, S/R = 70.895) for Case III

These results, in conjunction with those of the other streamlines traced through the shock layer, were used to predict the spatial distribution and proportional contribution of the independent subspecies to the radiation transport calculations described in another section.

2.4 RADIATION PROPERTIES AND RADIATIVE TRANSFER

2.4.1 General

There are presently in existence the results of several studies of the radiation properties of air. Equilibrium emissivities have been studied in at least three serious, theoretical works (Refs. 27, 28, and 29). Unfortunately, the predictions for the radiative properties of air differ by as much as an order of magnitude at thermodynamic states corresponding to typical reentry conditions. Much less is known about the nonequilibrium radiative properties. Some special cases have been studied; e.g., the effects of collision limiting, but, for the most part, semi-empirical methods (Ref. 30) are required. It has been found necessary to re-examine both the techniques used in the emissivity predictions and the manner in which these are used to calculate radiative transport. Two theoretical methods for the calculation of frequency-dependent and integrated radiative properties have recently become available at LMSC. The first has been developed by Armstrong and offers a very high degree of precision in the calculation of equilibrium properties. The second was developed specifically for the present study for the purpose of predicting nonequilibrium radiation. The analysis which is presented in subsection 3.3 is somewhat less accurate than Armstrong's analysis, but has greater utility in that the emissivities can be more readily generated. In addition, of course, it has sufficient generality to handle (approximately) nonequilibrium radiation.

In order to evaluate the radiative heating to the FIRE vehicle, it is necessary to carefully examine the applicability of the thin-gas approximation. In this approximation it is assumed that the shock-layer gas emits but does not absorb radiative energy.

Rigorously, this must be true at every frequency if the approximation is to be valid. Both Armstrong's spectral emission coefficient data and the data generated in Section 3 indicate that the shock layers for Cases I and II are not optically thin and that the use of this approximation will significantly overpredict the radiative flux to the body. The stagnation-point radiative heat transfer to the FIRE vehicle was calculated both with and without the effect of self-absorption for Case I. A significant effect of self-absorption in reducing the radiative heating was observed.

The effect of energy loss by radiation was also considered. A good measure of the importance of this effect is the radiation loss parameter, Γ , which is defined by

$$\Gamma = \frac{\text{energy loss in time } \delta/v_\delta}{\text{total energy}}$$

where δ and v_δ are the shock standoff distance and normal velocity behind the shock, respectively. It was found that this parameter was about 0.05 for Case I and less for Case III. Therefore, radiation cooling losses were neglected in the present calculations.

In the following sections, the primary results of the radiative heat-transfer calculations are presented and discussed. The data are presented in both graphical and tabular form (Tables, 8, 9, and 10).

2.4.2 Radiative Heat Transfer

2.4.2.1 Equilibrium Radiation, Case I and II

In order to calculate the radiative heat-transfer distribution one must know the details of the inviscid flow field and the dependence of the emission coefficient of the gas in question with thermodynamic properties. In the present analysis the inviscid flow field discussed in the previous section was used to obtain the temperature and density distribution in the shock layer and in the separated flow region. With the temperature and

Table 8a

RADIATIVE HEATING DISTRIBUTION – CASE I

Arc Length, s (in.)	LMSC Lower Bound, q_R (Btu/sec-ft^2)	LMSC Upper Bound, q_R (Btu/sec-ft^2)	AVCO Data, q_R (Btu/sec-ft^2)	Armstrong's Data, q_R (Btu/sec-ft^2)	Present Calculation of q_R (Btu/sec-ft^2)
0	186	1630	640	450	375
4.03	180	1600			
7.88	157	1460			
9.93	119	12100			
10.79	105	1080			
13.0	10.1				
13.8	3.31				
21.5	0.316				

Table 8b

CONVECTIVE HEATING DISTRIBUTION – CASE I

Arc Length, s (in.)	Heating Based on Cohen's Theory, q_c (Btu/sec-ft^2)	Heating Based on Lee's Theory, q_c (Btu/sec-ft^2)
0	601	601.3
1.968	601	
3.858	589	616.7
5.906	624	
7.383	637	646
9.26	649	645
11.02	670	658
11.78-	662	650
11.78+	717	
12.047		619
12.35	560	537
12.76	364	361
12.87		313
12.99		265
13.15		234
13.33	140	145
13.48		109
13.63		78.0
13.79		70.77

Table 9

SPECTRAL INTENSITY DISTRIBUTION – CASE I

λ (microns)	$\left(\frac{I_\lambda \text{ ergs}}{cm^2\text{-sec-micron}}\right)$	λ (microns)	$\left(\frac{I_\lambda \text{ ergs}}{cm^2\text{-sec-micron}}\right)$
8×10^{-2}	3.3×10^{9}	6.1×10^{-1}	1.4×10^{8}
9×10^{-2}	1.05×10^{10}	7×10^{-1}	1.33×10^{8}
10^{-1}	1.25×10^{10}	7.5×10^{-1}	1.4×10^{8}
1.1×10^{-1}	2.05×10^{9}	8.4×10^{-1}	1.6×10^{9}
1.2×10^{-1}	1.12×10^{9}	8.6×10^{-1}	7.4×10^{8}
1.4×10^{-1}	1.42×10^{8}	9.4×10^{-1}	1.35×10^{9}
2×10^{-1}	6.0×10^{8}	1.0	1.7×10^{8}
2.7×10^{-1}	1.55×10^{9}	1.1	1.1×10^{8}
2.9×10^{-1}	1.35×10^{9}	1.25	2.5×10^{7}
3×10^{-1}	1.7×10^{9}	1.5	1.43×10^{7}
3.1×10^{-1}	1.08×10^{9}	2.0	8.5×10^{6}
3.2×10^{-1}	7.2×10^{8}	3.0	4.7×10^{6}
3.4×10^{-1}	6.0×10^{8}	4.0	3×10^{6}
4.1×10^{-1}	6.0×10^{8}	5.0	2.05×10^{6}
4.4×10^{-1}	7.7×10^{8}	6.0	1.45×10^{6}
4.8×10^{-1}	4.3×10^{8}		
5×10^{-1}	2.3×10^{8}		
5.2×10^{-1}	1.65×10^{8}		
5.6×10^{-1}	1.39×10^{8}		

Table 10a

RADIATIVE HEATING DISTRIBUTION – CASE III

Cut No.	Upper Estimate (Btu/ft^2-sec)	Lower Estimate (Btu/ft^2-sec)	Upper Bound From Ref. 30 (Btu/ft^2-sec)	Lower Bound From Ref. 30 (Btu/ft^2-sec)
1	85	26	160	52
2	80.5			
3	40.8			

Table 10b

CONVECTIVE HEATING DISTRIBUTION – CASE III

Arc Length, s (in.)	Convective Heating, q_c (Btu/sec-ft^2)	Convective Heating With Nonequilibrium Viscosity, q_c (Btu/sec-ft^2)
0	145	
4.33	143.55	
5.71	145	
8.28	152.1	
10.29	154.1	
11.84	158.3	
13.02	156.21	
13.23	151.08	
13.44	108.3	88.9
13.76	25.65	
14.37	20.85	
14.62	20.49	15.36
15.36	21.2	
16.25	25.14	18.04

density known, the local emission can be evaluated at each point in the flow field. If the gas is assumed to be optically thin, the radiative heat transfer to the vehicle surface can be determined by summing up the intensity from each point in the flow field. One can simplify the analysis by making the tangent slab approximation in which it is assumed that the emission varies only in the normal direction and is given by the variation at the body point of interest. The slab is assumed to be infinite in extent so that the solid angle is equal to 2π . This approximation is valid on the FIRE vehicle in the region of the stagnation point but is not valid in the corner or separated flow region and, hence, was not used at all in the present analysis. Instead, the local emission at each point in the flow field was calculated and its contribution to the intensity to the surface was properly taken into account in the manner described in subsection 3.3.8. The gas was assumed to be optically thin in the analysis presented in subsection 3.3.8. The effect of self-absorption was estimated, however, but only at the stagnation point for Case I.

In Fig. 12* (see Table 8) the radiative heat-transfer distribution is shown for Case I. Because of the current uncertainty in the emission coefficient, the radiative heat-transfer distribution was determined using both the emissivity results obtained by Meyerott, et al. (Ref. 27), and Breene, et al. (Ref. 29). The distribution obtained using the data of (Ref. 27) is labeled LMSC lower bound, while the distribution obtained using the results of (Ref. 29) is labeled LMSC upper bound. The difference between the radiative heating levels is approximately an order of magnitude. The distribution along the body, however, appears to be quite insensitive to the emissivity data used. The effect of self-absorption in reducing the radiative heating is also shown in Fig. 12. The effect of self-absorption was estimated using the spectral emission coefficient data of Armstrong and also by using the spectral emission coefficient data obtained by the analysis presented in subsection 3.3. Self-absorption was approximately accounted for by assuming that the gas was optically thin up to the point, in terms of frequency, where the intensity became equal to the black-body value. The gas was then assumed to radiate

*The convective heating shown in this and subsequent figures is discussed in subsection 2.5.

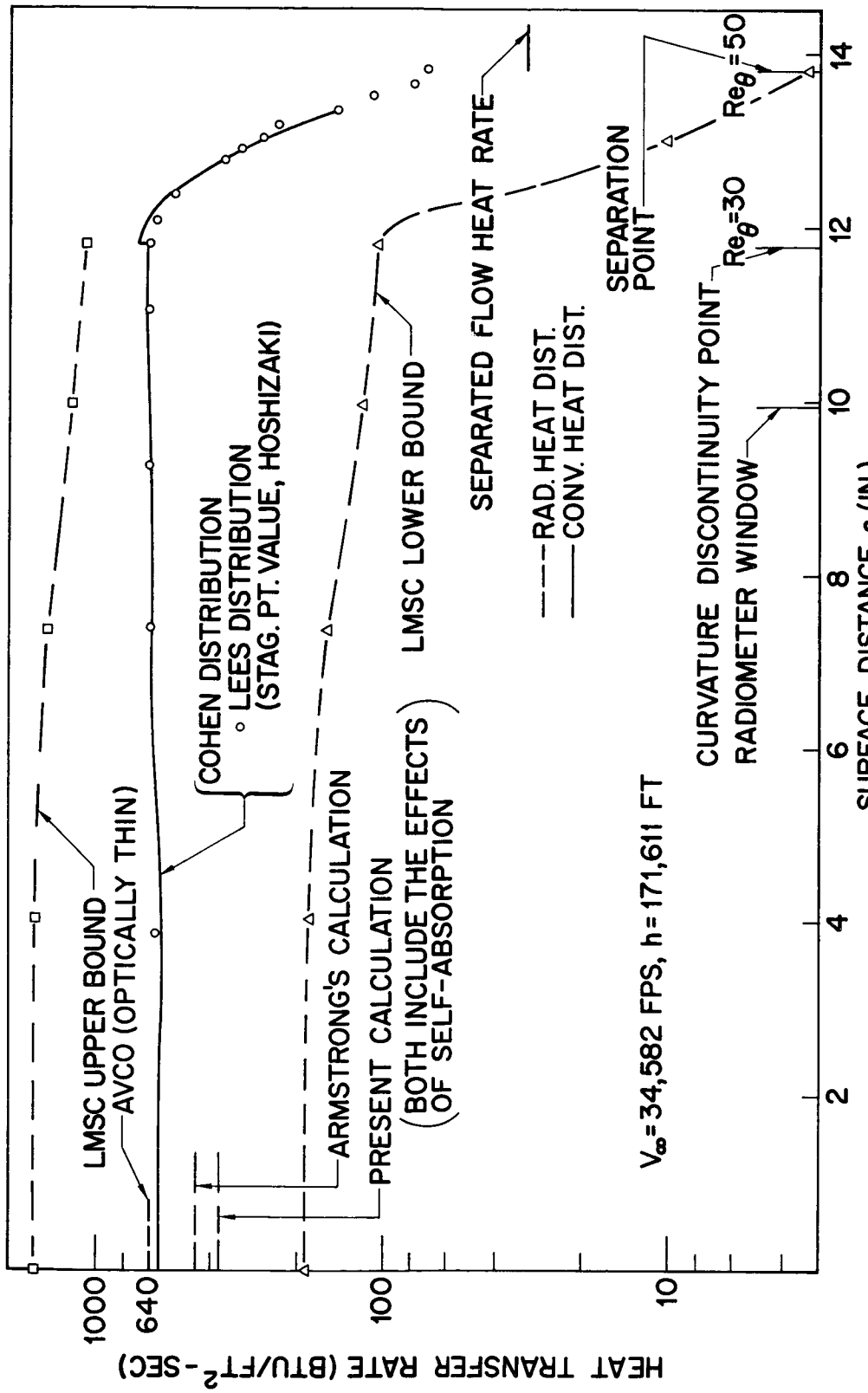

Fig. 12 Convective and Radiative Heat-Transfer Rate for Case I

as a black body at all higher frequencies. This estimate of self-absorption is dependent on the spectral distribution of the emission coefficient and gives the least effect of self-absorption in reducing the radiative heat transfer to the body. The slight difference between Armstrong's calculations and the present calculation is due to the differences in the spectral distribution of the emission coefficient. Additional discussions of the manner in which the reduction of the radiative heat transfer by self-absorption was estimated are presented in subsections 2.4.3 and 2.4.4.

Probably the most interesting result of the present calculations of the radiative heating to the FIRE vehicle is that the effect of self-absorption will reduce the upper bound estimate, which includes the vacuum ultraviolet, to slightly below the level predicted by using the emissivity data of Kivel and Bailey (Ref. 28). It will be difficult to conclude, from a comparison of these theoretical results with flight-test data, whether or not the vacuum ultraviolet portion of the spectrum is present and was partially self-absorbed or if the vacuum ultraviolet is not present and the theoretical estimates of the emission coefficient by Kivel and Bailey are correct.

The details of the radiative heat-transfer distribution in the corner region are presented in Fig. 13. Also shown is the distribution obtained by Wick (Ref. 31) for similarly shaped bodies. The agreement between the present and Wick's results for the radiative distribution is good in the forward region where the influence of the corner flow is small. In the corner region the present results give radiative heating rates somewhat higher than one would obtain using Wick's distribution. This difference between the two results in the corner region is attributed to the manner in which the geometry of the flow in determining the radiative heating to the surface was treated. Wick employed the tangent slab approximation throughout the flow field whereas, in the present analysis, the geometry was precisely accounted for by numerical integration as described in subsection 3.3.8. The flow in the corner region is irradiated by a much larger volume of gas than the tangent slab approximation utilizes and, therefore, the heating rates, according to the present analysis, are higher than those obtained by Wick. In the region of separation point the radiative heat transfer is seen to be orders of magnitude less than the heating rates on the forward portion of the vehicle. These results indicate that the radiative heating from the air to the base region of the vehicle is relatively unimportant.

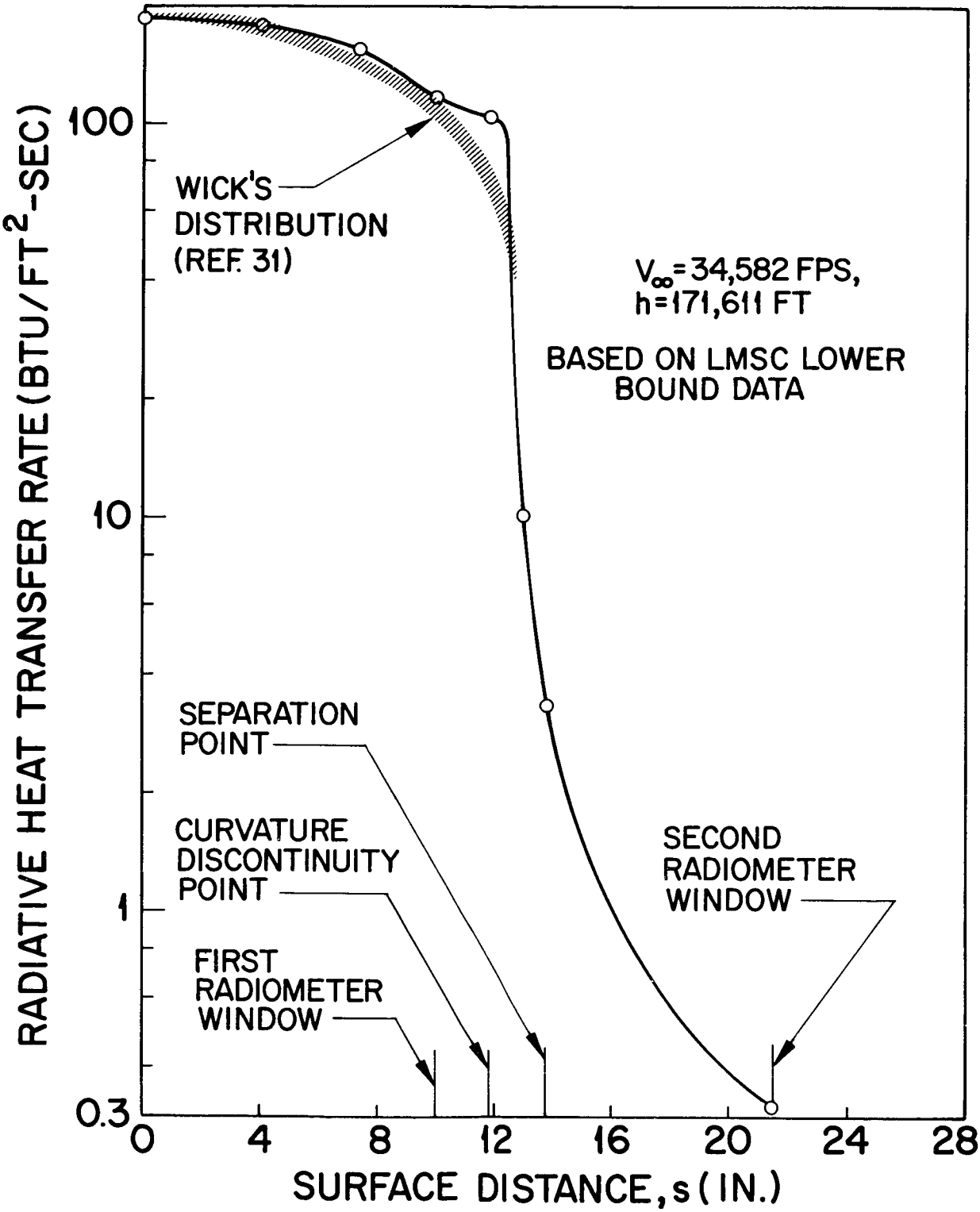

Fig. 13 Radiative Heat-Transfer Rate for Case I

The total heat transfer to the vehicle surface is shown in Fig. 14. The total was obtained by summing the convective heating, which is discussed in subsection 2.5, and 0.5 of the radiative heating. Only 0.5 of the radiative heating was used since the absorptivity of the surface was assumed to be 0.5.

The spectral intensities at the stagnation point of the body for Cases I and II were calculated using the least upper bound approximation and the emission coefficient data given in subsection 3.3. The results are plotted as a function of wavelength in Fig. 15 and tabulated in Table 9. It should be noted that an estimate to the atomic line intensity is also plotted in this figure. The emission coefficient data required for this estimate were obtained by using Armstrong's program to calculate the mean emission coefficients (over 250 Å increments) up to the maximum wavelength for which it is applicable (0.85 microns), then using the calculated data to scale the measured data from Ref. 30 by the formula

$$j_\nu(0.85 \leq \lambda \leq 1) = \frac{j_m(0.85 \leq \lambda \leq 1) j_c(0.8 \leq \lambda \leq 0.85)}{j_m(0.8 \leq \lambda \leq 0.85)} \qquad (2.7)$$

to obtain the remaining emission coefficients. In Eq. (2.7) the subscript c refers to a value calculated at an arbitrary thermodynamic state, and the subscript m refers to a value obtained from (Ref. 30) measured at a fixed thermodynamic state. It is seen in Fig. 15 that the line contribution is important but not dominant.

A precise definition of the inviscid flow field for Case II was not obtained. For this reason, the radiative heat-transfer distribution shown in Fig. 16 for Case II was obtained by extrapolating the results obtained for Case I. The distributions were obtained only in the pitch plane. The stagnation point was first assumed to rotate an amount equal to the angle-of-attack ($\alpha = 5°$). On the windward side the radiative distribution was assumed to be equal to the zero angle-of-attack distribution in terms of distance from the stagnation point up to the curvature discontinuity point. Beyond

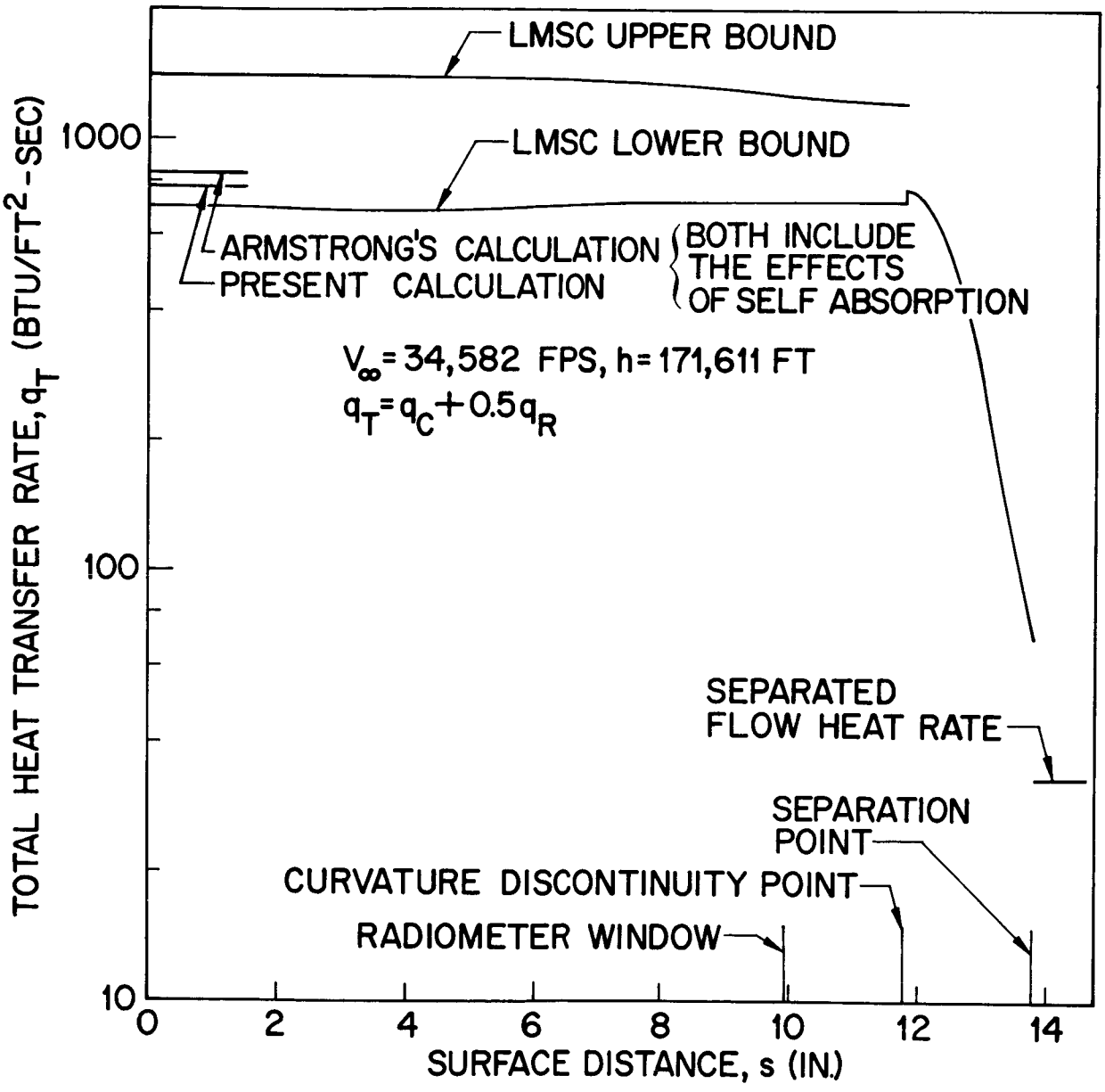

Fig. 14 Total Heat-Transfer Rate for Case I

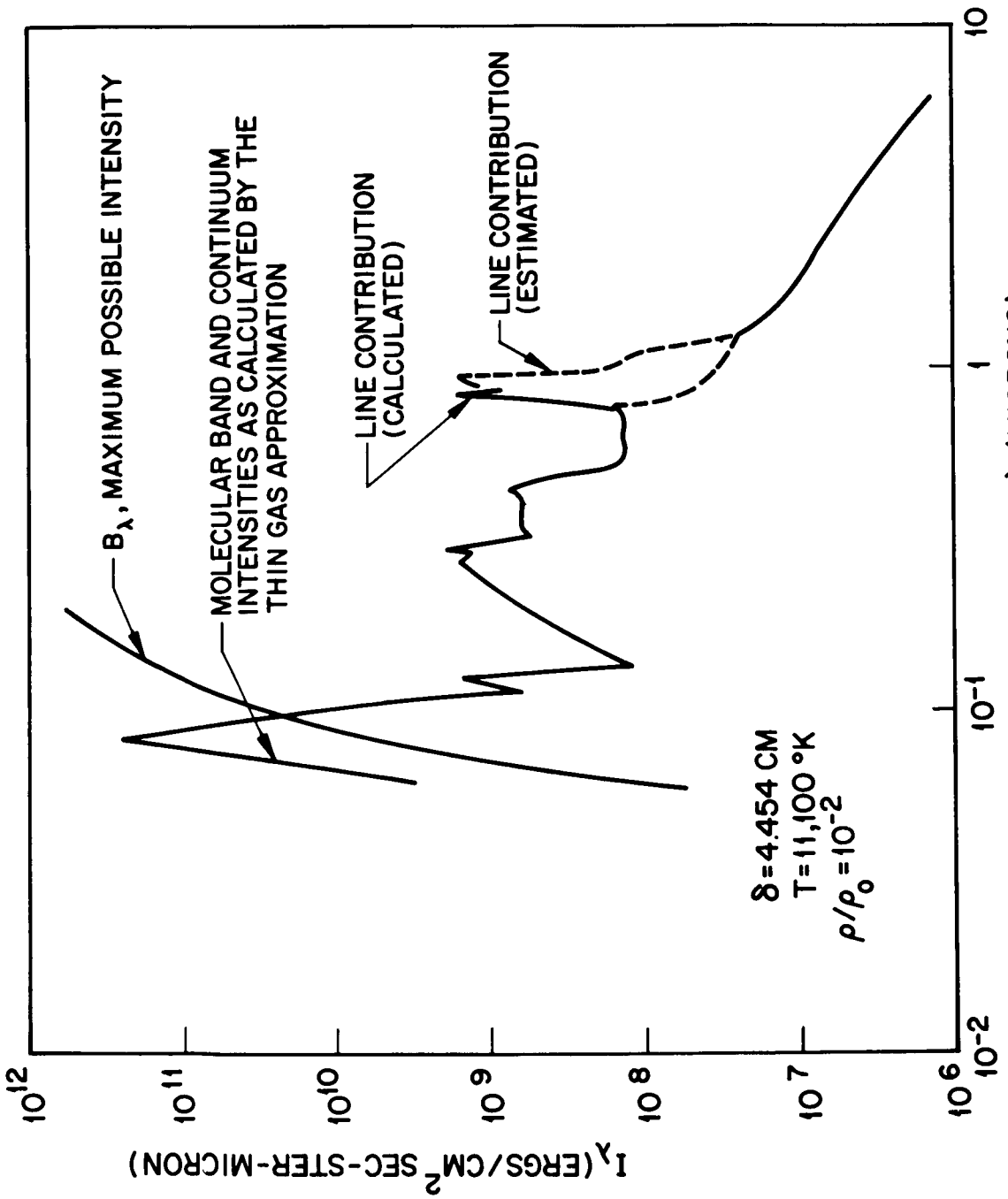

Fig. 15 Stagnation Point Spectral Intensity for Case I

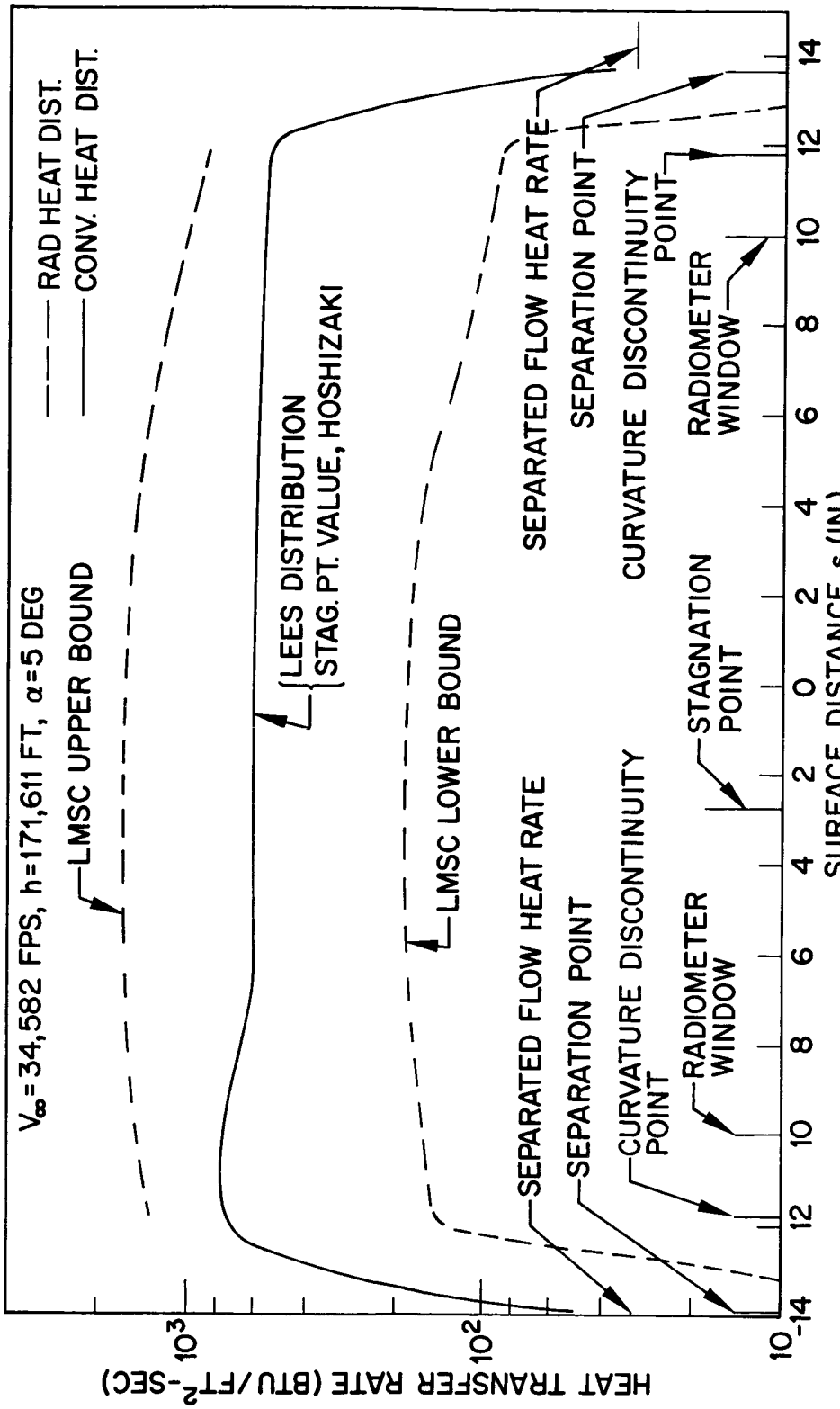

Fig. 16 Convective and Radiative Heat-Transfer Rate for Case II

this point the radiative heat transfer was assumed to fall off in a manner similar to that of Case I. On the leeward side, the radiative distribution was obtained in a similar manner with the one exception that it was necessary to extrapolate the zero angle-of-attack distribution in order to obtain the distribution up to the curvature discontinuity point. Again, in the region beyond the curvature discontinuity point, the radiative heat transfer was assumed to decrease in a manner similar to the zero angle-of-attack case. The total heating rate for Case II is presented in Fig. 17.

2.4.2.2 Nonequilibrium Radiation, Case III

Much less is known about nonequilibrium properties than is known about the equilibrium properties. Some special cases have been studied; e.g., the effects of collision limiting, but for the most part semi-empirical methods (Ref. 30) have been the only ones available. Given the populations of the atomic and molecular levels, the radiation code developed in subsection 3.3 and described in detail in Appendixes A.6 and A.7, has sufficient generality to calculate the nonequilibrium source functions, emission coefficients, and absorption coefficients which are required to solve the radiative transport equation. However, the populations of the atomic and molecular levels are not known and their estimation introduces an abundance of uncertainties.

The cross sections required to calculate the absorption coefficient are the same for equilibrium and nonequilibrium properties. The cross sections required in the calculation of the other properties (emission coefficient and source function) differ, however. The method developed by Hansen in Ref. 32 is generally followed in calculating the additional properties for the molecular-band radiation. For the free-bound and free-free radiation properties, the technique of detailed balancing is applied to the fundamental rate equations to obtain the required cross sections. Having obtained the cross sections, the required properties can be calculated if the populations can be obtained. For nonequilibrium flows, the species populations along streamlines can be calculated with the streamtube program as described in subsection 2.3. For the molecular band and atomic line radiation, the populations of the excited electronic

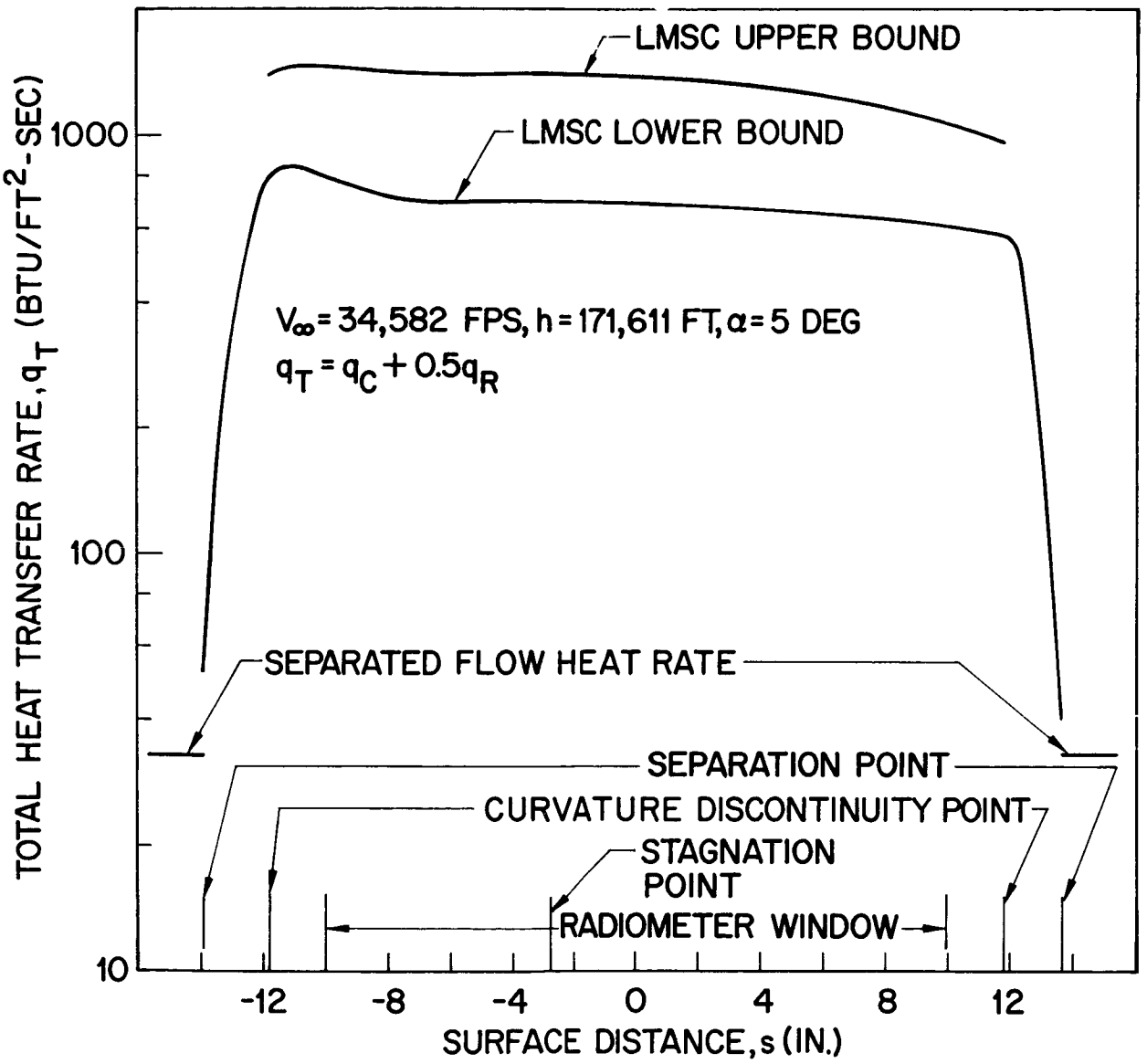

Fig. 17 Total Heat-Transfer Rate for Case II

levels are also required. A technique is suggested in subsection 3.3 whereby the populations of these levels can be estimated from the known rate coefficients for the species reactions.

The nonequilibrium radiative heating distributions associated with Case III are presented in Figs. 18 and 19 and tabulated in Table 10. The data presented in Fig. 18 were obtained by using the plane slab approximation in connection with the upper and lower bound estimates to the radiative properties as defined below and described in subsection 3.3. Also presented are radiative heating values at the stagnation point as obtained from the semi-empirical bounds given by Allen, et. al., (Ref. 30). It is seen that the two bounds overlap although the values obtained in the present study tend to be somewhat lower. Presented in Fig. 19 are the total heating distributions using the upper estimate to the radiative properties and assuming that the absorptivity of the surface is 0.5.

Presented in Fig. 20 is the emission coefficient profile along the stagnation streamline showing the dominant contributors. As discussed in subsection 3.3 and at the end of this section, it is quite uncertain if the O_2(S-R) and atomic lines contribute as much as indicated. Consequently, an upper estimate was defined as the sum of all three constituents; whereas, a lower estimate was defined such that the O_2(S-R) and atomic line contributions were not included.

In using the plane slab approximation in the calculation of radiative heating, it is required that emission coefficients be known along radial cuts rather than streamlines (see subsection 3.3.8). Three radial cuts were selected for Case III and are shown in Fig. 21. Cut No. 1 coincides with the stagnation streamline; consequently, the required species populations were available directly from the streamtube program. For Cuts Nos. 2 and 3, however, species populations were available only at the rather limited number of points corresponding to the intersections of the radial cuts with the streamlines. These points are indicated in Fig. 21. In the region very close to the shock, the populations vary quite rapidly and greater resolution is required. This was obtained

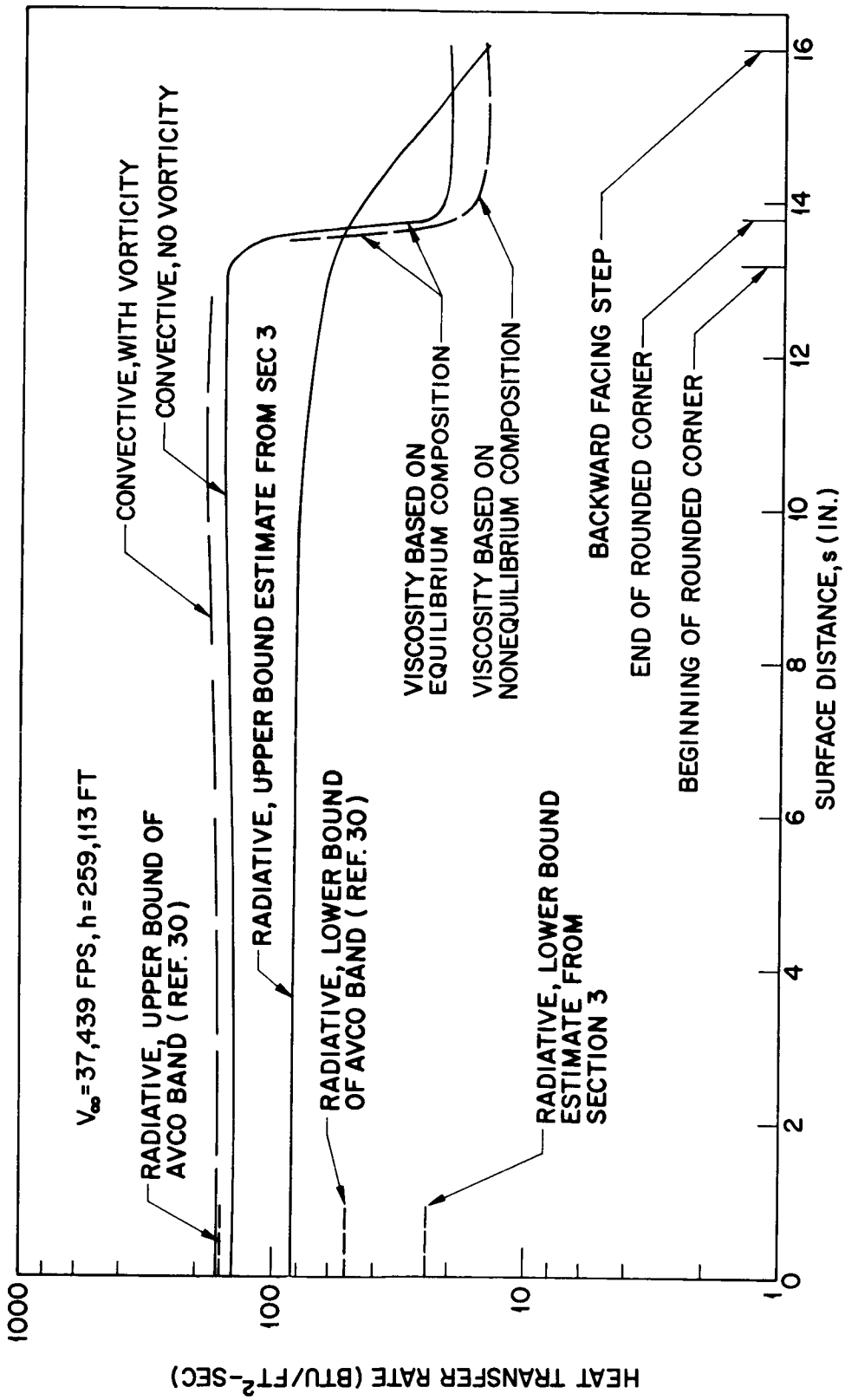

Fig. 18 Convective and Radiative Heat-Transfer Rate for Case III

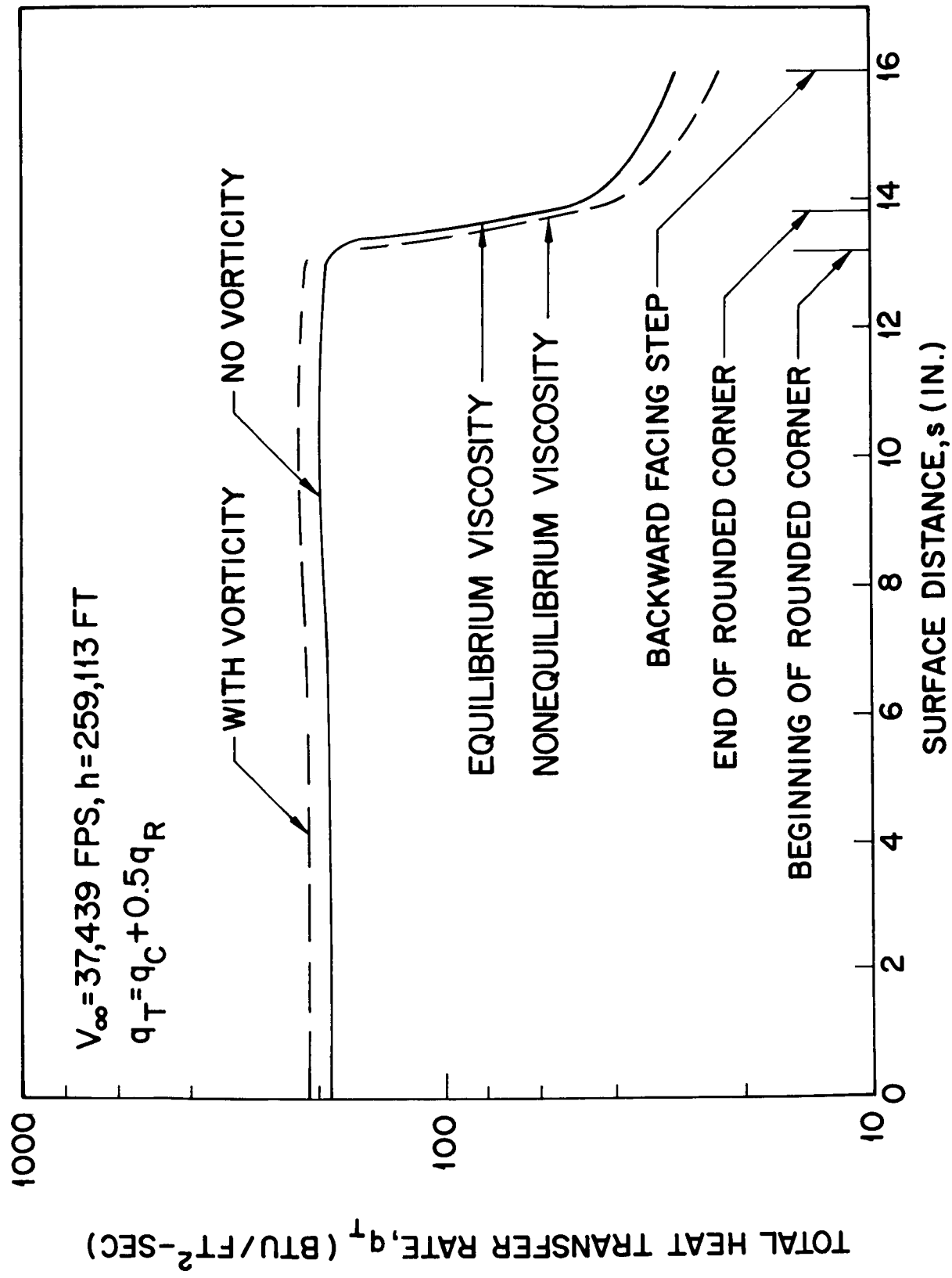

Fig. 19 Total Heat-Transfer Rate for Case III

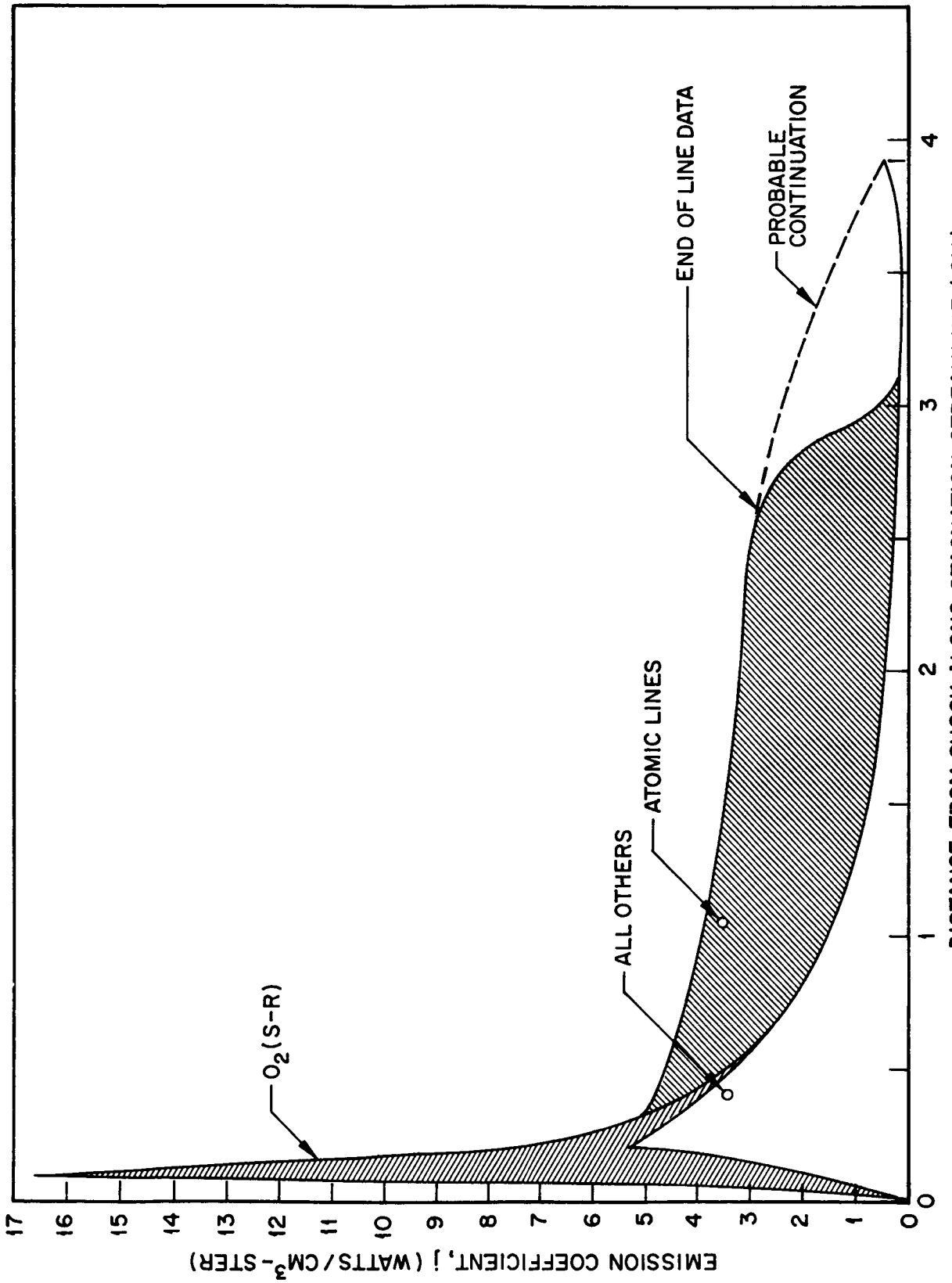

Fig. 20 Dominant Contributors to the Stagnation Streamline Emission Coefficients for Case III

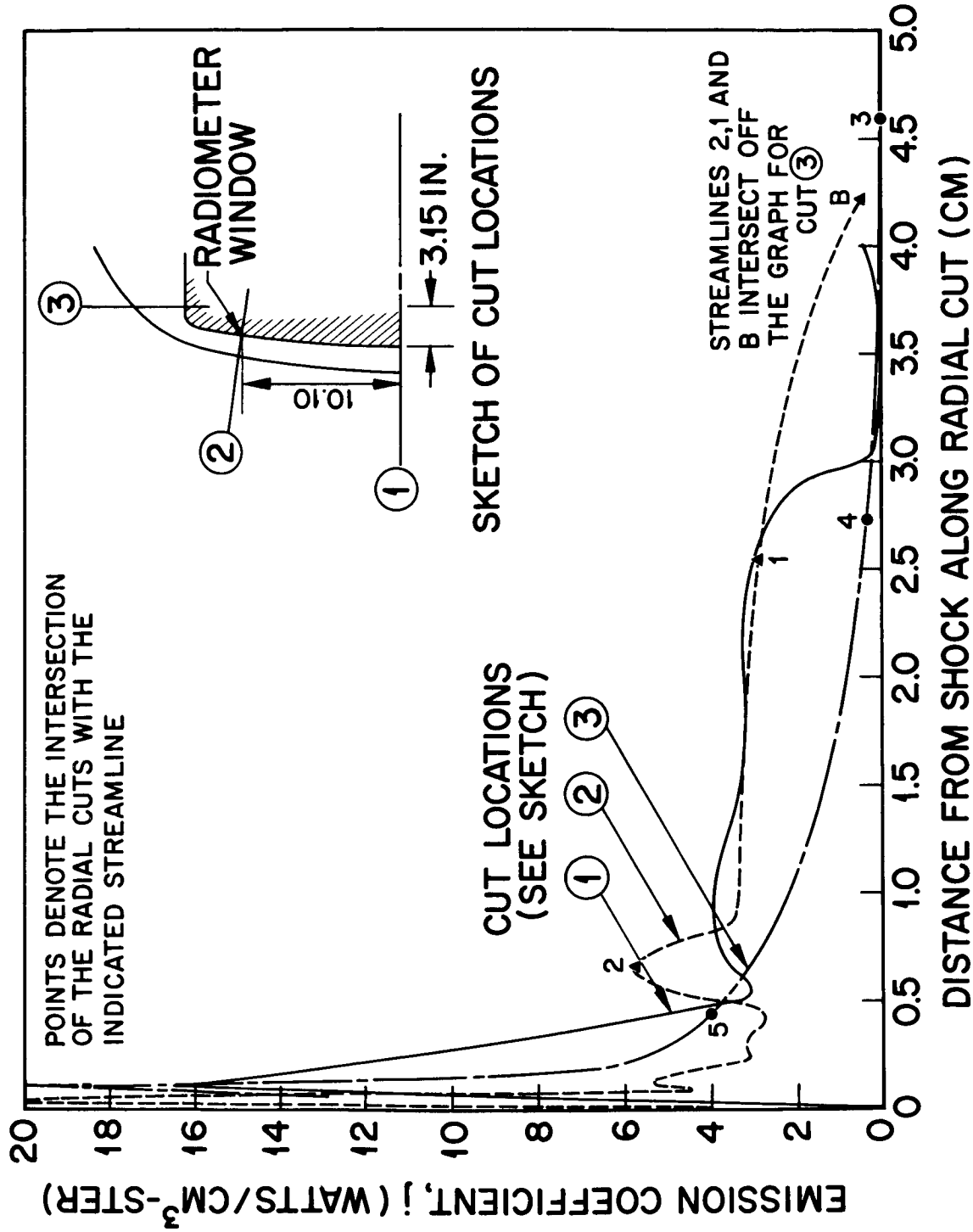

Fig. 21 Emission Coefficient Profiles Along Radial Cuts for Case III

by mapping the population of the nearest streamline (Streamlines 2 and 5, Fig. 9, for Cuts Nos. 2 and 3, respectively) onto the radial cut such that the populations remained fixed for a fixed (normal) distance from the shock. The emission coefficients were calculated by the nonequilibrium radiation code and are also presented in tabular form in Table 11.

The measurements presented in Ref. 30 indicate that atomic line radiation can be important in nonequilibrium shock-layer flows. An estimate of this radiation was obtained by taking the product of the Planck mean absorption coefficient as calculated by Armstrong's program with the Planck function evaluated at the local kinetic temperature. While the Planck function is not the correct source function, it is probably a fairly good approximation, since in the region where atomic line radiation is important, all the electronic levels and species populations are nearing equilibrium (at the local kinetic temperature), excepting only N^+ , O^+ and e^- which are not important in line emission. The atomic line contributions are included in the total emission coefficient curves given in Fig. 21 and are presented separately in tabular form in Table 8. It is to be emphasized that this calculation will tend to be high due both to errors in the source function and the neglect of self-absorption in the individual lines.

The spectral distribution at the stagnation point for Case III is given in Fig. 22 and Table 12. The method used for this calculation was that given in subsection 3.3. The O_2(S-R) overshoot is assumed to be present; consequently, the results represent the upper bound estimate in the 0.3 to 0.5 micron region. The atomic line contribution was not included as the appropriate spectral data are not available from Armstrong's program. This means that the intensity in the 0.8 to 2 micron region is probably too small.

Table 11

EMISSION COEFFICIENT DISTRIBUTION – CASE III
(Consisting of Tables 11.1 Through 11.7)

Table 11.1

TABULATED DATA – AXIAL STREAMLINE*

S	N_2 (1+)	N_2 (2+)	O_2	NO β	NO γ	N_2^+	N^+	O^+	N_{lines}	j
0.05	–	–	3.34494^{+7}	2.69771^{+5}	9.60330^{+4}	–				3.38152^{+7}
0.1	3.99078^{+5}	0	1.51562^{+8}	1.07282^{+7}	3.82488^{+6}	–				1.66514^{+8}
0.2	1.91553^{+7}	0	1.45310^{+7}	2.46924^{+7}	8.81012^{+6}	4.31027^{+3}				6.71931^{+7}
0.35	2.48909^{+7}	1.34828^{+5}	5.17323^{+6}	1.40554^{+7}	5.01754^{+6}	5.95922^{+4}				4.91966^{+7}
0.5	1.20555^{+7}	8.71057^{+6}	2.43457^{+6}	6.80545^{+6}	2.43038^{+6}	2.72229^{+5}				3.27087^{+7}
1	8.93904^{+5}	9.24035^{+6}	1.38670^{+5}	4.79177^{+5}	1.71221^{+5}	2.57656^{+6}	2.564^{+2}	4.101^{+1}	2.8×10^7	4.14998^{+7}
1.5	4.65409^{+4}	4.58894^{+5}	–	2.25994^{+4}	8.07653^{+3}	4.10893^{+6}	9.629^{+2}	4.818^{+1}	2.8×10^7	3.2645^{+7}
2	6.11770^{+2}	5.88376^{+3}	–	2.88058^{+2}	1.02954^{+2}	7.39848^{+6}	3.384^{+3}	1.584^{+2}	2.8×10^7	3.54046^{+7}
2.5	–	–				4.68716^{+6}	1.260^{+4}	5.734^{+2}	2.8×10^7	3.26998^{+7}
3	–	–				1.67855^{+6}	5.877^{+4}	2.595^{+3}	–	1.73758^{+6}
3.5	–	–				3.74748^{+5}	3.474^{+5}	1.323^{+4}	–	7.3537^{+5}
3.92	–	–				9.21058^{+3}	4.883^{+6}	1.495^{+5}	–	5.04171^{+6}

*S is distance (cm) from the shock along the indicated streamline. The remaining quantities are the partial or total (j) emission coefficients in ergs/cm^3-sec-ster.

Table 11.2

TABULATED DATA – BODY STREAMLINE*

S	N_2 (1+)	N_2 (2+)	O_2	NO β	NO γ	N_2^+	N^+	O^+	N_{lines}	j
.12	1.63423^{+2}	2.40349^{+2}	2.81760^{+1}	1.65939^{+2}	5.99317^{+1}	4.25749^{+3}	4.499500^{+6}	2.45763^{+5}	1.4×10^6	6.150178^{+6}
16	1.45234^{+2}	2.05610^{+2}	2.52988^{+1}	1.49844^{+2}	5.41366^{+1}	3.80308^{+3}	4.3914^{+6}	1.34188^{+5}	1.4×10^6	5.929971^{+6}
21	1.22865^{+2}	1.62459^{+2}	2.13870^{+1}	1.29021^{+2}	4.66416^{+1}	2.99119^{+3}	4.1938^{+6}	1.27953^{+5}	1.4×10^6	5.725227^{+6}
26	9.26611^{+1}	1.08654^{+2}	1.60139^{+1}	9.99291^{+1}	3.61646^{+1}	1.97750^{+3}	3.8858^{+6}	1.18328^{+5}	1.4×10^6	5.406458^{+6}
31	4.84672^{+1}	4.38302^{+1}	8.39127	5.59124^{+1}	2.02865^{+1}	8.14223^{+2}	3.3198^{+6}	1.00619^{+5}	1.4×10^6	4.821410^{+6}
32	3.90246^{+1}	3.24395^{+1}		4.61907^{+1}	1.67739^{+1}	6.12984^{+2}	3.164^{+6}	9.57451^{+4}	1.4×10^6	4.660493^{+6}
33	2.85490^{+1}	2.10414^{+1}	5.03116	3.51864^{+1}	1.27944^{+1}	4.09405^{+2}	2.9598^{+6}	8.93581^{+4}	1.4×10^6	4.449670^{+6}
34	2.75884^{-1}	3.40072^{-1}	1.07375^{-1}	9.67482^{-1}	3.60494^{-1}	1.81215	1.3016^{+6}	3.78901^{+4}	1.4×10^6	2.739494^{+6}
35	5.23768^{-9}	2.65266^{-13}	4.32612^{-8}	1.10304^{-6}	4.77740^{-7}	5.37065^{-10}	1.6149^{+5}	3.99337^{+3}	1.4×10^6	1.565483^{+6}
36	3.81426^{-9}	1.66347^{-13}	3.19471^{-8}	8.39949^{-7}	3.64845^{-7}	1.74206^{-10}	1.57767^{+5}	3.88877^{+3}	–	1.61655^{+5}
37	2.99310^{-9}	1.16450^{-13}	2.51616^{-8}	6.77972^{-7}	2.95137^{-7}	1.27828^{-10}	1.5485^{+5}	3.80765^{+3}	–	1.58657^{+5}
39	7.52830^{-9}	4.50665^{-13}	5.02909^{-8}	1.30368^{-6}	5.62813^{-7}	3.81139^{-10}	1.6565^{+5}	4.11095^{+3}	–	1.69760^{+5}
41	1.74060^{-7}	4.47087^{-11}	6.10526^{-7}	1.35236^{-5}	5.67313^{-6}	1.93133^{-8}	2.1169^{+5}	5.41827^{+3}	–	2.17108^{+5}

*S is the distance (cm) from the stagnation point along the body.

Table 11.3

TABULATED DATA – STREAMLINE 1 (S/R = 70.895)*

S	N_2 (1+)	N_2 (2+)	O_2	NO β	NO γ	N_2^+	N^+	O^+	N_{lines}	j
0.1			4.48846^{+8}	2.89820^{+5}	7.84083^{+4}	–				4.49214^{+8}
0.2	3.61103^{+5}	0	2.63815^{+7}	2.66674^{+7}	7.25427^{+6}	1.57649^{+3}				6.06658^{+7}
0.3	1.30080^{+7}	0	1.01604^{+7}	2.97285^{+7}	8.11274^{+6}	8.72314^{+3}				6.1018^{+7}
0.4	2.40435^{+7}	0	6.56537^{+6}	2.31679^{+7}	6.34064^{+6}	2.26790^{+4}				6.0140^{+7}
0.6	1.54089^{+7}	1.36685^{+7}	3.07464^{+6}	1.15393^{+7}	3.17738^{+6}	1.75293^{+5}				4.7044^{+7}
1	4.62644^{+6}	3.07102^{+7}	8.60360^{+5}	3.42366^{+6}	9.48038^{+5}	1.01175^{+6}	9.8197^{+1}	6.46568^{+0}		4.15805^{+7}
1.5	1.32780^{+6}	1.34106^{+7}	2.02277^{+5}	9.44965^{+5}	2.62438^{+5}	2.64605^{+8}	2.291^{+2}	1.38114^{+1}		2.80753^{+8}
2	4.19856^{+5}	4.06356^{+6}		2.80792^{+5}	7.81180^{+4}	4.23285^{+8}	4.1766^{+2}	2.35296^{+1}	2.8×10^7	4.56127^{+8}
3	4.48160^{+4}	4.17281^{+5}	–	3.03813^{+4}	8.46565^{+3}	6.82296^{+7}	9.2087^{+2}	4.8726^{+1}	2.8×10^7	9.6731^{+7}
4	2.47866^{+2}	2.26181^{+3}	–	4.14545^{+3}	1.15607^{+3}	8.00786^{+6}	1.58485^{+3}	8.1097^{+1}	2.8×10^7	3.6017^{+7}
6	–	–		1.18826^{+2}	3.31760^{+1}	7.48177^{+6}	3.2045^{+3}	1.7492^{+2}	2.8×10^7	3.5485^{+7}
10					–	4.90655^{+6}	8.11737^{+3}	3.6992^{+2}	2.8×10^7	3.2915^{+7}
15						2.96051^{+6}	1.48108^{+4}	6.459^{+2}		2.97597^{+6}
19						1.81776^{+6}	1.6699^{+4}	7.963^{+2}		1.83526^{+6}
21						1.04213^{+6}	1.182^{+4}	5.749^{+2}		1.0545^{+6}
22						6.25975^{+5}	9.1654^{+3}	4.335^{+2}		6.35574^{+5}
23						3.29647^{+5}	7.096^{+3}	3.372^{+2}		3.3708^{+5}
25						4.67710^{+4}	4.253^{+3}	1.9988^{+2}		5.1224^{+4}
30						7.78011^{+2}	5.324^{+3}	8.406^{+1}		6.186^{+3}

*S is the distance (cm) from the shock along the indicated streamline.

Table 11.4

TABULATED DATA – STREAMLINE 2 (S/R = 70.385)*

S	N_2 (1+)	N_2 (2+)	O_2	NO β	NO γ	N_2^+	N^+	O^+	N_{lines}	j
0.05	–	–	1.69396^{+8}	–	–	–				1.69396^{+8}
0.1	–	–	9.13717^{+8}	4.49152^{+3}	1.59306^{+3}	2.59591^{+1}				9.13723^{+8}
0.2	6.35360^{+1}	0	1.84932^{+8}	6.26342^{+6}	2.22829^{+6}	3.69003^{+2}				1.93424^{+8}
0.3	1.42503^{+6}	0	2.36217^{+7}	1.59624^{+7}	5.68240^{+6}	2.01071^{+3}				4.66935^{+7}
0.4	9.01759^{+6}	0	1.09148^{+7}	2.18196^{+7}	7.77060^{+6}	6.30261^{+3}				4.95288^{+7}
0.6	2.11354^{+7}	1.71454^{+1}	6.39461^{+6}	1.64947^{+7}	5.87665^{+6}	3.81979^{+4}				4.99395^{+7}
1	1.29933^{+7}	3.49283^{+6}	2.33437^{+6}	7.12996^{+6}	2.54171^{+6}	3.17214^{+5}				2.88094^{+7}
1.5	5.09185^{+6}	2.37781^{+7}	7.79998^{+5}	2.71702^{+6}	9.68994^{+5}	1.08533^{+6}				3.44213^{+7}
2	2.24708^{+6}	2.14745^{+7}	3.06625^{+5}	1.14344^{+6}	4.07886^{+5}	2.10913^{+6}				2.76887^{+7}
3	5.55317^{+6}	4.96336^{+7}	6.77823^{+4}	2.68477^{+5}	9.57936^{+4}	4.30852^{+6}				5.99273^{+7}
4	1.54986^{+5}	1.34623^{+6}	1.76517^{+4}	7.34566^{+4}	2.62122^{+4}	6.06901^{+6}	–	–	2.8×10^7	3.5687^{+7}
6	1.54104^{+4}	1.28956^{+5}	1.72903^{+3}	7.18320^{+3}	2.56360^{+3}	7.74468^{+6}	–	–	2.8×10^7	3.59005^{+7}
8	2.08910^{+3}	1.68103^{+4}	–	–	–	–	–	–	2.8×10^7	2.80189^{+7}
10	3.49544^{+2}	2.74468^{+3}		1.72585^{+2}	6.16082^{+1}	7.13883^{+6}	–	–	2.8×10^7	3.51422^{+7}
12	6.93417^{+1}	4.94381^{+2}		4.30635^{+1}	1.53782^{+1}	5.90012^{+6}				5.90074^{+6}
15	1.90097	4.29425		–	–	1.56703^{+6}				1.56704^{+6}
18	3.75283	1.24225^{+1}				1.26779^{+6}				1.26780^{+6}
20	1.27458	3.10576				4.48788^{+5}				4.48792^{+5}
30	1.36186^{-2}	5.70374^{-3}				1.56871^{+4}				1.56871^{+4}

*S is the distance (cm) from the shock along the indicated streamline.

Table 11.5

TABULATED DATA – STREAMLINE 3 (S/R = 69.96)*

S	N_2 (1+)	N_2 (2+)	O_2	NO β	NO γ	N_2^+	N^+	O^+	N_{lines}	j
0.05	–	–	5.74620^{+7}	–	–					5.7462^{+7}
0.1	–	–	9.38065^{+8}	–	–					9.38065^{+8}
0.2	–	–	3.85917^{+8}	6.67860^{+6}	2.37610^{+6}					3.94972^{+8}
0.3	4.61032^{+5}	0	6.24898^{+7}	1.69081^{+7}	6.01887^{+6}	–				8.58778^{+7}
0.4	6.29078^{+6}	0	1.66986^{+7}	2.37270^{+7}	8.44953^{+6}	3.49554^{+3}				5.51694^{+7}
0.6	2.28243^{+7}	0	7.75921^{+6}	1.96330^{+7}	6.99394^{+6}	2.17572^{+4}				5.72322^{+7}
1	1.88192^{+7}	0	3.45293^{+6}	1.00651^{+7}	3.58765^{+6}	2.04689^{+5}				3.612956^{+7}
1.5	7.89585^{+6}	2.29733^{+5}	7.88412^{+5}	4.18412^{+6}	1.49216^{+6}	7.81711^{+5}	7.61846^{+1}	9.94878^{+0}		7.47614^{+6}
2	4.18579^{+6}	3.77277^{+6}	5.58243^{+5}	2.11138^{+6}	7.53153^{+5}	1.68831^{+6}	1.33130^{+2}	8.7092^{+0}		8.8838^{+6}
3	1.23717^{+6}	1.07462^{+7}	1.46295^{+5}	5.86840^{+5}	2.09408^{+5}	3.67264^{+6}	2.75487^{+2}	1.7633^{+1}		1.65988^{+7}
4	4.39386^{+6}	3.67686^{+6}	4.93468^{+4}	2.05234^{+5}	7.32457^{+4}	5.40830^{+6}	4.3538^{+2}	2.6439^{+1}	2.8×10^7	4.18073^{+7}
5	1.71233^{+5}	1.36678^{+6}	1.77025^{+4}	7.64985^{+4}	2.73062^{+4}	6.48880^{+6}	5.7895^{+2}	3.40506^{+1}	2.8×10^7	3.61489^{+7}
6	6.87591^{+4}	5.30948^{+5}	–	3.19484^{+4}	1.14054^{+4}	6.99885^{+6}	6.81194^{+2}	3.92184^{+1}	2.8×10^7	3.5643^{+7}
8	1.68437^{+4}	1.16732^{+5}	–	7.50083^{+3}	2.67888^{+3}	6.30621^{+6}	7.09849^{+2}	4.0063^{+1}	2.8×10^7	3.44507^{+7}
10	5.53937^{+3}	3.16820^{+4}		2.51517^{+3}	8.99008^{+2}	4.32121^{+6}	5.65813^{+2}	3.15911^{+1}		4.36244^{+6}
15	4.68201^{+2}	1.34159^{+3}		3.19626^{+2}	1.14673^{+2}	1.02095^{+6}				1.02319^{+6}
20	5.66824^{+1}	7.88453^{+1}		–	–	2.49354^{+5}				2.49490^{+5}
30	1.67934	6.58452^{-1}				2.21688^{+5}				2.21705^{+5}
40	1.39206^{-1}	2.07268^{-2}				4.18196^{+3}				4.18196^{+3}

*S is the distance (cm) from the shock along the indicated streamline.

Table 11.6

TABULATED DATA – STREAMLINE 4 (S/R = 68.5621)*

S	N_2 (1+)	N_2 (2+)	O_2	NO β	NO γ	N_2^+	N^+	O^+	N_{lines}	j
0.05	–	–	–	–	–				–	
0.1	–	–	1.0144^{+8}	–	–				–	1.0144^{+8}
0.2	–	–	6.92120^{+8}	–	–				–	6.9212^{+8}
0.3	–	–	4.21447^{+8}	2.57871^{+5}	9.16462^{+4}				–	4.21796^{+8}
0.4	–	–	1.27552^{+8}	5.69381^{+6}	2.02640^{+6}				–	1.35272^{+8}
0.6	–	–	1.59523^{+7}	1.32743^{+7}	4.72737^{+6}	–			–	3.3954^{+7}
1	2.82292^{+5}	2.18763^{+5}	6.01901^{+6}	1.60507^{+7}	5.72017^{+6}	3.48641^{+4}			–	2.83258^{+7}
2	9.82866^{+6}	7.16237^{+7}	1.97056^{+6}	6.58247^{+6}	2.34815^{+6}	3.64892^{+5}			–	9.271843^{+7}
3	6.42462^{+6}	4.87697^{+7}	8.02829^{+5}	3.07970^{+6}	1.09951^{+6}	7.73649^{+5}			–	6.09500^{+7}
4	3.27285^{+6}	2.02677^{+7}	3.85267^{+5}	1.69420^{+6}	6.05355^{+5}	9.49043^{+5}			–	2.71744^{+7}
5	1.94207^{+6}	1.03176^{+7}	2.27094^{+5}	1.03426^{+6}	3.69803^{+5}	1.02214^{+6}			–	1.491297^{+7}
8	4.91067^{+5}	1.68909^{+6}	6.78522^{+4}	3.25021^{+5}	1.16477^{+5}	7.12999^{+5}	5.2344^{+1}	4.1086^{+0}	–	3.402562^{+6}
10	2.38297^{+5}	6.53199^{+5}	3.10506^{+4}	1.78055^{+5}	6.39000^{+5}	5.06954^{+5}	4.0239^{+1}	3.2579^{+0}	–	2.246556^{+6}
15	3.51660^{+4}	5.24297^{+4}	5.49488^{+3}	3.60060^{+4}	1.29823^{+4}	1.51174^{+5}	1.9219^{+1}	1.5395^{+0}	–	2.93252^{+6}
20	9.51844^{+3}	8.52269^{+3}	1.61102^{+3}	1.18912^{+4}	4.30867^{+3}	8.03951^{+4}	1.3462^{+1}	1.0696^{+0}	–	1.16247^{+5}
40	1.05683^{+2}	1.89918^{+1}	2.04246^{+1}	–	–	5.12066^{+3}	2.90719^{+0}	2.2389^{-1}	–	5.26576^{+3}

*S is the distance (cm) from the shock along the indicated streamline.

Table 11.7

TABULATED DATA – STREAMLINE 5 (S/R = 62.5113)*

S	N_2 (1+)	N_2 (2+)	O_2	NO β	NO γ	N_2^+	N^+	O^+	N lines	j
0.1	–	–	–	–	–				–	
0.2	–	–	–	–	–				–	
0.3	–	–	9.95708^{+6}	–	–				–	9.95708^{+6}
0.4	–	–	8.84311^{+7}	–	–				–	8.84311^{+7}
0.6	–	–	1.98822^{+8}	–	–				–	1.98822^{+8}
1	–	–	6.72691^{+7}	4.64014^{+4}	1.65082^{+4}	–			–	6.7332^{+7}
2	–	–	4.25316^{+7}	5.25215^{+6}	1.87377^{+6}	3.24931^{+4}			–	4.9690^{+7}
3	1.41918^{+3}	7.36762^{+1}	2.36153^{+7}	8.33620^{+6}	2.97712^{+6}	6.81175^{+4}			–	3.4998^{+7}
4	7.33888^{+4}	3.10169^{+4}	1.57377^{+7}	5.93599^{+6}	2.12140^{+6}	1.13273^{+5}	5.27586^{+0}	6.77047^{-1}	–	2.40128^{+7}
5	3.47758^{+5}	3.48183^{+5}	1.15966^{+7}	4.31972^{+6}	1.54491^{+6}	1.37780^{+5}	6.42359^{+0}	8.4553^{-1}	–	1.82950^{+7}
8	2.53207^{+6}	8.70936^{+6}	4.88891^{+6}	1.86121^{+6}	6.66997^{+5}	1.43601^{+5}	7.23208^{+0}	1.01356^{+0}	–	1.88021^{+7}
10	1.28141^{+6}	3.51248^{+6}	2.78246^{+6}	1.11676^{+6}	4.00780^{+5}	1.22487^{+5}	6.54026^{+0}	9.31804^{-1}	–	9.21638^{+6}
15	3.99452^{+5}	7.43415^{+5}	1.03710^{+6}	4.43753^{+5}	1.59703^{+5}	7.53823^{+4}	4.9789^{+0}	7.16468^{-1}	–	2.85925^{+6}
20	1.78882^{+5}	2.57700^{+5}	5.17681^{+5}	2.32561^{+5}	8.38777^{+4}	4.99198^{+4}	3.49339^{+0}	4.9700^{-1}	–	1.32063^{+6}
30	4.52009^{+4}	4.23246^{+4}	1.39688^{+5}	7.16513^{+4}	2.59500^{+4}	2.11472^{+4}	1.75964^{+0}	2.4900^{-1}	–	3.45962^{+5}

*S is the distance (cm) from the shock along the indicated streamline.

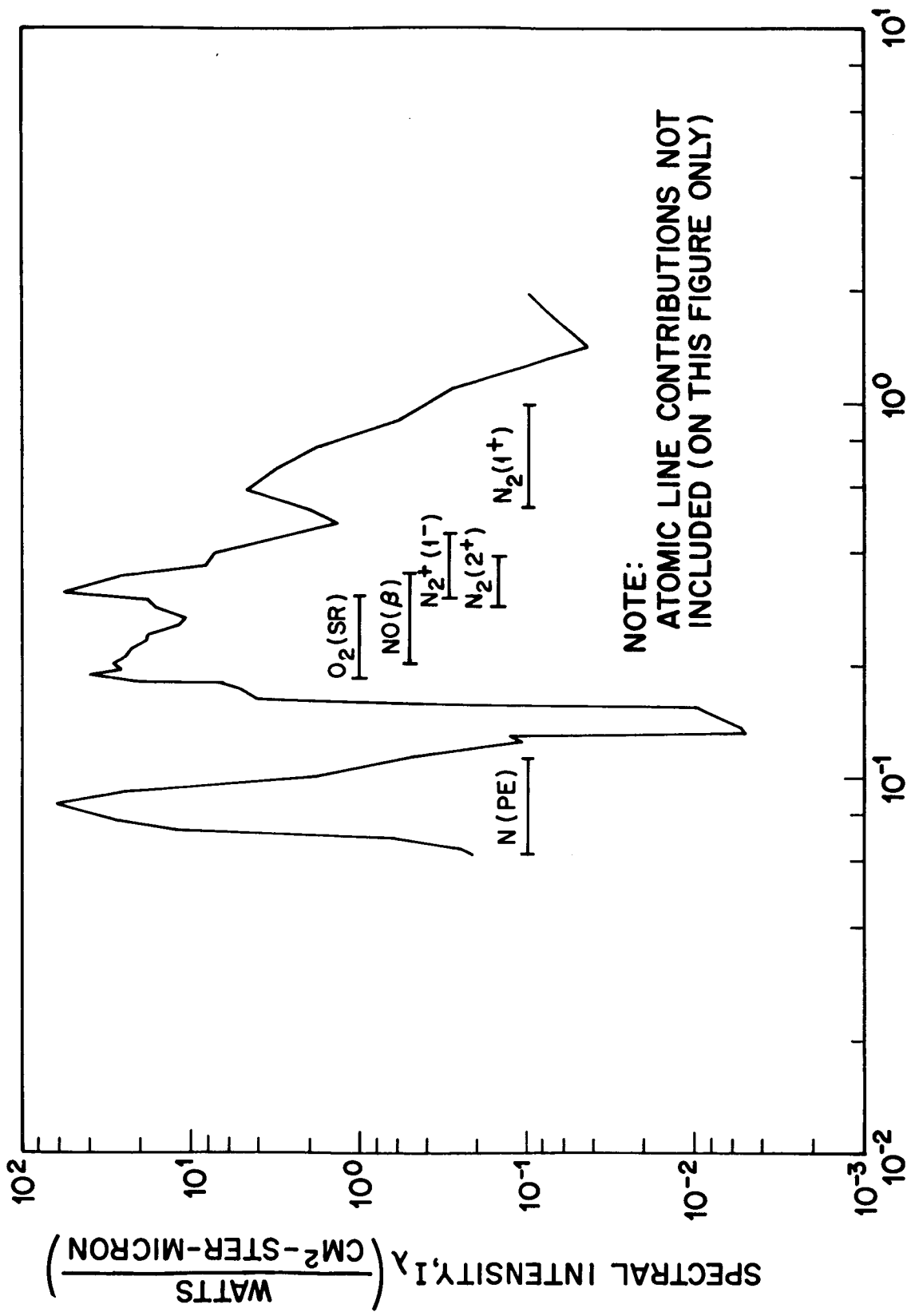

Fig. 22 Spectral Intensity at the Stagnation Point for Case III

Table 12

SPECTRAL INTENSITY DISTRIBUTION – CASE III

$h\nu$ (ev)	λ (microns)	$I_{h\nu}$ (ergs/cm^2-ster-ev)	I_λ (ergs/cm^2-ster-micron)
6.23800^{-1}	1.99	3.16529^{+5}	9.89^{+5}
8.71647^{-1}	1.425	7.12004^{+5}	4.35^{+5}
1.11949	1.11	2.77015^{+6}	2.79^{+6}
1.36734	0.912	3.84428^{+6}	5.72^{+6}
1.61519	0.767	8.21470^{+6}	1.73^{+7}
1.86304	0.667	1.09604^{+7}	3.07^{+7}
2.11088	0.588	1.30345^{+7}	4.67^{+7}
2.35873	0.526	4.49103^{+6}	2.01^{+7}
2.60658	0.476	2.41572^{+6}	1.32^{+7}
2.85442	0.435	5.20995^{+6}	3.42^{+7}
3.10227	0.40	9.29221^{+6}	7.20^{+7}
3.35012	0.37	9.03562^{+6}	8.19^{+7}
3.59797	0.345	2.67580^{+7}	2.79^{+8}
3.84581	0.323	1.86668^{+7}	5.51^{+8}
4.09366	0.303	1.31531^{+7}	1.78^{+8}
4.34151	0.286	1.09699^{+7}	1.67^{+8}
4.58935	0.271	6.33264^{+6}	1.07^{+8}
4.83720	0.256	6.14861^{+6}	1.16^{+8}
5.08505	0.244	8.60526^{+6}	1.79^{+8}
5.33290	0.233	7.97596^{+6}	1.83^{+8}
5.58074	0.222	8.75988^{+6}	2.21^{+8}
5.82859	0.213	8.77560^{+6}	2.40^{+8}
6.07644	0.204	9.61795^{+6}	2.86^{+8}
6.32428	0.196	7.97108^{+6}	2.57^{+8}
6.57213	0.189	1.12502^{+7}	3.91^{+8}
6.81998	0.182	5.32866^{+6}	2.00^{+8}
7.06783	0.176	1.68372^{+6}	6.74^{+7}
7.31567	0.170	1.19732^{+6}	5.12^{+7}
7.56352	0.164	8.88900^{+5}	4.10^{+7}
7.81137	0.159	1.49168^{+5}	7.35^{+6}
8.05921	0.154	1.79003^{+3}	9.37^{+4}
8.30706	0.1495	1.45650^{+3}	8.11^{+4}
8.55491	0.145	1.21548^{+3}	7.19^{+4}
8.80275	0.141	9.82754^{+2}	6.14^{+4}
9.05060	0.137	7.98648^{+2}	5.26^{+4}
9.29845	0.133	6.95778^{+2}	4.88^{+4}
9.54630	0.130	1.70032^{+4}	1.25^{+6}
9.79414	0.126	1.31824^{+4}	1.03^{+6}
1.00420^{+1}	0.124	1.45260^{+4}	1.17^{+6}
1.09790^{+1}	0.113	5.01045^{+4}	4.88^{+6}
1.21970^{+1}	0.1015	1.49208^{+5}	1.80^{+7}
1.34160^{+1}	0.0925	1.73147^{+6}	2.51^{+8}
1.46340^{+1}	0.0848	3.58505^{+6}	6.19^{+8}
1.60960^{+1}	0.077	1.20424^{+6}	2.52^{+8}
1.70710^{+1}	0.0727	5.27924^{+5}	1.24^{+8}
1.80460^{+1}	0.0688	2.34077^{+4}	6.14^{+6}
1.90210^{+1}	0.0652	8.54155^{+3}	2.49^{+6}
1.97520^{+1}	0.063	6.90359^{+3}	2.16^{+6}

2.4.3 A Criteria for Self-Absorption

Self-absorption in a gas arises from the fundamental fact that a good emitter is also a good absorber. This can be seen by examining the transport equation. For an emitting and absorbing gas, the transport equation is

$$\frac{dI_\nu}{ds} = j_\nu - \mu'_\nu I_\nu \tag{2.8}$$

where I_ν is the spectral intensity, s is the geometrical length, j_ν is the emission coefficient, and μ'_ν is the spectral absorption coefficient corrected for induced emission. It can be seen that for a gas with uniform properties an upper bound on intensity is given by the optically thick limit where $dI_\nu/ds = 0$ and, hence

$$I_\nu \leq \frac{j_\nu}{\mu'_\nu}$$

If the gas is in local thermodynamic equilibrium,

$$j_\nu = \mu'_\nu B_\nu \qquad (B_\nu \text{ is the Planck function})$$

hence

$$I_\nu \leq B_\nu$$

or

$$\frac{I_\nu}{\delta} \leq \frac{B_\nu}{\delta} \qquad (\delta \text{ is the path length}) \tag{2.9}$$

which provides an upper bound which must always hold. A second upper bound to the intensity (the optically thin case) can be obtained by discarding the third term (absorption term) in Eq. (2.8) and integrating the remaining two terms. This yields the optically thin gas formula which takes the following form for a gas with uniform properties:

$$I_\nu \leq j_\nu \delta \tag{2.10}$$

where δ is the length of the ray.

The upper bounds, represented in Eqs. (2.9) and (2.10),are shown schematically in Fig. 23. Note that the two upper bounds intersect and that a composite of the two represents a least upper bound. The slope of the optically thin gas curve is j_ν ; hence, when

$$j_\nu \delta \leq B_\nu \tag{2.11}$$

or

$$j_\nu \leq B_\nu/\delta \tag{2.12}$$

the optically thin gas formula represents the least upper bound; likewise, when

$$j_\nu \delta \geq B_\nu \qquad \text{(optically thick gas)}$$

or

$$j_\nu \geq B_\nu/\delta \tag{2.13}$$

the least upper bound is the Planck function.

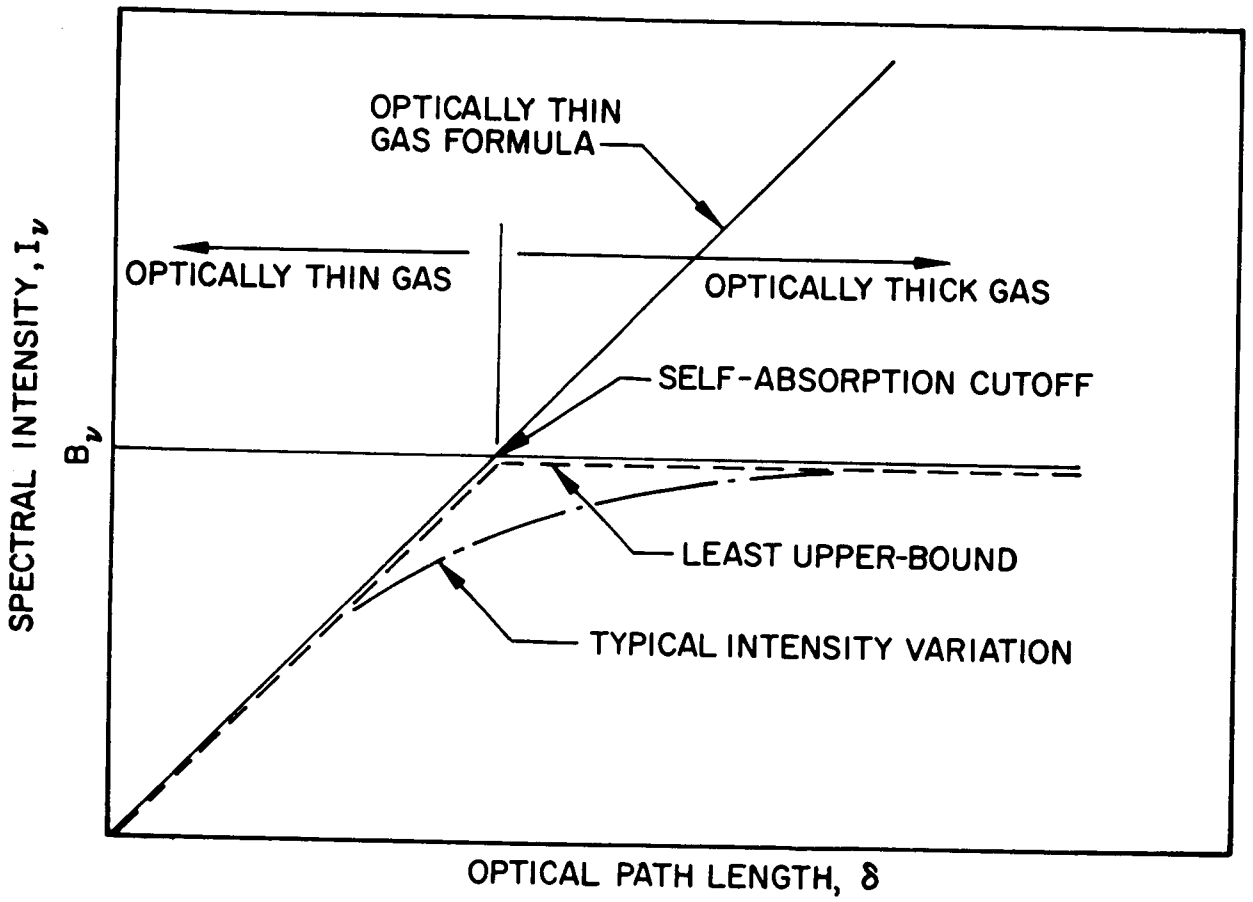

Fig. 23 Theoretical Limits on the Spectral Intensities

The composite upper bound represents a reasonably good approximation to the intensity variation. The asymptotes are rigorously correct and the transition region is probably not greatly in error. It is obvious from Fig. 23 that the thin gas formula becomes a very poor approximation to the intensity when

$$\delta > B_\nu / j_\nu \tag{2.14}$$

It is straightforward to extend these concepts to the nonequilibrium case. The Planck function is merely replaced by the source function $\mathcal{J}_\nu$ appropriate to the nonequilibrium gas. The optically thin gas formula represents the least upper bound when

$$j_\nu \leq \frac{\mathcal{J}_\nu}{\delta} \tag{2.15}$$

and when

$$j_\nu \geq \frac{\mathcal{J}_\nu}{\delta} \tag{2.16}$$

the source function $\mathcal{J}_\nu$ represents the upper bound on the intensity.

In dealing with problems in heat transfer, it is often convenient to work with integrated (over frequency) quantities. It is to be emphasized that if an attempt is made to check for self-absorption by replacing the spectral quantities in Eqs. (2.12) and (2.13) with integrated quantities , the results can be very misleading. The importance of self-absorption on the integrated intensity can be ascertained only by integrating the solution to Eq. (2.8) over all frequencies. This is a rather tedious calculation if an exact solution is required. However, if the least upper bound, as defined above, can be used as

an approximate solution to Eq. (2.8), the calculation becomes relatively straightforward. This will be a quite accurate approximation when the radiant energy in the frequency range where

$$B_\nu/\delta \sim j_\nu$$

is small compared to that in the frequency ranges where

$$B_\nu/\delta \gg j_\nu$$

or where

$$B_\nu/\delta \ll j_\nu$$

which is quite often the case. Assuming the least upper bound approximation to be accurate, the integrated intensity I_{SA} becomes

$$\frac{I_{SA}}{\delta} \sim \int_0^{\nu_1} j_\nu \, d\nu + \int_{\nu_1}^{\infty} \frac{B_\nu}{\delta} \, d\nu \qquad (2.17)$$

where ν_1 represents the frequency at which j_ν and B_ν/δ intersect, and the subscript SA indicates that the effects of self-absorption have been included. For the non-equilibrium case, the integrated intensity is

$$\frac{I_{SA}}{\delta} \sim \int_0^{\nu_1} j_\nu \, d\nu + \int_{\nu_1}^{\infty} \frac{\mathcal{J}_\nu}{\delta} \, d\nu \qquad (2.18)$$

where the symbols have their usual meanings.

2.4.4 Equilibrium Radiation Properties

It is generally known that wide disagreement exists between the three existing theoretical predictions (Refs. 27, 28, and 29). It is felt that insufficient data presently exist to indicate clearly which of the three theoretical works is the most accurate. In the present work these data were used to attempt to obtain approximate upper and lower limits on the emissivities. The upper limit was calculated from a curve fit from Ref. 33 which fitted the maximum emissivities (at the thermodynamic states of interest) predicted by the three theoretical works; the lower limit was obtained from a curve fit from Ref. 34 which fitted the minimum emissivities from the three theoretical works.

In addition to the three predictions discussed above, two new theoretical methods for the calculation of optical properties have become available at LMSC. The first has been developed by Armstrong, et al. (Refs. 35 and 36) and offers a very high degree of precision for the prediction of emissivities by atomic processes (applicable to air when temperatures are greater than about 10,000° K). The second was developed specifically for this investigation and is presented in detail in subsection 3.3. It is somewhat less accurate than Armstrong's method but has greater utility in that emissivities can be more readily generated. In addition,it is applicable to temperatures as low as about 1000° K and as high as about 20,000° K.

A brief summary of the two theoretical methods is presented below. Consider first the work by Armstrong, et al. (Ref. 35).

a. Photoelectric Transitions

The Burgess-Seaton Coulomb approximation (Ref. 37) is used near threshold and a Born approximation to the dipole acceleration matrix element is used at high photon energies. The use of these two approximations and a method for joining them was selected upon comparison with the results of a Hartree-Fock code due to Dalgarno, Henry, and Stewart (Ref. 38).

b. Atomic Line Transitions

The program compares all pairs of levels, applies selection rules as appropriate and thereby picks out the allowed transitions. The contribution to the absorption coefficient due to each transition is then computed, using Hartree-Fock-Slater radial dipole integrals and Baranger-Stewart electron collision broadening in a Voigt profile.

A progressive lumping of the atomic levels is employed. For principal quantum numbers $n = 2$ and 3 , most multiples are treated distinctly; for $n = 4$ to 8 and $\ell \geq 3$, transition arrays are computed; and for larger ℓ and $n > 9$, hydrogenic approximations are made.

This part of the code is not fully operational. It can be used to calculate mean absorption coefficients over small frequency increments, and it can be used to calculate Planck means, but it cannot be used to calculate the detailed spectral absorption coefficients required for accurate solutions to the transport equation when self-absorption at the line centers is present. It has the additional limitation that it cannot be used for wavelengths greater than about 0.85 microns.

c. Free-Free Transitions

A hydrogenic approximation is used.

d. Occupation of Atomic States

The set of occupation numbers presently used is the result of a previous evaluation, computed on a fixed grid of six densities and five temperatures. This grid is inflexible and,when intermediate states are desired, interpolation is required.

Consider now the theoretical analysis given in subsection 3.3.

a. Photoelectric Transition

The hydrogenic approximation is used in much the same manner that it was used by Stewart and Pyatt (Ref. 39). The two differences of significance between the two approaches are that in the LMSC code the Gaunt factors

were taken from the work of Karzas and Latter (Ref. 40) rather than assumed to be unity, and fractional parentage coefficients were included.

b. Free-Free Transitions
A hydrogenic approximation is used.

c. Molecular Transitions
The approach developed by Mulliken (See Ref. 41 for example) and his co-workers was used. The electronic oscillator strengths were obtained from recent work by D. Churchill at LMSC (Ref. 42).

d. Occupation of Atomic States
The neutral, ionic, and electronic populations are obtained from Ref. 43. These then are divided into the level populations by the code itself, which can handle Boltzmann statistics.

Selected values of the integrated (continuum) emission coefficients as calculated by the above two methods are presented in Figs. 24 and 25 for comparison with the three well known works (Refs. 27, 28, and 29).

It is seen in Fig. 24 that for the thermodynamic states corresponding to the (approximately constant) stagnation streamline values of Cases I and II ($T = 11,100°K$ and $\rho/\rho_o = 10^{-2}$), the results of the present calculation agree quite well with the results of the G. E. calculation (although significant differences occur at lower densities as seen in Fig. 25).

The corresponding spectral emission coefficients were calculated and are presented in Figs. 26 and 27. Several curves of B_ν/δ are also plotted in these figures to illustrate the spectral dependence of self-absorption. These data were used to evaluate I_{SA} from Eq. (2.17). It should be noted that for typical values of δ(1-30 cm) there is a relatively small transition region (where $B_\nu/\delta \sim j_\nu$); consequently, one would expect Eq. (2.17) to yield rather accurate results. The calculated intensities normalized against I_{OT}, the integrated intensities as calculated by the thin-gas approximation, are presented in Fig. 28. It is seen that for an optical path length of 4.45 cm (the standoff distance

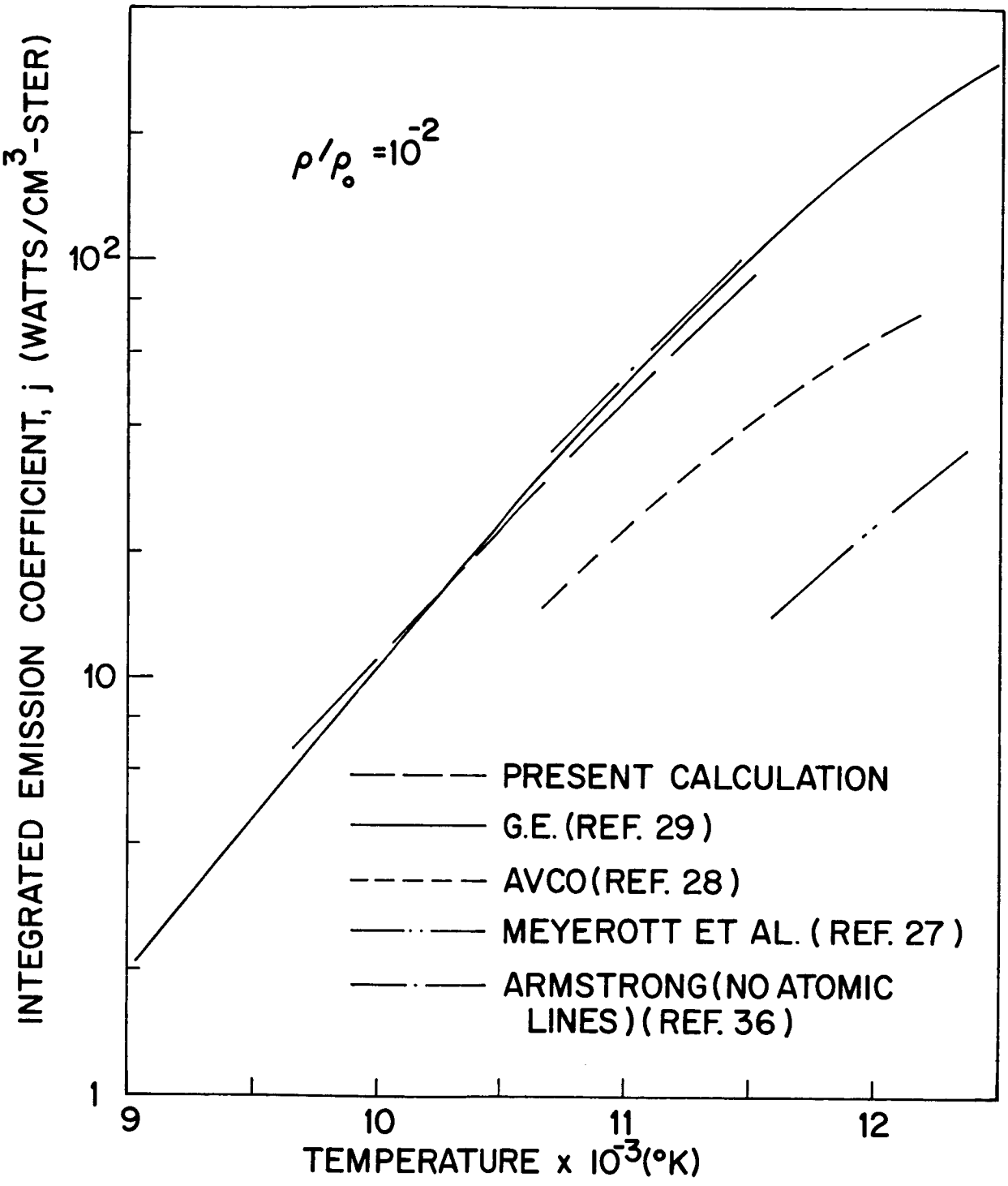

Fig. 24 Comparison Between Various Theoretical Predictions of Integrated Emission Coefficients

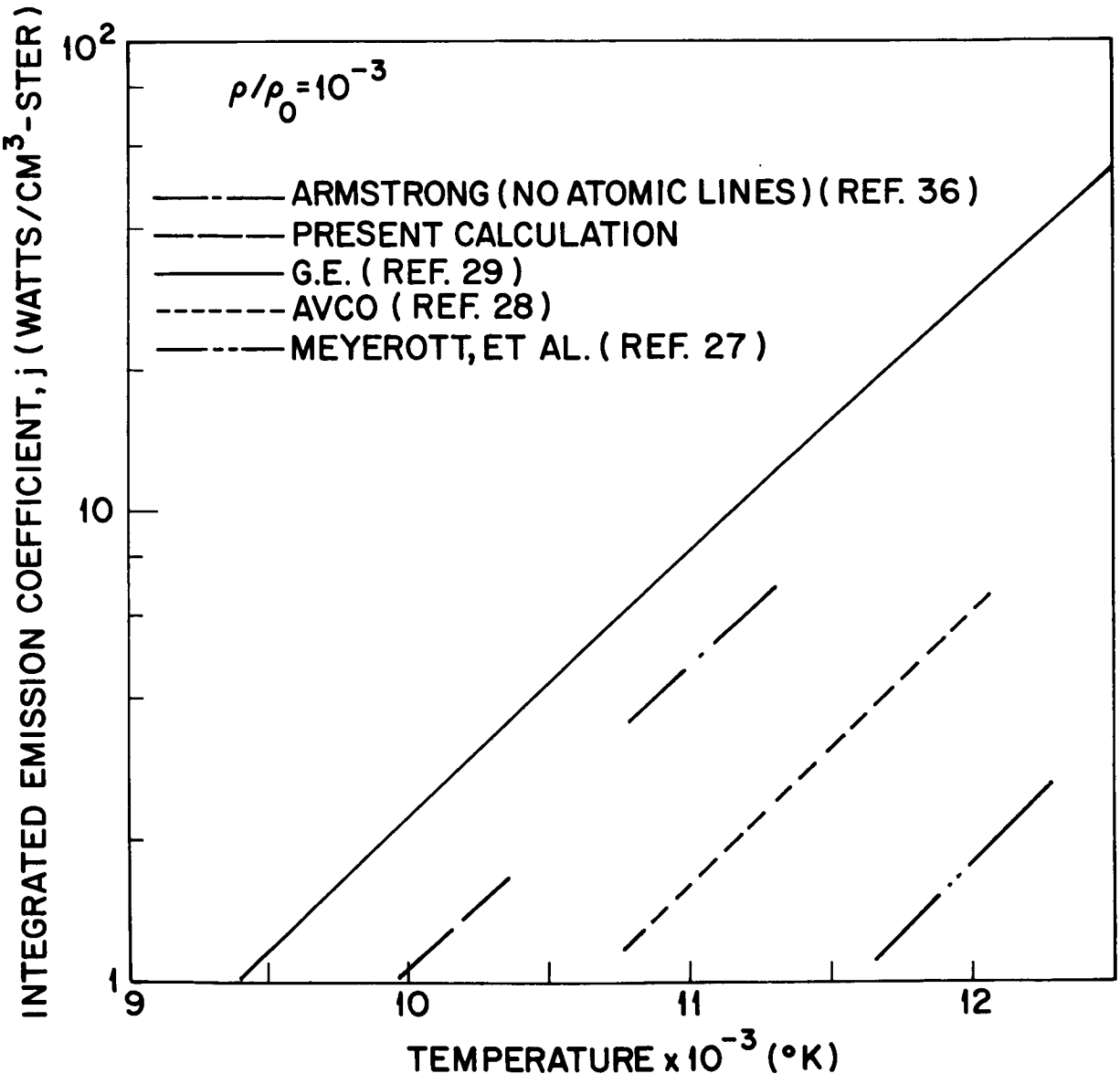

Fig. 25 Comparison Between Various Theoretical Predictions of Integrated Emission Coefficients

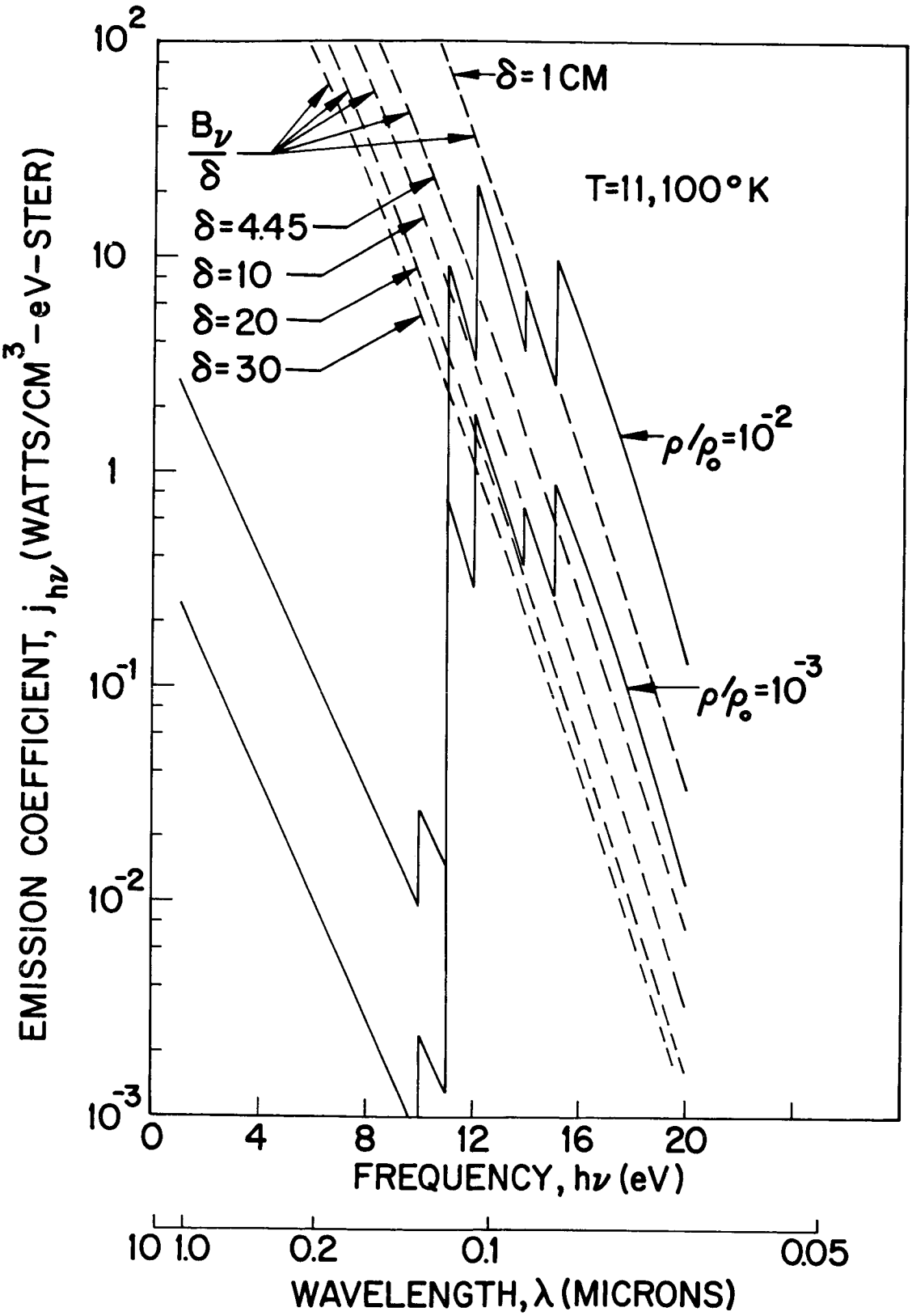

Fig. 26 Emission Coefficients as Calculated by Armstrong (No Atomic Lines)

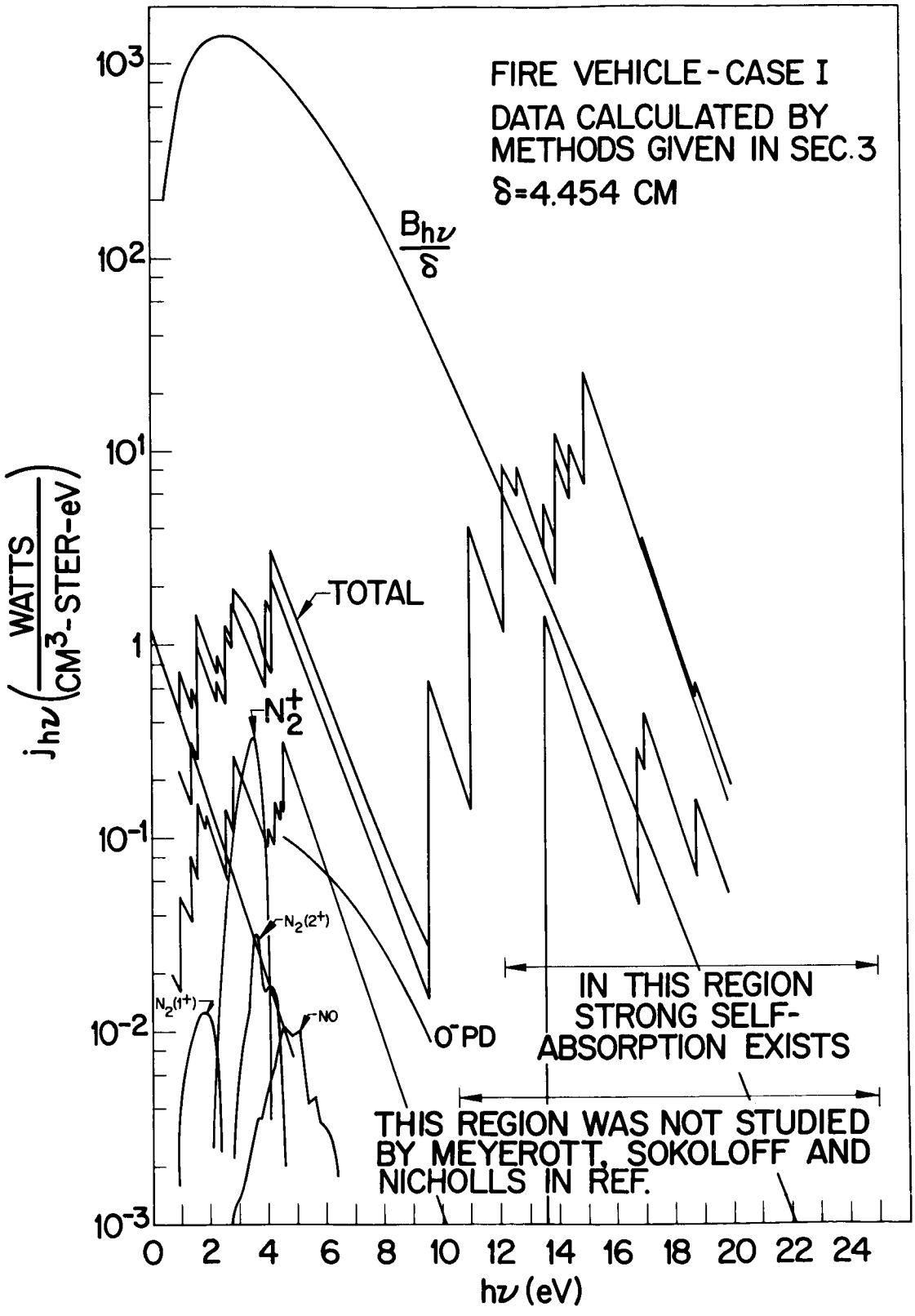

Fig. 27 Equilibirum Emission Coefficients

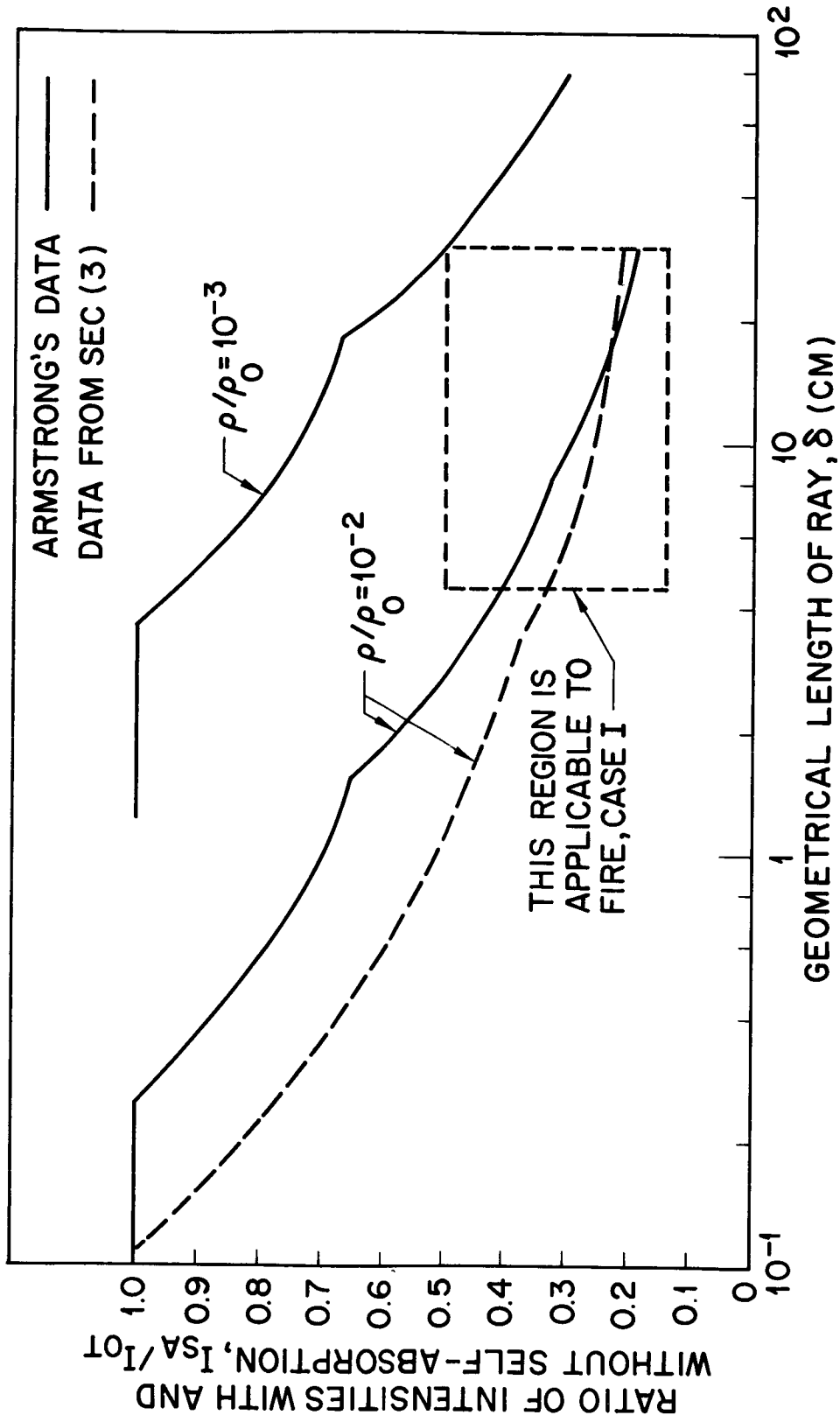

Fig. 28 The Ratio of the Integrated Intensity With Self-Absorption to That Without Self-Absorption, at 11,100°K

for Cases I and II), the actual intensity is about 0.4 of the intensity based on the thin-gas formula. The effect of self-absorption on the angular distribution of integrated intensity is given in Fig. 29 for the stagnation point of Case I. In this figure, the normalizing intensity, I_{OT}, is the optically thin intensity for the optical path length for a given value of θ. It is seen that the angular dependence is rather weak, which indicates that, to a good approximation, one can correct the total intensity for self-absorption effects by using the shock standoff distance as the optical path length.

2.5 CONVECTIVE HEATING

2.5.1 Stagnation Point Convective Heat Transfer

The stagnation-point heat-transfer rate due to convection was calculated for Case I using the following equation from Ref. (44).

$$q_c\sqrt{R} = C\left(\frac{\beta R}{V_\infty}\right)^{1/2}(\rho_\infty)^{1/2}\bar{V}^{3.19}\left(1 - \frac{h_w}{h_e}\right) \qquad (2.19)$$

where

q_c = convective heat-transfer rate, $Btu/ft^2\text{-}sec$

C = 2.6×10^4 $Btu\text{-}ft^{1/2}\ lb^{-1/2}\text{-}sec^{-2}$

$\beta R/V_\infty$ = nondimensional stagnation point velocity gradient

ρ_∞ = free-stream density, $slugs/ft^3$

R = nose radius, ft

$\bar{V}$ = nondimensional free-stream velocity, $V_\infty/10^4$ $ft\text{-}sec^{-1}$

h_w, h_e = enthalpy at the wall, edge of boundary layer

The stagnation point velocity gradient was obtained from the inviscid flow-field analysis.

For Case II, where the vehicle is at 5-deg angle-of-attack, the inviscid subsonic solution showed that the stagnation point was also shifted by 5 deg. The stagnation point is still on the spherical portion of the heat shield and cross-flow effects are negligible. Therefore, the same prediction equation used in Case I was also used in Case II.

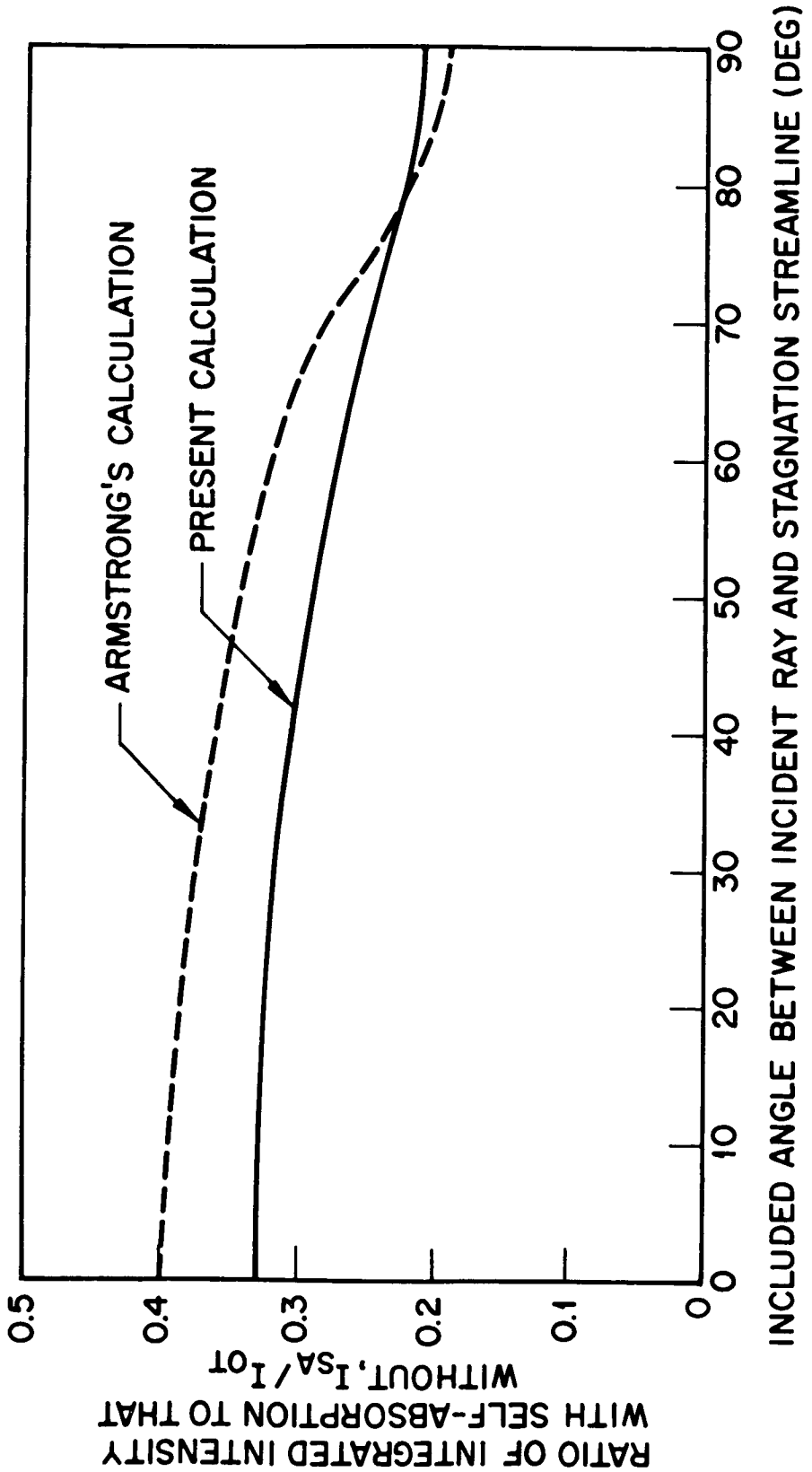

Fig. 29 Angular Dependence of the Integrated Intensity at the Stagnation Point of Case I

For Case III, the high-altitude nonequilibrium case, the same equation was again used since Adam's results (Ref. 45) have shown that nonequilibrium effects are small in an ionized boundary layer if the surface is catalytic. The effect of vorticity was estimated using the summary curves given in Ref. 46. The appropriate Reynolds number and density ratio across the shock are

$$\tilde{\mathrm{Re}} = \frac{\rho_\infty V_\infty R}{\mu_s} = 1300$$

$$\bar{\rho} = \frac{\rho_\infty}{\rho_s} = 0.106$$

which results in an increase in the stagnation-point heat-transfer rate of 5 and 16 percent according to the theories of Van Dyke (Ref. 47) and Ferri, et al. (Ref. 48), respectively. The stagnation-point heat-transfer data are shown in Figs. 12, 16, and 18.

2.5.2 Convective Heat-Transfer Distribution

The convective heat-transfer distribution was calculated for Case I using the self-similar solutions of Lees (Ref. 49) and Cohen (Ref. 50). The results are presented in Fig. 12 and Table 8. It is seen that the difference between the two theories is quite small. The boundary-layer edge conditions were obtained from the inviscid solutions of subsection 2.2.

Since the difference between the two theories is negligible, the simpler theory of Lees was used for Case II, the 5-deg angle-of-attack case. Using the pressure distribution of Section 2, the convective heat distribution was obtained. The pressure distribution is presented in Fig. 5 and the resulting heat-transfer distribution is shown in Fig. 16.

For Case III, the nonequilibrium inviscid solution was used directly to obtain the edge conditions with the exception of the viscosity. The inviscid nonequilibrium solution gives the pressure and translational temperature from which the viscosity can be

calculated. Since the gas is not in equilibrium, it was necessary to calculate the viscosity using the nonequilibrium composition and thermodynamic properties from the inviscid solution. This calculation is discussed in Appendix C.

The heat-transfer distribution was calculated using both the equilibrium and nonequilibrium viscosity. The heat-transfer distributions are shown in Fig. 18, and Table 10, where it is seen that the effect of the nonequilibrium viscosity is to reduce the convective heating by about 20 percent in the corner region. The effect of shock-generated vorticity on heat transfer was assumed to be uniform over the face of the vehicle. The uniform increase is shown in Fig. 18. This assumption that the increase in heat transfer is uniform over the frontal portion of the vehicle is based on Ferri's results (Ref. 48) from an investigation of the effect of external vorticity on the heat-transfer distribution.

2.5.3 Wake Heating

The heat transfer to the back of the body from the wake was calculated assuming that Reynold's Analogy holds between the heat transfer and skin friction. This assumption is certainly true if the temperature of the dead-air region equals that of the body, and probably is a good approximation otherwise. In addition, it was assumed that Prandtl Number = Lewis Number = 1. With these assumptions, the heat transfer to the body was computed from the total energy transferred across the dividing streamline, using the results of Ref. 21. Assuming that the heat transferred was distributed uniformly over the total surface area of the base region, one gets an average base heating rate of 31.5 Btu/ft^2-sec.

To the order of the approximations made in analyzing Case II, and in consideration of the approximate nature of the wall-heating analysis, the Case II base-heating rate is indistinguishable from Case I.

Section 3
THEORETICAL METHODS

3.1 FLOW-FIELD ANALYSIS

3.1.1 Inverse Method for the Subsonic Flow Regions of Cases I and II

In this section, the inverse method of Swigart is described in greater detail. The discussion will be limited to three-dimensional flows, the only flows of interest here. In cylindrical polar coordinates with the origin at the shock vertex, and with the shock nose radius as the unit of length, the assumed conic-section shock wave has the equation

$$r = 2x - Bx^2 \tag{3.1}$$

where B characterizes the eccentricity of the conic section, and the x-axis points in the downstream direction. An orthogonal coordinate system containing the shock wave as a coordinate surface is defined by:

$$x = \frac{1}{B}\left[1 - \sqrt{(1 - B\xi^2)(1 - B + B\eta^2)}\right] \tag{3.2}$$

and

$$r = \xi\eta \tag{3.3}$$

The shock wave is described by $\eta = 1$. The uniform free stream makes an angle ϵ with the x-axis. Equation (2.1) is satisfied by the introduction of two stream functions, ψ_1 and ψ_2 , satisfying the relation

$$\rho\vec{V} = \nabla\psi_1 \times \nabla\psi_2 \tag{3.4}$$

The intersection of the surfaces ψ_1 = constant and ψ_2 = constant are therefore streamlines, and by virtue of Eq. (2.3), are also lines of constant entropy. The gas law which is assumed is that for a "locally" perfect gas, i.e., one for which the isentropic index

$$\gamma = (\partial \log p/\partial \log \rho)_S \tag{3.5}$$

can be considered approximately constant throughout the subsonic region. The first and second laws of thermodynamics then require that the enthalpy satisfy Eq. (2.5), where A is an arbitrary function of entropy, assumed here to be also constant. It then follows from Eqs. (2.3), (3.4), and (3.5) that

$$p/\rho^{\gamma} = g(\psi_1 , \psi_2) \tag{3.6}$$

where the function g will be determined from the boundary conditions at the shock wave. Eliminating $\vec{V}$ and p with the aid of Eqs. (3.4) and (3.6), and introducing the (ξ , η , φ) coordinate system through Eqs. (3.2) and (3.3), one obtains from Eq. (2.2) a set of three nonlinear equations in ρ , ψ_1 , ψ_2 , as functions of ξ , η and φ .

The arbitrariness in the definition of ψ_1 and ψ_2 is removed by considering the uniform free stream as an axisymmetric flow with the body streamline (ahead of the shock) chosen as the axis of symmetry, and setting ψ_2 equal to the azimuthal angular coordinate of such a flow; ψ_1 then becomes the familiar Stokes stream function, which is commonly set equal to zero on the axis of symmetry. Since the location of the body

streamline ahead of the shock wave is not known a priori, it is necessary to introduce a parameter δ, which measures the distance of the body streamline in the free stream from a given reference streamline. The boundary conditions at the shock wave ($\eta = 1$) and the function $g(\psi_1, \psi_2)$, both involving the parameter δ and the shock angle-of-attack ϵ, can now be explicitly written. The boundary condition at the body is simply

$$\psi_1 = 0 \qquad \text{at} \qquad \eta = \eta_b(\xi, \varphi ; \epsilon) \tag{3.7}$$

The method of solution essentially consists of separation of variables by expanding the dependent variables and boundary conditions in double MacLaurin series in ξ and ϵ about $\xi = 0$ and $\epsilon = 0$. If $\vec{V}$, ρ, p, and ψ, are nondimensionalized by V_∞, ρ_∞, $\rho_\infty V_\infty^2$, and $\rho_\infty V_\infty$, respectively (where the subscript ∞ refers to free-stream conditions), then the initial conditions at the shock wave determine expansions of the form:

$$2\bar{\psi}_1 = f_o(\eta)\xi^2 + f_1(\eta)\xi^4 + f_2(\eta)\xi^6 + \ldots$$

$$+ \epsilon \cos\varphi \left[f_4(\eta)\xi + f_5(\eta)\xi^3 + f_6(\eta)\xi^5 + \ldots \right] + 0(\epsilon^2) \tag{3.8}$$

$$\bar{\psi}_2 = \varphi + \epsilon \sin\varphi \left[\frac{h_4(\eta)}{\xi} + h_5(\eta)\xi + h_6(\eta)\xi^3 \right] + 0(\epsilon^2) \tag{3.9}$$

$$\frac{\gamma - 1}{\gamma + 1} \bar{\rho} = g_o(\eta) + g_1(\eta)\xi^2 + g_2(\eta)\xi^4 + \ldots$$

$$+ \epsilon \cos\varphi \left[g_4(\eta)\xi + g_5(\eta)\xi^3 + g_6(\eta)\xi^5 + \ldots \right] + 0(\epsilon^2) \tag{3.10}$$

where bars indicate nondimensional variables.

Substituting the above expansions into the partial differential equations and boundary conditions, and equating coefficients of like powers of ξ and ϵ, one obtains sets of ordinary differential equations in η. Each set contains one more unknown than the number of equations (e.g., the zero order set results in two equations for f_o, g_o, and g_1), reflecting the backward influence due to the ellipticity of the equations in the subsonic region. The equations are solved by setting the unknown from the higher-order expansion term equal to zero, and integrating the resulting set numerically by standard means from the shock wave ($\eta = 1$) in steps of $\Delta\eta$. Condition (3.7) determines the shape of the body, as well as the value of the parameter δ when $\epsilon \neq 0$. For angles-of-attack, solutions have been programmed only to the first order in ϵ, with three terms in the expansions in ξ, and a perfect gas law assumed throughout. For zero angle-of-attack, four term expansions in ξ have been programmed, and the gas law obeys Eq. (2.5). Considerable hand reduction remains to determine the body shape and flow variables. A program which performs the reduction automatically is available for zero angle-of-attack, with four term expansions in ξ, but only for a perfect gas.

In applying the method to Case I (zero angle-of-attack), one encounters two problems. The first arises in the attempt to duplicate the desired body shape, and is due to an inherent limitation of the method. Due to the small shoulder radius of the body, the best approximation (limited to conic sections of revolution) to the actual shock shape is a fairly blunt oblate ellipsoid ($B > 0$). The sonic region near the body turns out to be close to the focus of the generating ellipse, which is a singularity of the coordinate system. The expansions in ξ diverge (since the expansion of the factor $(1 - B\xi^2)$ of the coordinate transformation diverges as $\xi \rightarrow B^{-1/2}$), thus rendering the solutions invalid in that region. The physical explanation of this breakdown is that the actual shock-wave slope must remain greater than that of the free-stream Mach wave, and consequently the shock wave cannot be represented far from the axis by an ellipse whose slope becomes zero. The method used to overcome this limitation was discussed in subsection 2.2.2. The shock wave that best approximated the actual shock wave was one with a bluntness of $B = 5.6$.

The concurrent problem of duplicating the thermodynamic state of the real, equilibrium air in the subsonic region was resolved by choosing γ and A so as to duplicate conditions at the body sonic point. (See subsection 2.2.2). The resultant values of $\gamma = 1.192$ and $A/V_\infty^2 = 0.1188$ correspond to a value of $A/h = 0.25$, indicating that the modification of the perfect gas law is important for this case. Unfortunately, the many trial solutions which were required to duplicate the desired body shape necessitated the use of the automated program, which was only available for a perfect gas law. We note, however, that the enthalpy constant A is only used in the shock boundary conditions. Furthermore, for hypersonic flow, the state of the gas behind the shock wave can be approximately written in terms of the shock angle and the density only. For a flow whose gas obeys Eq. (2.5) downstream of the shock wave, the density ratio can be shown to be given by:

$$\frac{\rho_\infty}{\rho_s} = \frac{\gamma}{\gamma+1}\left[1 + \frac{1}{\gamma_\infty (M_\infty \sin\phi)^2}\right] - \frac{1}{\gamma+1}\left[1 + \frac{2A(\gamma^2-1)}{V_\infty^2 \sin^2\phi} + \frac{2(\gamma_\infty - \gamma^2)}{\gamma_\infty(\gamma_\infty - 1)(M_\infty \sin\phi)^2} + \frac{\gamma^2}{\gamma_\infty^2 (M_\infty \sin\phi)^4}\right]^{1/2} \tag{3.11}$$

where ϕ is the shock angle measured with respect to the free-stream direction. Both $A/V_\infty^2 \sin^2\phi$ and $1/(M_\infty \sin\phi)^2$ are small in our case, permitting an expansion of Eq. (3.11) which, to first order, gives

$$\frac{\rho_\infty}{\rho_s} \approx \frac{\gamma-1}{\gamma+1} + \frac{1}{(\gamma+1)\sin^2\phi}\left[\frac{(\gamma+\gamma_\infty)(\gamma-1)}{\gamma_\infty(\gamma_\infty-1)M_\infty^2} - \frac{A(\gamma^2-1)}{V_\infty^2}\right] \tag{3.12}$$

Comparing Eq. (3.12) with the expression for a perfect gas law, we see that the density (and therefore other variables) behind the shock wave is approximately that given by the flow of a perfect gas with the real γ but a fictitious equivalent Mach number M_e defined by

$$\frac{2}{M_e^2} = \frac{(\gamma + \gamma_\infty)(\gamma - 1)}{\gamma_\infty(\gamma_\infty - 1)M_\infty^2} - \frac{A}{V_\infty^2}(\gamma^2 - 1) \tag{3.13}$$

Since the second term dominates, and $A > 0$ in our case, this corresponds to an imaginary Mach number. Since the free-stream Mach number always appears as the square in all the shock boundary conditions, this formal result causes no difficulty. Fortunately, it was simple to modify the automated program to input the square of the free-stream Mach number, instead of the Mach number itself. The value of M_e^2 for Case I was -40.71.

As one moves along the shock wave from the axis, and $\sin^2\phi$ decreases, the approximate result Eq. (3.12) becomes poorer. Also, Eq. (3.11) predicts a monotonic variation of the density, while the actual density (from a real-gas solution) actually increases at first, and then starts to decrease, thus indicating the deficiency of the simple "locally" perfect gas approximation. Fortunately, the error in expansion Eq. (3.10) due to the slight divergence of the solution at the shock wave as ξ increases, compensated for the errors due to the approximate treatment of the thermodynamic state. Thus, there was good agreement between the values of the shock density ratio as calculated by the machine program, and the exact values determined iteratively, using Ref. 10, all the way out to the starting line. The comparison is shown below:

Location	ρ_∞/ρ_s (Machine Calculation)	ρ_∞/ρ_s (Exact)
Axis	0.0652	0.0658
Point of Maximum Deviation ($\xi = 0.25$)	0.0631	0.0651
Starting Line	0.0620	0.0621

The use of Eq. (3.13) to determine M_e is therefore justified. Away from the shock wave, where the calculated and real thermodynamic state did not agree as well, the pressure and flow geometry as derived from the program were chosen to be correct (see discussion in subsection 2.2.2). Additional information on the modified, automated zero angle-of-attack program used for Case I may be found in Appendix A.1.

The problem of duplicating the body shape for Case II (5-deg angle-of-attack) was resolved by choosing the same shock shape ($B = 5.6$) as in Case I. (See discussion in subsection 2.2.2). The duplication of the thermodynamic state of the gas was more difficult. It proved impossible in the time allotted to effect the modification of the perfect gas program by introducing M_∞^2 as the input parameter, as was done for the automated program for Case I. It was therefore decided to utilize the existing perfect-gas angle-of-attack program, choosing for the equivalent γ', that value which would satisfy Eq. (2.5) at the body sonic point, with A set equal to zero. This gave the value $\gamma' = 1.1367$. The corresponding equivalent Mach number, given by Eq. (3.13) with $A = 0$, was $M_e = 57.44$. Further information on the angle-of-attack program used for Case II may be found in Appendix A.2.

3.1.2 Analytic Solution for Supersonic Flow Around Spheres

This subsection presents further details on the approximate analytic solution, developed at LMSC, for the subsonic flow region generated by a sphere moving at supersonic speeds. The method is an extension of Lighthill's solution, which was based on the single assumption of constant density, and thus restricted to the stagnation region for hypersonic flow. The extension consists essentially of removing this restriction, in order to calculate the complete subsonic region, and part of the supersonic region.

The spherical coordinate system (R, θ, φ) indicated in Fig. 6 is used. Equation (2.1) is satisfied by introducing the Stokes stream function, ψ, given by

$$\rho V_\theta = \frac{1}{R \sin\theta} \frac{\partial \psi}{\partial R} \quad , \quad \rho V_R = -\frac{1}{R^2 \sin\theta} \frac{\partial \psi}{\partial \theta} \tag{3.14}$$

where V_θ, V_R are velocity components in the θ and R directions, respectively. Equations (2.2) through (2.4) can be combined with the laws of thermodynamics to yield an equation for the vorticity (Crocco's Law). Substituting Eq. (3.14), one obtains the final form

$$\frac{1}{R^2}\frac{\partial}{\partial\theta}\left(\frac{1}{\sin\theta}\frac{\partial\psi}{\partial\theta}\right) + \frac{1}{\sin\theta}\frac{\partial^2\psi}{\partial R^2}$$

$$= R^2 \sin\theta\left\{\frac{\rho V^3}{a^2 R \sin\theta\,\mathcal{R}} - \rho^2 T\frac{dS}{d\psi}\left[1 - V^2\left(\frac{\partial \log\rho}{\partial h}\right)_p\right]\right\} \qquad (3.15)$$

where $\mathcal{R}$ and a are the local streamline radius of curvature and speed of sound, respectively. In Lighthill's solution the terms in the curly brackets are replaced by a constant. In the present solution these terms are approximated by a linear function in R and $\cos\theta$. Introducing the nondimensionalizations of subsection 3.1.1, with the body radius R_B as the unit of length, we can rewrite Eq. (3.15) as

$$\frac{1}{\bar{R}^2}\frac{\partial}{\partial\theta}\left(\frac{1}{\sin\theta}\frac{\partial\bar{\psi}}{\partial\theta}\right) + \frac{1}{\sin\theta}\frac{\partial^2\bar{\psi}}{\partial\bar{R}^2} = \bar{R}^2\sin\theta\left[A + B\bar{R} + (C + D\bar{R})\cos\theta\right] \qquad (3.16)$$

where the constants A, B, C, and D are yet to be determined. Applying the boundary condition, $\bar{\psi} = 0$ at $\bar{R} = 1$, we obtain the formal solution

$$\bar{\psi} = \bar{R}^2\sin^2\theta\left[f_1(\bar{R}) + f_2(\bar{R})\cos\theta + f_3(\bar{R})(1 - 5\cos^2\theta) + f_4(\bar{R})\cos\theta\,(3 - 7\cos^2\theta)\right] \qquad (3.17)$$

where

$$
\begin{aligned}
f_1(\bar{R}) &= b_1(\bar{R}^{-3} - 1) + \frac{A}{10}(\bar{R}^2 - 1) + \frac{B}{18}(\bar{R}^3 - 1) \\
f_2(\bar{R}) &= b_2(\bar{R}^{-4} - \bar{R}) + \frac{C}{6}(\bar{R}^2 - \bar{R}) + \frac{D}{14}(\bar{R}^3 - \bar{R}) \\
f_3(\bar{R}) &= b_3(\bar{R}^{-5} - \bar{R}^2) \\
f_4(\bar{R}) &= b_4(\bar{R}^{-6} - \bar{R}^3)
\end{aligned}
\tag{3.18}
$$

Equation (3.17) has been truncated at four terms in order to yield the proper number of unknowns in the final set of equations. In order to determine the constants A through D, and b_1 through b_4, we focus attention on the points labeled 0, 1, 2, and 3 in Fig. 6. The flow geometry at the last three of these points is specified by introducing the parameters $\bar{R}_1$, $\bar{K}_1$, $\bar{R}_2$, θ_2, $\bar{K}_2$, and θ_3, respectively, where $\bar{K}$ is the non-dimensional shock-wave curvature, and θ is expressed in radians. Since $\mathcal{K}$ can be expressed in terms of K at the shock wave, and the thermodynamic state is known at points 0, 1, 2, and 3, it follows that the curly bracket in Eq. (3.15) can be evaluated at those four points. One can therefore express the constants A through D in terms of the six newly defined parameters. The latter, together with the solution constants b_1 through b_4, comprise ten unknowns which are solved for by applying boundary conditions on $\bar{\psi}$ and its derivatives at the points 1, 2, and 3, yielding precisely ten equations. The constants b_1 through b_4 appear linearly in these ten equations, and can be easily eliminated, reducing the system to a set of six nonlinear algebraic equations in the six unknowns $\bar{R}_1$, $\bar{K}_1$, $\bar{R}_2$, θ_2, $\bar{K}_2$, and θ_3. This set cannot be solved analytically. Instead, Newton's method of iterating on initial guesses is employed, using an electronic computer. Once the six geometric parameters are known, the constants A through D, and b_1 through b_4 can be calculated, and the

stream function $\bar{\psi}$ can then be evaluated at any point from Eqs. (3.17) and (3.18). The complete flow picture can be obtained in the following manner:

The shock-wave shape can be determined from the condition

$$\bar{\psi}_S = \frac{\bar{R}^2 \sin^2 \theta}{2} \tag{3.19}$$

This yields an equation for the shock shape $\bar{R}(\theta)$ which implicitly determines the function $\alpha(\bar{\psi})$, where α is the complement of the shock angle ϕ. The oblique shock solutions for the specified gas and free-stream conditions determine S and $\bar{\rho}^* \bar{a}^*$ behind the shock wave as a function of α, where the superscript $*$ refers to critical conditions. The functions $S(\bar{\psi})$ and $\bar{\rho}^* \bar{a}^*(\bar{\psi})$ are therefore known. Using Eq. (3.14), the quantities S and $\bar{\rho}\bar{V}/\bar{\rho}^* \bar{a}^*$ can then be evaluated at any point. The remaining thermodynamic variables (and the velocity) follow from the equations of state of the gas.

A feature of the solution is that the self-consistency of the solution at points other than 0, 1, 2, and 3 can be checked. Using Eq. (3.14), the component of $\bar{\rho}\bar{V}$ normal to the shock wave at the location given by Eq. (3.19) can be calculated. The departure from the exact value $\cos \alpha$ is then a measure of how well the shock boundary conditions are satisfied at points other than 1 and 2. Similarly, the sonic line is determined by solving iteratively for the sonic throat condition

$$\rho \vec{V} \cdot \nabla (\rho^2 V^2) = 0 \tag{3.20}$$

using Eq. (3.14). By comparing the value of $\bar{\rho}^2 \bar{V}^2$ at the location determined by Eq. (3.20) with the value of $\bar{\rho}^{*2} \bar{a}^{*2}$ from the shock solution for the same streamline, the self-consistency of the solution at any point on the sonic line can also be checked.

While the solution described above is valid for an arbitrary gas law it has only been programmed for a perfect gas. The quantity $\rho V/\rho^* a^*$ and the flow angle β are

automatically printed out on selected streamlines at prescribed intervals of $\Delta\theta$. The nondimensional cylindrical $(\bar{r}, \bar{z})$ coordinates of the points are also printed, with $\bar{z}$ measured from the stagnation point, and the $\bar{z}$-axis pointing upstream. On the body streamline, the Mach number, pressure, temperature, and density are also calculated. Conditions at the shock and sonic points are presented, including the self-consistency checks. A sonic corner option is also available, as described in subsection (2.2.3). Further details on the machine program are found in Appendix A.3.

3.2 FLOW CHEMISTRY

The spatial distribution of the molar concentrations of component species in the shock-layer gas were predicted by a digital-computer solution of the coupled chemical rate processes. This digital code, developed at LMSC, integrates the coupled rate equations along selected streamlines. The streamline pressure distribution (determined from a prior, equilibrium calculation) governs the coupled flow and chemistry history along a streamline through simultaneous solution of the one-dimensional momentum equation, the coupled rate chemical processes, energy conservation expressed by the enthalpy function,

$$\bar{h}(x) = \sum_{i=1}^{10} \bar{n}_i(x) \left[\bar{c}_{p_i} \bar{T}(x) + \bar{e}_{D_i} + \bar{e}_{I_i}\right] + 1.40235 \times 10^{-2} \exp\left(-10^{-2}/\bar{n}_{10}(x)\right) \qquad (3.21)$$

and an equation of state

$$\bar{p}(x) = \bar{\rho}(x) \bar{T}(x) \sum_{i=1}^{10} \bar{n}_i(x) \qquad (3.22)$$

for the 10 species components considered in the solution. The barred quantities are nondimensional forms of the variables, identified in the text following.

In the original formulation, the energy (enthalpy) equation used in the streamtube computer code neglected contributions from the excitation of the bound electronic states. Although the fundamental mechanisms for such coupled excitation, in a reacting gas, are not well understood (the reader's attention is directed to Refs. (24 and 26) a simulation of the energy decay to the known equilibrium reservoir conditions is necessary for the subsequent radiation calculations. An exponential term was empirically developed to simulate this excitation. This term, functionally dependent on the free electron population appears as the last term in Eq. (3.21). For the known asymptotic limit prescribed by the equilibrium reservoir conditions, the contribution of the term alters the enthalpy so that the corresponding temperature tends to the proper limiting value. The temperature alteration at this limit was of the order of 1000°K or slightly less than a 10-percent decrease in computed kinetic temperature.

As indicated in a previous discussion (subsection 2.3) the computational method is based on the "streamtube" approximation. In outline, the streamtube treatment is based on the assumption that throughout most of the inviscid hypersonic shock layer, the pressure distribution is relatively insensitive to the chemical processes, and that diffusion of species normal to the streamlines is a second-order effect and may be neglected. Under these assumptions,a computational procedure is developed which makes use of equilibrium flow-field results yielding streamline patterns and pressure distributions conceptually unaltered by the rate chemistry. The motion of a fluid element is thus governed by the equilibrium pressure distribution, following an equilibrium streamline, which represents a prescribed boundary condition for the solution of a set of coupled differential rate equations along each streamline traced.

In the absence of simultaneous nonequilibrium transitions in internal energy modes, the reverse-rate constant for a chemical reaction is simply a ratio of the forward-rate constant to the equilibrium constant,

$$K_{R_i} = \frac{K_{F_i}}{K_{C_i}} \tag{3.23}$$

The physical significance of this in the present calculation is equivalent to the assumption of instantaneous equilibration between rotational, vibrational, and translational degrees of freedom. The species composition is assumed frozen in the undisturbed or ambient state at the initial shock point. This initial-state point for the gas is computed for each streamline at a point just after shock transition. The state is separately calculated for input to the program, based on the known equilibrium pressure behind the shock front and initial specific heat ratio (9/7) characteristic of an ideal gas fully excited in rotational and vibrational degrees of freedom and equilibrated to the translational mode. In the present calculations the ambient air is treated as a two-component mixture of oxygen and nitrogen molecules in the proportions 21 and 79 parts per 100, respectively.

Twelve chemical processes are considered in the present calculations governing the production of the component species considered. The rate processes considered are:

(1) $$O_2 + M \underset{K_{R_1}}{\overset{K_{F_1}}{\rightleftharpoons}} O + O + M \qquad (3.24.1)$$

(2) $$N_2 + M \underset{K_{C_2}}{\overset{K_{F_2}}{\rightleftharpoons}} N + N + M \qquad (3.24.2)$$

(3) $$NO + M \underset{K_{R_3}}{\overset{K_{F_3}}{\rightleftharpoons}} N + O + M \qquad (3.24.3)$$

(4) $$O_2 + N \underset{K_{R_4}}{\overset{K_{F_4}}{\rightleftharpoons}} NO + O \qquad (3.24.4)$$

(5) $$N_2 + O \underset{K_{R_5}}{\overset{K_{F_5}}{\rightleftharpoons}} NO + N \qquad (3.24.5)$$

$$(6) \qquad N_2 + O_2 \underset{K_{R_6}}{\overset{K_{F_6}}{\rightleftharpoons}} NO + NO \qquad (3.24.6)$$

$$(7) \qquad NO^+ + e^- \underset{K_{R_7}}{\overset{K_{F_7}}{\rightleftharpoons}} N + O \qquad (3.24.7)$$

$$(8) \qquad N_2^+ + e^- \underset{K_{R_8}}{\overset{K_{F_8}}{\rightleftharpoons}} N + N \qquad (3.24.8)$$

$$(9) \qquad O^+ + e^- + M \underset{K_{R_9}}{\overset{K_{F_9}}{\rightleftharpoons}} O + M \qquad (3.24.9)$$

$$(10) \qquad N^+ + e^- + M \underset{K_{R_{10}}}{\overset{K_{F_{10}}}{\rightleftharpoons}} N + M \qquad (3.24.10)$$

$$(11) \qquad N + e^- \underset{K_{R_{11}}}{\overset{K_{F_{11}}}{\rightleftharpoons}} N^+ + e^- + e^- \qquad (3.24.11)$$

$$(12) \qquad O + e^- \underset{K_{R_{12}}}{\overset{K_{F_{12}}}{\rightleftharpoons}} O^+ + e^- + e^- \qquad (3.24.12)$$

The dissociation and ionization energies used are on an atomic basis for dissociation and ionic basis for ionization, with the ground level taken to be that of the vibrational

ground state for the original diatomic molecules. The energies were taken from Peng and Pindroh (Ref. 51) and Herzberg (Ref. 52).

	Species	e_D	e_I
(1)	O_2	2.5575 ev	--
(2)	N_2	4.878 ev	15.576 ev
(3)	NO	0.9325 ev	9.258 ev
(4)	O	--	13.614 ev
(5)	N	--	14.540 ev

The equilibrium constants and rate constants used are on a molar concentration basis, so that they are functions of temperature only. The equilibrium constants are developed from the concentration partition functions, taken from Peng and Pindroh (Ref. 51), with additional electronic states and statistical weighting from the molecular spectroscopic data of Herzberg (Ref. 52) and atomic data from Gilmore (Ref. 53).

The applicable concentration equilibrium constants are computed at each integration step from the following relations, having the physical dimensions shown.

$$\ln K_{C_1} = 2 \ln Qc(O) - \ln Qc(O_2) - \Delta E_1, \quad K_{C_1} \text{ (moles/cc)} \tag{3.25.1}$$

$$\ln K_{C_2} = 2 \ln Qc(N) - \ln Qc(N_2) - \Delta E_2, \quad K_{C_2} \text{ (moles/cc)} \tag{3.25.2}$$

$$\ln K_{C_3} = \ln Qc(N) + \ln Qc(O) - \ln Qc(NO) - \Delta E_3, \quad K_{C_3} \text{ (moles/cc)} \tag{3.25.3}$$

$$\ln K_{C_4} = \ln K_{C_1} - \ln K_{C_3} - \Delta E_4, \quad K_{C_4} \text{ (dimensionless)} \tag{3.25.4}$$

$$\ln K_{C_5} = \ln K_{C_2} - \ln K_{C_3} - \Delta E_5, \quad K_{C_5} \text{ (dimensionless)} \tag{3.25.5}$$

$$\ln K_{C_6} = \ln K_{C_4} + \ln K_{C_5} - \Delta E_6, \quad K_{C_6} \text{ (dimensionless)} \tag{3.25.6}$$

$$\ell n\ K_{C_7} = \ell n Qc(N) + \ell n Qc(O) - \ell n Qc(NO^+) - \ell n Qc(e^-) - \Delta E_7, \quad K_{C_7}\ (\text{dimensionless}) \tag{3.25.7}$$

$$\ell n\ K_{C_8} = 2\,\ell n Qc(N) - \ell n Qc(N_2^+) - \ell n Qc(e^-) - \Delta E_8, \quad K_{C_8}\ (\text{dimensionless}) \tag{3.25.8}$$

$$\ell n\ K_{C_9} = \ell n Qc(O) - \ell n Qc(O^+) - \ell n Qc(e^-) - \Delta E_9, \quad K_{C_9}\ (\text{cc/mole}) \tag{3.25.9}$$

$$\ell n\ K_{C_{10}} = \ell n Qc(N) - \ell n Qc(N^+) - \ell n Qc(e^-) - \Delta E_{10}, \quad K_{C_{10}}\ (\text{cc/mole}) \tag{3.25.10}$$

$$\ell n\ K_{C_{11}} = -\ \ell n\ K_{C_{10}}, \qquad K_{C_{11}}\ (\text{mole/cc}) \tag{3.25.11}$$

$$\ell n\ K_{C_{12}} = -\ \ell n\ K_{C_9}, \qquad K_{C_{12}}\ (\text{mole/cc}) \tag{3.25.12}$$

In the foregoing relations, ΔE_i symbolizes the sum of the contributing reaction energies associated with the particular reaction

$$\left(\Delta E_i = \sum_j \pm \frac{e_{D_j}}{kT} \pm \frac{e_{I_j}}{kT}\right)$$

while Qc(i) represents the concentration partition function of the ith specie determined from the previously referenced data.

The forward rate constants are those of J. G. Hall, et al., (Ref. 24) and M. H. Bortner (Ref. 26). The three-body rate processes are explicitly weighted with respect to the

concentration of the third-body partner (M) at each integration step in each of the applicable reactions. The set of forward-rate constants used in the present calculations are:

$$K_{F_1}(M = O_2) = 3.2 \times 10^{21}\, T^{-3/2} \exp - (59,380/T)\ , \left(\frac{cc}{mole\text{-}sec}\right) \tag{3.26.1}$$

$$K_{F_1}(M = O) = 2.1 \times 10^{18}\, T^{-1/2} \exp - (59,380/T)\ , \left(\frac{cc}{mole\text{-}sec}\right) \tag{3.26.2}$$

$$K_{F_1}(M = N_2, N, NO) = 1.2 \times 10^{21}\, T^{-3/2} \exp - (59,380/T)\ , \left(\frac{cc}{mole\text{-}sec}\right) \tag{3.26.3}$$

$$K_{F_2}(M = N_2) = 3.0 \times 10^{21}\, T^{-3/2} \exp - (113,260/T)\ , \left(\frac{cc}{mole\text{-}sec}\right) \tag{3.26.4}$$

$$K_{F_2}(M = N) = 1.5 \times 10^{22}\, T^{-3/2} \exp - (113,260/T)\ , \left(\frac{cc}{mole\text{-}sec}\right) \tag{3.26.5}$$

$$K_{F_2}(M = O_2, O, NO) = 9.9 \times 10^{20}\, T^{-3/2} \exp - (113,260/T)\ , \left(\frac{cc}{mole\text{-}sec}\right) \tag{3.26.6}$$

$$K_{F_3} = 5.2 \times 10^{21}\, T^{-3/2} \exp - (75,490/T)\ , \left(\frac{cc}{mole\text{-}sec}\right) \tag{3.26.7}$$

$$K_{F_4} = 1.0 \times 10^{12}\, T^{1/2} \exp - (3120/T)\ , \left(\frac{cc}{mole\text{-}sec}\right) \tag{3.26.8}$$

$$K_{F_5} = 5.0 \times 10^{13} \exp - (38,000/T)\ , \left(\frac{cc}{mole\text{-}sec}\right) \tag{3.26.9}$$

$$K_{F_6} = 9.1 \times 10^{24}\, T^{-5/2} \exp - (65,000/T)\ , \left(\frac{cc}{mole\text{-}sec}\right) \tag{3.26.10}$$

$$K_{F_7}(T \leq 3000\ K) = 7.22 \times 10^{19}\ T^{-1}\ ,\ \left(\frac{cc}{mole\text{-}sec}\right) \tag{3.26.11}$$

$$K_{F_7}(T > 3000\ K) = 3.98 > 10^{21}\ T^{-3/2}\ ,\ \left(\frac{cc}{mole\text{-}sec}\right) \tag{3.26.12}$$

$$K_{F_8} = 1.8 \times 10^{21}\ T^{-3/2}\ ,\ \left(\frac{cc}{mole\text{-}sec}\right) \tag{3.26.13}$$

$$K_{F_9}(M = N, O) = 6.0 \times 10^{24}\ T^{-5/2}\ ,\ \left(\frac{(cc)^2}{mole^2\text{-}sec}\right) \tag{3.26.14}$$

$$K_{F_9}(M = N_2) = 2.0 \times 10^{26}\ T^{-5/2}\ ,\ \left(\frac{(cc)^2}{mole^2\text{-}sec}\right) \tag{3.26.15}$$

$$K_{F_9}(M = O_2) = 9.0 \times 10^{26}\ T^{-5/2}\ ,\ \left(\frac{(cc)^2}{mole^2\text{-}sec}\right) \tag{3.26.16}$$

$$K_{F_9}(M = NO) = 1.0 \times 10^{28}\ T^{-5/2}\ ,\ \left(\frac{(cc)^2}{mole^2\text{-}sec}\right) \tag{3.26.17}$$

$$K_{F_{10}}(M = x_i) = K_{F_9}(M = x_i)\text{, for all } x_i \text{ components}\ ,\ \left(\frac{(cc)^2}{mole^2\text{-}sec}\right) \tag{3.26.18}$$

$$K_{F_{11}} = 2.7 \times 10^{13} \times T^{1/2} \times \exp - (168,800/T)\ ,\ \left(\frac{cc}{mole\text{-}sec}\right) \tag{3.26.19}$$

$$K_{F_{12}} = 1.63 \times 10^{13} \times T^{1/2} \times \exp - (157,800/T)\ ,\ \left(\frac{cc}{mole\text{-}sec}\right) \tag{3.26.20}$$

Variations in the concentration of ionic species produced by ionization rates K_{F_9} and $K_{F_{10}}$ are governed by the difference in concentration of the parent atom in the mixture, and the slight variations in the reverse reactions induced by small differences in the applicable equilibrium constants.

The set of coupled differential equations, governing the chemistry for species production, is written following the general method and notation developed by G. Emanuel (Ref. 54). Use has been made of species conservation to reduce the resulting set of coupled differential equations to 7, with 3 simultaneous algebraic equations completing the necessary array. This effectively reduces the number of differential equations in the integration array, hence the time necessary for computation.

In the nondimensional variable notation, introduced previously, the coupled rate equations have the following form:

$$\frac{d}{dx}\bar{n}(O_2) = \frac{d\bar{n}_1}{dx} = -\frac{\rho_\infty n_o}{\bar{V}(x)V_\infty}\left(\frac{L_1}{\theta_1} + \frac{L_4}{\theta_4} + \frac{L_6}{\theta_6}\right), (cm^{-1}) \qquad (3.27.1)$$

$$\frac{d}{dx}\bar{n}(N_2) = \frac{d\bar{n}_2}{dx} = -\frac{\rho_\infty n_o}{\bar{V}(x)V_\infty}\left(\frac{L_2}{\theta_2} + \frac{L_5}{\theta_5} + \frac{L_6}{\theta_6}\right), (cm^{-1}) \qquad (3.27.2)$$

$$\frac{d}{dx}\bar{n}(NO) = \frac{d\bar{n}_3}{dx} = -\frac{\rho_\infty n_o}{\bar{V}(x)V_\infty}\left(\frac{L_3}{\theta_3} + \frac{L_4}{\theta_4} + \frac{L_5}{\theta_5} + 2\frac{L_6}{\theta_6}\right), (cm^{-1}) \qquad (3.27.3)$$

$$\frac{d}{dx}\bar{n}(NO^+) = \frac{d\bar{n}_6}{dx} = -\frac{\rho_\infty n_o}{\bar{V}(x)V_\infty}\left(\frac{L_7}{\theta_7}\right), (cm^{-1}) \qquad (3.27.4)$$

$$\frac{d}{dx}\bar{n}(N_2^+) = \frac{d\bar{n}_7}{dx} = -\frac{\rho_\infty n_o}{\bar{V}(x)V_\infty}\left(\frac{L_8}{\theta_8}\right), (cm^{-1}) \qquad (3.27.5)$$

$$\frac{d}{dx}\bar{n}(O^+) = \frac{d\bar{n}_8}{dx} = \frac{\rho_\infty n_o}{\bar{V}(x)V_\infty}\left(\frac{L_{12}}{\theta_{12}} - \frac{L_9}{\theta_9}\right), (cm^{-1}) \qquad (3.27.6)$$

$$\frac{d}{dx}\bar{n}(N^+) = \frac{d\bar{n}_9}{dx} = \frac{\rho_\infty n_o}{\bar{V}(x)V_\infty}\left(\frac{L_{11}}{\theta_{11}} - \frac{L_{10}}{\theta_{10}}\right), (cm^{-1}) \qquad (3.27.7)$$

The three algebraic equations which complete the set of species production processes have the form:

$$\bar{n}(O) = \bar{n}_4 = 2\bar{n}_1\Big|_{x=0} - 2\bar{n}_1(x) - (8/15)\,\bar{n}_3(x) - (8/15)\,\bar{n}_6(x) - \bar{n}_8(x) \qquad (3.27.8)$$

$$\bar{n}(N) = \bar{n}_5 = 2\bar{n}_2\Big|_{x=0} - 2\bar{n}_2(x) - (7/15)\,\bar{n}_3(x) - (7/15)\,\bar{n}_6(x) - 2\bar{n}_7(x) - \bar{n}_9(x) \qquad (3.27.9)$$

$$\bar{n}(e^-) = \bar{n}_{10} = \sum_{i=6}^{9}\bar{n}_i(x). \qquad (3.27.10)$$

In these equations, the L_i/θ_i terms represent the component reactions contributing to each species production process. These are manipulated into a form incorporating the nondimensional variables and the weighted rate constants for consideration of

the effects of specific multiple third-body reaction partners. The explicit forms for the L_i/θ_i are:

$$L_1/\theta_1 = \bar{\rho}(x)\left[K_{F_1}\bar{n}_1(x)M_1(x) - \bar{\rho}(x)\frac{K_{F_1}}{K_{C_{1*}}}\bar{n}_4(x)^2 M_1(x)\right] \tag{3.28.1}$$

$$K_{C_{1*}} = K_{C_1}\cdot(\rho_\infty n_o)^{-1}$$

$$M_1(x) = \bar{n}_1(x) + \frac{7}{12}\cdot 10^{-3}\cdot T\cdot\bar{n}_4(x) + \frac{1}{3}\left[\bar{n}_2(x) + \bar{n}_3(x) + \bar{n}_5(x)\right]$$

$$L_2/\theta_2 = \bar{\rho}(x)\left[K_{F_2}\bar{n}_2(x)M_2(x) - \bar{\rho}(x)\frac{K_{F_2}}{K_{C_{2*}}}\bar{n}_5(x)^2 M_2(x)\right] \tag{3.28.2}$$

$$K_{C_{2*}} = K_{C_2}\cdot(\rho_\infty n_o)^{-1}$$

$$M_2(x) = \bar{n}_2(x) + 5\bar{n}_5(x) + 0.330\,[\bar{n}_1(x) + \bar{n}_3(x) + \bar{n}_4(x)]$$

$$L_3/\theta_3 = \bar{\rho}(x)\left[K_{F_1}\bar{n}_3(x)\bar{n}_{11}(x) - \bar{\rho}(x)\frac{K_{F_3}}{K_{C_{3*}}}\bar{n}_4(x)\bar{n}_5(x)\bar{n}_{11}(x)\right] \tag{3.28.3}$$

$$K_{C_{3*}} = K_{C_3}\cdot(\rho_\infty n_o)^{-1}$$

$$\bar{n}_{11}(x) = \sum_{i=1}^{5}\bar{n}_i(x)$$

$$L_4/\theta_4 = \bar{\rho}(x)\left[K_{F_4}\bar{n}_1(x)\bar{n}_5(x) - \frac{K_{F_4}}{K_{C_4}}\bar{n}_3(x)\bar{n}_4(x)\right] \tag{3.28.4}$$

$$L_5/\theta_5 = \bar{\rho}(x)\left[K_{F_5}\bar{n}_2(x)\bar{n}_4(x) - \frac{K_{F_5}}{K_{C_5}}\bar{n}_3(x)\bar{n}_5(x)\right] \tag{3.28.5}$$

$$L_6/\theta_6 = \bar{\rho}(x)\left[K_{F_6}\bar{n}_1(x)\bar{n}_2(x) - \frac{K_{F_6}}{K_{C_6}}\bar{n}_3(x)^2\right] \tag{3.28.6}$$

$$L_7/\theta_7 = \bar{\rho}(x)\left[K_{F_7}\bar{n}_6(x)\bar{n}_{10}(x) - \frac{K_{F_7}}{K_{C_7}}\bar{n}_4(x)\bar{n}_5(x)\right] \tag{3.28.7}$$

$$L_8/\theta_8 = \bar{\rho}(x)\left[K_{F_8}\bar{n}_7(x)\bar{n}_{10}(x) - \frac{K_{F_8}}{K_{C_8}}\bar{n}_5(x)^2\right] \tag{3.28.8}$$

$$L_9/\theta_9 = \bar{\rho}(x)\left[\bar{\rho}(x)K_{F_9}^{*}\bar{n}_8(x)\bar{n}_{10}(x)M_3(x) - \frac{K_{F_9}}{K_{C_9}}\bar{n}_4(x)M_3(x)\right] \tag{3.28.9}$$

$$K_{F_{9*}} = K_{F_9}(\rho_\infty n_o)$$

$$M_3(x) = \bar{n}_4(x) + \bar{n}_5(x) + 150.0\,\bar{n}_1(x) + \frac{100}{3}\bar{n}_2(x) + \frac{10^4}{6}\bar{n}_3(x)$$

$$L_{10}/\theta_{10} = \bar{\rho}(x)\left[\rho(x)K_{F_{10*}}n_9(x)n_{10}(x)M_3(x) - \frac{K_{F_{10}}}{K_{C_{10}}}n_5(x)M_3(x)\right] \tag{3.28.10}$$

$$K_{F_{10*}} = K_{F_{10}}(\rho_\infty n_o)$$

$$L_{11}/\theta_{11} = \bar{\rho}(x)\left[K_{F_{11}} \cdot \bar{n}_5(x) \cdot \bar{n}_{10}(x) - \bar{\rho}(x)\frac{K_{F_{11}}}{K_{C^*_{11}}}\bar{n}_9(x) \cdot \left[\bar{n}_{10}(x)\right]^2\right] \quad (3.28.11)$$

$$K_{C_{11^*}} = K_{C_{11}} \cdot (\rho_\infty n_o)^{-1}$$

$$L_{12}/\theta_{12} = \bar{\rho}(x)\left[K_{F_{12}} \cdot \bar{n}_4(x) \cdot \bar{n}_{10}(x) - \frac{K_{F_{12}}}{K_{C_{12^*}}}\bar{\rho}(x) \cdot \bar{n}_8(x) \cdot \left[\bar{n}_{10}(x)\right]^2\right] \quad (3.28.12)$$

$$K_{C_{12^*}} = K_{C_{12}} \cdot (\rho_\infty n_o)^{-1}$$

The component relations, L_i/θ_i, have dimensions of cc mole^{-1} sec^{-1}.

The computer code integrates the coupled chemical and flow processes in variable steps from the initial streamline point just after shock transition over the specified extent of the streamline. As indicated by the equations, the integration is over the intrinsic streamline distance, x, with the equilibrium and rate constants evaluated at each step, corresponding to their temperature dependence. Printout at each distance increment includes: temperature, velocity, pressure, enthalpy, density, compressibility, and species concentrations for the 10 species considered. The integration step size is automatically monitored, depending on the sensitivity of the solution to any of the species production processes. Care must be taken in specifying the values of $\bar{p}(x)$ or $\bar{V}(x)$ in the input statement. If discontinuities exist in the variable or its derivative, a double entry must be made reflecting values to either side of the discontinuity. The sequence of values taken by this variable, the initial "state" conditions previously discussed, and the free-stream conditions are specified as initial input for a calculation.

3.3 RADIATION PROPERTIES AND RADIATIVE TRANSFER

3.3.1 General

As pointed out in subsection 2.3, the rotational, vibrational, and translational degrees of freedom are assumed to be in equilibrium with each other at the shock front. As the flow progresses downstream, collisions between particles excite the electronic states and initiate dissociation, ionization, and other chemical processes. The kinetic temperature drops monotonically (in a uniform flow) from a high kinetic temperature at the shock front to the fully equilibrated temperature some distance downstream. Those states which excite rapidly are soon populated in a quasi-equilibrium manner at the local kinetic temperature (hence, they are overpopulated relative to the equilibrium temperature). If such states are active radiators, they emit radiation as though they are at the local kinetic temperature. This is the phenomenon which accounts for the so-called "overshoot" radiation. Conversely, those states which are slowly excited (especially the free electronic states which are populated by ionization) tend to be underpopulated and, hence, can be said to emit "undershoot" radiation.

For air, the overshoot radiation comes from overpopulated electronic states of the constituent molecules. The undershoot radiation comes from free-bound and free-free transitions. The general reaction governing these phenomena* is

$$\begin{array}{l} A_2 + M \rightleftharpoons A_2^* + M \\ \qquad\qquad\quad \big\downarrow\big\uparrow \\ \qquad\qquad\quad A_2 + h\nu \end{array} \tag{3.29}$$

where A_2 is a molecule (say) in its ground state, A_2^* is the same molecule in an excited state, M is a noninteracting (neutral or charged) particle and $h\nu$ designates

*There is some question as to the applicability of Eq. (3.29) to O_2 overshoot radiation. This matter is discussed in subsection 3.3.7.

the emission of radiation. Excitations by collisions, as given in the first part of Eq. (3.29), were considered in subsection 2.3. In that analysis the coupling with the radiative reactions was ignored. This is justified as there are a greater number of excitations and deexcitations by collisions than there are by radiation. In this section, techniques are developed for the prediction of the forward and reverse rates of the radiative reactions. Using these rates and the results of subsection 3.2, the radiative properties required to solve the transport equation are easily generated (it should be noted that equilibrium is a special case for Eq. (3.29); hence, equilibrium radiative properties will be a by-product of the analysis).

3.3.2 The Radiative Transitions

The radiative reactions for air which were considered to be important enough to evaluate are the following:

- Molecular Reactions

$$N_2^+(B^2\Sigma^+) \rightleftarrows N_2^+(X^2\Sigma^+) + h\nu \qquad \text{(First Negative)}$$

$$O_2(B^3\Sigma^-) \rightleftarrows O_2(X^3\Sigma^-) + h\nu \qquad \text{(Shumman-Runge)}$$

$$NO(A^2\Sigma^+) \rightleftarrows NO(X^2\Pi) + h\nu \qquad (\gamma \text{ Bands})$$

$$NO(B^2\Pi) \rightleftarrows NO(X^2\Pi) + h\nu \qquad (\beta \text{ Bands})$$

$$N_2(B^3\Pi) \rightleftarrows N_2(A^3\Sigma) + h\nu \qquad \text{(First Positive)}$$

$$N_2(C^3\Pi) \rightleftarrows N_2(B^3\Pi) + h\nu \qquad \text{(Second Positive)}$$

- Free-Bound Reactions

Nitrogen

$$e^- + N^+(2p^2\ ^3P) \rightleftarrows N(2p^3\ ^4S) + h\nu$$

$$\rightleftarrows N(2p^3\ ^2D) + h\nu$$

etc.

(through all the reactions involving the ^3P parent state)

$$e^- + N^+(2p^2\ ^1D) \rightleftarrows N(2p^3\ ^2D) + h\nu$$

$$\rightleftarrows N(2p^3\ ^2P) + h\nu$$

etc.

(through all the reactions involving the ^1D parent state)

$$e^- + N^+(2p^2\ ^1S) \rightleftarrows N(2p^3\ ^2P) + h\nu$$

$$e^- + N^+(2p^3\ ^5S) \rightleftarrows N(2p^4\ ^4P) + h\nu$$

$$e^- + N^+(2p^3\ ^3D) \rightleftarrows N(2p^4\ ^4P) + h\nu$$

$$e^- + N^+(2p^3\ ^3P) \rightleftarrows N(2p^4\ ^4P) + h\nu$$

Oxygen

$$e^- + O^+(2p^3\ ^4S) \rightleftarrows O(2p^4\ ^3P) + h\nu$$

$$\rightleftarrows O(3s\ ^5S) + h\nu$$

etc.

(through all the reactions involving the ^4S parent state)

$$e^- + O^+(2p^3\ ^2D) \rightleftarrows O(2p^4\ ^3P) + h\nu$$

$$\rightleftarrows O(3s\ ^3D) + h\nu$$

etc.

(through all the reactions involving the ^2D parent state)

$$e^- + O^+(2p^3\ ^2P) \rightleftarrows O(2p^4\ ^3P) + h\nu$$

$$\rightleftarrows O(2p^4\ ^1D) + h\nu$$

$$\rightleftarrows O(2p^4\ ^1S) + h\nu$$

In the above lists of reactions, excited states with principal quantum numbers up through $n = 5$ were considered. More highly excited states were discarded.

- Free-Free

$$e^- + N^+ \rightleftarrows e^- + N^+ + h\nu$$

$$e^- + O^+ \rightleftarrows e^- + O^+ + h\nu$$

3.3.3 The Rate Equations

It is well known that rate equations can be written which describe the forward and reverse reaction rates for chemical systems having the same form as those in the above list. The rate equations for the radiative reactions are the following:

- Molecular Reactions

$$\frac{d^2 n_{L,\nu}}{\delta\nu\, dt} = k_{m,f} n_{U,\nu} - k_{m,r} n_{L,\nu} \frac{4\pi I_\nu}{h\nu} \qquad (3.30)$$

- Free-Bound Reactions

$$\frac{d^2 n_{a,\nu}}{d\nu\, dt} = k_{fb,f} n_{a^+,\nu} n_{e^-} - k_{fb,r} n_{a,\nu} \frac{4\pi I_\nu}{h\nu} \tag{3.31}$$

- Free-Free Reactions

$$\frac{d^2 n_{e^-}}{d\nu\, dt} = k_{ff,f} n_{a^+,\nu} n_{e^-} - k_{ff,r} n_{a,\nu} n_{e^-} \frac{4\pi I_\nu}{h\nu} \tag{3.32}$$

where the k's are the forward (subscript f) or reverse (subscript r) rate coefficients for the molecular (subscript m), free-bound (subscript fb) and free-free (subscript ff) reactions. The n's are number densities for upper (subscript U) or lower (subscript L) states which interact to emit radiation between the frequencies ν and $\nu + \delta\nu$ for molecular reactions or $\nu + d\nu$ for free-bound or free-free reactions. The other symbols have their usual meanings.

3.3.4 The Rate Coefficients

It is possible to express the rate coefficients in terms of fundamental quantities. The work by Hansen (Ref. 32) is applicable to the molecular rate coefficients. His results may be put in the following form:

- Molecular

$$k_{m,f} = \frac{8\pi\nu^2}{c^2} \frac{g_L}{g_U} \frac{\pi e^2}{m_e c} f_{LU} q' \tag{3.33}$$

$$k_{m,r} = \frac{\pi e^2}{m_e c} f_{LU}\, q \left(1 - \frac{g_L q'}{g_U q} \frac{n_U}{n_r}\right) \tag{3.34}$$

where

$$q \equiv \frac{1}{\delta\nu} \sum_{V''} \sum_{V'} \frac{n_{LV''}}{n_L} q_{L-U,\, V''-V'} \tag{3.35}$$

and

$$q' \equiv \frac{1}{\delta\nu} \sum_{V''} \sum_{V'} \frac{n_{UV'}}{n_U} q_{L-U,\, V''-V'} \tag{3.36}$$

and

$$n_U \equiv \sum_{V'} n_{UV'} \tag{3.37}$$

and

$$n_L = \sum_{V''} n_{LV''} \tag{3.38}$$

The quantity f_{LV} is the electronic oscillator strength (the values used and their sources are presented in Table 13, the quantities $q_{L-U,\, V''-V'}$ are Franck-Condon Factors taken from Ref. 42, and g_L and g_U are the statistical weights of the lower and upper states, respectively.

- Free-Bound Reactions

A formula is given in Ref. 55 which easily can be converted to yield the forward rate coefficient. The result is

$$k^{k-j}_{fb,\,f} = v\, \alpha^{k-j}_{fb}\, f(v) \frac{dv}{d\nu} \tag{3.39}$$

Table 13

OSCILLATOR STRENGTHS

Species	Transition	f_{LV}	Source (Ref. No.)
NO:	$B^2\Pi \rightarrow X^2\Pi$	0.008	42
	$A^2\Sigma \rightarrow X^2\Pi$	0.0025	42
N_2^+:	$B^2\Sigma \rightarrow X^2\Sigma$	0.0348	42
O_2:	$B^2\Sigma \rightarrow X^3\Sigma$	0.163	29
N_2:	$B^3\Pi \rightarrow A^3\Sigma$	0.02	35
	$C^3\Pi \rightarrow B^3\Pi$	0.07	35

The reverse rate constant which is consistent with Eqs. 3 and 11 is

$$k_{fb,r}^{j-k} = \sigma_{fb}^{j-k}\left(1 - \frac{\sigma_{fb,I}^{k-j}}{\sigma_{fb}^{j-k}} \frac{n_{a^+}^{k} n_{e^-}}{n_a^j} f(v)\right) \tag{3.40}$$

where α_{fb}^{k-j} is the radiative recombination cross section, σ_{fb}^{j-k} is the bound-free cross section for induced absorption, $\sigma_{fb,I}^{k-j}$ is the bound-free cross section for induced emission, v is the velocity of the interacting electron, $f(v)\,dv$ represents the fraction of electrons with velocities between v and $v + dv$, and the superscripts k and j represent ionic and atomic levels, respectively, and, when used in combination, designate a transition between the two.

It is consistent with the assumptions of the streamtube method given in subsection 2.3. to assume that the electron velocity distribution is in equilibrium at the local kinetic temperature. Hence, Maxwell's velocity distribution can be used.

$$f(v) = 4\pi\left(\frac{m_e}{2\pi k T_i}\right)^{3/2} v^2 \exp\left(-\frac{m_e v^2}{2k T_i}\right) \tag{3.41}$$

The relationship between frequency and electron velocity is (see Ref. 55)

$$\frac{m_e v^2}{2} = h\nu - \xi^{j-k} \tag{3.42}$$

where ξ^{k-j} is the binding energy of the electron.

If one combines Eqs. (3.31, 3.39, 3.40, 3.41, and 3.42) and applies the technique of detailed balancing, the relationships between the cross sections can be obtained in terms of fundamental quantities. The results are the following:

$$\alpha_{fb}^{k-j} = \sigma_{fb}^{j-k} \frac{\nu^2 h^2 g^j}{m_e^2 c^2 v^2 g^k} \tag{3.43}$$

and

$$\sigma_{fb}^{j-k} = \sigma_{fb,I}^{k-j} \frac{g^k}{g^j} \frac{8\pi m_e^3 v^2}{h^3} \tag{3.44}$$

Hence, if one cross section can be determined, Eqs. (3.43) and (3.44) will yield the other two. It is known that a modified form of Kramer's formula gives a good approximation to the cross section for induced absorption for a hydrogen-like atom. The resulting formula is (see Ref. 56).

$$\sigma_{fb}^{j-k} = \frac{2^6 \pi^4 m_e e^{10}}{3\sqrt{3}\, c\, h^6} \left(\frac{\xi^{j-k} F^{j-k}}{Ry} \right)^2 \frac{G_{bf}^{j-k}}{n^j \nu^3} \quad \text{for} \quad h\nu \geq \xi^{j-k} \tag{3.45a}$$

$$\sigma_{fb}^{j-k} = 0 \quad \text{for} \quad h\nu < \xi^{j-k} \tag{3.45b}$$

where Ry is the Rydberg constant, G_{bf}^{j-k} is the Gaunt factor (which for this investigation was obtained from curve fits to the data published in Ref. 40) and F^{j-k} (not included in the formula given in Ref. 40) was introduced to account for the effects of fractional parentages. The fractional parentages used in this investigation were obtained from Ref. 57 for the strongest transitions. They are presented in Table 14.

Table 14

FRACTIONAL PARENTAGE COEFFICIENTS $(F^{j-k})^2$

NITROGEN

Atomic State	Ionic State					
	$2p^2\ ^3P$	$2p^2\ ^1D$	$2p^2\ ^1S$	$2p^3\ ^5S$	$2p^3\ ^3D$	$2p^3\ ^3P$
$2p^3\ ^4S$	3	0	0	0	0	0
$2p^3\ ^2D$	3/2	3/2	0	0	0	0
$2p^3\ ^2P^o$	3/2	5/6	2/3	0	0	0
$2p^4\ ^4P$	0	0	0	5/4	5/3	1

OXYGEN

Atomic State	Ionic State		
	$2p^3\ ^4S^o$	$2p^3\ ^2D^o$	$2p^3\ ^2P^o$
$2p^4\ ^3P$	4/3	5/3	1
$2p^4\ ^3P$	0	3	1
$2p^4\ ^1D$	0	0	4

Equations 3.39 through 3.45 can be combined to yield the rate coefficients for transtions between the k^{th} and j^{th} levels of the ion and atom, respectively. It is often more convenient to work in terms of total rate coefficients $\left(k_{fb,f}^T \text{ and } k_{fb,r}^T\right)$

which account for all the contributing transitions at a given frequency. These are given by the following equations

$$k^{T}_{fb,f} = \sum_{j}\sum_{k} \frac{n^{k}_{a+}}{n_{a+}} \, k^{k-j}_{fb,f} \tag{3.46}$$

and

$$k^{T}_{fb,r} = \sum_{j}\sum_{k} \frac{n^{j}_{a}}{n_{a}} \, k^{j-k}_{fb,r} \tag{3.47}$$

where

$$n_{a+} = \sum_{k} n^{k}_{a+} \tag{3.48}$$

and

$$n_{a} = \sum_{j} n^{j}_{a} \tag{3.49}$$

- Free-Free

The forward and reverse rate coefficients can be obtained from formulas for hydrogen-like atoms given in Ref. 58. They are the following:

$$k_{ff,f} = \frac{32(4\pi)\pi^{2} Z^{2} e^{6}}{3\sqrt{3}\, hc(2\pi m_{e})^{3/2}(kT_{i})^{1/2}} \exp\left(-\frac{h\nu}{kT_{i}}\right) \tag{3.50}$$

and

$$k_{ff,\,f} = \frac{2^4 \pi^2 Z^2 e^6 g_{ff} \nu^{-3}}{3\sqrt{3}\, hc(2\pi m_e)^{3/2}(kT_i)^{1/2}} \left[1 - \exp\left(-\frac{h\nu}{kT_i}\right)\right] \tag{3.51}$$

where Z is the effective charge (taken to be 1) and g_{ff} is the free-free Gaunt factor (taken to be 1). It should be noted that the forward and reverse rate coefficients are functions of the kinetic temperature. This is a direct result of the assumption that the electron velocity is Maxwellian.

3.3.5 The Radiative Parameters

The parameters required to solve Eq. (2.8) are obtained from a linear sum of the constituent contributions

$$j_\nu = j_m + j_{fb} + j_{ff} + \ldots . \tag{3.52}$$

$$\mu'_\nu = \mu'_m + \mu'_{fb} + \mu'_{ff} + \ldots . \tag{3.53}$$

where other classes of reactions are sometimes important; e.g., atomic lines. The constituent contributions are related to the rate coefficients through the following equations:

$$j_m = \frac{n_u k_{m,f} h\nu}{4\pi} \tag{3.54}$$

$$\mu'_m = n_L k_{m,r} \tag{3.55}$$

$$j_{fb} = \frac{n_{a^+} n_{e^-} k_{fb,f} h\nu}{4\pi} \tag{3.56}$$

$$\mu'_{fb} = n_a k^T_{fb,r} \tag{3.57}$$

$$j_{ff} = \frac{n_{a^+} n_{e^-} k_{ff,f} h\nu}{4\pi} \tag{3.58}$$

$$\mu'_{ff} = n_{e^-} n_{a^+} k_{ff,r} \tag{3.59}$$

where the number densities refer to the sum of all the substates in the electronic state indicated by the subscript. The rate coefficients are all known from the preceding development; consequently, if the number densities of the states can be obtained, the required calculation can be made.

3.3.6 Equilibrium Populations

There are several rather complete sources of the populations of the electronic levels of equilibrium air (Refs. 43, 53, and 59). The data from Ref. 43 were selected as the accuracy seems quite adequate and a large number of temperatures are considered ($10,000° K \leq T \leq 24,000° K$, $\Delta T = 1000$). For the molecular species, the populations of the vibrational levels are required. A computer code was prepared to make this calculation based on Boltzmann's Law and two models of the vibrational energy levels. The first model selected was the anharmonic oscillator model with the required constants being obtained from Herzberg (Ref. 52). Populations were calculated for either 26 vibrational levels per electronic level or for whatever number of vibrational levels there were which had energies less than the dissociation energy of their particular electronic level. The second model selected was the Morse model with the required constants again being obtained from Herzberg (Ref. 52). With this model the populations were calculated for 26 vibrational levels for all the electronic levels. The two models were used since it was desired to use this code for the nonequilibrium case also, and it was feared that the (usual) anharmonic oscillator model would be significantly in error at the very high temperatures encountered just behind the shock wave. It was found, however, that the

emissivities predicted by both models were in substantial agreement. The data presented are based on the anharmonic oscillator model.

3.3.7 Nonequilibrium Populations

It is required that the specie populations from subsection 2.3 be divided into the populations of their constituent electronic states. From an examination of the activation energies listed in Table 15, one would expect the population of the electronic levels to proceed about as slowly as such familiar processes as dissociation and ionization; consequently, they must be treated carefully. If the excitation mechanisms and the rate coefficients were known, the populations could be calculated in a manner similar to that used in the streamtube calculation. Unfortunately, even the excitation mechanisms have not been established and any techniques presently available require rather serious assumptions.

Table 15

ELECTRONIC EXCITATION REACTIONS

Reaction	Activation Energy (eV)
$N_2^+ + M \rightleftarrows N_2 (B^2\Sigma^+) + M$	3.15
$O_2 + M \rightleftarrows O_2 (B^3\Sigma^-) + M$	6.05
$NO + M \rightleftarrows NO (B^2\Pi) + M$	5.69
$NO + M \rightleftarrows NO (A^2\Sigma) + M$	5.75
$N_2 + M \rightleftarrows N_2 (B^3\Pi) + M$	7.4
$N_2 + M \rightleftarrows N_2 (C^3\Pi) + M$	11.0
$O + M \rightleftarrows O (^3S) + M$	1.96, 4.18, ... 13.6
$N + M \rightleftarrows N (^2P) + M$	2.36, 3.57, ... 14.54

Insight into the excitation mechanism of O_2 is particularly limited. It has been suggested by Hemmerling and Teare (Ref. 60) that the population rate of the $B^3\Sigma^-$ level of O_2 (the upper level in the Shumman-Runge transition) is determined by competition between the reactions

$$O_2 + M \rightleftarrows O_2(B^3\Sigma) + M \tag{3.60}$$

$$O_2(B^3\Sigma) + M \rightleftarrows 2O(^3P) + M \tag{3.61}$$

and

$$O_2(B^3\Sigma) + M \rightleftarrows O_2 + M + h\nu \tag{3.62}$$

They performed a series of experiments at relatively low Mach number flows (equilibrium temperatures were less than about 5000°K) and observed that oxygen emission did not overshoot its equilibrium value. They concluded that the forward reaction rates for Eq. (3.61) are fast enough to keep the $O_2(B^3\Sigma)$ level depleted and severely limit emission. This result is to be contrasted with the calculations of Hansen and Chapin (Ref. 61) where they found that O_2 emission dominated the overshoot region. Little is known about the rate coefficients associated with Eq. (3.61); consequently, its effect cannot be accurately ascertained. The approach taken in the present study was to estimate upper and lower bounds by assuming that Eq. (3.61) is fast compared to Eq. (3.60) in which case the emission was taken as the equilibrium value (lower bound estimate) and to assume that Eq. (3.61) is slow compared to Eq. (3.60), in which case the O_2 excitation rate was calculated in the same manner as the remaining reaction rates given in Table 15, as discussed below.

For the N_2^+, NO, N_2 bands and for the estimate to the upper bound on O_2, it was assumed that the upper levels are populated by transitions from the ground level. This being the case, it is reasonable to make a rough estimate of the time, τ_e, required for the

electronic levels to come to equilibrium with each other, by logarithmic interpolation (based on activation energies) of the species concentration profiles for similar reactions. The electronic levels of the atomic species were handled in the same fashion with the $3s\ ^2P$ level of N (activation energy of 10.6 ev) and the $3s\ ^3S$ level of O (activation energy of 9.5 ev) being taken as typical for the entire configuration.

The species concentration profiles selected were those of O_2 and N_2. Consequently, this technique was roughly equilvalent to using a rate coefficient

$$k_f \sim \frac{3 \times 10^{21}}{6.02 \times 10^{23}} T^{-3/2} \exp(-E/kT)$$

which requires that the collision efficiency in dissocation be about the same as that for the excitation of the electronic levels.

For times equal to or greater than τ_e, the required populations were obtained from an equilibrium calculation based on the local kinetic temperature. For times earlier than τ_e, the populations were estimated by fairing a linear, monotonic electronic temperature curve between the boundary condition value at the shock and the kinetic temperature calculated at τ_e. The populations were calculated from an equilibrium calculation at the local electronic temperature by the following equation

$$\frac{n_U}{n_L} = \frac{g_U}{g_L} \frac{Q_U(T_i)}{Q_L(T_i)} e^{-\frac{E}{k\theta}}$$

where E is the energy difference between the upper and lower electronic levels and $Q_U(T_i)$ and $Q_L(T_i)$ are the partition functions of the upper and lower levels, respectively, and are based on the local kinetic temperature.

Hansen and Chapin (Ref. 61) and Wray and Teare (Ref. 62) have very recently published articles in which they attempt to determine the rate coefficients for the electronic levels. Both assume that the primary excitation process is one of two body collisions between molecules, and both measure rate coefficients over a limited range of temperatures and attempt to develop equations for scaling to arbitrary conditions. A general forward-rate coefficient applicable to any molecule was developed in Ref. 61 . It is

$$k_f = 10^{-4}\left(\frac{T}{10^4}\right)^5\left(\frac{8kT}{\pi\mu}\right)^{1/2} S\,\frac{g^*}{g^o + g^*}\exp(-E/kT) \qquad (3.63)$$

where μ is the reduced molecular mass, S is the cross section (assumed to be 10^{-15}) g^* is the statistical weight of the upper electronic level, g^o is the statistical weight of the lower electronic level, E is the activation energy and the other symbols have their usual meanings. The authors of Ref. 62 confined themselves to the rate coefficients for the levels of the first positive system of nitrogen. The resulting forward rate coefficient was found to be

$$k_f \sim 2.2\times 10^{-17}\,T^{1/2}(E/kT)^2\exp(-E/kT)\,\frac{cm^3}{\text{particle sec}} \qquad (3.64)$$

$$E = 6.17 \text{ ev}$$

For comparitive purposes we have evaluated Eqs. (3.63) and (3.64) for the first positive system of nitrogen for the conditions just behind the shock for Case III (T_i = 45,210° K). The results are

$$(k_f)_{\text{Eq. (28)}} \sim 1.51\times 10^{-11} \qquad (3.65)$$

and

$$(k_f)_{\text{Eq. (29)}} \sim 2.41\times 10^{-15} \qquad (3.66)$$

Using the interpolation procedure described in the preceding paragraph, the forward rate coefficient was found to be

$$k_f \sim 1 \times 10^{-10} \tag{3.67}$$

The comparison between the three values above gives a fairly accurate indication of the state-of-the-art.

3.3.8 Radiative Heating Program

This section describes the machine program which was used to calculate the radiative heat transfer from the shock layer to the body surface for Case I. The program, developed at LMSC, performs an exact numerical integration to obtain the heat transfer in the transparent limit (i.e., assuming negligible self-absorption) to any point on the surface of an arbitrary, convex body in an axisymmetric hypersonic flow.

From the definition of the specific intensity I_ν, the radiative heat transfer q_R to the surface is given by

$$dq_R = I_\nu \cos\theta \, d\nu \, d\omega \tag{3.68}$$

where ω is the solid angle, ν is the frequency, and θ is the angle between the direction of I_ν and the inward normal to the surface. Let s be the distance from a given point on the surface to a point in the shock layer, measured along a specified ray. If $\bar{s}$ denotes the distance to the shock wave, then $I_\nu(\bar{s}) = 0$, since we assume that no energy is radiated from the gas outside the shock layer. Integrating the transport equation (2.8), we obtain for I_ν at the surface, the expression

$$I_\nu = \int_0^{\bar{s}} j_\nu \, e^{-\int_0^s \mu'_\nu \, ds'} \, ds \tag{3.69}$$

Substituting into Eq. (3.68), and integrating over all frequencies and all solid angles that the surface point can "see," we obtain

$$q_R = \int_\omega \int_\nu \int_o^{\bar{s}} j_\nu \, e^{-\int_o^s \mu'_\nu \, ds'} \cos\theta \, ds \, d\nu \, d\omega \tag{3.70}$$

Under the transparent (thin gas) approximation

$$\int_o^s \mu'_\nu \, ds' << 1 \tag{3.71}$$

for all ν and for all points in the shock layer which make an important contribution to q_R. Introducing the integrated emission coefficient

$$j = \int_o^\infty j_\nu \, d_\nu \tag{3.72}$$

and the transformation

$$ds \, d\omega = dV/s^2 \tag{3.73}$$

where dV is an element of volume at a distance s from the surface point, we obtain the following expression which is convenient for numerical calculation:

$$q_R = \int_V \frac{j \cos\theta}{s^2} \, dV \tag{3.74}$$

For surface points on the front of the body, the contributing volume elements are contained within the three-dimensional "cap" bounded by the shock surface and the plane tangent to the body at the surface point under consideration. For surface points on the back of a finite body, the volume of integration is theoretically infinite. In practice, the integration is then terminated at an arbitrary plane downstream of the body beyond which the radiation has negligible influence on q_R.

The numerical calculation is carried out using a rectangular grid in the $\varphi = 0$ plane of the shock-oriented cylindrical (x, r, φ) coordinate system described in subsection 3.1.1. The integral is evaluated by summing the contribution of each elemental torus of rectangular cross section (with sides $\Delta x, \Delta r$), radius r, for which j is constant due to the axial symmetry of the flow. Introducing the quantity

$$E = 2\pi j \; ; E_o = E \text{ at the stagnation point,} \tag{3.75}$$

we can write Eq. (3.74) as

$$\frac{q_R}{E} = \frac{1}{2\pi E_o} \int E \cos\theta \frac{dV}{s^2}$$

$$= \frac{1}{2\pi E_o} \sum_{V_i} w \cdot E \cdot \Delta I \tag{3.76}$$

where $\Delta I = \int \cos\theta \, dV/s^2$ for the portion of the elemental torus which is "seen" by the surface point, where s is the distance to the center of the rectangular cell. (For the cell adjoining the surface point, the formula for s is modified to properly account for the singular behavior there.)

and w = weight factor determining the fraction of rectangular cell in the flow field. Thus, $w = 1$ for all cells except those at the shock wave or tangent plane, for which $w \leq 1$.

The computation of ΔI involves the integration with respect to φ around a given elemental torus, the limits of integration being the tangent plane intersection with the torus. This integration is complicated, but is easily reduced to elliptic integrals. The latter can then be expanded to give an algebraic expression for ΔI for each elemental torus. The weight factor w is automatically computed by the machine for the prescribed shock shape and tangent plane.

The input for the program involves the specification of the shock shape (either analytically, or through a table), the surface point coordinates, and the slope of the plane tangent to the body at the surface point. In addition, the emission coefficient j must be specified for each cell. If the radiation can be considered to be in local thermodynamic equilibrium, then j can be expressed as

$$j = \sigma \mu_P T^4 / \pi \tag{3.77}$$

where σ is the Stefan-Boltzmann constant, and μ_P is the Planck mean absorption coefficient. For a given gas, μ_P and T are, in principle, known functions of any two independent thermodynamic variables. For air, μ_P and T can be calculated from an LMSC curve-fitting program as functions of the pressure p and enthalpy h. This program is based on the curve fits of Refs. 33 and 34 for various emissivity data. Since the distribution of j(or p and h) throughout the shock layer is, in general, the result of extensive numerical calculation, a simple analytic expression is not available. The distribution is therefore expressed as third-order double-polynomial expansions in x and r, using different expansions in different sections of the flow, to account for large gradients in flow variables. Since a finite body is followed by a base flow region of essentially constant properties, the radiation program has provisions for the specification of a separating streamline (approximated by a straight line) below which j (or p and h) assumes a constant value.

Since the flow for Case I was determined to be in local thermodynamic equilibrium, the pressure and enthalpy distributions, as determined by the flow-field calculations (see subsection 2.2), were converted into double-polynomial expansions using the two-dimensional curve-fit program of Ref. 20. (This is the same program used to extend the Mollier curve fit of equilibrium air, as discussed in subsection 2.2.4).

The constant values of p and h in the base flow region were set equal to their respective values on the separating streamline. The radiative heating was calculated for a sufficient number of points on the body surface to define the heating distribution over the entire body, including the back portion. Calculations were performed for both the LMSC upper- and lower-bound emissivity data for μ_P. Since the upper-bound correlation in the curve fit for μ_P is not valid for the lower temperature ranges found downstream of the corner region, results from the use of upper-bound emissivity are presented only over the front face of the vehicle. For the calculation of total heating distribution, an absorptivity of 0.5 was assumed for the surface.

Due to the poor knowledge of the flow field for Case II, (angle-of-attack), it was decided not to attempt an exact three-dimensional radiative heating program. Instead, the Case I radiative heating distributions were utilized. Over the front face, the distribution was assumed rotated by 5 deg, consistent with the rotation of the inviscid flow by that amount and in view of the fact that the shock-wave radius of curvature does not vary much in this region. In the rounded corner region, the original Case I distribution was assumed unchanged.

For Case III, it was originally intended to calculate j directly from the results of the streamtube chemistry and radiative properties programs. Unfortunately, the large gradients in j near the shock made the use of the polynomial expansions for spatial distribution of the emission coefficient impractical. Since results were needed primarily over the front face only, it was decided not to use the exact radiative heating program discussed above. Instead, the plane parallel slab approximation was used. Further details on the radiative-heating program may be found in Appendix A.8.

Section 4
REFERENCES

1. Project FIRE Work Statement (L-2649) (To be Enclosed with Final Report).
2. M. D. Van Dyke, "Supersonic Blunt Body Problem – Review and Extension," J. Aeronaut, Sci., Vol. 25, 1958, p. 8
3. M. D. Van Dyke and H. D. Gordon, Supersonic Flow Past a Family of Blunt Axi-Symmetric Bodies, NASA TR R-1, 1959
4. R. J. Swigart, "A Theory of Asymmetric Blunt Body Flows," AIAA Jour., Vol. 1, No. 5, 1963, pp. 1034–1042
5. R. J. Swigart, "Real Gas Hypersonic Blunt Body Flows," AIAA Jour., Vol. 1, No. 11, 1963, pp. 2642–2644
6. R. J. Swigart, "Hypersonic Blunt Body Flow Fields at Angle-of-Attack," AIAA Jour., Vol. 2, No. 1, 1964, p. 115
7. J. M. Kendall, Experiments in Supersonic Blunt Body Flows, Jet Propulsion Laboratory Rept. 20-372, Feb 1959
8. J. C. Boison and H. A. Curtiss, "An Experimental Investigation of Blunt Body Stagnation Point Velocity Gradient," J. ARS, Vol. 29, No. 2, 1959, p. 130
9. L. Lees, "Recent Developments in Hypersonic Flow," Jet. Prop. Vol. 27, 1957, p. 11
10. W. E. Moeckel and K. C. Weston, Composition & Thermodynamic Properties of Air in Chemical Equilibrium, NASA TN 4265, 1958
11. J. Hilsenrath and C. W. Beckett, Tables of Thermodynamic Properties of Argon-Free Air to 15,000° K, AEDC Report TN 56-12, 1956
12. M. J. Lighthill, "Dynamics of a Dissociating Gas, Part I, Equilibrium Flow," J. Fluid. Mech., Vol. 2, 1957, p. 1

13. M. Vinokur, Inviscid Hypersonic Flow Around Blunt Bodies, Lockheed Missiles & Space Company Report, LMSD 48454, Mar 1959

14. M. Vinokur, "Hypersonic Flow Around Bodies of Revolution Which are Generated by Conic Sections," Paper delivered at 6th Midwestern Conf. on Fluid Mech., U. of Texas, Austin, Texas, 9–11 Sep 1959

15. M. Vinokur, "Analytic Solution for Supersonic Flow Around Spheres," Paper Delivered at APS, Fluid Mech. Div. Meeting, U. of Calif., Berkeley, Calif., 20–22 Nov, 1961

16. M. Vinokur, "An Analytic Approach to the Supersonic Blunt Body Problem," (to be published)

17. R. Capiaux and L. Karchmar, "Flow Past Slender Blunt Bodies – A Review and Extension," IAS/ARS, Preprint 61-210-1904, Jun 1961

18. A. Wood, Machine Programming for Method of Characteristics Computations, AVCO Corp. (RAD), Tech. Rel. 58-47, 1958

19. J. E. Moriello, et al., Polynomial Approximations to the Gas Properties of Equilibrium Air, AVCO Corp. (RAD) Tech. Memo. 2-TM-58-122, 1959

20. R. H. Moore and R. K. Zeigler, The Solution of the General Least Squares Problem With Special Reference to High-Speed Computers, Los Alamos Scientific Laboratory, LA-2367, Mar 1960

21. M. Denison and E. Baum, "Compressible Free Shear Layer With Finite Initial Thickness," AIAA Jour., Vol. 1, No. 2, 1963, pp. 342–349

22. D. Chapman, A Theoretical Analysis of Heat Transfer in Regions of Separated Flow, NACA TN-3792, Oct 1956

23. C. I. Wang, J. B. Peterson, and R. Anderson, Gas Flow Tables, Space Technology Laboratories, GM-TR-154, Mar 1957

24. J. G. Hall, A. Q. Eschenroeder, and P. V. Marrone, "Inviscid Hypersonic Air Flows With Coupled Non-Equilibrium Processes," Jour. Aerospace Sci., Vol. 29, 1962, p. 1038

25. P. V. Marrone, Normal Shock Waves in Air: Equilibrium Composition and Flow Parameters for Velocities from 26,000 to 50,000 ft/sec, Cornell Aero. Lab. Rept. AG-1729-A-2, Aug 1962

26. M. H. Bortner, Chemical Kinetics in a Re-entry Flow Field, G. E. Research Rept. R63SD63, Aug 1963

27. R. E. Meyerott, J. Sokoloff, and R. W. Nicholls, Absorption Coefficients of Air, Geophysical Research Paper 58, GRD-TN-60-277, Jul 1960

28. B. Kivel and K. Bailey, Tables of Radiation from High Temperature Air , AVCO Research Report 21, Dec 1957

29. M. C. Nardone, R. G. Breene, S. S. Zelden, and T. R. Riethof, Radiance of Species in High Temperature Air, GE-MSD Document R63SD23, Jun 1963

30. R. A. Allen, P. H. Rose and J. C. Camm, Nonequilibrium and Equilibrium Radiation at Super-Satellite Re-Entry Velocities, AVCO Research Report 156, Sep 1962

31. B. H. Wick, Radiative Heating of Vehicles Entering the Earth's Atmosphere, a paper presented to the Fluid Mechanics Panel of Advisory Group for Aeronautical Research and Development, Brussels, Belgium, 3-6 Apr, 1962

32. C. F. Hansen, Radiation from Non-Equilibrium, Molecular Gases, Report No. TR 62-209A, Santa Barbara, Calif., G. M. Defence Research Labs, Dec 1962

33. K. H. Wilson and H. Hoshizaki, "Inviscid, Nonadiabatic Flow About Blunt Bodies," J. AIAA , Vol. 3, No. 1, 1965, pp. 67-74

34. John R. Viegas and John T. Howe, "Thermodynamic and Transport Property Correlation Formulas for Equilibrium Air From 1000° K to 15,000° K," NASA TN-D-1429, Ames Research Center, Moffett Field,Calif., Oct 1962

35. B. H. Armstrong, S. Brush, H. DeWitt, R. R. Johnston, P. S. Kelley, and O. R. Platas, Opacity of High-Temperature Air, Air Force Weapons Laboratory, Final Report under Contract AF 29(601)-5006, (to be issued)

36. B. H. Armstrong, Private Communication

37. A. Burgess and M. J. Seaton, "A General Formula for Calculation of Atomic Photo-ionization Cross Sections," Monthly Notices of the Royal Astronomical Society, Vol. 120, 1960, p. 121

38. A. Dalgarno, R. Henry, and A. L. Stewart, Queen's Univ. of Belfast and Geophysics Corp. of America, to be published

39. J. C. Stewart and K. O. Pyatt Jr., Theoretical Study of Optical Properties, Air Force Special Weapons Center, Final Report AFSWC-TR-61-71, Sep 1961

40. W. J. Karzas and R. Latter, Astrophics J. Suppl. No. 55, May 1961

41. R. S. Mulliken, "Intensities of Electronic Transitions in Molecular Spectra," J. Chem. Phys, Vol. 7, 1939, p. 14-34

42. D. R. Churchill, S. A. Hagstrom, and R. K. M. Landshoff, The Calculation of Spectral Absorption in Heated Air, LMSC Report No. 3-27-63-4, Dec 1963

43. B. H. Armstrong and M. Scheibe, Equilibrium Occupation Numbers and Species Concentrations for Air, Nitrogen, and Oxygen to 24,000° K, LMSC Report No. 6-74-64-33, Jun 1964

44. H. Hoshizaki, "Heat Transfer in Planetary Atmospheres at Super-Satellite Speeds," ARS Preprint 2173-61, Oct 1961

45. M. C. Adams, "A Look at the Heat Transfer Problem at Super Satellite Speeds," ARS Preprint 1556-60, 1960

46. H. Hoshizaki, "The Viscous Blunt Body Problem," Proc. of Symposium on Aerothermo-Elasticity," ASD TR 61-645, Oct 1961

47. M. D. Van Dyke, Higher Approximations in Boundary Layer Theory, Lockheed M&S Co. Report. LMSC 703097, Oct 1960

48. A. Ferri, et al., Blunt Body Heat Transfer at Hypersonic Speeds and Low Reynolds Number, Poly. Inst. of Brooklyn Rept. ARL TN 60-140, June 1960

49. L. Lees, "Laminar Heat Transfer Over Blunt-Nosed Bodies at Hypersonic Flight Species," JET Prop., Vol. 26, 1956, p. 4

50. N. B. Cohen, Boundary Layer Similar Solutions and Correlation Equations for Laminar Heat Transfer Distributions in Equilibrium Air at Velocities Up to 41,000 feet per second, NASA TR R-118, 1961

51. T. C. Peng and A. L. Pindroh, An Improved Calculation of Gas Properties at High Temperatures: Air, Boeing Co., Aerospace Div., TR D2-11722, 1962

52. G. Herzberg, Molecular Spectra and Molecular Structure, I. Spectra of Diatomic Molecules, 2nd ed., New Jersey, D. Von Nostrand, 1950

53. F. R. Gilmore, Energy Levels, Partition Functions, and Fractional Electronic Populations for Nitrogen and Oxygen Atoms and Ions to 25,000°K, Rand Corp., RM 3748-PR, 1963

54. G. Emanuel, Problems Underlying the Numerical Integration of the Chemical and Vibrational Rate Equations in Non-Equilibrium Flow, AEDC TDR 63-82, 1963

55. L. H. Aller, The Atmospheres of the Sun and Stars, New York, The Ronald Press Co., 1953

56. A. N. Cox, "Stellar Absorption Coefficients and Opacities," Chapter 2 in G. Kuiper (ed.), Stars and Stellar Systems, Vol. 8, to be published

57. D. H. Menzel and L. Goldberg, "Multiplet Strengths for Transitions Involving Equivalent Electrons," The Astrophysical Journal, Vol. 84, No. 1, 1936, p. 1

58. C. St. Pierre, Review of Fundamentals on Gas Emissivity, CARDE Tech. Memo AB-33, Mar 1959

59. F. W. Fenter, Thermodynamic Properties of High Temperature Air, Chance Vought Research Center Report No. RE-IR-14, Jun 1961

60. B. Kivel, P. Hammerling, and J. D. Teare, "Radiation from the Non-Equilibrium Region of Normal Shocks in Oxygen, Nitrogen, and Air," Planetary and Space Science, Vol. 3, Feb 1961, pp. 132–137

61. C. F. Hansen and C. E. Chapin, Nonequilibrium Radiation from the Stagnation Region of High-Velocity Bodies, a paper presented to the Third Conference on the Performance of High Temperature Systems, Pasadena, California, 7-9 Dec 1964

62. K. L. Wray and J. D. Teare, "Excitation Mechanism for the $N_2(1+)$ Band System in Shock-Heated Nitrogen," Atomic Collision Processes, M. R. C. McDowell (ed), Amsterdam, North-Holland Publishing Co., 1964, pp. 1123–1132

63. R. F. Chisnell, "Stagnation Point Flow With Radiation," (to be published)

64. N. C. Freeman, "On the Theory of Hypersonic Flow Past Plane and Axially Symmetric Bluff Bodies," Jour. Fluid Mech., Vol. 1, 1956, p. 366

65. C. F. Hansen, Approximations for the Thermodynamic and Transport Properties of High Temperature Air, NASA TR-R-50, 1959

66. J. M. Yos, Transport Properties of Nitrogen, Hydrogen, Oxygen, and Air to 30,000° K., AVCO Corp., RAD-TM-63-7, Mar 1963

Appendix A

PROGRAM DESCRIPTIONS
(All programs are written in FORTRAN II, version 2.)

A.1 MODIFIED AUTOMATED INVERSE (SUBSONIC) SOLUTION FOR CASE I

A sample IBM listing of the program appears below. The listing starts with a printout of the six quantities on the input data card (Format 6E12.7), as follows:

FOURTH TRUNC GEN CASE(HEADING)

γ	$\Delta\eta$	M_∞^2	B	No. of Cases	No. of $\Delta\eta$ steps Between Printouts
1.1920000E 00	9.9999999E-04	-4.0709999E 01	5.8000000E 00	1.0000000E 00	2.0000000E 00

The output follows immediately below the input statements and has the following arrangement:

(η) V(1)= 0.09999999E 01

SONIC LINE COORDINATES – For this value of η

XISL (ξ)	XSL (x)	RSL (r)
0.21902351E-00	0.25936481E-01	0.21902351E-00

VALUES OF QUANTITIES IN FLOW FIELD. FIRST SIX VARIABLES ARE FOR METHOD OF CHARACTERISTICS STARTING LINE (SUBTRACT STANDOFF DISTANCE FROM XSTL BEFORE INPUT).

XSTL (x)	RSTL (r)	PSTLPI (p/p_∞)	PTOTPI (P_{total}/P_∞)	AMU (Mach angle-radians)	DELTA (Flow angle-radians)	XISTL (ξ)
-0.	0.	-0.44363429E 02	-0.45968700E 02	0.80081427E 00	0.	0.
0.12501560E-04	0.49999999E-02	-0.44362321E 02	-0.45977134E 02	0.80090778E 00	0.71567938E-01	0.49999999E-02
0.50008810E-04	0.99999999E-02	-0.44358998E 02	-0.46002445E 02	0.80118843E 00	0.14228302E-00	0.99999999E-02

and on the next sheet, the remaining statements associated with the same value of η:

RHOSTL (ρ/ρ_∞)	Constants No Longer Used			PSTL ($p/p_\infty V_\infty^2$)	XMSTL (Local Mach No.)	XISTL (ξ)
	CXI2	CXI4	CXI6			
0.15342402E 02	-0.	-0.	-0.	0.91421378E 00	0.24456275E-00	0.
0.15342534E 02	-0.22810218E-04	-0.27372260E-08	-0.32846710E-12	0.91419095E 00	0.24528079E-00	0.49999999E-02
0.15342931E 02	-0.91240872E-04	-0.43795616E-07	-0.21021894E-10	0.91412248E 00	0.24742211E-00	0.99999999E-02

For a given η, the 12 output statements are printed at intervals of $\Delta\xi = 0.005$ from $\xi = 0$ to $\xi = 0.995$. If $B > 1$, it is obvious from Eq. (3.2) that for

$\xi > 1/B^{1/2}$ the output is fictitious, and also not too useful for values of ξ that are slightly smaller. The local Mach number, Mach angle, sonic line coordinates, and density are correct only for a perfect gas, being in error for an approximate "locally" perfect gas. Note also that a fictitious Mach angle is provided for subsonic Mach numbers. If $M_\infty^2 < 0$, then the quantities p/p_∞ and p_{total}/p_∞ are negative, but the latter quantity is still useful as a streamline (i.e., constant entropy) label. As discussed in subsection (2.2.2), the pressure $p/\rho_\infty V_\infty^2$ and flow angle δ are assumed correct at each point. From the exact shock-wave solution and the values of p_{total}/p_∞ at the shock ($\eta = 1$), a plot of S/R vs. p_{total}/p_∞ is prepared, enabling us to determine the entropy at each point from the value of p_{total}/p_∞. The remaining state variables can then be obtained from Ref. 10.

Subsequent sheets repeat this pattern of output for decreasing increments of η which are multiples of $\Delta\eta$ specified by the sixth input quantity. This pattern ends when η_{body} on the axis ($\xi = 0$) is reached. The following two sheets print quantities pertaining to the shock and body coordinates as follows:

SHOCK AND BODY COORDINATES

XI (ξ)	XS (x_{shock})	RS (r_{shock})	XB (x_{body})	RB (r_{body})	ETAB (η_{body})
0.	-0.	0.	0.45670268E-01	0.	0.95956082E 00
0.49999999E-02	0.12501560E-04	0.49999999E-02	0.45680911E-01	0.47977984E-02	0.95955970E 00
0.99999999E-02	0.50008810E-04	0.99999999E-02	0.45712801E-01	0.95955637E-02	0.95955639E 00

and

XI(ξ)	XP ($x_{body} - \Delta$)	RP ($r_{body}^2/x_{body} - \Delta$)
0.	0.	0.
0.49999999E-02	0.10642689E-04	0.21628810E 01
0.99999999E-02	0.42532571E-04	0.21648078E 01

where XB, RB, and ETAB are extrapolated results calculated by the machine. The quantities XP and RP are useful in fitting a conic section to the body shape. Here Δ is the shock standoff distance.

The next section of printout is self-explanatory, but only useful for a perfect gas. The final section of printout consists of data which are not utilized.

A typical run requires about 3 minutes on the IBM 7090.

A.2 INVERSE (SUBSONIC) SOLUTION FOR CASE II (ANGLE-OF-ATTACK)

The sample listing starts with a printout of the four quantities on the input data card (Format 6E12.7), as follows:

```
                                    3D AT ANGLE, THIRD TRUNCATION (HEADING)
        γ                Δη              M∞              B
1.4000000E 00   9.9999999E-04   1.0000000E 04   1.0000000E 00
```

The next listing contains the output for the zero angle-of-attack functions of η arranged in groups of three rows, as follows:

η	g'_o	g'_o	f'_o	f''_o	f_o	g_1
g'_1	f'_1	f''_1	f_1	g_2	g'_2	f'_2
f''_2	f_2					

where the functions are defined by Eqs. (3.8) and (3.10), and primes denote derivatives with respect to η. Succeeding groups repeat this output for decreasing $\Delta\eta$ intervals until η_{body} on the axis is reached.

The next two listings can be ignored. The final listing contains the output for the following functions of η arranged in groups of six rows and repeated for decreasing $2\Delta\eta$ intervals:

η	g_4	g_4'	f_4'	f_4''	f_4	h_4'
h_4''	h_4	g_5	g_5'	f_5'	f_5''	f_5
h_5'	h_5''	h_5	g_6	g_6'	f_6'	f_6''
f_6	h_6'	h_6''	h_6	A_{381}	A_{382}	A_{383}
A_{384}	A_{385}	A_{386}	A_{387}	A_{388}	A_{389}	A_{390}
A_{391}						

The functions $f_4, f_5, f_6, h_4, h_5, h_6$, and g_4, g_5, g_6 are defined by Eqs. (3.8), (3.9) and (3.10), and primes denote derivatives with respect to η. The functions A_{381}, A_{382}, etc. appear in the following expression for the pressure

$$\begin{aligned}\bar{p} = \frac{g_o^\gamma}{\gamma(\gamma-1)^\gamma(\gamma+1)} \Bigg\{ & K_2 K_4^\gamma + \left(A_{381} + \gamma K_2 K_4^\gamma \frac{g_1}{g_o}\right)\xi^2 \\ & + \left(A_{382} + \gamma A_{381}\frac{g_1}{g_o} + \gamma K_2 K_4^\gamma A_{389}\right)\xi^4 \\ & + \epsilon\cos\varphi\left[\left(A_{383} + \gamma K_2 K_4^\gamma \frac{g_4}{g_o}\right)\xi \right. \\ & \left. + \left(A_{384} + \gamma A_{383}\frac{g_1}{g_o} + \gamma A_{381}\frac{g_4}{g_o} + \gamma K_2 K_4^\gamma A_{390}\right)\xi^3\right]\Bigg\}\end{aligned} \tag{A.1}$$

where

$$K_2 K_4^{\gamma} = \left[2\gamma - \frac{(\gamma - 1)}{M_\infty^2} \right] \left[(\gamma - 1) + \frac{2}{M_\infty^2} \right]^{\gamma} \qquad (A.2)$$

and in the expression for the sonic line shape which is not quoted here since it is only valid for a perfect gas.

The last line of the listing contains four quantities. Only the last one is of interest. It is the parameter δ, discussed in subsection 3.1.1, which locates the body streamline in the free stream. It is utilized (see below) in determining the stream function $\bar{\psi}_1$ at the shock wave. A typical run requires about 3 minutes on the IBM 7090.

If η_o is the value of η at which $f_o(\eta) = 0$, then the body shape is given by the expression

$$\eta_b = A_o + A_2 \xi^2 + A_4 \xi^4 + \ldots + \epsilon \cos \varphi \left(A_1 \xi + A_3 \xi^3 + \ldots \right) + \ldots \qquad (A.3)$$

where A_o through A_4 are functions of η_o defined by

$$A_o = \eta_o$$

$$A_2 = - f_1 / f_o'$$

$$A_4 = - \frac{1}{f_o'} \left(f_1' A_3 + f_2 + \frac{1}{2} f_o'' A_3^2 \right) \qquad (A.4)$$

$$A_1 = - \frac{1}{f_o'} \left(f_5 + f_4' A_3 \right)$$

$$A_3 = - \frac{1}{f_o'} \left(f_4' A_5 + \frac{1}{2} f_4'' A_3^2 + f_o'' A_1 A_2 + f_5' A_2 + f_1' A_1 + f_6 \right)$$

In order to determine the axis of symmetry of the body shape in the angle-of-attack plane (and thus determine the body angle-of-attack α), the body shape is first expressed in cylindrical polar coordinates. In the $\varphi = 0$ plane it has the expanded form

$$x_b = a_o + a_2 r^2 + a_4 r^4 + \ldots + \epsilon \left(a_1 r + a_3 r^3 + \ldots\right) + \ldots \qquad (A.5)$$

If Eq. (A.5) is expressed in terms of ξ and η, using Eqs. (3.2) and (3.3), one can show by comparison with Eq. (A.3) that

$$\begin{aligned}
a_o &= \left(1 - b_o^{1/2}\right)/B \\
a_1 &= - A_1/b_o^{1/2} \\
a_2 &= - b_2 b_o^{1/2}/A_o^2 \\
a_3 &= \left[b_o^{1/2} (Bb_1 b_2 - b_3) - 2a_2 A_o A_1 - a_1 A_2\right]/A_o^3 \\
a_4 &= \left[b_o^{1/2} \left(\tfrac{1}{2} Bb_2^2 - b_4\right) - 2a_2 A_o A_2\right]/A_o^4
\end{aligned} \qquad (A.6)$$

where

$$\begin{aligned}
b_o &= 1 - B + BA_o^2 \\
b_1 &= A_o A_1/b_o \\
b_2 &= (A_o A_2/b_o) - 1/2 \\
b_3 &= (A_1 A_2 + A_o A_3 - A_o A_1 B)/b_o \\
b_4 &= \left(\tfrac{1}{2} A_2^2 + A_o A_4 - A_o A_2 B\right)/b_o
\end{aligned} \qquad (A.7)$$

and B is the bluntness parameter defined by Eq. (3.1). We now look for a transformed coordinate system $(\tilde{r}, \tilde{x})$ with respect to which the body shape is symmetric to lowest order; i.e., for which the transformed coefficients $\tilde{a}_1$ and $\tilde{a}_3$ vanish. The transformation from (r, x) to $(\tilde{r}, \tilde{x})$, in general, involves a translation and a clockwise rotation through an angle β. Using the transformation relations, one can show that the desired rotation is given by:

$$\frac{\epsilon}{\beta} = \frac{2\left(a_4 - a_2^3\right)}{2a_1a_4 - a_2a_3} \tag{A.8}$$

Substituting the numerical results of Case II, we obtain the value $\epsilon/\beta = -19.68$. Since this first-order analysis is only good to $0(\epsilon) \approx 0.1$ for our case, it is obvious that to the order of accuracy of the analysis, the body rotation (from the shock axes) is negligible, and the body and shock angles-of-attack are equal.

The pressure in the angle-of-attack plane was calculated by assuming that Eq. (A.1) gave the correct fractional change in pressure due to angle-of-attack, and applying the change to the more accurate zero angle-of-attack pressure distribution derived for Case I. The calculated surface pressure distribution demonstrated that the stagnation point had shifted 5 degrees, as predicted by Newtonian theory.

If ϕ is the shock angle measured with respect to the free-stream direction, then the following relations hold at the shock wave $(\eta = 1)$

$$\sin^2\phi = \frac{1}{1 + (1 - B)\xi^2}\left[1 - B\xi^2 - 2\epsilon\cos\varphi\xi\sqrt{1 - B\xi^2}\right] \tag{A.9}$$

and

$$\bar{\psi}_{1_s} = \frac{\xi^2}{2} + \epsilon\cos\varphi\xi\left(\frac{\sqrt{1 - B\xi^2}}{B} + \delta\right) \tag{A.10}$$

From the known oblique shock solution (which determines S/R as a function of ϕ), a plot of S/R vs. $\bar{\psi}_1$ was prepared for $\varphi = 0$ and $\varphi = \pi$. The entropy in the angle-of-attack plane was then calculated for the value of $\bar{\psi}_1$ as determined by Eq. (3.8).

A.3 ANALYTIC (SUBSONIC) SOLUTION FOR CASE III

As discussed in subsection (2.2.3), the Case III solution was obtained by first finding the sphere solution for the given free-stream conditions and then using the sonic corner option to duplicate the given shape.

The sample listing starts with a printout of the input data, as shown below:

```
                    SUPERSONIC FLOW ABOUT A SPHERE

INPUT DATA

 TH2 =     0.14422224E 02   XN    = 0.15000000E 02   SK    = 1
 TH3 =     0.23000000E 02   STMLN= 0.                 ST    = 1
 R1  =     0.10419469E 01   OUT   = 0.                 CASE  = 1
 R2  =     0.10438398E 01   DELT  = 0.41999999E 01    SWT   = 1
 K1  =     0.92584868E 00   VTEST= 0.99999999E-04     C3    = 1
 K2  =     0.78280701E 00   CTEST= 0.99999999E-05     IT    = 0
 STOP=     0.30000000E 02
 M   =     0.81629999E 02   GAM   = 0.11172000E 01
```

where the first card contains the quantities (see Fig. 6) (Format 6E 12.8)

TH2	Initial guess of θ (degrees) at point 2
TH3	Initial guess of θ (degrees) at point 3
R1	Initial guess of R/R_B at point 1
R2	Initial guess of R/R_B at point 2
K1	Initial guess of KR_B (K = shock curvature) at point 1
K2	Initial guess of KR_B at point 2

The second card contains the controls (Format 6E 12.8)

XN	Number of streamlines calculated between the body and the shock sonic point (point 2).
STMLN = 0,	Calculates streamlines in the output
$\neq$ 0,	Does not calculate streamlines
OUT = 0,	Output is called for if convergence is not obtained in the main program
$\neq$ 0,	Output is not called if there is no convergence
DELT	$\Delta\theta$ interval (degrees) for which streamline calculations are made
VTEST	Convergence criteria in the main program
CTEST	Convergence criteria in the output subroutine (i.e., iteration for sonic points, shock points)

The third card contains the single control (Format 6E 12.8)

STOP	Maximum value of θ (degrees) calculated in the program

The fourth card contains the controls (Format 6I5)

SK = 1	(Formerly used to test if $\bar{K}_1 < 0$)
ST = 1	(Formerly used to test if $\theta_2 < 0$)
CASE	Number of different free-stream (i.e., M_∞ and γ) cases to be run consecutively, all other input being the same
SWT = 0	Sphere solution
$\neq$ 0	Sonic corner option
C3 = 0,	Performs Newton's iteration for all six variables
$\neq$ 0,	Keeps θ_3 fixed, iterates on the others
IT	Maximum number of iterations allowed in the main program. If IT = 0, output subroutine calculates the flow based on the input values of the six geometric parameters.

The fifth (and succeeding) cards contain the free-stream conditions (6E.12.8)

M	M_∞
GAM	γ

If IT $\neq$ 0 , the next part of the printout contains the results of each iteration step in the main program until convergence is achieved or the number of iterations = IT. This is not included in this sample printout (IT = 0). The next printout contains the final coefficients in the solution for $\overline{\psi}$, as follows:

SUPERSONIC FLOW ABOUT A SPHERE

A	B	C	D	B1 (b_1)	B2 (b_2)	B3 (b_3)	B4 (b_4)	M (M_∞)	GAMMA (γ)
-3.8780E 04	3.7146E 04	4.0077E 04	-3.8180E 04	-9.3837E 02	8.1584E 02	7.8769E 01	-1.6499E 01	8.1630E 01	1.1172E 00

The final printout contains the solution along each streamline, starting with the stagnation streamline, and including the shock and sonic point data. Only the first two streamlines are shown here:

	SR (r/R_B)	Z (z/R_B)	R (R/R_B)	THETA (θ-deg)	Q	H ($\rho^*a^*/\rho_\infty V_\infty$)	PSI ($\psi/\rho_\infty V_\infty R_B^2$)	RHO (ρ/ρ_∞)	ALPHA (α-deg)
SONIC PTS.	3.9073E-01	-7.9495E-02	1.0000E 00	2.3000E 01	1.0000E 00	2.6807E 00	0.		
SHOCK PTS.	0.	4.1947E-02	1.0419E 00	0.	1.0000E 00			1.0000E 00	0.

STREAMLINE AXIS	SR	Z	R	THETA	RV/H ($\rho V/\rho^*a^*$)	BETA (β-Flow angle – degrees)
	0.	3.9151E-02	1.0352E 00	0.	3.4066E-01	
	0.	3.6354E-02	1.0364E 00	0.	3.0921E-01	
	0.	3.3558E-02	1.0336E 00	0.	2.7876E-01	
	0.	3.0761E-02	1.0308E 00	0.	2.4931E-01	
	0.	2.7965E-02	1.0280E 00	0.	2.2091E-01	
	0.	2.5168E-02	1.0252E 00	0.	1.9358E-01	
	0.	2.2372E-02	1.0224E 00	0.	1.6733E-01	
	0.	1.9575E-02	1.0196E 00	0.	1.4220E-01	
	0.	1.6779E-02	1.0168E 00	0.	1.1821E-01	
	0.	1.3982E-02	1.0140E 00	0.	9.5425E-02	
	0.	1.1186E-02	1.0112E 00	0.	7.3790E-02	
	0.	8.3894E-03	1.0084E 00	0.	5.3434E-02	
	0.	5.5929E-03	1.0056E 00	0.	3.4319E-02	
	0.	2.7965E-03	1.0028E 00	0.	1.6475E-02	

BODY						MB (M_{local})	PB ($p/\rho_\infty V_\infty^2$)	TB (RT/V_∞^2)	RB (ρ/ρ_∞)
	0.	0.	1.0000E 00	0.	0.	0.	9.7275E-01	5.2587E-02	1.8498E 01
	7.3238E-02	-2.6855E-03	1.0000E 00	4.2000E 00	2.0818E-01	1.2551E-01	9.6423E-01	5.2538E-02	1.8353E 01
	1.4608E-01	-1.0728E-02	1.0000E 00	8.4000E 00	4.1888E-01	2.5951E-01	9.3691E-01	5.2380E-02	1.7887E 01
	2.1814E-01	-2.4083E-02	1.0000E 00	1.2600E 01	6.2705E-01	4.0952E-01	8.8617E-01	5.2075E-02	1.7017E 01
	2.8903E-01	-4.2681E-02	1.0000E 00	1.6800E 01	8.1567E-01	5.8263E-01	8.0623E-01	5.1561E-02	1.5636E 01
	3.5837E-01	-6.6420E-02	1.0000E 00	2.1000E 01	9.5742E-01	7.9502E-01	6.8776E-01	5.0709E-02	1.3563E 01

	SR	Z	R	THETA	Q	H	PSI	RHO	ALPHA
SONIC PTS.	4.2426E-01	-9.1232E-02	1.0029E 00	2.5025E 01	1.0093E 00	2.8179E 00	3.4556E-03		
SHOCK PTS.	8.3133E-02	3.8753E-02	1.0421E 00	4.5757E 00	1.0016E 00			1.8018E 01	4.3875E 00

STREAMLINE	SR	Z	R	THETA	RV/H	BETA
	1.4852E-01	5.7843E-03	1.0167E 00	8.4000E 00	6.0711E-01	7.1263E 01
	2.1998E-01	-1.5857E-02	1.0084E 00	1.2600E 01	7.3444E-01	7.3647E 01
	2.9052E-01	-3.7752E-02	1.0051E 00	1.6800E 01	8.6914E-01	7.1535E 01
	3.5967E-01	-6.3029E-02	1.0036E 00	2.1000E 01	9.7197E-01	6.8196E 01
	4.2702E-01	-9.2540E-02	1.0029E 00	2.5200E 01	1.0093E 00	6.4427E 01
	4.9218E-01	-1.2652E-01	1.0026E 00	2.9400E 01	9.6434E-01	6.0481E 01

The printout is self explanatory, with all the quantities defined in Section 3.1.2. The quantities Q are the self-consistency checks at the shock and sonic points, and are equal to one if there is a perfect check. A typical run requires about 3 minutes on the IBM 7090. A schematic flow chart of the program is given in Fig. 30.

The pressure $\bar{p}$, stream function $\bar{\psi}$, and flow angle β are assumed valid for the solution, and the other variables are found in the same manner as described for the Case I shape.

A.4 CHARACTERISTICS SOLUTION

The sample listing starts with a printout of the input data in four sections. (The symbols will be defined below in the order in which they appear on the input data cards.) The first section contains various controls and free-stream conditions:

```
INPUT -
NO. SEG. =    3      KBTK =    2      V(I)   =  0.34582E 05     H/RTO  =  0.71193E 03     RZERO  =  0.24980E-02
K1       =    2      NIP  =    2      RHO(I)=  0.14995E-05     RTO    =  0.84750E 06     DB     =  -0.
IDATA P  =   13      NO.IT=   25      P(I)   =  0.12546E 01     PZERO  =  0.21170E 04     DS     =  0.10000E 12
                                      R      =  0.31030E 04     PCD    =  1.00000E-02     CRE    =  0.20000E-01
                                      STOP   =  0.50000E 03     CP     =  0.30990E-00     GAM    =  0.14000E 01
                                      SO/R   =  0.24000E 02     SEP    =  0.96650E 01     DBP    =  0.20000E 02
```

The second section contains the coefficients defining the equation of each body region, in groups of two rows for each region, commencing at the starting line and progressing downstream:

```
      A                    B                    C                    D                    E              END POINT
     BK
0.09999999E 01    -0.55880111E 02    0.09999999E 01    -0.17613500E 02    0.84556039E 03    0.96649999E 01
0.59999999E 00
0.09999999E 01    -0.55880111E 02    0.09999999E 01    -0.17613500E 02    0.84556039E 03    0.10005888E 02
0.59999999E 00
0.                 0.09999999E 01    0.                 0.35819513E-00    -0.34871741E 02    0.60000000E 03
0.09999999E 01
```

The third section contains the starting line data, one line for each point, starting with the shock point and progressing toward the body:

```
      XI                   YI                 THETAI                VI                 SI/R              PHI
0.23146752E 01    0.32521112E 02    0.95505738E 00    0.16794000E 05    0.56820875E 02    0.10672098E 01
0.23632141E 01    0.32486770E 02    0.95640000E 00    0.16370000E 05    0.57099000E 02    -0.
0.24384663E 01    0.32433759E 02    0.95819999E 00    0.15840000E 05    0.57419999E 02    -0.
0.26326220E 01    0.32296754E 02    0.96190000E 00    0.14740000E 05    0.58049999E 02    -0.
0.28753170E 01    0.32125501E 02    0.96520000E 00    0.13640000E 05    0.58580000E 02    -0.
```

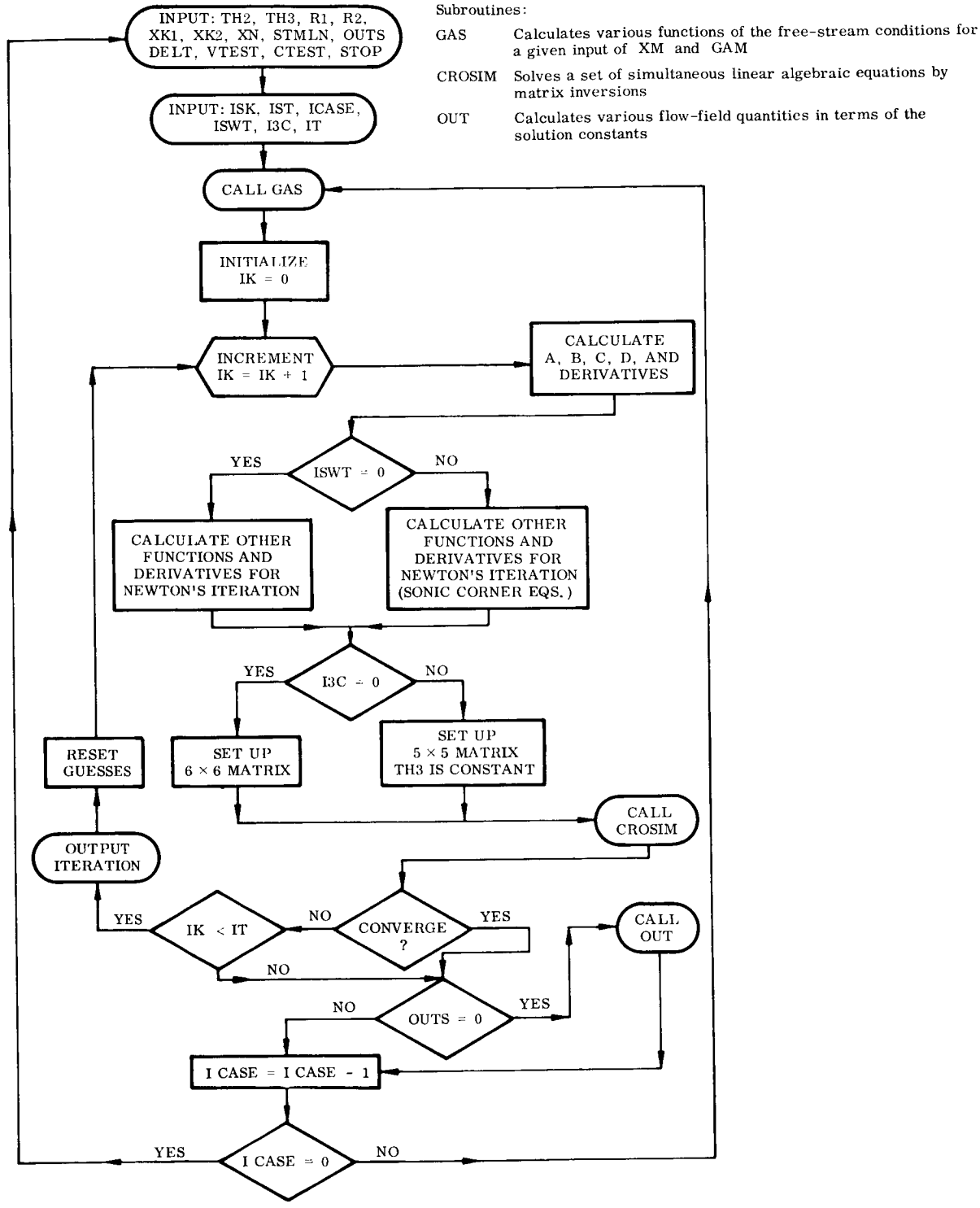

Fig. 30 Flow Chart, Case III Subsonic Program

The fourth section contains the coefficients in the polynomial curve fits for $\log_{10} \rho/\rho_o$, T, and $\log_{10} p/p_o$ for air:

LOG RHO/RHO ZERO 3 H/RTO 7	7 H/RTO 15	15 H/RTO 30	30 H/RTO 80	80 H/RTO 150	150 H/RTO 250	250 H/RTO 400
-0.65609529E 00	0.22169790E-00	0.10739528E 01	-0.50311711E 01	-0.32429337E 01	-0.18624917E 01	-0.54166791E 00
-0.14503939E 01	-0.14384256E 01	-0.14101414E 01	-0.30680882E 01	-0.27954399E 01	-0.25033885E 01	-0.21741065E 01
0.14606722E-00	0.13873605E-00	0.13839252E-00	0.54612748E 00	0.35301907E-00	0.33456594E-00	0.31427588E-00
-0.10792354E-03	-0.17035609E-01	-0.24044055E-01	0.99863213E-01	0.81855256E-02	0.64613728E-01	0.72290125E-01

The various input quantities appear in the input data deck in the following order:
The first card contains the single quantity (Format 18I4)

No. SEG. Number of body regions defining the body

There next follow a series of card groups (one for each body region) specifying the body shapes. The first card in each group contains the single control (Format 18I4)

KBTK = 1, Body region defined by table. Subsequent cards in the group contain the number of body points used, the slope of the body at the first point, and a list of the coordinates of each point

= 2, Body region defined by an equation of the form

$$Ay^2 + By + Cx^2 + Dx + E = 0 \qquad (A.11)$$

where x , y are cylindrical coordinates with the x-axis pointing downstream. The origin and dimensions are arbitrary. In the present case the origin was chosen at the body nose, and lengths were measured in centimeters, as this was the dimension employed in the streamtube chemistry program. A must be equal to either 1 or 0.

If KBTK = 2, the next card in the group contains the 6 quantities (Format 6E 12.8)

A, B, C, D, E Coefficients defined by Eq. (A.11)

END POINT Right end point of the interval over which Eq. (A.11) defines the body region.

The third (and last) card in the group contains the single quantity (Format 6E 12.8)

BK	The maximum allowable distance between successive points on the K^{th} body region.

The next card contains the quantities (Format 18I4)

I DATA P	Number of points on the initial data line
NO. IT	Maximum number of iterations permitted in the calculation of any point
K1	Number of corners on the body. A separation point is treated as a corner. There must always be one false corner at XC > STOP (see definitions of XC and STOP below). Thus, if the body has n corners (including separation point if not at a corner), $n \geq 0$, $K1 = n + 1$.
NIP = 1,	Perfect gas (constant γ) option
2,	Equilibrium gas (polynomial curve fits) option

The next group of cards contains the starting line data, one card for each point, starting with the shock point, as follows: (Format 6E 12.8)

XI	x_i (coordinate of the ith point)
YI	y_i (coordinate of the ith point)
THETA I	Flow angle θ_i (in radians)
VI	Velocity V_i (in feet per second)
SI/R	S_i/R, Dimensionless entropy
PHI	Shock angle ϕ (in radians) (for first point only)

The next group of cards contains the Mollier curve fit coefficients. The next card contains the following quantities: (Format 6E 12.8)

V(I)	V_∞ (ft/sec)
RHO (I)	ρ_∞ (slugs/ft^3)
P (I)	p_∞ (lb/ft^2)
H/RTO	h_{total}/RT_o (Dimensionless total enthalpy)
RTO	RT_o (84.75×10^4 ft^2/sec^2 for air)
PZERO	$p_o = 2117$ lb/ft^2

The next card contains the following quantities: (Format 6E 12.8)

RZERO	$\rho_o = 2.498 \times 10^{-3}$ slugs/ft^3
R	Gas constant (3.103×10^3 ft^2/sec^2 °K for air)
PCD	Convergence criterion for iteration at a point (defined as fractional change in the velocity between two successive iterations)
DB	Constant no longer used (leave space)
CRE	Fraction of original velocity at a corner defining velocity increments for the Prandtl-Meyer expansion
STOP	Program stops when a point on the body is computed having an abscissa x such that x > STOP

The next card contains the following quantities: (Format 6E 12.8)

DS	The maximum allowable distance between successive points on the shock.
CP	Specific heat C_p (Btu/lb° K) (for perfect gas option)
GAM	Specific heat ratio γ (for perfect gas option).
SO/R	Dimensionless reference entropy So/R = 24

SEP — The abscissa of the separation point. If there is no separation, SEP > STOP

DBP — The maximum allowable distance between successive points on the separating streamline

The next card contains the single control (Format 6E 12.8)

CHOP > 0 — Characteristics are cut off at x = STOP

≦ 0 — Characteristics are traced until their intersection with the shock wave

The next card group contains, in the order in which they are encountered, the quantities (Format 6E 12.8)

XCI — The abscissa of the i^{th} corner

The last card group contains, in the order in which they are encountered, the quantities (Format 6E 12.8)

DTI — $\Delta\theta$, The change in angle (in radians) of the body at the ith corner. For a separation point which is not at a real corner, set DTI > 10

The following sheets contain the printout of the output data, one sheet for each left-running characteristics, as shown below:

X (x)	Y (y)	THETA (θ-radians)	V (V-ft/sec)	S/R	H/RTO (h/RT_o)	T (°K)
SOUND SPEED	ALPHA (ft/sec)	BETA (Mach angle-rad)	P (p-lb/ft^2)	RHO (ρ-slugs/ft^3)	PHI (φ-radians, where applicable)	
0.23632141E 01	0.32486770E 02	0.95640000E 00	0.16370000E 05	0.57099000E 02	0.55383153E 03	0.88030025E 04
0.81430188E 04	0.52064004E 00	0.12801040E 04	0.23489190E-04			
0.23689286E 01	0.32547540E 02	0.95403548E 00	0.16592243E 05	0.56956806E 02	0.54950961E 03	0.87360737E 04
0.81097265E 04	0.51067483E 00	0.12845854E 04	0.23811334E-04			
0.23692912E 01	0.32547382E 02	0.95406877E 00	0.16587402E 05	0.56958409E 02	0.54960439E 03	0.87377898E 04
0.81105725E 04	0.51089686E 00	0.12854727E 04	0.23821919E-04			

A typical run, using a 0.01 convergence criterion and starting with 13 initial data points, required about 5 minutes on the IBM 7090. Flow charts of the IBM program appear in Fig. 31 a, b, c, d.

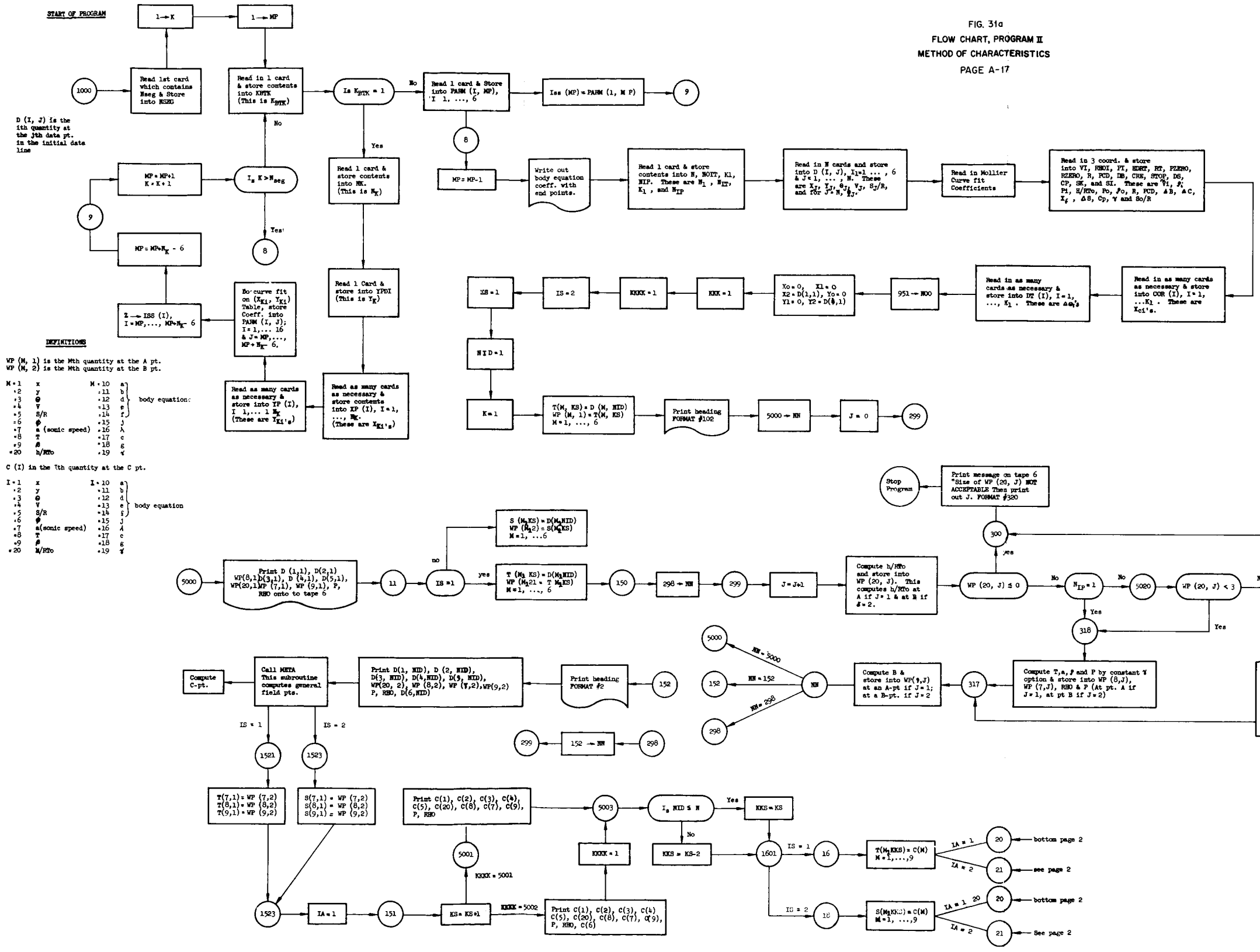
START OF PROGRAM
1 → K
1 → MP
1000
Read 1st card which contains Nseg & Store into NSEG
Read in 1 card & store contents into KBTK (This is K_{BTK})
Is K_{BTK} = 1
No
Read 1 card & Store into PARM (I, MP), I 1, ..., 6
Iss (MP) = PARM (1, M P)
9
8
MP = MP-1
Write out body equation coeff. with end points.
Read 1 card & store contents into N, NOUT, K1, NLP. These are N_1, N_{IT}, K_1, and N_{IP}
Read in N cards and store into D (I, J), I=1 ... , 6 & J = 1, ... , N. These are X_f, Y_f, θ_f, V_f, S_J/R, and for J = N, ϕ_J.
Read in Mollier Curve fit Coefficients
Read in 3 coord. & store into VI, RNOI, PI, HDRT, RT, PZERO, RZERO, R, PCD, DB, CRK, STOP, DS, CP, SK, and SI. These are Vi, ρi, Pi, R/MWo, Po, ρo, R, PCD, ΔR, ΔC, X_f, ΔS, Cp, γ and So/R
Read in as many cards as necessary & store into DT (I), I = 1, ..., K_1. These are $\Delta\phi_J$'s
Read in as many cards as necessary & store into CUR (I), I = 1, ...K_1. These are X_{ci}'s.
KS = 1
IS = 2
KKKK = 1
KKK = 1
Xo = 0, Xl = 0
X2 = D(1,1), Yo = 0
Y1 = 0, Y2 = D(ϕ,1)
951 → MOO
K I D = 1
K = 1
T(M, KS) = D (M, MID)
WP (M, 1) = T(M, KS)
M = 1, ..., 6
Print heading FORMAT #102
5000 → MN
J = 0
299
MP = MP+1
K = K + 1
I_s K > N_{seg}
Yes
No
9
MP = MP+ N_K - 6
Z → ISS (I), I = MP, ..., MP+N_K - 6
8
Read 1 card & store contents into NK. (This is N_K)
Yes
No
Read 1 Card & store into YPDI (This is Y_K)
Read as many cards as necessary & store contents into XP (I), I = 1, ..., N_K. (These are X_{Ki}'s)
Read as many cards as necessary & store into TP (I), I 1,... 1 N_K (These are Y_{Ki}'s)
Bo-curve fit on (X_{Ki}, Y_{Ki}) Table, store Coeff. into PARM (I, J); I = 1,... 16 & J = MP,..., MP+N_K- 6.
DEFINITIONS
WP (M, 1) is the Mth quantity at the A pt.
WP (M, 2) is the Mth quantity at the B pt.
M = 1 x
2 y
3 φ
4 V
5 S/R
6 ϕ
7 a (sonic speed)
8 T
9 ρ
20 M/MWo
M = 10 a
11 b
12 d
13 e
14 f
15 j
16 λ
17 c
18 g
19 ψ
body equation:
C (I) in the Ith quantity at the C pt.
I = 1 x
2 y
3 φ
4 V
5 S/R
6 ϕ
7 a(sonic speed)
8 T
9 ρ
20 M/MWo
I = 10 a
11 b
12 d
13 e
14 f
15 j
16 λ
17 c
18 g
19 ψ
body equation
Print D (1,1), D(2,1) WP(8,1)D(3,1), D (4,1), D(5,1), WP(20,1)WP (7,1), WP (9,1), P, RHO onto to tape 6
5000
11
IS = 1
yes
no
T (M, KS) = D(M, MID) WP (M_{21} = T (M_{KS}) M = 1, ..., 6
S (M, KS) = D(M, MID) WP (M_{22}) = S(M_{KS}) M = 1, ...6
150
298 → NN
299
J = J+1
Compute h/MWo and store into WP (20, J). This computes h/MWo at A if J = 1 & at B if J = 2.
WP (20, J) ≤ 0
No
Yes
N_{IP} = 1
No
Yes
5020
WP (20, J) < 3
No
Yes
WP (20, J) ≤ 400
No
Yes
318
Print message on tape 6 "Size of WP (20, J) NOT ACCEPTABLE Then print out J. FORMAT #300
Stop Program
300
Compute T,a, ρ & P by Mollier curve fits & store into WP(8,J), WP (7, J), RHO & P (At on A-pt. if J = 1 & at a B-pt. if J = 2).
Compute T,a, ρ and P by constant % option & store into WP (8,J), WP (7,J), RHO & P (At pt. A if J = 1, at pt B if J = 2)
317
Compute B & store into WP(9,J) at an A-pt if J = 1; at a B-pt. if J = 2
NN
5000
NN = 5000
152
NN = 152
298
NN = 298
Print D(1, MID), D (2, MID), D(3, MID), D(4,MID), D(5, MID), WP(20, 2), WP (8,2), WP (9,2),WP(9,2) P, RHO, D(6,MID)
Print heading FORMAT #2
152
299
152 → NN
298
Compute C-pt.
Call META This subroutine computes general field pts.
IS = 1
IS = 2
1521
1523
T(7,1) = WP (7,2) T(8,1) = WP (8,2) T(9,1) = WP (9,2)
S(7,1) = WP (7,2) S(8,1) = WP (8,2) S(9,1) = WP (9,2)
Print C(1), C(2), C(3), C(4) C(5), C(20), C(8), C(7), C(9), P, RHO
5003
I_s MID ≤ M
Yes
No
KKS = KS
KKS = KS-2
1601
IS = 1
IS = 2
16
18
T(M_{KKS}) = C(M) M = 1,...,9
S(M_{KKS}) = C(M) M = 1, ...,9
IA = 1
IA = 2
20
21
bottom page 2
see page 2
bottom page 2
See page 2
5001
KKKK = 5001
KKKK = 1
1523
IA = 1
151
KS = KS+1
KKKK = 5002
Print C(1), C(2), C(3), C(4) C(5), C(20), C(8), C(7), C(9), P, RHO, C(6)

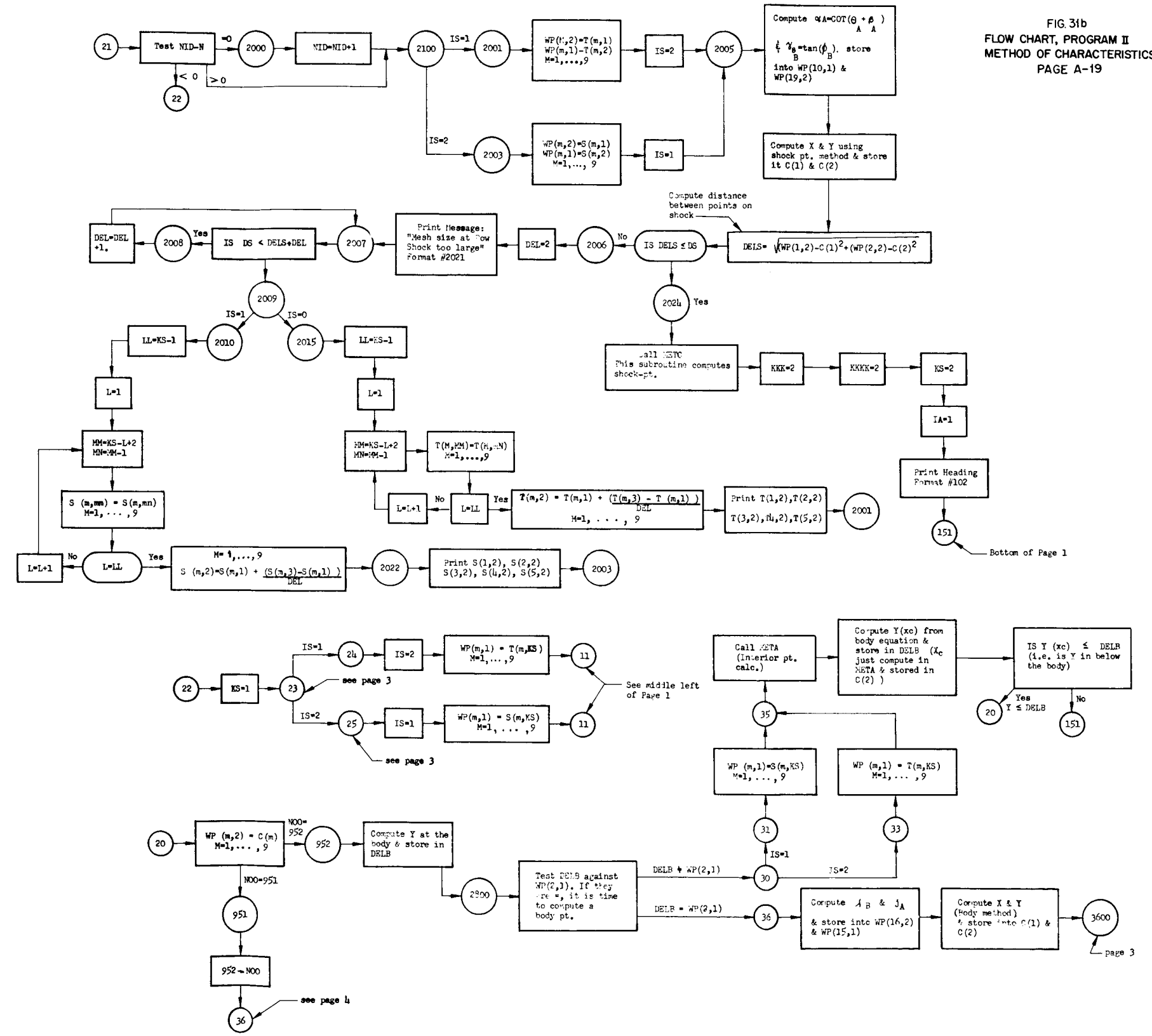

FIG. 31b
FLOW CHART, PROGRAM II
METHOD OF CHARACTERISTICS
PAGE A-19

FIG. 31c
FLOW CHART, PROGRAM II
METHOD OF CHARACTERISTICS
PAGE A-21

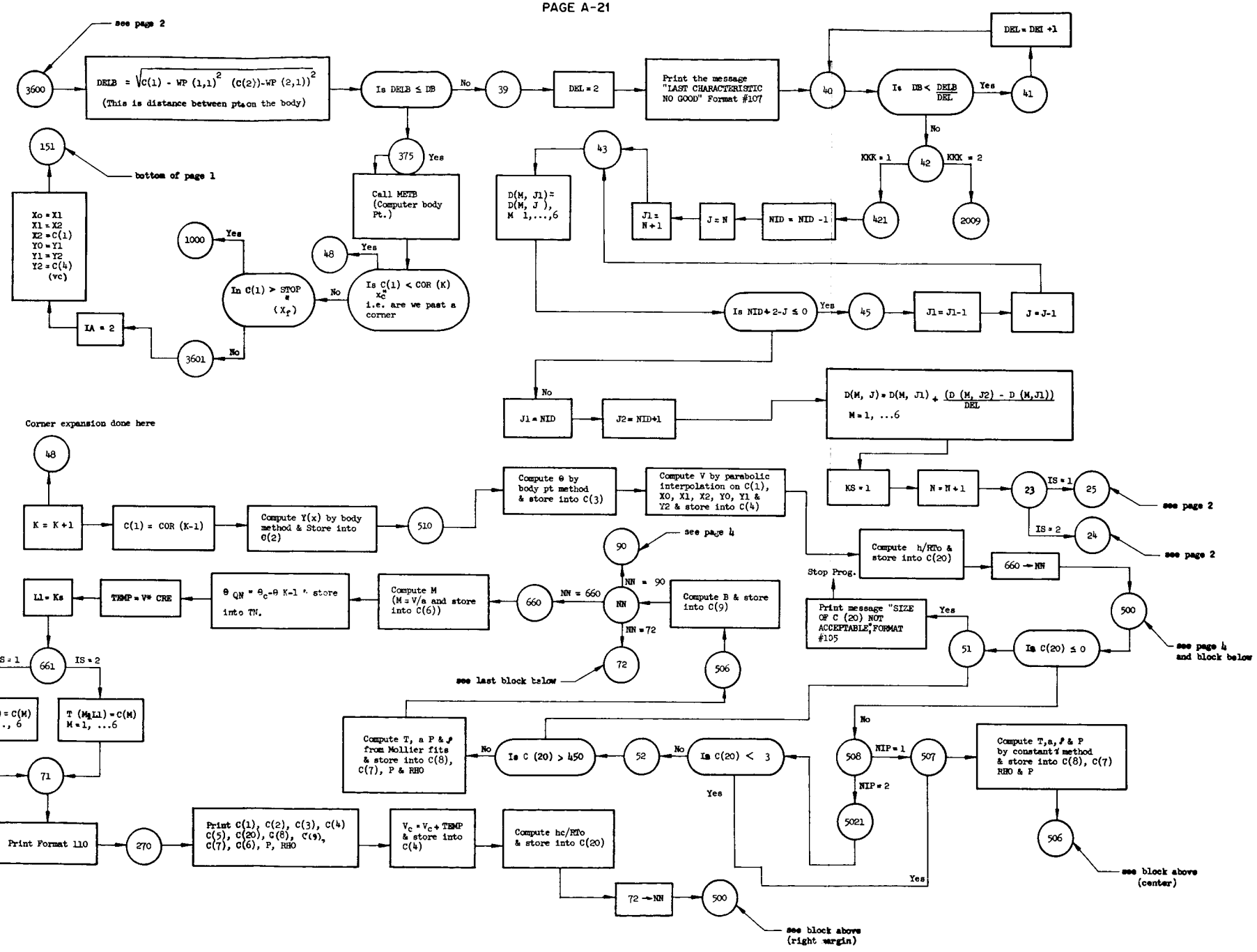

θ_{qn} is computed here

Simpson's rule is used. Integration is from V_{qn-1} to V_{qn}

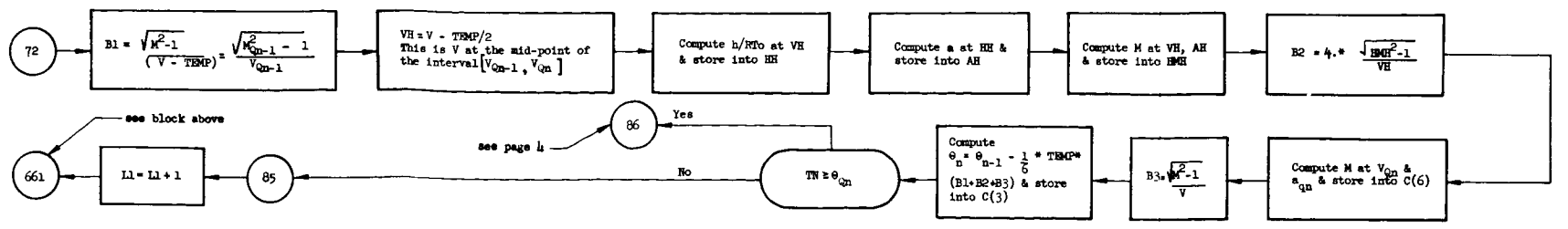

FIG. 31d
FLOW CHART, PROGRAM II
METHOD OF CHARACTERISTICS
PAGE A-23

OUTPUT

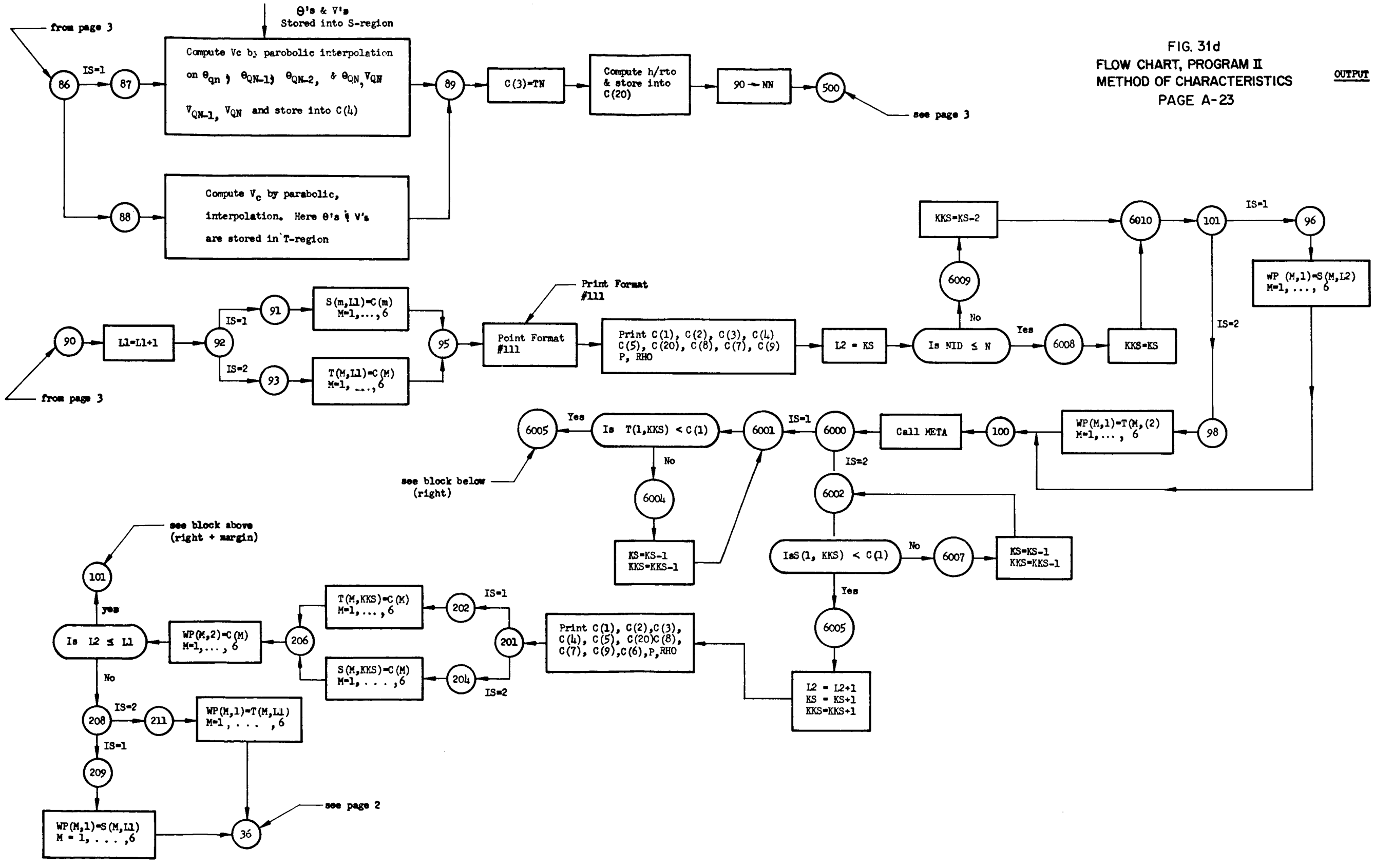

A.5 SUPPLEMENTAL INFORMATION ON RATE CHEMISTRY CODE OPERATION

The calculation of the nonequilibrium chemistry and associated thermodynamic variables is accomplished using the one-dimensional (stream-tube) chemistry IBM computer code discussed in subsection 3.2. The present discussion is directed to input quantities and procedures used for a code calculation. Also an explicit display is made of the printout array to help identify the location of output quantities.

Input quantities include variables which identify the thermodynamic state of the initial datum point. This point corresponds to the specified state of a fluid element immediately after transition through a normal or oblique shock. As such, it effectively identifies the particular streamline for which the calculation is to be performed. Each respective streamline is a separate computation case although several such cases (streamlines) may be computed in one sequence by running the code solutions back-to-back by using appropriate sets of input data cards corresponding to each of the streamlines.

Data specified at the start of a calculation are listed in the input card sequence shown and discussed in the following table (see pp. A-26 through A-29).

The heading of the printout sheet lists most of the initial quantities previously identified, useful as a basis for identification of the case and a check on initial conditions. In addition, certain supplementary quantities evaluated at the initial step are listed in the heading. These are:

H(0) — Nondimensional initial static enthalpy

$$\bar{h}(x)\Big|_{x=o} = \frac{h(0)}{V_\infty^2}$$

T(0) — Nondimensional initial temperature

$$\bar{T}(x)\Big|_{x=o} = \frac{T(0) \cdot R \cdot n_o}{V_\infty^2}$$

Table 16

NONEQUILIBRIUM CHEMISTRY INPUT DATA CARDS

Card Group	Line	Format	FORTRAN Symbol	Algebraic Symbol	Comment
1	1	I3(Fixed Point)	M1	$\sum_i x_i$	Total no. of species considered (presently 10)
2	1	6E12.8	N1	$\bar{N}_1$	Initial Mole Fraction O_2 (0.21)
	2	6E12.8	N2	$\bar{N}_2$	Initial Mole Fraction N_2 (0.79)
	3	6E12.8	N3	$\bar{N}_3$	Initial Mole Fraction NO (0)
	4	6E12.8	N4	$\bar{N}_4$	Initial Mole Fraction O (0)
	5	6E12.8	N5	$\bar{N}_5$	Initial Mole Fraction N (0)
	6	6E12.8	N6	$\bar{N}_6$	Initial Mole Fraction NO^+ (0)
3	1	6E12.8	N7	$\bar{N}_7$	Initial Mole Fraction N_2^+ (0)
	2	6E12.8	N8	$\bar{N}_8$	Initial Mole Fraction O^+ (0)
	3	6E12.8	N9	$\bar{N}_9$	Initial Mole Fraction N^+ (0)
	4	6E12.8	N10	$\bar{N}_{10}$	Initial Mole Fraction $\bar{e}$ (0)
4	1	6E12.8	PZ	$\bar{p}_o$	Initial equilibrium streamline pressure behind shock, $\bar{p}_o = \frac{p(o)}{\rho_\infty V_\infty^2}$
	2	6E12.8	RHOZ	$\bar{\rho}_o$	Initial density behind the shock, $\rho(o)/\rho_\infty$. Computed from a preliminary shock solution for a fully excited, but chemically inert gas ($\gamma = 9/7$)
	3	6E12.8	VZ	$\bar{V}_o$	Initial equilibrium streamline velocity behind shock $\bar{V}_o = \frac{V(o)}{V_\infty}$
	4	6E12.8	R	R	Gas constant $\left(8.3143 \times 10^7 \frac{\text{ergs}}{\text{mole} - °K}\right)$
	5	6E12.8	CONST	$\bar{H}_{total}$	Total enthalpy $\frac{H_{total}}{V_\infty^2}$
	6	6E12.8	DEL	δ	Physical entity reserved for specialized calculations (assign a zero)

Table 16 (cont.)

Card Group	Line	Format	FORTRAN Symbol	Algebraic Symbol	Comment
5	1	6E12.8	ALF	α	Coefficient on integration step control (presently 0.8)
	2	6E12.8	VINF	V_∞	Free-stream velocity (cm/sec)
	3	6E12.8	RHOINF	ρ_∞	Free-stream density (gm/cc)
	4	6E12.8	XNZ	n_o	Inverse of the molecular weight of ambient gas (air $\sim 3.45280 \times 10^{-2}$ moles/gm
	5	6E12.8	BET	β	Sets "farthest acceptable deviation" between x_{final} (independent variable specified) and that developed in integration. (presently $\beta = 10^{-5}$)
	6	6E12.8	EP	ϵ	Control monitor not presently used (set $\epsilon = 0$)
6	1	6E12.8	TOP	$x_{optional}$	Value of independent variable at which a switch occurs between dependent variables [i.e., $\bar{p}(x)$ goes to $\bar{V}(x)$]. If not used, assign a zero
	2	6E12.8	XNOPC	Option Switch	Specifies whether or not the above switch takes place. If 1.0, no switch takes place. If 2.0, switch takes place at $x_{optional}$
7	1	6E12.8	ANORD	Order of Array	Total number of independent reaction systems used (presently 10)
	2	6E12.8	TTP	$t(x = x_o)$	Time at initial step (presently 0)
	3	6E12.8	DTP	Δt(Print)	Print increment at initial time (presently 0)
	4	6E12.8	RMAX	R_{max}	Maximum relative truncation error allowed in array (presently 10^{-3})
	5	6E12.8	RTAB	No. of Discontinuities	Number of points at which the dependent variable or its first derivative is discontinuous. If used, a double entry at the discontinuity must be made in the table of values
	6	6E12.8	TO	x(0)	Initial value of independent variable (cm) usually zero at shock

Table 16 (cont.)

Card Group	Line	Format	FORTRAN Symbol	Algebraic Symbol	Comment
8	1	6E12.8	TF	x(Final)	Final value of independent variable (cm) measured along streamline from shock
	2	6E12.8	QUAD	Quadrature System	Selection of integration routine (usually 0 which calls for a 4th order Runge-Kutta Quadrature)
	3	6E12.8	RNPD	Print Increment	Controls printout increments (1 designates printout at each integration step)
	4	6E12.8	HMIN	Δx Minimum	Lower bound on integration step size (presently 10^{-8})
	5	6E12.8	XNOPT	Dependent Variable Identity Signal	1.0 $\bar{P}(x)$ is table value 2.0 $\bar{V}(x)$ is table value 3.0 $\bar{P}(x)$ is an equation
9	1	I3(Fixed Point)	M	Total Number of Entries in Table of Values Input + 4	Total all line entries in table cards used (cards 10, 11, 12, ... n) add 2 extra for initial point and 2 extra for final point
First Table Card					
10	1	6E12.8	TXZ	x_o	x_o(cm) initial point
	2	6E12.8	PXZ	$\bar{P}(x_o)$	$\bar{P}(x_o)$ initial dependent variable
	3	6E12.8	TXZ	x_o	Repeat initial point location and initial value of the dependent variable
	4	6E12.8	PXZ	$\bar{P}(x_o)$	
	5	6E12.8	TXI	x_1	
	6	6E12.8	PXI	$\bar{P}(x_1)$	

Table 16 (cont.)

Card Group	Line	Format	FORTRAN Symbol	Algebraic Symbol	Comment
11 . . . N	1 2	6E12.8 6E12.8	TX 2 PX 2 . . . TX_N PX_N	x_2 $\bar{P}(x_2)$ . . . x_N $\bar{p}(x_N)$	Table cards are continued with entries for all points <u>including</u> an entry at x final specified in card 8. Special instructions: 1. If discontinuities in dependent variable or its first derivative are encountered (see card 7) a double entry must be made at the discontinuity. 2. If discontinuities in the second derivative of the dependent variable are encountered "smoothness" is insured in the integration by placing table points in close juxtaposition at the point of inflection (RTAB is <u>not</u> used for this)
N+1	1	6E12.8		Closure	Card signals table of variables is closed by assigning a number to the independent variable $> 10^9$
N+2	1	6E12.8	XRTAB	x(Discontinuity)	List all locations of points x (cm) at which discontinuities exist in the dependent variable or its first derivative (i.e., points for which RTAB, card 7, was used as a counter and for which a double entry was made in table. (See Comment 1, card 11.)

$KF_i(0)$, i = 1, 2, . . . , 12	Initial values taken by forward rate constants
$Kc_i(0)$, i = 1, 2, . . . , 10	Initial values taken by equilibrium constants
$L_i(0)$, i = 1, 2, . . . , 12	Initial values taken by components of species production processes
$DN_i(0)$, i = 1, 2, . . . , 10	Initial values taken by total derivatives of species production processes
$N_i(0)$, i = 1, 2, . . . , 10	Initial values of concentrations of species (Optional: present initial values are set at 0.21 and 0.79 for initial molecular oxygen and nitrogen concentration, respectively. All other species are considered nonexistent, initially)

A sample printout heading appears below:

```
METHOD RUNGE KUTTA      X(INITIAL)= 0.                                          X(FINAL)= 0.30000000E 01
INITIAL CONDITIONS
RHO(0)= 0.79795E 01 KF1= 0.10184E 15 KF6 = 0.58559E 13 L1= 0.17065E 15 L6 = 0.77520E 13 DN1=-0.17209E 02 DN6 =-0.
V(0)  = 0.58823E-01 KF2= 0.20481E 14 KF7 = 0.53937E 15 L2= 0.12911E 15 L7 = 0.          DN2=-0.13202E 02 DN7 =-0.
T(0)  = 0.11806E-00 KF3= 0.96166E 14 KF8 = 0.24394E 15 L3= 0.          L8 = 0.          DN3= 0.14955E 01 DN8 =-0.
H(0)  = 0.50148E 00 KF4= 0.17930E 15 KF9 = 0.11686E 06 L4= 0.          L9 = 0.          DN4=NOT COMPUTED DN9 =-0.
P(0)  = 0.94209E 00 KF5= 0.18347E 14 KF10= 0.11686E 06 L5= 0.          L10= 0.          DN5=NOT COMPUTED DN10=NOT COMPUTED

                    KC1= 0.11249E 11 KC6 = 0.39118E 01 N1= 0.21000E-00 N6 = 0.
                    KC2= 0.13624E 11 KC7 = 0.72636E 05 N2= 0.79000E 00 N7 = 0.
                    KC3= 0.62592E 10 KC8 = 0.12600E 06 N3= 0.          N8 = 0.
                    KC4= 0.17971E 01 KC9 = 0.51520E-04 N4= 0.          N9 = 0.
                    KC5= 0.21767E 01 KC10= 0.46071E-04 N5= 0.          N10= 0.
                                                                       N11= 1.00000E 00

CONST= 0.50321E 00 R  = 0.83143E 08 VINF= 0.96000E 06 HMIN=10.000E-09 HMAX= 2.4630E-04
 RHOINF= 1.57762E-07 XNZ= 3.45280E-02 TOP = 1.00000E 00 NUPT= 1.00000E 00
```

The output is listed in two separate sections due to space limitations. The listing is completed for all the x intervals for the variables covered in the first section, followed by a separate array for the same x intervals covering the variables of the second section. The first section of the printout includes some quantities which have not been previously discussed. These are, in the notation adopted for listing:

Delta X Max	Integration step size (cm)
NSUM	Local compressibility $Z(x) = \sum_{i=1}^{10} \frac{M_o}{M_i(x)} = \sum_{i=1}^{10} \bar{n}_i(x)$
T Prime (X)	Dimensional local temperature (°K)

RHO P (X)	Dimensional local density (gm/cc)
NE/cc	Local number density of free electrons $(cc)^{-1}$

The other quantities listed at each printout station, V(X) , P(X) , N10, refer to the nondimensional (barred) form of the variables previously introduced and discussed. A partial sample listing of the first section appears below:

X	DELTA X MAX	V(X)	P(X)	H(X)	NSUM	T PRIME(X)	RHO P(X)	N10	NE/CC
2.01139E-02	8.05391E-04	5.88235E-02	9.42093E-01	5.01479E-01	1.49054E 00	2.44925E 04	1.30697E-06	1.10878E-03	3.01366E 13
2.09192E-02	8.33898E-04	5.88235E-02	9.42093E-01	5.01479E-01	1.50042E 00	2.42336E 04	1.31223E-06	1.17506E-03	3.20665E 13
2.17531E-02	8.65105E-04	5.88235E-02	9.42093E-01	5.01479E-01	1.51040E 00	2.39728E 04	1.31774E-06	1.24423E-03	3.40969E 13
2.26182E-02	8.99306E-04	5.88235E-02	9.42093E-01	5.01479E-01	1.52048E 00	2.37101E 04	1.32351E-06	1.31653E-03	3.62363E 13
2.35176E-02	9.36838E-04	5.88235E-02	9.42093E-01	5.01479E-01	1.53065E 00	2.34454E 04	1.32956E-06	1.39222E-03	3.84946E 13

The second section of the listing repeats the stations, x , and the integration step size, Delta X , followed by the nondimensional concentrations of the species $\bar{N}_i$, i = 1 , 2 , . . . , 9. The number indices refer to particular species identified in subsection 3.2 and Table 7 of this report.

X	N1	N2	N3	N4	N5	N6	N7	N8	N9
2.01139E-02	7.77568E-04	5.09775E-01	2.21676E-02	4.06067E-01	5.49531E-01	1.13497E-04	2.13414E-05	4.94386E-04	4.79554E-04
2.09192E-02	7.52865E-04	4.99972E-01	2.19680E-02	4.06198E-01	5.69184E-01	1.28349E-04	2.48387E-05	5.11630E-04	5.10238E-04
2.17531E-02	7.30822E-04	4.90080E-01	2.17441E-02	4.06336E-01	5.89027E-01	1.44959E-04	2.88546E-05	5.28614E-04	5.41802E-04
2.26182E-02	7.10491E-04	4.80094E-01	2.14966E-02	4.06482E-01	6.09062E-01	1.63536E-04	3.34613E-05	5.45324E-04	5.74209E-04
2.35176E-02	6.91135E-04	4.70014E-01	2.12258E-02	4.06637E-01	6.29295E-01	1.84313E-04	3.87411E-05	5.61742E-04	6.07420E-04

Computational time per streamline on the IBM 7094 varies considerably, depending on the initial conditions (more energetic flows are generally associated with rapid changes in concentration, hence smaller integration intervals and longer run times) and the magnitude of variations in the initial distribution of specified streamline pressure or velocity. Thus, for streamlines imbedded in a hypersonic shock layer near the body, with high initial temperature and characteristically large variations in pressure or velocity, computation times of the order of 18 minutes may be encountered. On the other hand, for relatively cool streamlines in the outer shock layer of a reentry body, the computation time for a streamline might be as short as 3 minutes or less.

Flow charts descriptive of the complete IBM program appear in Figures 32a, 32b, 32c.

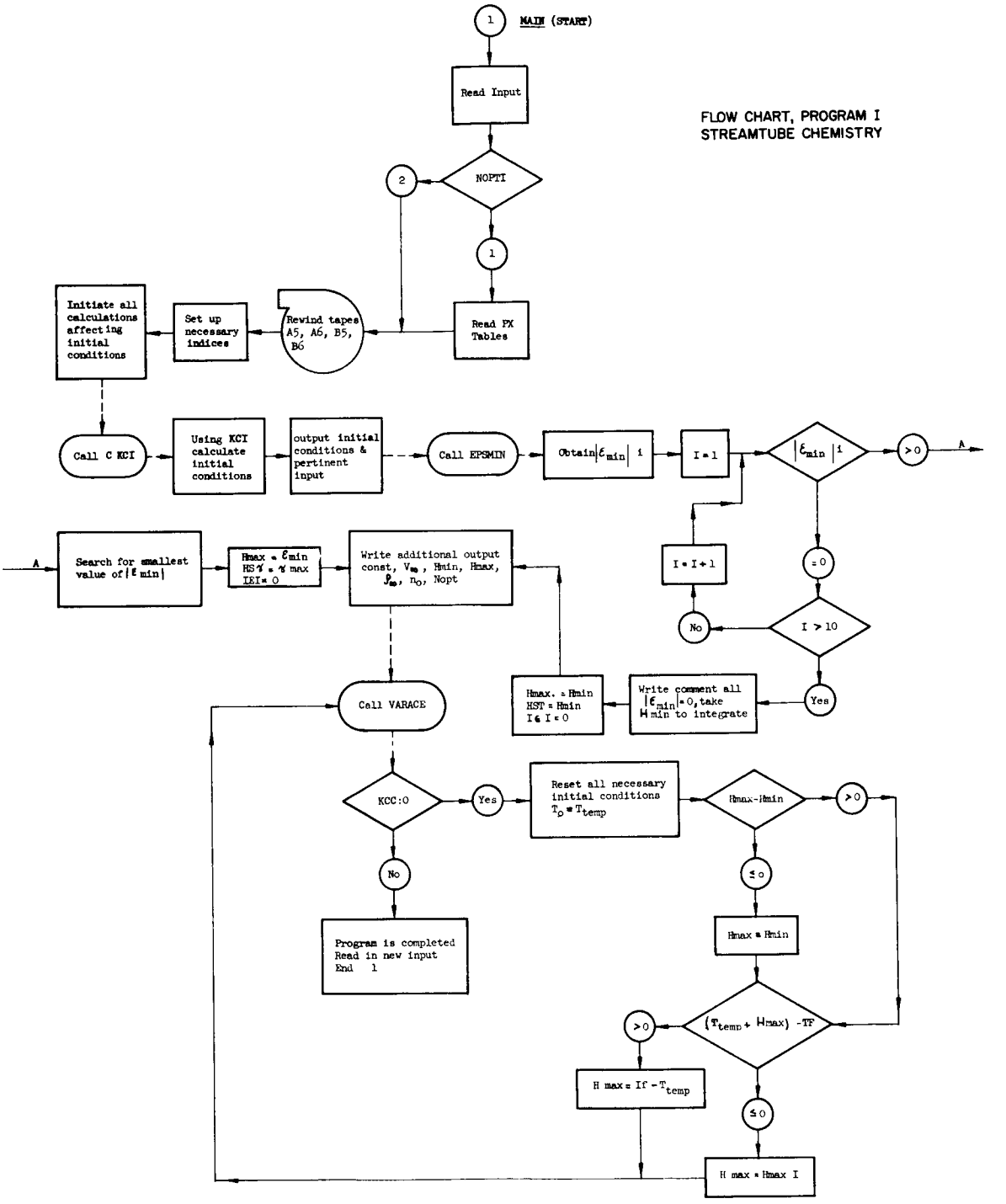

CKCI (T', n) This subroutine calculates all $K_{ci's}$ & returns

EPSMIN This subroutine calculates all $\frac{\partial \bar{g}(x)}{\partial ni}$, $\frac{\partial Fi}{\partial ni}$, $\frac{2V \partial V}{\partial ni}$, ε_{min_i}, and transfer the Values of $|\varepsilon_{min}|_i$ to appropriate programs: necessary in the determination of ΔX_{max}

Fig. 32a Flow Chart, Program I Streamtube Chemistry

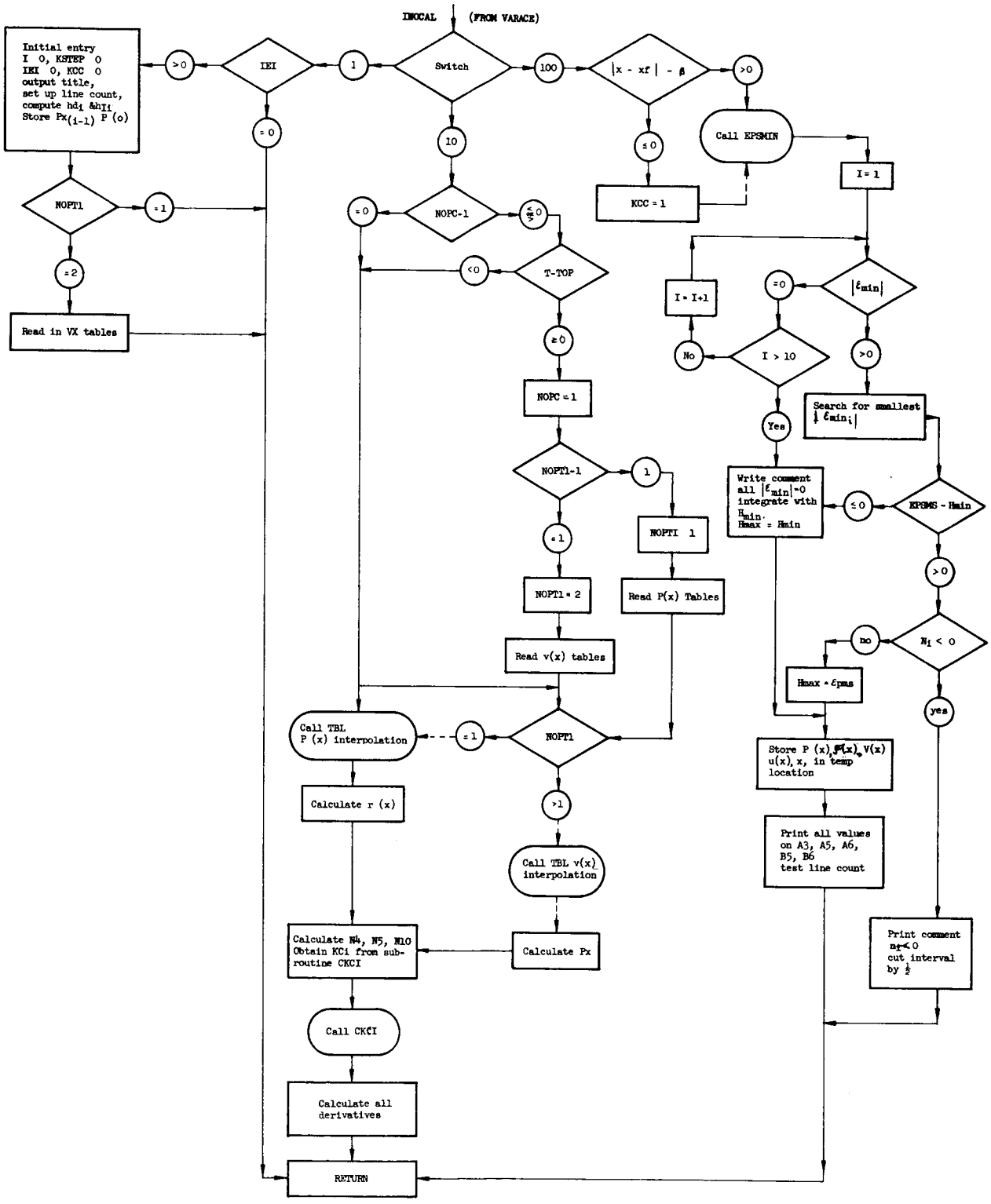

TBL This subroutine is a table look up with parabolic interpolation.

Fig. 32b Flow Chart, Program I Streamtube Chemistry

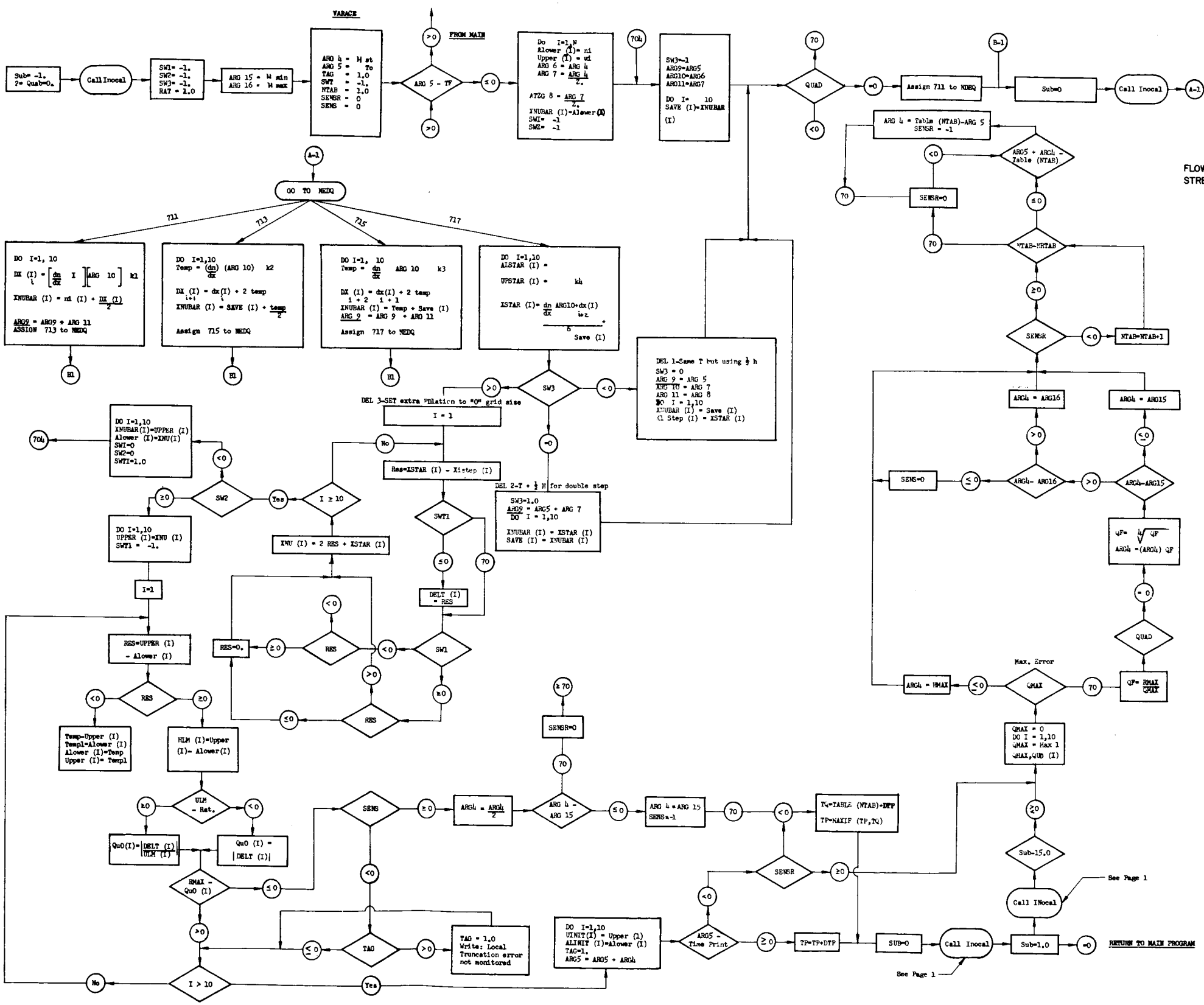

FIG. 32c
FLOW CHART, PROGRAM I
STREAMTUBE CHEMISTRY
PAGE A-35

A.6 MOLECULAR SPECIES RADIATION PROGRAM

This program calculates equilibrium and/or nonequilibrium, spectral, radiation properties for the band systems of diatomic molecules. In its present form it contains the data required in the visible and ultraviolet ($0.5 \leq h\nu \leq 8$ ev) band systems of air. However, it has sufficient flexibility to be expanded to calculate the radiation properties of new band systems of air or for those of other chemical species.

A flow chart of the essential features of the code is given in Fig. 33. This chart is described in physical terms and is meant to give an overview of the code as a whole. It is self-explanatory except for the reference to the inner sums, which are the double summations in Eqs. (3.35) and (3.36).

The FORTRAN notation is defined and presented in Table 17 along with a description of the first 10 card groups of the deck which contain the input data required to run the code. It should be noted that only card groups 9 and 10 need be changed for each new case (electronic temperature, kinetic temperature, number density, and specie) whereas card groups 1 through 8 must be changed to include new band systems and/or species.

Consider now the format of the output tapes. Reproductions of these for a typical run are presented below in Figs. 34 through 37. Figure 34 gives the results of the statistical mechanical calculation. The J index identifies each electronic level; the V(K) index identifies each vibrational level, and the K index equals V(K) + 1. It should be noted that symbols followed by the Roman numeral 1[Q1(J), N1(J), etc.] have been calculated from the anharmonic oscillator model; whereas, those symbols followed by the Roman numeral 2 have been calculated from the Morse Model. The energy levels (in cm^{-1}) and number densities (cm^{-3}) are presented for each vibrational level [E1(J, K), E2(J, K), N1(J, K) and N2(J, K)]. The number densities (in cm^{-3}) and partition functions are presented for each electronic level [N1(J), N2(J), Q1(J) and Q2(J)]. The remaining quantities are input data and are defined in card groups 3 and 9 of Table 17.

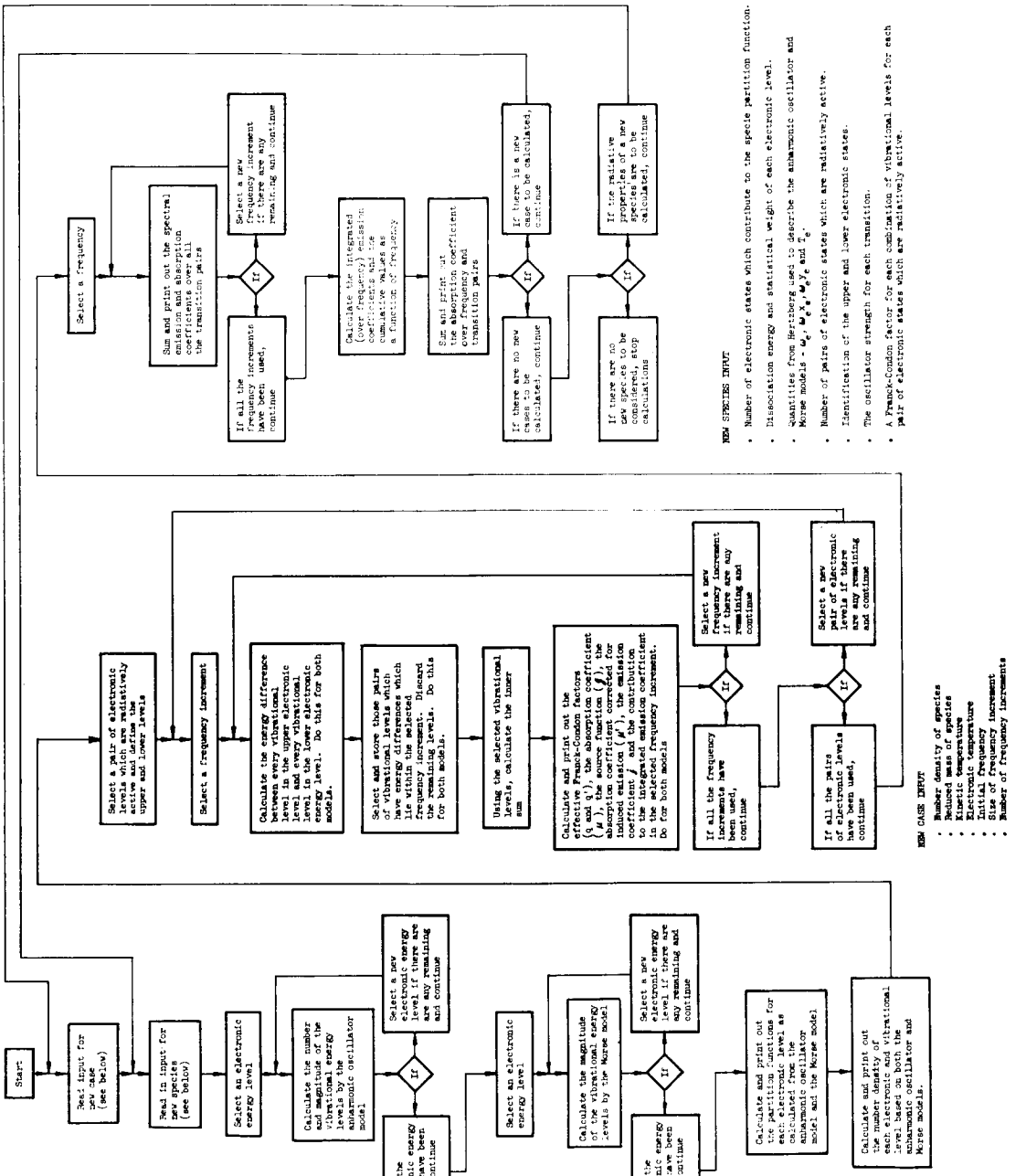

Fig. 33 Flow Chart, Molecular Species Radiation Program

Table 17

INPUT DATA FOR THE MOLECULAR SPECIES RADIATION PROGRAM

Card Group	Format	FORTRAN Symbol	Algebraic Symbol	Comment
1	72H		Title	Any information may be punched in Columns 2-72
2	I6	NES		Number of electronic states (maximum of 10)
3	6E12.8	DE(J)	$D_e(cm^{-1})$	Dissociation energy of electronic state
		WE(J)	$\omega_e(cm^{-1})$	Molecular constants in standard notation
		WEXE(J)	$\omega_e x_e(cm^{-1})$	
		TE(J)	$T_e(cm^{-1})$	
		WEYE(J)	$\omega_e y_e(cm^{-1})$	
		G1(J)	g	Statistical weight
		(1 ≤ J ≤ NES)		(One of these cards is read in for each electronic state)
4	I6	NSPS		Number of transition pairs (maximum of 6) (one transition pair per band system)
5	6E12.8	FLU(L)	f_{LU}	Electronic oscillator strength
		(1 ≤ L ≤ NSPS)		
6	12I6	NS1(L)		Upper state of each transition pair
		NS2(L)		Lower state of each transition pair
		(1 ≤ L ≤ NSPS)		
7	2I6	NVP		Number of v' entries in $q_{v'v''}$ table (maximum of 26)
		NVPP		Number of v'' entries in $q_{v'v''}$ table (maximum of 26)

Table 17 (cont.)

Card Group	Format	FORTRAN Symbol	Algebraic Symbol	Comment
8	6E12.8	QV(L, M, N) (1 ≤ N ≤ NVPP) (1 ≤ M ≤ NVP)	$q_{v', v''}$	Franck-Condon factors v'' varies first, viz. input QV(L, 1, 1) QV(L, 1, 2) : QV(L, 2, 1) QV(1, 2, 2) : etc. (Card groups 7 and 8 are repeated for each transition pair)
9	6E12.8	XNI	$N_i(cm^{-3})$	Species number density
		XMUA	μ_a(atomic units)	Reduced molecular mass
		TI	T(°K)	Kinetic temperature
		THETA	θ(°K)	Electronic temperature
		VL	$\nu_L(cm^{-1})$	Lower spectral limit
		DV	$\Delta\nu(cm^{-1})$	Spectral step size
10	2I6	NC		Number of steps between lower and upper spectral limits (maximum of 100)
		NEWDAT		If NEWDAT = 0 after completing calculations program reads in new cards 9 and 10 and redoes calculation If NEWDAT = 0 after completing calculations program reads in new specie beginning with card group 1.

MOLECULAR SPECIES RADIATION CHEMICAL CONSTITUENT - N2
T(I)= 23200.0 N(I)= 1.11500E 16 MU(A)= 7.00377E 00 THETA= 6330.0

J	DE	WE	WEXE	TE	WEYE	Q1(J)	N1(J)	Q2(J)	N2(J)
1	7.87064E 04	2.35961E 03	1.44560E C1	0.	7.51000E-03	7.68590E 00	1.11491E 16	7.82311E 00	1.11491E 16
2	2.89300E 04	1.46037E 03	1.38910E C1	5.02060E 04	-2.50000E-02	1.16676E 01	7.65011E 11	1.20879E 01	7.78710E 11
3	3.73525E 04	1.73411E 03	1.44700E C1	5.96260E 04	0.	1.01370E 01	1.42411E 11	1.05799E 01	1.46044E 11
4	4.67914E 04	1.69201E 03	1.27910E C1	6.92900E 04	-3.48900E-01	1.07136E 01	5.65640E 09	1.04163E 01	5.40266E 09
5	6.72829E 04	2.03510E 03	1.70800E C1	8.91470E 04	-2.15000E 00	1.30274E 01	2.01847E 08	8.85859E 00	1.34802E 08

J	K	V(K)	E1(J,K)	N1(J,K)	E2(J,K)	N2(J,K)
1	1	-0.	1.17619E C3	1.45059E 15	1.17521E 03	1.42514E 15
	2	1.0000CE 00	3.50691E C3	1.25540E 15	3.49910E 03	1.23390E 15
	3	2.0000CE 00	5.80879E C3	1.08842E 15	5.78764E 03	1.07067E 15
	4	3.0000CE 00	8.08187E C3	9.45343E 14	8.04081E 03	9.31072E 14
	5	4.0000CE 00	1.03262E C4	8.22535E 14	1.02586E 04	8.11451E 14
	6	5.0000CE 00	1.25418E C4	7.16956E 14	1.24411E 04	7.08750E 14
	7	6.0000CE 00	1.47288E C4	6.26041E 14	1.45482E 04	6.20407E 14

Fig. 34 Plate 1, Molecular Species Output Format

Figure 35 gives pertinent radiation property data associated with the transition between two specified electronic levels; viz., Transition pair 3 and 2 are averaged over a specified frequency range (in ev.). The absorption coefficients (in cm^{-1}) are presented (MUBAR1 and MUBAR 2) as are the effective Franck-Condon factors (SM. Q1 and SM. Q2) as defined by Eq. (3. 35) and the effective Franck-Condon factors (SM. QP1 and SM. QP2) as defined by Eq. (3. 36). The remaining quantities are input data.

MOLECULAR SPECIES RADIATION CHEMICAL CONSTITUENT - N2
T(I)= 23200.0 N(I)= 1.11500E 16 MU(A)= 7.00377E 00 THETA= 6330.0

TRANSITION PAIR 3 AND 2

FREQUENCY RANGE		MUBAR1	MUBAR2	SM.Q1	SM.Q2	SM.QP1	SM.QP2
1.23954E 00	1.48745E 00	5.15049E-07	5.26580E-07	3.80209E-05	3.81882E-05	4.00248E-05	3.98897E-05
1.48745E 00	1.73536E 00	7.55157E-07	7.62129E-07	5.57456E-05	5.52705E-05	5.18448E-05	5.11386E-05
1.73536E 00	1.98327E 00	6.97668E-07	7.16399E-07	5.15018E-05	5.19541E-05	4.21354E-05	4.24507E-05
1.98327E 00	2.23118E 00	5.92185E-07	5.29935E-07	4.37150E-05	3.84315E-05	3.20143E-05	2.84107E-05
2.23118E 00	2.47909E 00	1.19761E-07	1.24235E-07	8.84073E-06	9.00970E-06	5.84822E-06	6.08283E-06

Fig. 35 Plate 2, Molecular Species Output Format

Figure 36 gives the source functions [CAP. J (NUBAR) 1 and CAP. J (NUBAR) 2], the absorption coefficients corrected for induced emission [CAP. MU (NUBAR) 1 and CAP. MU (NUBAR) 2], the integrated emission coefficients (JI1 and JI2) and the spectral emission coefficients (J1 and J2), all for a particular transition pair (band system) and all averaged over the frequency increments specified in Fig. 35 although presented in Fig. 36 at discrete (mean) frequencies. The remaining quantities are input information.

MOLECULAR SPECIES RADIATION CHEMICAL CONSTITUENT - N2
T(I)= 23200.0 N(I)= 1.11500E 16 MU(A)= 7.00377E 00 THETA= 6330.0

TRANSITION PAIR 3 AND 2

NUBAR (EV)	CAP.J (NUBAR)1 (ERGS/CM2-SEC-EV-STER)	CAP.J (NUBAR)2 (ERGS/CM2-SEC-EV-STER),	CAP.MU (NUBAR)1 (1/CM)	CAP.MU (NUBAR)2 (1/CM)	JI1 (ERGS/CM3-SEC-STER)	JI2 (ERGS/CM3-SEC-STER)	J1 (ERGS/CM3-SEC-EV-STER)	J2 (ERGS/CM3-SEC-EV-STER)
1.36316E 00	1.38871E 10	1.38820E 10	4.64583E-07	4.75001E-07	0.	0.	6.45171E 03	6.59395E 03
1.61101E 00	1.99980E 10	2.00481E 10	6.89787E-07	6.96004E-07	2.50959E 03	2.54696E 03	1.37944E 04	1.39536E 04
1.85885E 00	2.67201E 10	2.68986E 10	6.44541E-07	6.61508E-07	6.35422E 03	6.48216E 03	1.72222E 04	1.77936E 04
2.10670E 00	3.45192E 10	3.51490E 10	5.51819E-07	4.93199E-07	1.08501E 04	1.08366E 04	1.90483E 04	1.73354E 04
2.35455E 00	4.32250E 10	4.45279E 10	1.12387E-07	1.16370E-07	1.38134E 04	1.36277E 04	4.85793E 03	5.18172E 03

Fig. 36 Plate 3, Molecular Species Output Format

Figure 37 gives the absorption coefficients, [MUBAR 1 and MUBAR 2], the absorption coefficients corrected for induced emission [CAP. MUT 1 and CAP. MUT 2], and the integrated emission coefficients [JT1 1 and JTI 2], all averaged over the indicated frequency ranges and all summed over all the band systems for the given specie. The absorption coefficients are in cm^{-1}. The remaining quantities are input information.

MOLECULAR SPECIES RADIATION CHEMICAL CONSTITUENT - N2
T(I)= 23200.0 N(I)= 1.11500E 16 MU(A)= 7.00377E 00 THETA= 6330.0

TOTAL MUBAR

FREQUENCY RANGE		MUBAR1	MUBAR2	CAP.MUT1	CAP.MUT2	JTI1 (ERGS/CM3-SEC)	JTI2 (ERGS/CM3-SEC)
1.23954E 00	1.48745E 00	5.15045E-07	5.26580E-07	4.64583E-07	4.75001E-07	0.	0.
1.48745E 00	1.73536E 00	7.55157E-07	7.62129E-07	6.89787E-07	6.96004E-07	2.02461E 07	2.05475E 07
1.73536E 00	1.98327E 00	6.97668E-07	7.16399E-07	6.44541E-07	6.61508E-07	5.12626E 07	5.22948E 07
1.98327E 00	2.23118E 00	5.9279CE-07	5.30090E-07	5.52422E-07	4.93353E-07	8.75338E 07	8.74240E 07
2.23118E 00	2.47909E 00	1.2304CE-07	1.25545E-07	1.15659E-07	1.17677E-07	1.11445E 08	1.09943E 08

Fig 37 Plate 4, Molecular Species Output Format

This program has been written in FORTRAN 2 version 3. It takes one case roughly one minute to run on the IBM 7094 computer facility at LMSC.

A.7 FREE-BOUND EMISSION COEFFICIENT PROGRAM

This program calculates the equilibrium and/or nonequilibrium, spectral, and total emission coefficients for the radiation properties associated with the atomic free bound emission process. In its present form, two distinct codes exist. One is used for nitrogen atoms and ions, and the other is used for oxygen atoms and ions. Both are applicable for frequencies from about 0.5 ev to 20 ev. In principle, the code has enough generality to be extended to include new species; however, it is recommended that this not be attempted due to the complexity of the input data.

A flow chart of the essential features of the code is given in Fig. 38. This chart is described in physical terms and is meant to give an overview of the code as a whole. It is self-explanatory except for the reference to the inner sums which are the double sums in Eq. (3.46).

The FORTRAN notation is defined and presented in Tables 18 and 19 along with a description of the first 9 card groups of the deck which contain the input data required to run the code. It should be noted that only card groups 6 and 7 need be changed for each new case (electronic temperature, kinetic temperature, and number density) whereas card groups 1 through 5, 8 and 9, must be changed for each new specie. Cases are stacked by adding new case input cards (with the same kind of information as that presented on card groups 6 and 7) behind card group 9.

Consider, now, the format of the output tapes. A reproduction of a typical run is presented in Fig. 39. Presented there are the frequencies [HNUI (EV) in ev and HNUI (1/CM) in cm^{-1}], the emission coefficient [JHNU(I)], the effective cross section [CJHNU(I)], the integrated (over frequency) emission coefficient (JHNUT in ergs/cm^3 sec ster), the integrated (over frequency) effective cross section (CJHNU in ergs cm^3/ sec ster), the partition function (Q), and the partial density of the specified specie (RHOI in gm/cm^3).

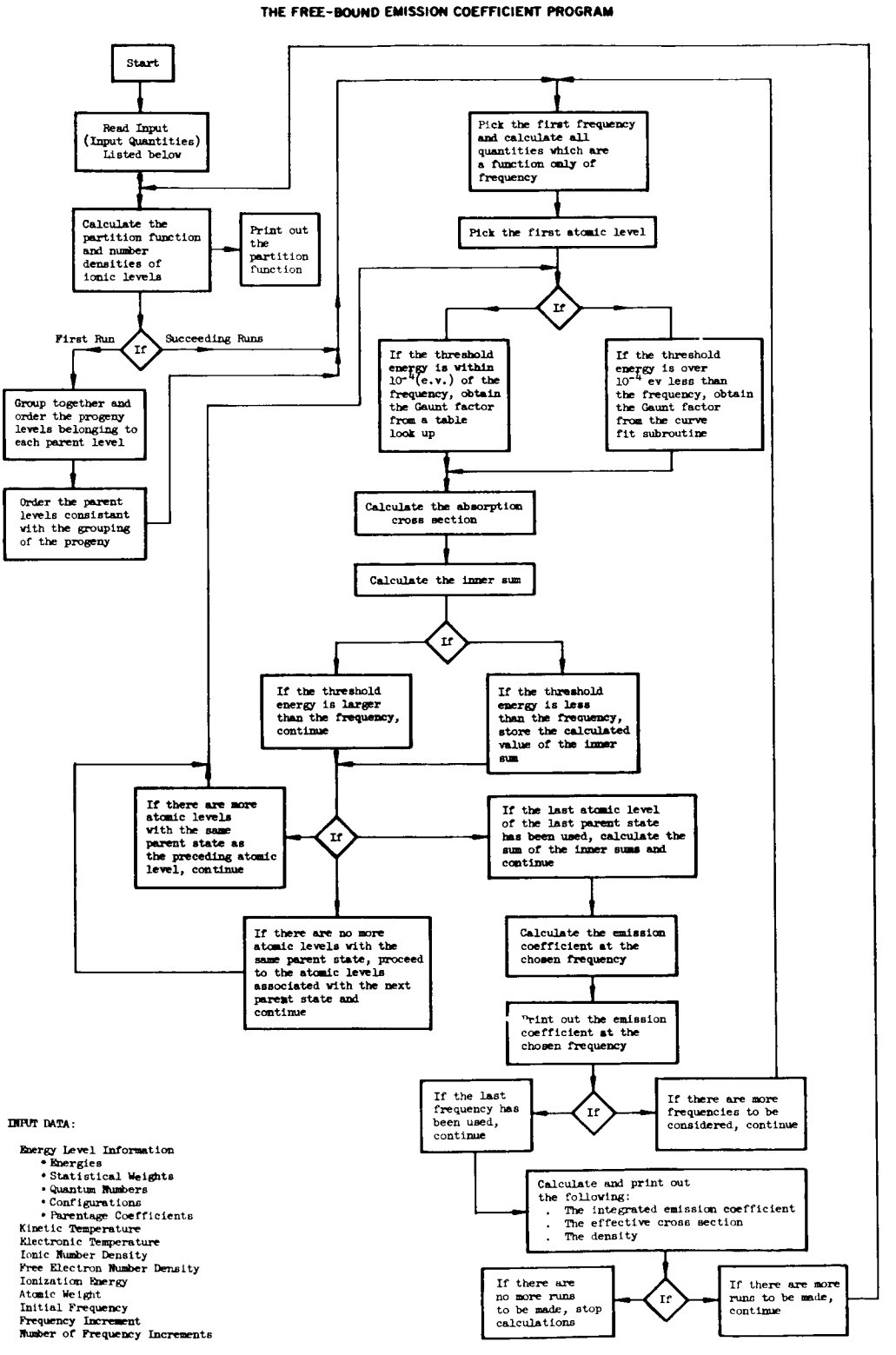

Fig. 38 Flow Chart, Free-Bound Emission Coefficient Program

Table 18

INPUT FOR NITROGEN VERSION OF FREE-BOUND EMISSION COEFFICIENT PROGRAM

Card Group	Format	FORTRAN Symbol	Algebraic Translation	Comment
1	72H		Title	Any Info CC 2-72
2	2I3	N, KN		N = NO. of PN(I), E1(1, I) G1(1, I), CODE (I). KN = NO. OF E1(2, I), G1(2. I).
3	4E12. 8	PN(I), E1(1, I), G1(1, I), CODE (I)	n, $E(cm^{-1})$ g	Principal quantum number, energy, and statistical weights of atomic levels
4	12X, 2E12. 8	E1(2, I), G1(2, I),	$E(cm^{-1})$ g	Energy of ionic levels Statistical weights of ionic levels
5	7F4. 2	XF(I, J)		I = 78, 85 J = 1, 7
6	3E12. 8, I3	DV, HNUMN, THETA, NC	$\delta\nu(cm^{-1})$, $h\nu_{min}(cm^{-1})$ $\theta(°K)$	Frequency increment, minimum frequency electronic temperature, number of frequency increments
7	5E12. 8	XNI, XNE, TI, XI, A	$N_i(cm^{-3})$, $N_e(cm^{-3})$, $T_i(°K)$, $X_i(cm^{-1})$, A_i	Number density of ions (N_i) and electrons (N_e), kinetic temperature, ionization potential, and atomic weight
8	4E12. 8	PN(I), E1(1, I), G(1, I), CODE (I)	n, $E(cm^{-1})$ g	Same information as in 5 except that these are read-in consistent with the fractional parentages. I = 1, N
9	12X, 2E12. 8	E(2, I) G(2, I)	$E(cm^{-1})$ g	I = 1, KKN Where KKN = KN - 6, (READ IN ONLY ONCE)

Note: Card groups 6 and 7 constitute 1st case. Additional cases are stacked after group 9.

Table 19

INPUT FOR OXYGEN VERSION OF FREE-BOUND EMISSION COEFFICIENT PROGRAM

Card Group	Format	FORTRAN Symbol	Algebraic Translation	Comment
1	72H		Title	Any Info CC 2-72
2	2I3	N, KN		N = NO. of PN(I), E1(1, I), G1(1, I), CODE (I). KN = NO. OF E1(2, I), G1(2, I).
3	4E12.8	PN(I), E1(1, I), G1(1, I), CODE (I)	n, $E(cm^{-1})$ g	Principal quantum numbers, energy and statistical weights of atomic specie levels
4	12X, 2E12.8	E1 (2, I) G1 (2, I)	$E\ (cm^{-1})$ g	Energy of ionic levels, statistical weights of ionic levels
5	3F4.2	XF (I, J)		I = 53, 57 J = 1, 3
6	3E12, 8, I3	DV, HNUMN, THETA, NC	$\delta\nu(cm^{-1})$, $h\nu_{min}(cm^{-1})$ $\theta(°K)$	Frequency increment, minimum frequency, electronic temperature, number of frequency increments
7	5E12.8	XNI, XNE, TI, XI, A	$N_i(cm^{-3})$, $N_e(cm^{-3})$, $T_i(°K)$, $X_i(cm^{-1})$, A	Number density of ions (N_i) and electrons (N_i), kinetic temperature, ionization potential and atomic weight
8	4E12.8	PN(I), E1(1, I), G(1, I), CODE (I)	n, $E(cm^{-1})$, g	Same information as in 5 except that these are read in consistent with fractional parentages. I = 1, N
9	12X, 2E12.8	E(2, I) G(2, I)	$E(cm^{-1})$ g	I = 1, KKN Where KKN = KN - 12 (READ IN ONLY ONCE)

Note: Card groups 6 and 7 constitute 1st case. Additional cases are stacked after card group 9.

```
FREE-BOUND EMISSION COEFFICIENTS      OXYGEN CASE

      JHNU IS IN THE UNITS ERGS/CM**3 SEC STER E.V.

     CJHNU IS IN THE UNITS ERGS CM**3/SEC STER E.V.

XNI= 4.78000E 15   XNE= 3.27900E 16   DV= 2.00000E 03   XI= 1.09837E 05

TI = 1.11000E 04   THETA= 1.11000E 04   Q= 1.08530E 00   A= 1.60000E 01

RHOI= 1.26949E-07   JHNUT= 2.66486E 07   CJHNU= 1.70022E-25


 HNUI(EV)       HNUI(1/CM)       JHNU(I)          CJHNU(I)

0.50000E-00     0.40337E 04     0.               0.
0.74791E 00     0.60337E 04     0.19506E 06      0.12445E-26
0.99582E 00     0.80337E 04     0.49054E 06      0.31297E-26
0.12437E 01     0.10034E 05     0.42036E 06      0.26820E-26
0.14916E 01     0.12034E 05     0.70195E 06      0.44786E-26
0.17395E 01     0.14034E 05     0.13330E 07      0.85044E-26
0.19875E 01     0.16034E 05     0.12010E 07      0.76627E-26
0.22354E 01     0.18034E 05     0.92231E 06      0.58845E-26
```

Fig. 39 The Output Format of the Free-Bound Emission Coefficient Program

A.8 RADIATIVE HEATING PROGRAM

The purpose of this program is to evaluate Eq. (3.76) for an arbitrary surface point of a body immersed in a given axisymmetric hypersonic flow. The program assumes that the flow field is described by a cylindrical (x, r, φ) coordinate system, with origin at the shock vertex, and the x-axis pointing downstream. In evaluating Eq. (3.76), it is usually desirable (and often necessary) to divide the flow region in the $\varphi = 0$ plane into several strips parallel to the x-axis, and to calculate the contribution from the gas in each strip. Each strip may in turn be divided into several regions, bounded by surfaces x = constant, for the purpose of curve-fitting the spatial distribution of the emission coefficient. The procedure for preparing the input-data deck for one such strip is detailed below.

Card group I (Format 6 I 4) contains the two controls

N — The number of curve-fit regions (in the x direction) for either E [see Eq. (3.75)], if IOPS = 5, or p and h, if IOPS < 5.

IOPS — If IOPS < 5, it designates the emissivity data used to construct the curve fits in subroutine PROP, which calculates μ_p and T as functions of p and h, for thermodynamic equalibrium. Thus

IOPS =	1	Sets $\mu_p = 0$
	2	AVCO data
	3	LMSC lower-bound data
	4	LMSC upper-bound data

IOPS — If IOPS equals 5, then E itself is specified in the flow field (by means of spatial curve fits)

Card Group II (Format 6E 12.8) consists of 4N cards, in groups of four cards for each curve fits region I, I = 1 to N. These contain the curve-fit coefficients in the spatial expansion of p and h,

A (I, J)	J = 1 to 11	on cards 1 and 2
B (I, J)	J = 1 to 11	on cards 3 and 4

defined by

$$\log_{10} P = A(I,1) + A(I,2)X + A(I,3)Y + A(I,4)X^2 + A(I,5)XY + A(I,6)Y^2 + A(I,7)X^3 + A(I,8)X^2Y + A(I,9)XY^2 + A(I,10)Y^3 \quad \text{(A. 12)}$$

and

$$H = B(I,1) + \ldots + B(I,10)Y^3 \quad \text{(A. 13)}$$

where

P = pressure p (atm) (if IOPS = 5, P = E)

H = h/h_r (leave blank if IOPS = 5); h_r = reference satellite enthalpy = 3.125×10^8 ft^2/sec^2 = 12,474 Btu/lb

X and Y are transformed coordinates defined by

$$X = AA(I,1)x + BB(I,1) \quad \text{(A. 14)}$$

$$Y = AA(I,2)r + BB(I,2) \quad \text{(A. 15)}$$

and A(I,11) = maximum value of x for curve-fit region I.

Card Group III (Format 6E12.8) contains the transformation coefficients (six to a card)

AA(I, 1), BB(I, 1)AA(I, 2)BB(I, 2) I = 1 to N

Card Group IV (Format 6E12.8) contains the two quantities

P1 The value of P at the stagnation point (if IOPS = 5, P1 = E_0, the value of E at the stagnation point)

H1 The value of H at the stagnation point (leave blank if IOPS = 5)

Card Group V (Format 6E12. 8) contains the six quantities

R0	The r coordinate of the given body surface point
XB1	The x coordinate of the given body surface point
TH	The slope of the plane tangent to the body at the given surface point (Leave blank if R0 = 0)
ALP	Angle-of-attack option which is not yet programmed, therefore leave blank
DUM < 0	Program returns to Group I input after completion
= 0	Program returns to Group V input after completion
> 0	Program returns to Group VI input after completion
XB0	x coordinate of the stagnation point

Card Group VI (Format 6I4) contains the four quantities

K	The number of r values in the integration strip
K1	Case number
IO ≦ 0	Shock coordinates read in
> 0	Shock coordinates calculated from an equation
NCP = 1 ,	Integration proceeds from the shock to either the tangent plane (if TH > 0) or to x = XF
= 2 ,	Integration proceeds from the tangent plane (for TH < 0) to x = XF
= 3 ,	Integration proceeds from x = ZD to x = XF (for TH < 0)

Card Group VII (Format 6E12. 8) contains the four quantities

DX	Δx, the mesh size in the x direction
DR	Δr, the mesh size in the r direction
XF	The maximum value of x for the entire integration (if R0 = 0, set XF = XB0)
ROO	The initial r coordinate for the integration

If NCP = 2 or 3, then Card Group VIII (Format 6E12. 8) contains the six quantities

XM	The slope of the separating streamline
X10	The x coordinate of the separation point

R10 The r coordinate of the separation point

P10 The constant value of P in the base flow region

H10 The constant value of H in the base flow region

ZD Initial value of x if NCP = 3 (leave blank if NCP = 2)

If NCP = 1, I0 $\leqq$ 0, Card Group VIII (Format 6E12.8) lists the x coordinates of points on the shock spaced at Δr intervals (six to a card)

XS(I) I = 1 to K

If NCP = 1, I0 > 0, Card Group VIII (Format 6E12.8) contains the coefficients

A(9,1), A(9,2), A(9,3),

defined by the shock equation

$$A(9,1)x^2 + A(9,2)x + A(9,3)r^2 = 0 \qquad \text{(A.16)}$$

The print out is for the most part self explanatory. It first lists the emissivity option, curve fit coefficients, transformation coefficients, and E_0 (E-stagnation). If IOPS < 5, the row headed E-STAGNATION is followed by seven numbers. The first number is the quantity $E_0/2\sigma = \mu_p T^4$ [in $(°K)^4$/ft], which is calculated from P1 and H1 using subroutine PROP. The other six numbers comprise the output of that subroutine which was used to evaluate the first one.

The next row lists the following input quantities for the particular case:

Case No., R0, XBI, ROO (labeled RF), DX, DR, and ALP

There then follow columns of output data presenting the cumulative results of summation over each row of cells. (For the first five rows results are presented for each

cell.) These are presented primarily for diagnostic purposes. The actual results of the program are embodied in the last line, illustrated in the sample listing

```
      R0          XB(R0)        Q(RMAX)      Q/E0*RS    K= 292
0.24841E 02 0.83818E 01 0.36209E 11 0.18821E 01
```

where

R0	=	r-coordinate of surface point
XB(R0)	=	XB1 = x-coordinate of surface point
Q(RMAX)	=	contribution of the last cell to the summation
Q/E0*RS	=	q_R/E_o as defined by Eq. (3.76)
K	=	number of rows in the summation

The value of q_R is then obtained by multiplying q_R/E_o by the value of E_o which is listed near the beginning of the printout. If IOPS < 5, as noted above, this number must be also multiplied by 2σ, in appropriate units.

The computing time required to calculate q_R for a given surface point varies greatly with the location of the point and the nature of the flow, which determine the number of strips required. Typical values range from 3 to 10 minutes on the IBM 7090. A schematic flow chart for the program appears in Fig. 40.

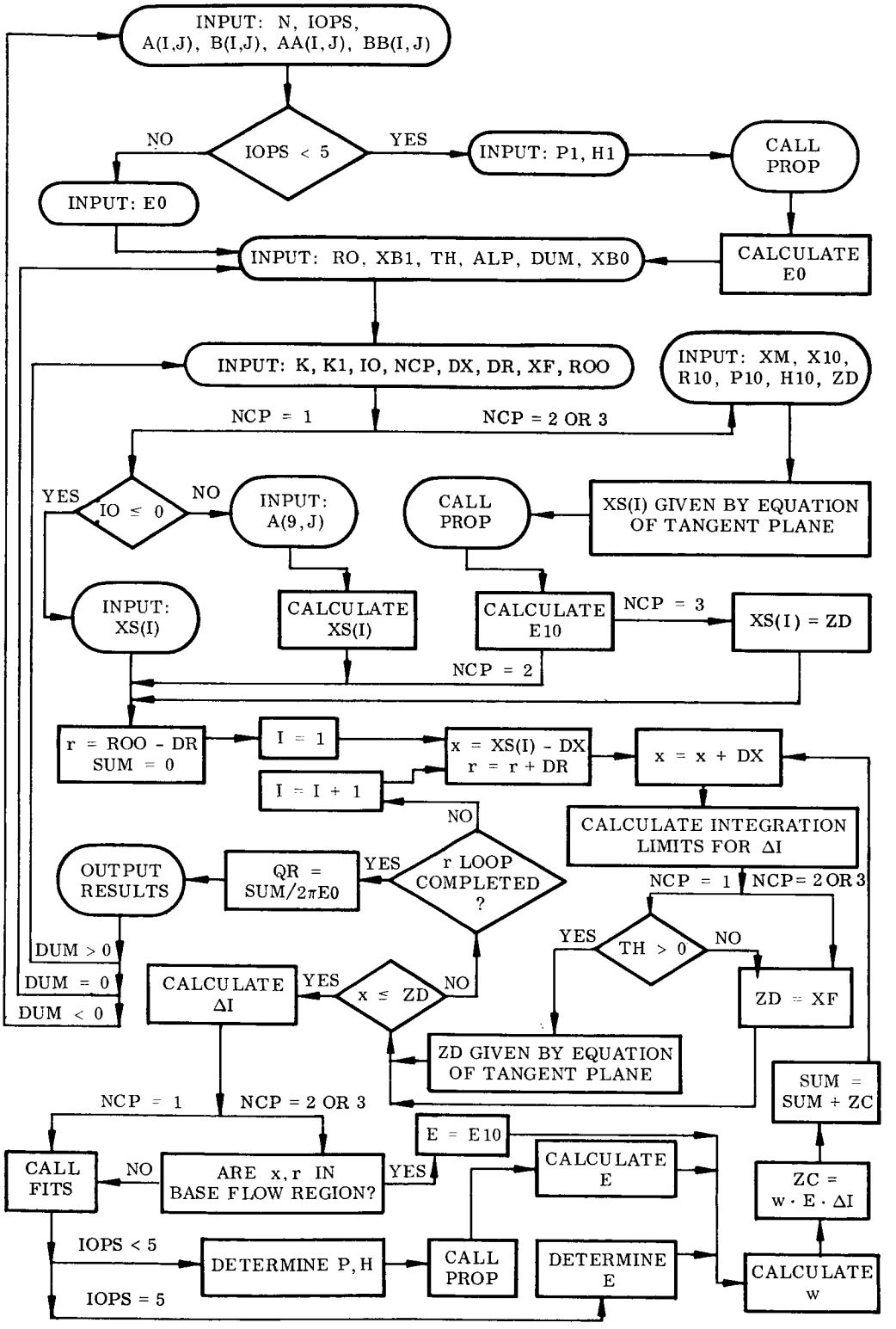

Fig. 40 Flow Chart – Radiative Heating Program

Appendix B
CHEMISTRY CALCULATION ALONG THE AXIAL STREAMLINE

As indicated in subsection 2.3, the underlying assumptions for the streamtube method break down in the vicinity of the axis of symmetry. This is due to the fact that the equilibrium pressure changes along streamlines in this region are so small as to be of the same order as the changes in pressure due to the nonequilibrium processes. Since the latter are assumed to be negligible, the equilibrium pressure distribution is not useful in relating spatial and time variations along streamlines. Similarly, the equilibrium velocity behind a normal shock (for hypersonic flow conditions) is so small as to be of the same order as its departure from the corresponding frozen velocity. Thus, the specification of the equilibrium velocity distribution also is not helpful.

Fortunately, Chisnell (Ref. 63) has recently derived a simple analytic expression for the velocity field in terms of the density distribution, valid in the stagnation regime of bodies in nonequilibrium hypersonic flow. The equations were previously derived by Freeman (Ref. 64). He showed that if the density in the shock layer is large, compared to the free-stream density, then the curvature terms and the pressure gradient term normal to the axis in the inviscid flow equations are correspondingly small. If we use the shock-oriented cylindrical (r, x) coordinates of subsection 3.1.1. which are non-dimensionalized by the shock nose radius, Eq. (2.1) and the r-component of Eq. (2.2) can be written (neglecting the small terms)

$$\frac{\partial}{\partial x}(\bar{\rho}\bar{u}) + \frac{1}{r}\frac{\partial}{\partial r}(\bar{\rho}\bar{v}r) = 0 \qquad \text{(B.1)}$$

$$\bar{v}\frac{\partial \bar{v}}{\partial r} + \bar{u}\frac{\partial \bar{v}}{\partial x} = 0 \qquad \text{(B.2)}$$

where $\bar{u}, \bar{v}$ are velocity components in the x, r directions, $\bar{\rho}$ is the density, and these variables have been nondimensionalized by their free-stream values. Note that these equations are equally valid for nonequilibrium flow, since the energy equation is not utilized. For solutions close to the axis we now make the Dorodnitzyn transformation

$$z = \int_0^x \bar{\rho}\, dx' \tag{B.3}$$

To the lowest order in $r, \bar{\rho}\bar{u}$ and $\bar{v}/r$ are functions of z only, with the boundary conditions at the shock wave

$$\bar{\rho}\bar{u} = 1, \quad \bar{v} = r \quad \text{at} \quad z = 0 \tag{B.4}$$

Equations (B.1) and (B.2), therefore, become ordinary differential equations in z, subject to conditions (B.4). The solution is readily found to be

$$\bar{\rho}\bar{u} = (1 - z)^2 \tag{B.5}$$

$$\bar{v} = r(1 - z) \tag{B.6}$$

From Eq. (B.5) it follows that the shock standoff distance in this approximation is given by $z = 1$.

In order to utilize Chisnell's solution in the streamtube program, the density distribution along the streamline must be given. But this distribution can be estimated using the streamtube program itself. We note that since the pressure and enthalpy change very little throughout the stagnation region, the timewise chemical history experienced by a fluid particle after crossing the shock wave is approximately that experienced in a constant-pressure, constant-enthalpy bath. We therefore carry out a streamtube calculation prescribing a constant pressure. Since velocity changes in that program

are determined by pressure changes (through the momentum equation), a constant velocity (and therefore constant enthalpy) will result. The fictitious distance along the streamline is then exactly proportional to the time. The output of the program can thus be interpreted as the timewise evolution of the chemical state of the fluid particle as it moves along the streamline. In particular, the time dependence of the density, $\bar{\rho}(t)$, is obtained. The integration is carried out for a time (or fictitious distance) long enough to enable $\bar{\rho}$ to approach its equilibrium value within a predetermined error, at which time it is terminated.

There remains the problem of relating the time to the actual physical distance along the streamline. For simplicity, this relation is derived for the axial streamline. If the time t is properly nondimensionalized, then $\bar{u}$ is given by

$$\bar{u} = \frac{dx}{dt} \tag{B.7}$$

Using Eqs. (B.3) and (B.5) we obtain

$$\bar{\rho}\bar{u} = \frac{dz}{dt} = (1 - z)^2 \tag{B.8}$$

whose solution is

$$t = z/(1 - z) \tag{B.9}$$

where we have set $t = 0$ at the shock wave. The physical distance x is then found by inverting (B.3) to obtain

$$x(z) = \int_0^z \frac{dz'}{\bar{\rho}\,[t(z')]}\,, \tag{B.10}$$

The integration being performed numerically, using the $\bar{\rho}(t)$ distribution found earlier. Equations (B. 9) and (B. 10) give the required relation between x and t. The standoff distance, x(1), as given by Eq. (B. 10) will not be equal to the equilibrium standoff distance, partly because of the approximate nature of the analysis and the changes in the shock-layer structure due to nonequilibrium effects. In order to be consistent with results of the streamtube program away from the stagnation region, which assumed the equilibrium flow geometry to be exchanged, the distance x as determined by Eq. (B. 10) was scaled in order to let x(1) equal the equilibrium standoff distance.

The above results give a first approximation to the state of the gas on the axial streamline. An improved distribution is obtained by solving Eq. (B. 5) for

$$\bar{u}(z) = (1 - z)^2/\bar{\rho}[t(z)] \qquad \text{(B. 11)}$$

which, together with Eq. (B. 10), gives a parametric representation of the velocity distribution on the streamline. This distribution is then used as input in a second streamtube calculation (specifying velocity instead of pressure) which gives improved results for the state of the gas. This calculation must also be terminated before the stagnation point is reached and graphical extrapolation to the known stagnation equilibrium values is required. The results for the axial streamline of Case III are shown in Fig. 10 and Table 7. 1.

Appendix C

CHECK OF THE EFFECT OF NONEQUILIBRIUM CONCENTRATIONS IN VISCOSITY CALCULATIONS

The particle transport coefficients, in particular the viscosity coefficients, used in the present study were obtained from tabulated values based on small departures from equilibrium states in high-temperature air (Ref. 65). A question naturally occurs concerning the validity of using these values for gaseous states in which the local species composition is out of equilibrium with the local temperature and pressure. These conditions exist in the present analysis. Emphasis here is directed to estimating the magnitude of the effects of the nonequilibrium composition on the values of the viscosity coefficients. These coefficients are, in turn, used in the convective heat-transfer analysis.

To check these effects, viscosity calculations were made, based on the actual gas composition found in the region of rapid expansion near the corner of the forebody. The effects of the chemical rate processes are magnified in this region because of the local existence of a large acceleration in the flow velocity. (In fact, the local composition in this region was found to be virtually frozen with a large concentration of ions ard free electrons as well as almost complete dissociation of the molecular species). The corresponding translational temperature in this region undershot the local equilibrium level by almost a factor of 4, with an associated nonequilibrium rise in the density level. The calculated local viscosity coefficients based on the nonequilibrium compositions were compared to those based on local equilibrium compositions. The latter were those used in the heat-transfer analysis.

The comparison can be seen in Fig. 41, which shows the viscosity values based on the nonequilibrium compositions as well as the Hansen (Ref. 65) "equilibrium-based" values corresponding to this range of temperature and pressure. The temperature range over which the check calculations were made is from 2780 to 7040° K, with an

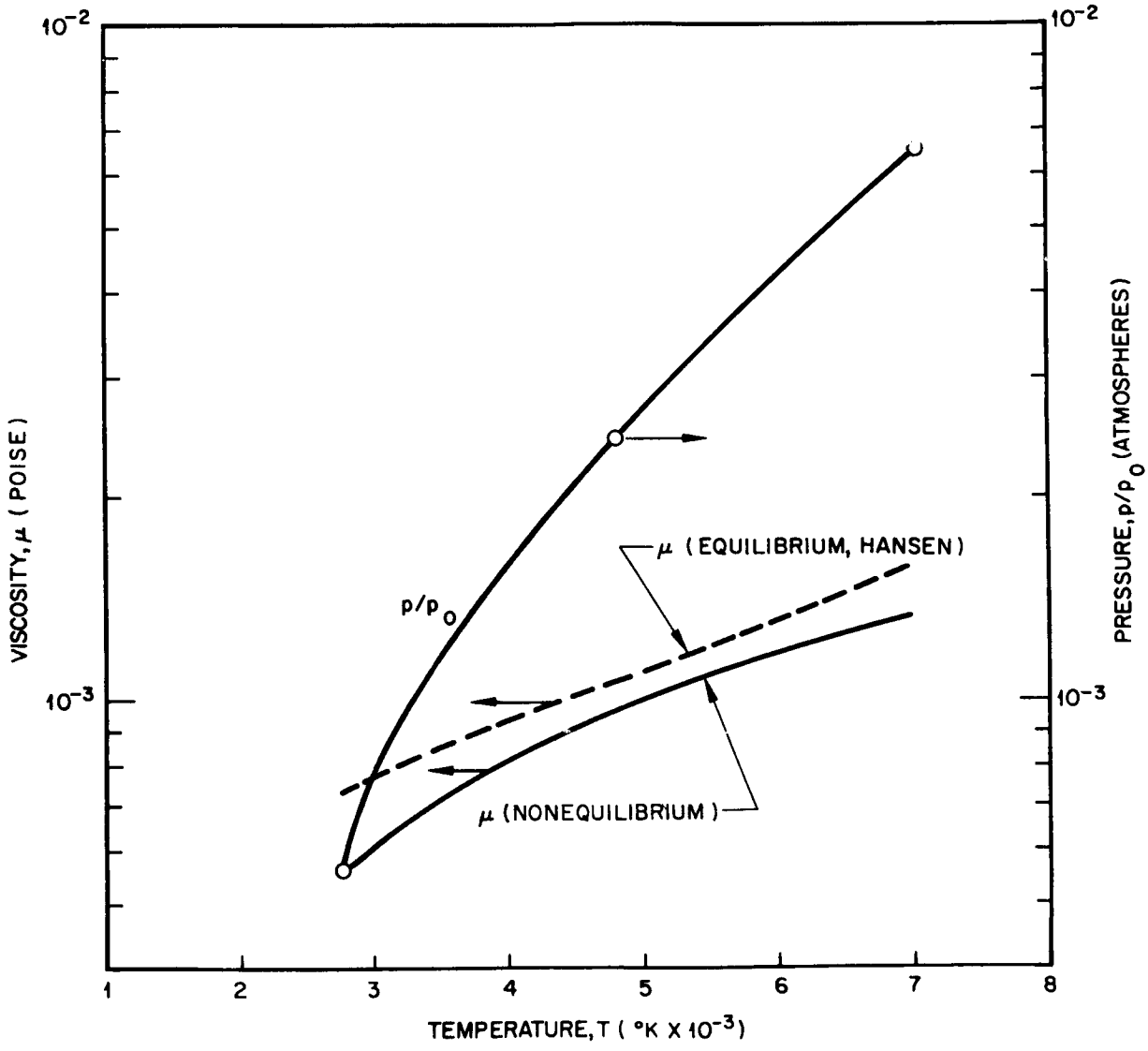

Fig. 41 Effect of Nonequilibrium Concentrations on Viscosity

associated pressure range of 5.6×10^{-4} to 6.6×10^{-3} atmospheres. This interval includes the region where pronounced variation between equilibrium and nonequilibrium composition was noted. The deviation from equilibrium based property values that was associated with use of the nonequilibrium composition is seen to result in a decrease in the viscosity coefficient values in this region. This decrease is small, ranging from a maximum difference of about 22 percent down to about 10 percent. The variation is of the same size or less than the differences existing between the values based on equilibrium compositions used by several investigators (Refs. 65, and 66). The relative size of deviations, considering uncertainties in the fundamental transport calculations and the rate constants governing the chemical kinetics, imply that the small deviations due to nonequilibrium composition can be disregarded in the present case without seriously prejudicing the accuracy of the results.

It is interesting to note the direction of the change corresponding to consideration of the nonequilibrium gas composition. The trends can be examined easily using a figure showing the appropriate cross sections for momentum transfer, hence the mean free paths for the various subspecies interactions.

Figure 42 shows the mean free paths computed from and associated with the calculated cross sections for the dominant momentum interaction processes considered. The mean free paths appear as a ratio of the computed value for the identified specie to the mean free path for an average "air particle" based on a Sutherland cross section. The species populous enough to affect the multiple momentum interactions, hence the viscosity in this region were (N), (O), (N^+), (O^+), and (e^-). The presence of significant nonequilibrium ion and free-electron concentrations in this range causes the decrease in viscosity as a result of the extremely short mean free paths associated with long-range electrostatic force fields in ion-ion and electron-electron interactions. It can be seen in the figure that, in this temperature range, the mean free paths associated with these coulombic interactions can be as much as 3 orders of magnitude less than those associated with neutral interactions which would dominate the corresponding equilibrium state compositions. It is clear that, for flow conditions which result in

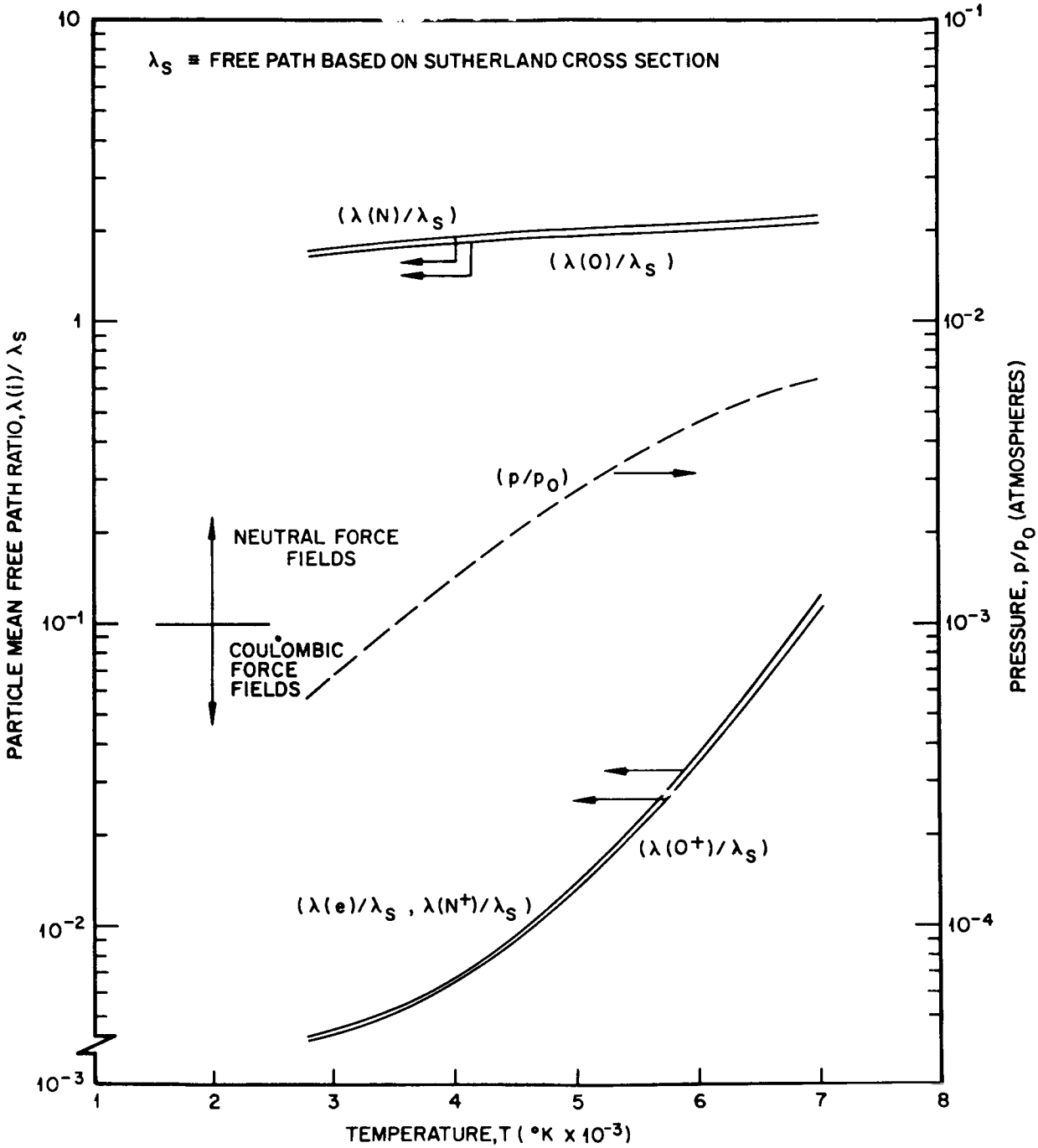

Fig. 42 Variation in Mean Free Path (Momentum Transfer) for Dominant Nonequilibrium Species

significant nonequilibrium concentrations of charged particles, care must be taken to ensure that the use of equilibrium-based values of the transport coefficients does not lead to serious error in the heat-transfer calculations.

To summarize, a comparison of the viscosity coefficients calculated using both equilibrium and nonequilibrium gas compositions indicate that relatively insignificant deviations result from the use of equilibrium-based values for Case III. The existence of such deviations does, however, indicate the importance of similar error estimates for shock-layer flows containing significant nonequilibrium populations of charged particles.